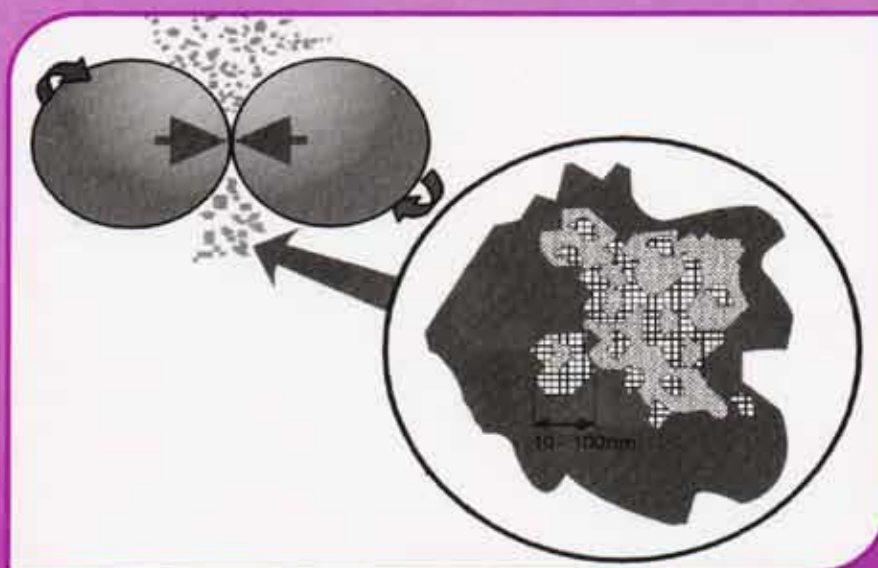


ISSN 0377-9416



Volume 32, December 2006

TRANSACTIONS OF POWDER METALLURGY ASSOCIATION OF INDIA



Editor - P. Ramakrishnan
Guest Editors - Bijoy Sarma, Ravi Kiran



Powder Metallurgy Association of India

**TRANSACTIONS OF
POWDER METALLURGY
ASSOCIATION OF INDIA**

Vol. 32, December 2006

Editor

P. Ramakrishnan

Guest Editors

Bijoy Sarma, Ravi Kiran

Powder Metallurgy Association of India

Office Bearers

President	:	D.K. Varshney
Vice Presidents	:	S.Majumdar Avinash Gore Varshney V.K. S.Ashok
General Secretary	:	Bijoy Sarma
Treasurer	:	V. Chandrasekharan
Jt.Secretaries	:	Anish Upadhyaya P. Sadeesh P.N.S. Sivan

Vol. 32, December 2006

Published by



Powder Metallurgy Association of India (PMAI)

c/o Powder Metallurgy Group, Defence Metallurgical Research Laboratory,
P.O. Kanchanbagh, Hyderabad - 500 058.

Mumbai Office : 1009, Kingston, Hiranandani Garden, Powai, Mumbai - 400 076

- Note** : Neither the Powder Metallurgy Association of India nor the editor assumes responsibility of opinions expressed by the authors of the papers published in this transaction.
- Price** : Rs. 300/- for Indian subscribers and US \$ 50 for Overseas subscribers.
- Cover** : Schematic of the collision as the main event of energy transfer

Editorial

Powder Metallurgy Association of India organized the 32nd Annual Technical Meeting with the theme-Powder Metallurgy at its best-at the Viceroy Hotel, Hyderabad during Jan.23-24, 2006. Our congratulations to Shri.D.K. Varshney, President, PMAI and Bijoy Sarma, General Secretary and their team for making this event a great success.

This issue of Transactions of PMAI Vol.32 contains a collection of selected papers presented at this meeting. The technical content of this issue is so diversified with various topics related to modern thrust chamber materials for space application, sintering of uranium oxide and mixed oxides for nuclear fuel elements ,microwave sintering of tungsten heavy alloys and stainless steels, to the development of multilayer coated super conducting substrates to diamond tools. There are also articles related to hot gas atomization, carbothermal reduction, reactive high energy milling, combustion synthesis. Modeling of compaction as well as microwave heating, sintering and high temperature sintering furnaces and near net shape component processing.

PMAI wishes its readers a very Happy and Prosperous New Year-2007.

P.Ramakrishnan

Editorial

The Annual Technical Meeting of PMAI, PM – 2006 was organized at Viceroy Hotel, Hyderabad and it turned out to be a huge success. Large number of participants including six delegates from abroad were in attendance to share their experiences and views. The Chief Guest, Dr. Dipankar Banerji, Chief Controller R&D (AMS), DRDO inaugurated the conference commenting on how finer particulates processing was the order of the day and that the Ministry of Defence was looking forward to great strides in materials development through better synergy between researchers and production agencies so that the turnaround time could be minimized. This was followed with felicitation of PMAI fellows. This year PMAI bestowed its greatest honour for lifetime achievement on Dr. V.S. Arunachalam, Dr. Sanjay Basu and Dr. K. K. Rao for their invaluable contributions to the growth of Powder Metallurgy in the country. Their names now adorn the PMAI scroll of honour as fellows.

After two scintillating memorial lecture presentations by Shri K. Ramesh, GM (Mktg), MIDHANI and Dr. A.Suri of BARC, the Technical sessions were organized which covered most recent developments and trends in powder metallurgy. Poster sessions were also organized on the second day of the meet. Over 70 abstracts for oral and poster presentations were received including the invited talks. A wide range of subjects, covering all facets of PM, were presented.

During the course of the conference two papers namely: Modeling of Microwave Heating of Particulate Metals by P. Mishra et.al. and Theoretical Advantages of Hot Gas Atomization of Melts by D. Fedorov et.al. Were adjudged the best papers. In the product exhibition DMRL was adjudged the best with an impressive display of tungsten alloy components.

The Editors wish to thank the authors who contributed their full papers and enabled bringing out this transaction.

Bijoy Sarma

Ravi Kiran

TRANSACTIONS OF POWDER METALLURGY ASSOCIATION OF INDIA

Vol. 32, December 2006

CONTENTS

- 1] **MODERN THRUST CHAMBER MATERIALS: A BRIEF APPRAISAL AND THE DEVELOPMENT APPROACH**
Suri Jyothi, K.Thomas Tharian and S.C. Sharma 01
- 2] **NEAR NET SHAPE COMPONENT PROCESSING IN COLUMBIUM BASE ALLOY (C-103) THROUGH POWDER METALLURGY TECHNIQUE**
G.P. Khanra, S. Girikumar, Gangadhar De and K. Suseelan Nair 06
- 3] **THEORETICAL ADVANTAGES OF HOT GAS ATOMIZATION OF MELTS**
Dr. D. Fedorov, John J. Dunkley 11
- 4] **MECHANICAL ALLOYING, REACTIVE- AND HIGH ENERGY MILLING -encouraging industrial applications for High Kinetic Processing-**
H. Zoz, H. Ren, H. U. Benz, G. Kaupp, S. Diaz de la Torre and David Jaramillo V. 17
- 5] **AN INVESTIGATION INTO EXTENSION OF SOLID SOLUBILITY OF Fe AND Ni, IN W BY HIGH-ENERGY MILLING**
R. Malawar, N. Alam, B. Sarma, B. S. Murty and S. K. Pabi 40
- 6] **FORMATION OF SPHERICAL POWDERS OF GRAY IRON BY CARBOTHERMAL REDUCTION OF IRON OXIDE (Fe_2O_3)**
R.V. Krishnarao, J.Subrahmanyam 46
- 7] **COMBUSTION SYNTHESIS OF ULTRAFINE NIO POWDER FOR NI-YSZ CERMET ANODE MATERIAL IN SOFC**
A.R.Ballal,R.Lenka , T.Mahata , P.K. Sinha , P.Gopalan, S.N. Malhotra 51
- 8] **DEVELOPMENT OF PREALLOYED METAL MATRIX POWDER FOR DIAMOND TOOL INDUSTRY**
Shaik Imam, G.V.Murali Krishna 54
- 9] **DEVELOPMENT OF TEXTURED SINGLE LAYER AND MULTILAYER COATED SUPERCONDUCTOR SUBSTRATES BY THE POWDER METALLURGY ROUTE**
P.P. Bhattacharjee, R.K. Ray and A. Upadhyaya 57
- 10] **POWDER SURFACE AREA REDUCTION AS A MEASURE OF EXTENT OF AGGLOMERATION**
Palanki Balakrishna, M Anuradha and B Narasimha Murty 62
- 11] **DERIVATION OF YIELD FUNCTION CONSTANTS FOR MODELING THE PM-COMPACTION**
Chidanand. G, Sachin,B.M., Thilak B.T., Shashidhar, U.G.,Shamasundar S. 66

12]	GREEN STRENGTH OF METAL SPONGE COMPACTS AND CERAMIC POWDER COMPACTS Palanki Balakrishna, Pradip Kumar Sahoo, T Gopalakrishna, Tapas Sanyal	72
13]	USE OF SODIUM STEARATE IN FABRICATION OF MIXED OXIDE ANNULAR PELLETS FOR FBTR S.K.Shrotriya, B.K.Shelke, Y.G.Nehete, B. Surendra, K.Subbaraya, M.K.Yadav, Niraj Kumar, A.K.Mishra, P.S.Somayajulu, J.P.Panakkal, H.S.Kamath	76
14]	SINTER PROCESSES FOR STEEL P/M COMPONENTS IN VARIOUS FURNACE ATMOSPHERES MAHLER GMBH INDUSTRIAL FURNACES Rolf Weiss	80
15]	HIGH PERFORMANCE SI-BEARING MATERIALS PROCESSED IN A VERSATILE HIGH TEMPERATURE SINTERING FURNACE N. Gopinath, Patrik King, S. Ashok	84
16]	MODELING OF MICROWAVE HEATING OF PARTICULATE METALS P. Mishra, G. Sethi, and A. Upadhyaya	89
17]	MICROWAVE SINTERING OF TUNGSTEN HEAVY ALLOYS S.K. Tiwari, P. Mishra and A. Upadhyaya	98
18]	EFFECT OF CONVENTIONAL VIS-À-VIS MICROWAVE SINTERING ON AUSTENITIC (316L) AND FERRITIC (434L) STAINLESS STEEL S.S. Panda, V. Singh, A. Upadhyaya ^a D. Agrawal	105
19]	AN INVESTIGATION ON THE EFFECT OF HEATING RATE ON THE SINTERING OF URANIUM DIOXIDE S V Ramana Rao, Debrupa Lahiri, M Anuradha, B Narasimha Murty, Palanki Balakrishna	110
20]	EFFECT OF HEATING MODE AND SINTERING TEMPERATURE ON DENSIFICATION AND MICROSTRUCTURE OF PREMIXED AND PREALLOYED BRONZE A. Upadhyaya, G. Sethi and D. Agrawal	114
21]	EFFECT OF COPPER POWDER TYPE AND SINTERING TEMPERATURE ON SINTERING OF Cu-10 Sn ALLOYS THROUGH CONVENTIONAL AND MICROWAVE HEATING Uddanti Ravikiran and Anish Upadhyaya	124
22]	MECHANICAL PROPERTIES OF BRASS POWDER COMPONENT PROCESSED THROUGH PARTICLE SURFACE HEATING (PSH) Akhter H. Ansari	128
23]	DEEP SUB ZERO PROCESSING OF COMPONENTS MANUFACTURED BY POWDER METALLURGY TECHNIQUES Kumar M. Iyer	132
24]	POWDER METALLURGY & DIAMOND TOOLS - AN OVERVIEW OF THE INDIAN INDUSTRY P. K. Korgaonkar	135
25]	TRENDS IN DIAMOND TOOLS FOR STONE PROCESSING R. R. Thorat	139

MODERN THRUST CHAMBER MATERIALS: A BRIEF APPRAISAL AND THE DEVELOPMENT APPROACH

Suri Jyothi, K.Thomas Tharian and S.C. Sharma

Materials Processing Division, Metallurgy and Materials Group
Vikram Sarabhai Space Centre, Trivandrum – 695 022.

ABSTRACT

To survive in the high temperature, high pressure environment of today's rocket engines, the combustion-chamber liner must be fabricated from high thermal conductivity materials and is to be actively cooled. To meet the critical design requirement, continuous efforts are under way to develop copper based alloys possessing exceptional high temperature strength. NARloy Z (Cu-Ag alloy) is being used for such applications operating temperature limited to 600 C. A more potential, next generation of elevated temperature material for the cryogenic thrust chamber application is Cu-8at%Cr-4%Nb, having the operating temperature capability of 800 C. Cu-8at%Cr-4%Nb alloy is a Cr₂Nb strengthened Cu based material used for applications ranging from welding electrode; high-voltage switches to more advanced active-cooling applications, such as first wall-and-diverter interactive components in fission, magnetic confinement fusion reactors, combustion chamber liners for reusable launch vehicle (RLV) engines, and rocket nozzle liners. This paper highlights salient features of this class of new generation combustion chamber liner materials for future RLV and other applications. It also presents the developmental approach being adopted to realize this material for our space programmes.

1. INTRODUCTION

The reusable launch vehicle (RLV) thrust cell liner, or thrust chamber, is a critical component of the Space Shuttle main Engine. Due to severity of in-service loading conditions, materials used in the fabrication of thrust cell liners must exhibit high thermal conductivity, high strength and creep resistance [1]. A number of Copper based alloys have, however, been developed specifically for use in high-performance rocket nozzles.

Pure Copper has very high conductivity, but its undesirable high temperature characteristics, particularly lack of creep resistance, limit its application in pure form. Within last 10-15 years, a variety of dispersion-strengthened (DS) Copper alloys have been developed due to their unique proclivity to provide a good combination of high mechanical strength and thermal/electrical conductivity [2]. We have also taken up the development of the state-of-the-art Cu alloy based on Cu-Cr-Nb system for applications in our space programmes. The present paper provides a comparative appraisal of various material developments which are occurring in this area. It also outlines the approach being formulated by us to realize Cu-Cr-Nb based alloy for thrust chamber applications in cryogenic and semi-cryogenic engines.

2. A COMPARATIVE APPRAISAL

The thrust chambers are fabricated by forming an inner wall for oxidation resistance and a structural outer shell. To reduce chamber wall temperatures, chambers should be cooled regeneratively and be made from a high-conductivity material such as copper. The selection criterion for the material for the inner liner considers following properties: a)High thermal conductivity, b)Low Co-efficient of expansion, c)high melting point, d)high temperature properties, e)Ease of fabrication as channel milling of helical & straight channels is involved for regenerative coolant passages, f)Ability to retain strength at high temperature, g)Good low cycle fatigue and better creep life, h)Ability to be made into required forms, i)compatibility with both hot and cold gases, j)retention of ductility at cryo temperatures and no ductile to brittle transition at low temperature, k)resistance to stress corrosion cracking and hydrogen embrittlement, l)Possess good UTS-YS spread.

Additionally, the materials used in the thrust chamber applications should be amicable with the following conditions: a)Extremely high temperatures are required, hence adequate cooling (regenerative cooling) should be ensured, b)Regenerative cooling demands that chamber be made into 2 shells with coolant passage channels in between

MODERN THRUST CHAMBER MATERIALS: A BRIEF APPRAISAL AND THE DEVELOPMENT APPROACH

and the shells are joined by brazing or the outer shell is electro-formed, c) Propellants like hydrogen have very low density and hence they are to be pumped at very high speeds to meet the required propellant flow rates.

AMZIRC, NARloy Z and Cu-Cr-Nb alloy are the copper based alloys which have been employed as experimental thrust cell liner materials [3]. AMZIRC is a zirconium-copper alloy, containing 0.15% Zirconium. NARloy-Z contains 3% Ag and 0.5% Zr. Cu-Cr-Nb alloy has 8at% Cr, and 4at% Nb. It exhibits enhanced creep resistance, high operating temperatures and low thermal expansion. Cu-Cr-Nb alloy is an elevated strengthened material processed through Powder Metallurgy. It can withstand temperatures up to 800 °C. Strengthening is provided by the precipitation of hard Cr_2Nb intermetallic particles, which are stable up to the congruent melting point of 1770° C [2]. Table 1 gives a comparison of the properties of these alloys.

Table 1:
Property comparison of the copper based alloys

Properties	AMZIRC	NARloy-Z	Cu-Cr-Nb alloy
Density, gm/cc	8.89	9.134	8.7
Ther. Expn. $\text{lm}/(\text{m.K})$	16.9	17.2	<17.2
Ther. Conductivity W/m.K	367	295	285
UTS, MPa (RT)	430	310	430
UTS, MPa (810K)	—	170	180
YS, MPa (RT)	68	200	280
YS, MPa (810K)	—	150	170

The Cr:Nb ratio of 2:1 was selected such that all Cr and Nb combine to form the insoluble Cr_2Nb compound to preserve the excellent thermal conductivity of a virtually pure copper matrix. The negligible solubilities of BCC refractory Cr and Nb in Cu up to 927 °C, their complete solubility in liquid Cu above solvus, and their Cr_2Nb formation provide the thermodynamic rationale behind the design of this alloy.

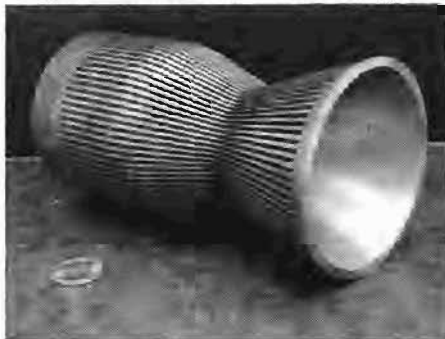


Fig1: Subscale thrust cell liner with NiCrAlY coating. (Adapted from ref. [5])

Cu-Cr-Nb alloy is produced by conventional gas atomization. Consolidation by extrusion, Hot Isostatic Pressing (HIPing), and Vacuum Plasma Spraying (VPSing) have been successfully demonstrated. These methods offer the opportunity to produce complex shapes and sizes through variety of processing paths.

Cu-Cr-Nb alloy has a high volume fraction of Cr_2Nb , approximately 14 Vol%. This intermetallic compound strengthens the copper matrix and also acts to refine and control the copper grain size[4]. Approximately 2/3rds of the strengthening comes from a Hall-Petch mechanism (Appendix A), while 1/3rd is from Orowan strengthening (Appendix B)

Cr_2Nb is extremely stable up to 800°C, because these particles do not coarsen significantly, the grain size remains nearly constant and even long-term exposures to temperatures under 800 C do not degrade the strength of Cu-Cr-Nb alloy much. Most other copper alloys suffer loss of strength and grain growth when exposed to these

temperatures. In the case of precipitation strengthened alloys such as NARloy-Z, either the precipitates grow too large to be effective for strengthening the alloy or they dissolve completely.

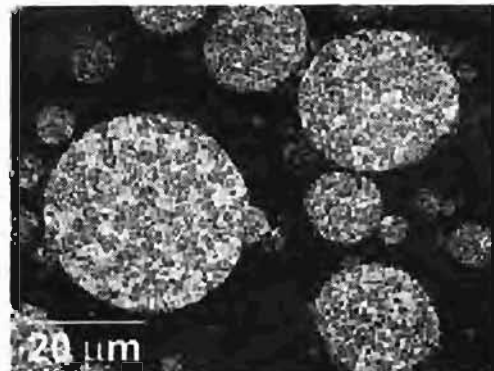


Fig 2: Cu-Cr-Nb alloy powder shows the pure copper matrix and the Cr_2Nb particles that precipitate from the molten solution during atomization. (Adapted from ref.[5])

Thermal Expansion is one of the most critical thermo physical property requirements for rocket engine liners. Most of the stresses and strains are thermally induced rather than mechanically generated. During the operation of a typical hydrogen-fueled engine, the hot wall temperature rises to somewhere between 400°C and 600°C while the cold wall between the cooling channels remain near room temperature, producing a large thermal gradient, thus creating plastic deformations and stresses[4].

Cu-Cr-Nb alloy has a lower thermal expansion, the decrease is almost 7 % relative to pure copper in the hot wall temperature range. For a liner application, a 2 to 100 times increase in life is expected from the direct substitution of Cu-Cr-Nb alloy for other copper alloys depending on the failure mechanism.

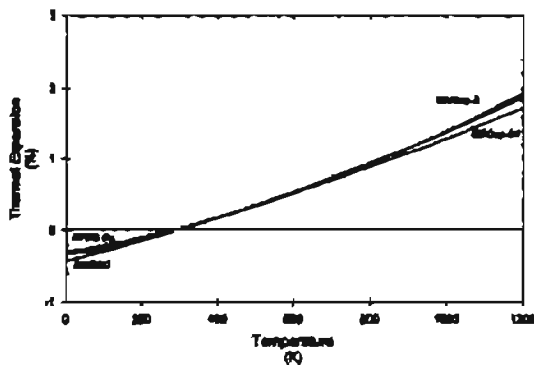


Fig. 3: Thermal Expansion of Cu-Cr-Nb alloy showing much lower value to most other high temperature, high heat-flux alloys. (Adapted from ref.[5])

Cu-Cr-Nb alloy has a thermal conductivity of between 305 and 320 W/mK or 75 to 84% of the value of pure copper over the operating temperature range. This is comparable to NARloy-Z near room temperature but lower at high temperatures such as those experienced at the hot wall. The lower thermal conductivity of Cu-Cr-Nb alloy does result in an increase in temperature, but analysis for rocket engine applications indicate that this increase is typically 35°C less, however this loss can be compensated with the fabrication design.

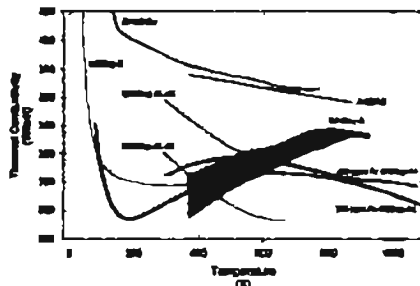


Fig 4: Thermal conductivity data of Cu-Cr-Nb alloy compared to other high temperature, High-heat-flux alloys.(Adapted from ref.[5])

Cu-Cr-Nb alloy was optimized for high temperature strength. As a result, its low temperature strength is inferior to Cu-Be and most other precipitation-strengthened copper-based alloys. However, unlike those alloys, Cu-Cr-Nb alloy retains good strength between 300° and 450°C, shows little decrease in strength of 20 to 35 MPa, even after exposure to very high temperatures in the range of 935° to 1000° C[8].

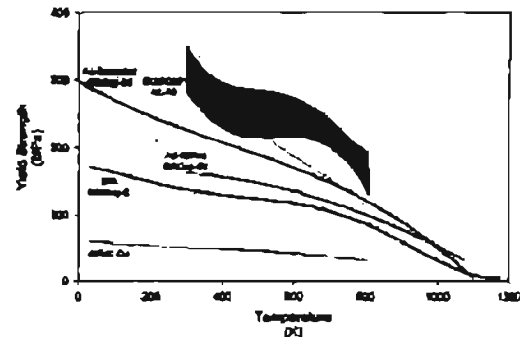


Fig 5: UTS of Cu-Cr-Nb alloy compared to other high temperature, high-heat-flux alloys.(Adapted from ref.[5])

Cu-Cr-Nb alloy has enhanced oxidation resistance up to 650°C [5] because it forms a layer of chromium-niobium oxides underneath the much thicker copper oxide layer. This inhibits diffusion and lowers the oxidation rate of Cu-Cr-Nb alloy almost a full order of magnitude below that of pure copper. For increased oxidation resistance, the alloys can be given protective coatings of NiCrAlY.

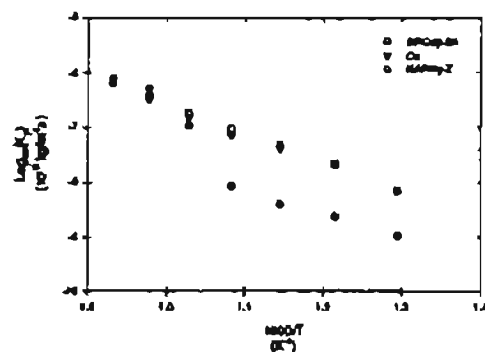


Fig 6: Oxidation behaviour of Cu-Cr-Nb alloy compared to other alloys.(Adapted from ref.[5])

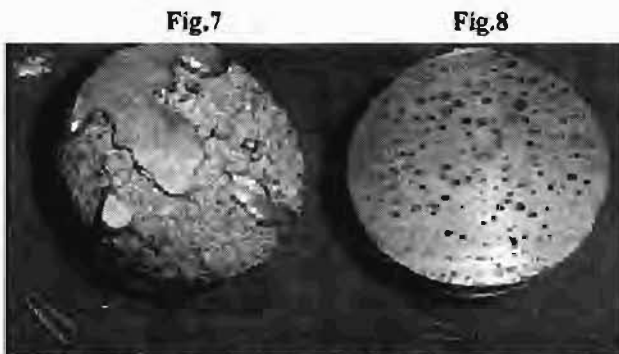
3. THE DEVELOPMENT APPROACH

The challenges involved in processing this alloy are high melting points, i.e. large gap in the melting points of atomic elements, large miscibility gap in the solubilities of the atomic elements. Due to very high melting points and high reactivity's of Nb and Cr, development of Cu-Cr₂Nb alloy through melting-casting route has been found extremely difficult. Segregation and non-homogenous distribution of Cr₂Nb in Cu is another problem in this route. Temperatures

MODERN THRUST CHAMBER MATERIALS: A BRIEF APPRAISAL AND THE DEVELOPMENT APPROACH

above 1900°C are required for dissolution and formation of Cr_2Nb . Most of the present day crucible materials (alumina, magnesia and graphite) will be reacting with the liquid metal ($\text{Cu-Cr}_2\text{Nb}$) at these temperatures.

In our initial attempts to realize this alloy through ingot metallurgy route, the elements were melted in Vacuum Induction melting furnace of 25 kg capacity in the graphite crucible under vacuum of 10^{-1} - 10^{-2} torr, and at sufficiently high temperatures of 2000°C. The niobium content in the ingot was found to be very low. To increase the solubility of niobium in copper-chromium alloy, chips of niobium metal were fed into the graphite crucible through a hopper at the top of the VIM furnace at temperatures of 2000°C, and then copper chromium was melted. This attempt also resulted in poor niobium recovery, and the cast ingot was fully porous, pictures of which are shown in Figs. 7 and 8.



Hence, because of the higher melting temperature of the Cu-Cr-Nb alloy, it was decided to switch over to powder metallurgy. Under powder metallurgy route, argon atomized pre-alloyed elemental powders of copper, 6.45 (wt%) chromium, and 5.79(wt%)niobium powders are to be mechanically alloyed using a high energy ball mill and consolidated to billets in secondary operation using hot press. Metallurgical characterization will be performed to optimize the processing parameters. Then these billets will be realized to sheets/slabs. The proposed process flow chart is given in Fig.9.

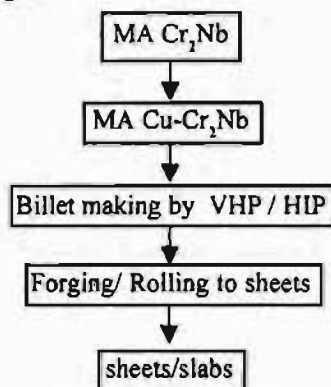


Fig.9 :Proposed Process Flow Chart

4. CONCLUSIONS:

$\text{Cu-8at\%Cr-4at\%Nb}$ is the state-of-the-art thrust chamber material for cryogenic engine. It has much higher operating temperature limits extending up to 800 C.high temperature strength in this alloy is derived mainly from Cr_2Nb intermetallic phase which is highly stable up to 800 C. However due to very high melting point and high reactivity of Nb and Cr, development of Cu-Cr-Nb alloy through liquid metallurgy route is very difficult. Powder metallurgy route is being worked out to realize the desired product of this alloy.

APPENDIX A:

Hall Petch Mechanism:

$$\sigma = \sigma_0 + k_y d^{-1/2} \quad [\text{MPa}]$$

Where d = grain size
 k_y = material constant related to ease of slip transfer across a grain boundary
 σ_0 = yield stress of single crystal

The strengthening effect is essentially due to stress concentrations and slip transfer across grain boundaries due to pile-ups of dislocations generated mainly by Frank-Read sources. Smaller grains would require higher applied stresses to generate enough dislocations to induce slip transfer, or flow. It turns out that the grain size d of a DS alloy will be effectively governed by particle size and volume fraction.

APPENDIX B:

Orowan Strengthening Mechanism

$$\Delta\sigma = \frac{0.84 M G b}{2\pi(1-\nu)^{0.5}(\lambda - 2r)} \ln \frac{r}{b} \quad [\text{MPa}]$$

Where

M = Taylor factor (~3 for FCC metals)
 G = Shear Modulus of copper matrix (MPa)
 b = burgers vector
 r = average particle radius
 ν = Poisson's Ratio
 λ = Planar particle spacing, expressed as

$$\lambda = r \sqrt{\frac{2\pi}{3f}} \quad [\text{nm}]$$

Where f is the volume fraction of particles.

REFERENCES:

1. Daniel T. Butler, Jr. and Marek-Jerzy Pindera, "Analysis of factors affecting the performance of RLV thrust cell liners", NASA/CR-2004-213141, NASA GRC, Cleveland, OH, (August 2004)
2. Kenneth Reed Anderson, "Effects of thermal and mechanical processing on microstructures and desired properties of particle-strengthened Cu-Cr-Nb alloys", NASA/CR-2000-209812, NASA GRC, Cleveland, OH, (February 2000)
3. Linus U. Thomas-Ogbuji and Donald L. Humphrey, and J.A. Setlock, "Oxidation-Reduction resistance of advanced Copper alloys", JCSE, vol6, paper H071.
4. David L. Ellis, "GRCop-84: A high-temperature Copper alloy for High-Heat-Flux applications", NASA/CR-2005-213566, NASA GRC, Cleveland, OH, (February 2005)
5. Linus U. Thomas-Ogbuji and Donald L. Humphrey, "Oxidation behaviour of GRCop-84 at intermediate and high temperatures", NASA/CR-2000-210369, NASA GRC, Cleveland, OH, (August 2000)

NEAR NET SHAPE COMPONENT PROCESSING IN COLUMBIUM BASE ALLOY (C-103) THROUGH POWDER METALLURGY TECHNIQUE

G.P. Khanra, S. Girikumar, Gangadhar De and K. Suseelan Nair

Vikram Sarabhai Space Centre, Trivandrum-695022

ABSTRACT

Columbium base C-103(Cb-10Hf-1Ti) alloy in near net shape components have been successfully manufactured by a duplex - Cold Iso-static Pressing(CIP) + Hot Iso-static Pressing(HIP) process starting from alloy machine chips. The alloy powder was made from the chips by hydriding/dehydriding operations. The combination of CIP+HIP was adopted for this developmental work instead of direct HIP due to low tap density (~38%theoretical density) of alloy powders. Prior to this developmental work, a study had been under taken on consolidation of alloy powder through conventional compaction and sintering route, which yielded only 86% theoretical density(TD). TD of 95% has been successfully achieved in the duplex processed specimens. The microstructure and mechanical properties at RT were measured on duplex processed specimens. It has been found that strength properties of duplex processed specimens are superior to even wrought material. However ductility on tension is found to be low where as ductility on compression is excellent. This behavior is discussed in terms of porosity and interstitial elements. The material recovery in this near-net shape component processing route has been found to be much better than that of ingot metallurgy route.

1. INTRODUCTION

Advances in high performance space craft and space vehicle system depends on the availability and effective use of strategic structural materials especially of refractory materials. These strategically important refractory metals and alloys are employed extensively in space vehicle hot-gas exhaust and attitude vector control system in the form of forgings that are machined to precise dimensions^{1,2}. However, over the past several years, raw material and manufacturing costs have increased significantly. It is mainly due to hardware fabrication through machining operations that results in large quantity of scrap of a costly raw material. A relatively new processing technique through powder metallurgy route, which could reduce manufacturing costs encompasses the combination of cold iso-static pressing(CIP) and hot iso-static pressing(HIP), designated as duplex process to produce near net shapes avoiding scrap generation³. In addition to minimizing the machining, the method also has the capacity to improve microstructural and mechanical properties.^{4,5} As metal removal of refractory alloys in most cases is tedious and difficult, CIP and HIP process are techniques that offer the potential both for reducing manufacturing costs and improving design performance capabilities for the above materials. CIP and HIP fabrication procedure have also been

developed and demonstrated successfully for other variety of materials^{6,7,8}.

Processing of columbium (C-103) alloy through ingot metallurgy(IM) route needs extensive homogenization and forging prior to rolling into sheets for component fabrication. However, columbium alloy is prone to forge cracking due to inherent micro/macro segregation of alloying elements and formation of oxide scales^{9,10}. Such a problem makes secondary processing difficult, and also leading to escalation of cost. Accordingly studies were undertaken towards development of attitude orbiter control thrusters in columbium alloy through powder metallurgy route, avoiding secondary operations¹¹. Prior to the study on CIP+HIP processing technique for near-net shaped components, an attempt was made to consolidate alloy powder by conventional compaction and sintering. It was found that densification to max of 86% TD could only be possible by this process. In this study, processing, mechanical properties and microstructure were evaluated. The properties achieved in duplex process also been compared with IM processed alloy.

2. PROCESSING EXPERIMENTS

The Process Flow Chart is shown in Fig.1. Powder was made from machine chips of C-103 alloy through hydride

NEAR NET SHAPE COMPONENT PROCESSING IN COLUMBIUM BASE ALLOY (C-103) THROUGH POWDER METALLURGY TECHNIQUE

- dehydride route. Near net shape pre-form of the components and test specimens were prepared from dehydrided powder employing CIP. Direct HIP of powder to pre-form is possible provided it satisfies $0.55 < D_d < 1$ condition, where D is tap density fraction¹². Metal powder with a mean particle size on the order of microns and packing density of $D < 0.55$ requires a combination of CIP+HIP instead of direct HIP for full densification. Since the tap density of the powder used in the present study is only 38%TD, a CIP+HIP combination technique was used for consolidation. CIPing was carried out using flexible PVC mould of desired shape for making the pre-form. CIPing was followed by a pre-sintering operation to obtain handling strength in the compacts. Further sintering at high temperature under high vacuum was carried out in order to realize a density of about 85% TD in the compacts prior to HIP. Thus a closed porosity condition was ensured in the perform prior to HIP to avoid dynamic argon leakage through pores thereby reducing the effectiveness of pressing. A slow heating/cooling rate was maintained with intermediate soaking to avoid crack formation. Sintering at 1600°C for 2 hrs was found to be optimum to obtain above targeted TD. The sintered pre-forms and test specimens were hot iso-statically pressed using argon gas at 1600°C and 1875°C. The average density of the components and test specimen was found to be 8.1(91%TD) and 8.34 g/cc (95% TD) respectively.

3. PROPERTIES EVALUATION

The consolidated specimens were evaluated for density, microstructure, XRD analysis and mechanical testing. Density at different stages was measured by Archimedes's principle. Phase analysis was carried out using XRD technique. An XRD pattern is shown in Fig.3. For mechanical property evaluation, specimens were machined into samples of 3.2 mm dia. and a gauge length of 13 mm, as per BS-18 standard. YS, UTS, % elongation (under tension), ultimate compressive strength(UCS) and %elongation(under compression) were measured at RT in an INSTRON machine. The result is given in table – II to IV. Polished specimens were etched with H_2SO_4 -HF- H_2O_2 solution and the microstructures are shown in Fig-4.

4. RESULTS & DISCUSSION

Evaluation of starting powder was made through particle size, size distribution, tap density and particle shape determination. The particle size distribution of the powder as shown in Fig-1, shows a narrow distribution. Particle shape was observed through optical microscope and found to be irregular. Irregular shape and narrow size distribution of the powder resulted in low tap density (~38%TD), which was found unfavorable for attempting direct HIP trials.

Hence, cold compaction of powder was carried out at different pressures. Change in green density (GD) as a function of pressure is shown in Fig-5. It has been observed that GD increases almost linearly with compaction pressure till 500 MPa, beyond which no significant change in green density is observed. The GD corresponding to 500 MPa compaction pressure resulted in about 65% TD. About 3% increase in density was observed for all specimens after sintering. Coining at 650 MPa showed marked densification (82%TD for all specimens) indicating that it has more effect on densification compared to sintering. Re-sintering at 1600°C for 2 hrs under vacuum showed no significant change in density of the specimens.

The alternate method, CIP+HIP (duplex process) was adopted for obtaining near net shape component having higher density. Consolidation of powder through CIP was the 1st step in duplex process. CIP pressure was optimized through experiments which showed that about 350MPa is required to achieve about 65% TD in green compact with enough handling strength. The microstructure of the PM processed and wrought alloys are compared in Fig-4. The average grain size was estimated from optical photomicrographs which are found to be 28 microns in PM specimens and 39 microns in wrought specimens. The amount of second phase particles in PM alloy is seen to be more compared to IM processed alloy. The chemical composition of the alloy processed through PM route is shown in Table-I. The results clearly reveal that during the powder metallurgy process, large pickup of oxygen and nitrogen occurs. This oxygen and nitrogen pick up during processing could be attributed to the high surface area of fine and reactive powder. The result also clearly reveals that the processing should be done in a pure hydrogen or argon atmosphere. However, the increased amount of interstitial elements like oxygen and nitrogen in PM alloy are observed not detrimental to strength properties at ambient temperature. They do not affect the near net shape processing too. It has been observed that there is a shift of columbium peaks indicating change in d-spacing which confirms alloying elements are in solid solution. However, other peaks as expected for the secondary phases, formed by interstitials are found to be absent probably due to less vol. % (detectable range > 5vol%). The presence of two minor peaks of Hf indicates free availability of the element in small amount apart from being in the solid solution. The results of mechanical tests (at RT) on the PM alloy and wrought IM alloy are given in table II to IV. The improved strength properties of the PM alloy compared to IM alloy could be attributed to the presence of higher amount of interstitials. However %elongation under tension of PM

NEAR NET SHAPE COMPONENT PROCESSING IN COLUMBIUM BASE ALLOY (C-103) THROUGH POWDER METALLURGY TECHNIQUE

alloy is only 2%, which is less compared to IM alloy. This could be attributed to the residual porosities leading to failure without much plastic flow^{13,14}. On the other hand, 48 %elongation under compression reveals appreciable deformation before failure. High compressibility of this material could be attributed to the closure of porosity under compression. Density was measured at different stages of processing and results are shown in Fig-6. It is observed that density has increased during each step of processing. The maximum rate of densification is observed by CIP. Intermediate sintering at 1600°C, for 2 hrs under vacuum improves densification beyond 80%TD through metallurgical bonding. Densification to about 95% TD was achieved in the pre-form after HIP.

5. CONCLUSIONS

(i) Conversion of columbium base C-103(Cb-Hf-Ti) alloy chips into powder, through hydride-dehydride process has been successfully achieved. (ii) Near net shape processing of C103 alloy has been successfully accomplished using the above powder through duplex (CIP+HIP) process. The consolidated product is having about 95% TD. The conventional process of cold compaction and sintering using same time-temperature parameters could achieve only up to 86% TD in C-103 alloy. (iii)Microstructure of P/M product indicates finer grain size and subsequently, higher amount of second phase compared to that of wrought IM product. (iv) Mechanical properties of PM processed material are superior to IM processed material at RT. However ductility on tension is found to be low where as ductility on compression is excellent.

6. ACKNOWLEDGEMENT

The authors wish to express their sincere gratitude to Dr. B.N. Suresh, Director, VSSC for approval of this developmental programme and presentation of this paper. Dr. K.N. Ninan, Deputy Director, VSSC(PCM) has shown keen interest and provided encouragement and valuable suggestions and the authors wish to record their profound thanks to him. The authors gratefully acknowledge the unstinted support and encouragement given by Mr. M.C. Mittal, Group Director, MMG /VSSC.

The authors also express their thanks to personnel of MCD, ASD, MEE of VSSC and LPE of LPSC for realization of final component and characterization.

The technical facility assistance provided by DMRL, Hyderabad for CIP and HIP operations is thankfully acknowledged.

7. REFERENCES

1. Refractory metals alloys, Metallurgy and Technology, Plenum Press, NY, 1968, pp329.

2. Refractory Metals and Alloys, Sam Gerardi et al.,Metals Hand book , vol2, 10th ed. Metal park, OH:ASM, pp 565-571.
3. Near net-shape Powder Metallurgy Rhenium thruster, Todd Leonhardt, Mark Hamister & Jan C. Carlex, JI. of American Institute of Aeronautic & Astronautic, July2000.
4. Microstructure effects on creep behavior of next generation of refractory alloys for very high temperature applications (final report no. AF RL SR AR TR 020222), Vijay K. Vasudevan & Kaith J. Leonard, Department of Material Sci. and Engg., Cincinnati University, Dec 2000.
5. Improvement in disk alloy quality due to application of powder metallurgy method & HIP, G.S. Garibov et al, Advance in powder metallurgy & particulate materials, part4-43, 1998.
6. Development of hot isostatic pressing techniques for producing high quality billet from titanium alloy powder, Gerald Friedman (final report no.AFML-TR-75-9), Air force materials laboratory, Ohio, 1975.
7. Consolidation of Si₃N₄ without additives by hot iso static pressing (final report no NASA CR 173279), Yeh, Hun C, 1983.
8. Numerical simulation of Hot isostatic pressing of boron powder, Advance in powder metallurgy and particulate materials, 1998, pp4-43.
9. Recent advances and developments in refractory alloys (final report no. UCRL JC 116117), T.G Nieh & J. Wadsworth Lawrence National Livermore laboratory, Livermore, 1993.
10. Refractory alloys for space nuclear electric propulsion systems, R.H. Cooper, ALAA paper 91-3495, 1991.
11. Creep behaviour of hot isostatically pressed niobium alloy powder compacts, J. Wadsworth et al, Lockheed Palo Alto Research laboratory & Lockheed Missile and Space company, Sunnyvale, USA, JI of Mat Sci 17 (1982), pp 2539-2546.
12. Metal powder properties for Hot isostatic pressing , Peter E. Price and Stever P Kohler, Messachusetts Institute of technology, USA, Metals hand book, 9th edn, vol-7, pp425-427.
13. Effect of porosity on tensile properties of powder metallurgy product, George E. Dieter, Mechanical Metallurgy, 2nd Ed., Magrow-Hill international book Co., pp604-607.
14. Strain hardening behaviour of powder metallurgy alloys, G. Straffelini, Powder Metallurgy, vol48-2, 2005.

**NEAR NET SHAPE COMPONENT PROCESSING IN COLUMBIUM BASE ALLOY (C-103)
THROUGH POWDER METALLURGY TECHNIQUE**

TABLE-I
Chemical compositions (wt%) of Cb (C-103) alloys

Hf	Ti	C	O	N	Cb	
PM product	10.8	0.9	0.008	1.43	0.35	bal
IM product	10.5	1.0	0.008	0.025	0.01	bal

TABLE-II
Room temperature tensile properties of Cb (C-103) alloys

	Yield Stress 0.2% offset (MPa)	Ultimate Tensile stress (MPa)	Elongation (%)
PM product	394	442	2
IM product	266	370	20

TABLE-III
Room temperature compressive properties of Cb (C-103) alloys

	Yield Stress 0.2% offset (MPa)	Ultimate compressive stress (MPa) at 48% EI
PM product	450	1557
IM product	—	—

TABLE-IV
Room temperature Hardness of Cb(C-103) alloys

		BHN
PM product	HIPped	150
	Conventional	98
IM product		130

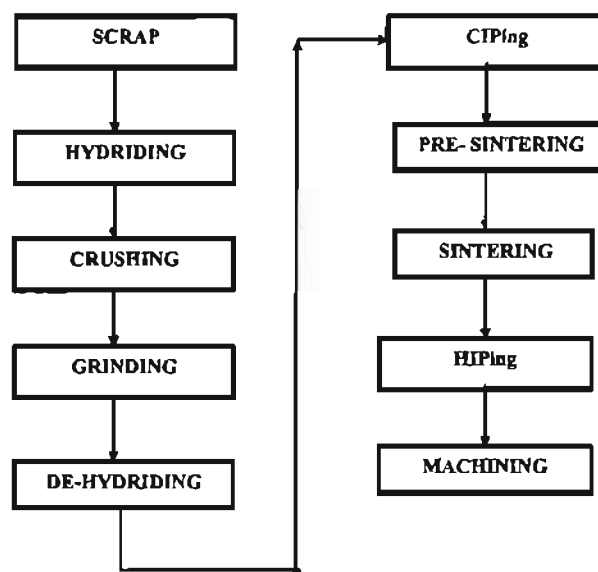


Fig.1. Process flow diagram of Cb(C-103) alloy processing

NEAR NET SHAPE COMPONENT PROCESSING IN COLUMBIUM BASE ALLOY (C-103) THROUGH POWDER METALLURGY TECHNIQUE

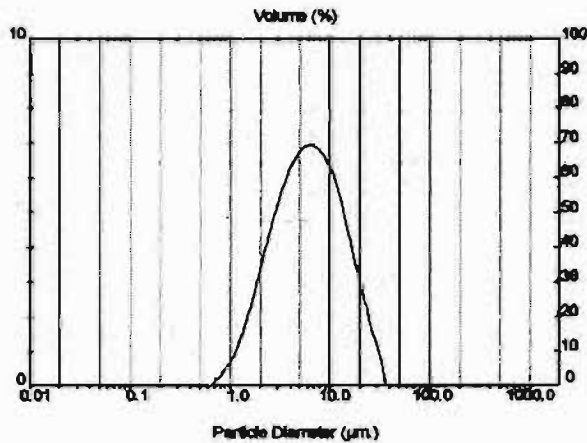


Fig.2 Particle size distribution of Cb(C-103) alloy powder

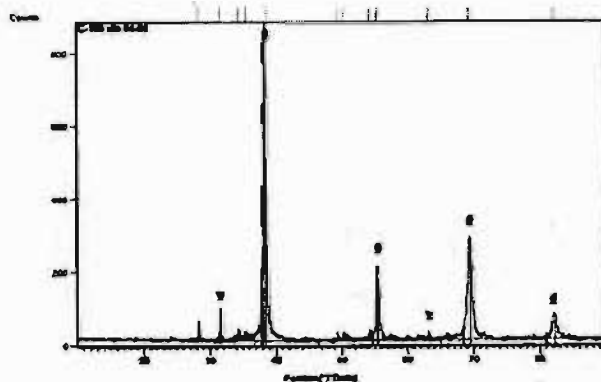
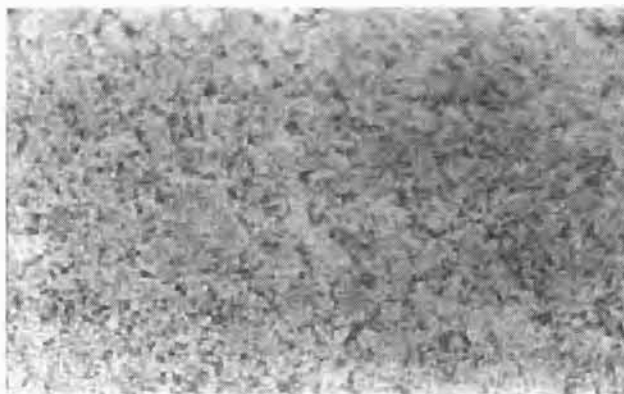
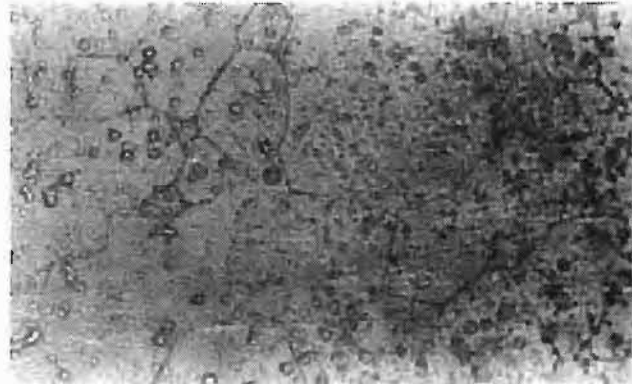


Fig.3. XRD pattern of Cb(C-103) alloy powder



(a) Mag. X 330



(b) Mag. X 330

Fig. 4 Microstructure of PM processed & wrought alloys

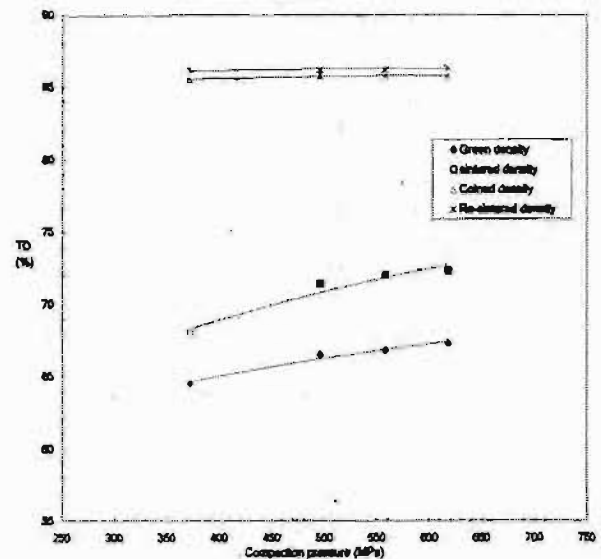


Fig. 5 Variation of density as a function of compaction pressure

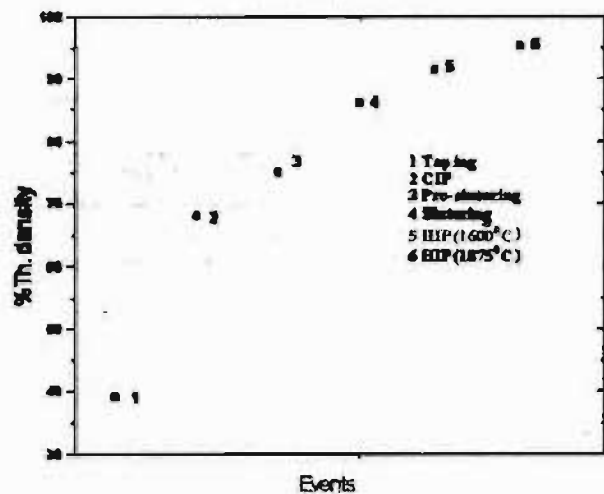


Fig.6 Densification with respect to processing stages

THEORETICAL ADVANTAGES OF HOT GAS ATOMIZATION OF MELTS

Dr. D. Fedorov, John J. Dunkley

Gas Institute of NASU, Kyiv, Ukraine, diolla@ukr.net, Atomising System Limited, Sheffield, United Kingdom

INTRODUCTION

The atomization of metal melts is a highly effective method to produce metal powders. The process has achieved great market success due to its very high productivity and flexibility. There are many attempts to develop an equation to describe gas atomization. Most of them are only empirical relationships between the particle size and a number of dimensionless groups. [1,2] These are not universal and cannot be applied to every case. The authors try to build a theoretical background of atomization to explain particularly the positive effect of the use of pre-heated gas, which has been observed by several authors. [3,4, 5,6].

The theory should include description of gas jet energy. One of the authors has tried to make such view. [7] But this study was limited by taking into consideration only parameters for 1 kg of the gaseous media. In practice it is very rare to have a variable area gas nozzle to keep mass flow rate constant. It is more normal to fix the nozzle profile and change initial gas parameters to influence the atomization process. In the paper we try to analyse the characteristics of gas jets for the case of fixed nozzle area.

THE EFFECT OF GAS PARAMETERS ON SUPERSONIC STREAM CHARACTERISTICS.

In his latest monograph [2] Dr. Ternovoy has surveyed the studies devoted to mechanism of molten metal atomization. According to him there are six stages of melt jet disintegration by a gas stream:

Transformation of the initial metal jet into conical film;

Development of the waves of instabilities parallel and orthogonal to the metal jet velocity vector;

Formation of a toroidal thickening of the liquid at the end of the film;

Development of instability in the toroidal thickening;

Formation of micro jets of the melt flowing from the area of maximum instability of the film;

Development of unstable waves within micro jets and their disintegration into droplets.

This treatment of the physical model allows the author to establish the equation:

$$d_k = (2.91 \cdot \dot{\epsilon}_m^{0.4} \cdot \rho_m^{0.2} \cdot D_j^{0.63}) / (\sigma_m^{0.026} \cdot \bar{n}_g^{0.17} \cdot w_g^{0.34}) * \{(gh + \ddot{A}P / \rho_m) / (gh + 2\ddot{A}P / \rho_m)\}^{0.086}$$

Where;

d_k – diameter of the droplet;

$\dot{\epsilon}_m$ – kinematic viscosity of the melt;

ρ_m – metal density;

D_j – diameter of metal jet;

σ_m – surface tension of the melt;

\bar{n}_g – gas density;

w_g – gas velocity;

g – gravitation acceleration;

h – height between metal level and focal point of atomization;

$\ddot{A}P$ – pressure difference between metal level and metal nozzle outlet.

In this equation the gas density and velocity are the most important parameters. But there is no gas to metal flow ratio at all. To include gas to metal flow ratio is more normal for empirical equations. Here instead the metal flow rate is involved through diameter of metal jet, height between metal level and focal point of atomization and pressure difference between metal level and metal nozzle outlet. We

also note a very small dependence on surface tension. Gas density and velocity present the effect of its parameters. So it could be concluded that gas density and velocity are the most important. But these are not sufficient to describe the atomization process.

To atomise the liquid melt the gas jet should have enough kinetic energy (power), dynamic pressure and quantity of momentum or jet force. All of these include gas flow rate.

Gases are compressible and continuous. Our analysis assumes only ideal fluids. The main characteristic of gaseous media is variable density (kg/m^3) which depends on Temperature and Pressure. So it is better to measure gas flow rate in kg/s then in normal m^3/s .

Our terms regarding fluids are:

G – mass flow rate, kg/second

\bar{n} – density, kg/m^3

T – temperature, Kelvin

P – pressure, MPa absolute value

w – velocity, m/s

R – gas constant is Universal Gas Constant $8314 \text{ J}/(\text{mol K}=\text{Degree of Kelvin})$ divided on mol of specific gas

v – specific volume, m^3/kg – the reciprocal of the density

a_0 – velocity of sound at standard condition ($P=0.1 \text{ MPa}$, $T=273\text{K}$)

a_{loc} – local velocity of sound ($P=\text{current}$, $T=\text{current}$)

A – area of the nozzle, m^2

M – Mach number is ratio of the actual jet velocity to the local sonic velocity

ξ – velocity coefficient; the ratio of actual velocity to local critical velocity (velocity at the narrowest cross-section at the current critical pressure and temperature)

k – adiabatic coefficient. $k = 1.66$ – for monoatomic gases (He, Ag), 1.40 – for diatomic (air, N_2), 1.31 for CO_2 , 1.33 – for steam

C_v , C_p – heat capacity ($\text{J}/(\text{molK})$) at constant volume and constant pressure correspondingly ($k=C_p/C_v$)

i – gas enthalpy, J/mol

$\text{sqrt}(\dots)$ – means square root (All basic gas equations here and further are quoted from [8], all gas thermodynamic parameters are taken from [9])

From the theory of gas dynamics it is known there is limitation of the maximum achievable gas jet velocity.

This is given by:

$$i_1 - i_2 = 0.5(w_2^2 - w_1^2) \quad (1)$$

Increasing the velocity depends on only the difference between initial and final gas enthalpy.

If the initial $w_1=0$ and the initial enthalpy is used entirely for acceleration ($i_2=0$) we have

$$w_{\text{max}} = \text{sqrt}(2i_1) \quad (2)$$

$$i_1 = C_p * T_1 \quad (3)$$

$$\text{hence } w_{\text{max}} = \text{sqrt}(2 C_p * T_1) \quad (4)$$

Thus for any initial gas temperature there is the only one maximum velocity of its jet. And it is clear that the higher the initial temperature of the gas the higher the velocity that can be achieved.

To accelerate a gas jet a Laval-type nozzle is applied.

A typical Laval nozzle profile is given in Fig. 1

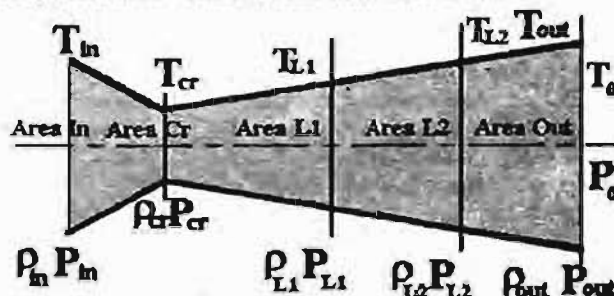


Fig. 1. Typical Laval nozzle profile

As a rule a Laval nozzle outlet cross-section is calculated assuming $P_{\text{out}} = P_0$

As the fluid medium is continuous it is known that its mass flow rate is constant:

$$G = \text{Const and } G = A w \rho \text{ (Area x Velocity x Density) kg/s} \quad (5)$$

Mach number is very often used to describe the behaviour of a gas stream passing through the nozzle.

$$(M^2 - 1) * \partial w / w = \partial A / A \quad (6)$$

By using the Mach number and differential equation (6) we can characterize the behaviour of the gas flowing along the nozzle.

If $M < 1$ (subsonic case) and Area reduces then Pressure falls and Velocity rises. This is the case of the jet acceleration of the stream till sonic velocity.

If $M > 1$ (super sonic case) and Area increases then Pressure falls and Velocity rises. This is the case for the acceleration of the stream above sonic velocity - acceleration of the stream up to $P_{\text{out}} = P_0$ (Pressure of environment media)

If $M=1$ it is the case of critical velocity of the jet. Velocity of the jet is equal to the local sonic velocity which depends on only initial gas parameters.

Velocity coefficient ϵ is very often used to calculate the nozzle profile because it simplifies the equation.

Gas flows through the nozzle adiabatically (i.e. without heat exchange with its surroundings). The gas parameters can thus be calculated using adiabatic process equations.

They are here:

$$P/\rho^k = \text{Const} \quad (7)$$

$$P_{\text{out}}/P_{\text{in}} = (\rho_{\text{out}}/\rho_{\text{in}})^k \quad (8)$$

$$T_{\text{out}}/T_{\text{in}} = (\rho_{\text{out}}/\rho_{\text{in}})^{(k-1)} \quad (9)$$

$$T_{\text{out}}/T_{\text{in}} = (P_{\text{out}}/P_{\text{in}})^{(k-1)/k} \quad (10)$$

Let consider the atomisation process from point of gas circulation as working media in whole. Such scheme is given in Fig. 2.

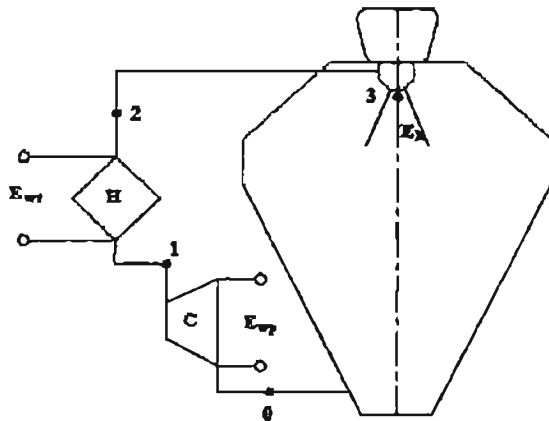


Fig. 2. Schematic gas circulation in the atomisation process

Here are C – compressor, H – gas heater, E_{wp} – energy applied to preheat the gas, E_{wt} – energy applied to compress the gas. Initial point of the process is marked here 0. Parameters of gas are P_0 and T_0 . The compressor C compresses the gas up to P_1 and T_1 (Point 1) One needs to apply energy E_{wp} here. Then gas comes to heater H where it is preheated up to T_2 at P_2 (Point 2). Applied energy is E_{wt} . The gas expands flowing through the Laval nozzle and releases energy E_k – kinetic energy of the gas jet (Point 3).

After interaction with metal jet, droplets and environment the gas returns to point 0.

According the scheme of the Laval nozzle (Fig 1) $P_1=P_2=P_{\text{in}}$, $T_0=T_1$, $T_2=T_{\text{in}}$, $P_{\text{out}}=P_0$, $T_{\text{out}} \neq T_0$

Thus there are following processes:-

- Points 0-1 apply compressing energy:

$$E_{wp} = [(P_0/\rho_0)^k * k / (k-1)] * [(P_{\text{in}}/P_0)^{(k-1)/k} - 1], \{J/kg\} - \text{specific energy per kg} \quad (11)$$

-Points 1 – 2 apply preheating energy:

$$E_{wt} = C_p(T_{\text{in}} - T_0), \{J/kg\} - \text{specific energy per kg} \quad (12)$$

(Full energy in {W} is multiplied with gas flow rate G_g in {kg/s})

- Points 2-3 release kinetic energy:

$$E_k = 0.5 w_{\text{out}}^2 G_g, \{W\} - \text{full kinetic energy of gas jet} \quad (13)$$

-Points 3-0 – interaction with metal jet and recycling process of the gas.

The main characteristic of any process is its effectiveness. It is necessary to apply an amount of energy to do any useful work. In our case the applied energy is E_{wp} (energy of work to pressurize the gas) and E_{wt} (energy to elevate its temperature). The useful energy is kinetic energy of the gas jets.

Hence, effectiveness η is:

$$\eta = E_k / [G_g * (E_{wp} + E_{wt})] \quad (14)$$

Assume that the initial pressure of the gas $P_{\text{in}} = \text{Const}$ and only T_{in} is variable hence $E_{wp} = \text{Const}$ too.

Using velocity coefficient ϵ and following equations:

$$w_g = \epsilon * w_{cr} \quad (15)$$

$$w_{cr} = \sqrt{k R_g T_{cr}} \quad (16)$$

$$T_{cr} = T_{\text{in}} * [1 - \epsilon_{cr}^2 * \{(k-1)/(k+1)\}] \quad (17)$$

$\epsilon_{cr} = 1$ – by definition

We obtain the following equation for the effectiveness as a function of initial gas temperature and velocity coefficient:

$$\eta = [0.5 \epsilon^2 k R_g T_{\text{in}} \{1 - (k-1)/(k+1)\}] / [E_{wp} + C_p(T_{\text{in}} - T_0)] \quad (18)$$

As for monoatomic gases $k=1.66$ and for diatomic gases $k=1.40$ we can make the equation (18) more clear:

$$\text{Monoatomic } \eta_1 = [0.624 \epsilon^2 R_g T_{\text{in}}] / [E_{wp} + C_p(T_{\text{in}} - T_0)] \quad (19)$$

$$\text{Diatomic } \eta_2 = [0.583 \epsilon^2 R_g T_{\text{in}}] / [E_{wp} + C_p(T_{\text{in}} - T_0)] \quad (20)$$

The equations (19) and (20) show that with T_{in} increasing both numerator and denominator will increase too. So with increasing of temperature of gas preheating the effectiveness of the process should change negligibly. But the opposite is true in the case of higher gas pressures. It is clear that with increasing compressing energy E_{wp} the effectiveness must decrease.

Dynamic pressure is:

$$P_d = 0.5 \rho_{out} w_{out}^2 \quad (21)$$

With using equations (8-10, 15-17) we can show that dynamic pressure does not depend on initial gas temperature at all. It is finally:

$$P_d = 0.624 \rho_{in}^2 P_{in}^* [(P_{out}/P_{in})^{0.602}] - \text{for monoatomic gases} \quad (22)$$

$$P_d = 0.583 \rho_{in}^2 P_{in}^* [(P_{out}/P_{in})^{0.714}] - \text{for diatomic gases} \quad (23)$$

According to our case $P_{in} = \text{Const}$ and $P_{out} = P_0 = \text{Const}$ the dynamic pressure of the gas jets will remain constant independent of initial gas temperature. It is clear that dynamic pressure will increase with increasing velocity coefficient and growth of initial pressure of the gas.

The quantity of momentum or jet force is the next gas jet characteristic.

It is :

$$F = G_g w_g, \{ \text{kg/s} \cdot \text{m/s} = \text{N} \} \quad (24)$$

This characteristic allows us to calculate average velocity of gas-metal spray.

According to conservation of momentum there is a balance:

$$G_g w_g + G_m w_m = w_s (G_g + G_m) \quad (25)$$

Here w_s means average velocity of gas-metal spray after impaction of the gas jet with metal jet in the focal point of atomisation.

Let $r = G_g/G_m$ (the gas/metal ratio) and after transformation one obtains:

$$w_s = (r w_g + w_m) / (r + 1) \quad (26)$$

For the case of the fixed nozzle area, with initial increase of temperature gas flow rate and correspondingly gas to metal (mass)flow ratio will decrease but gas velocity will be rise strongly. Hence, average spray velocity will go up having a positive influence on atomisation.

The examples of calculation illustrate the above conclusions:

Assume the following conditions:

Initial pressure	$P_{in} = 1 \text{ MPa (10 Bar)}$
Initial temperature	$T_{in} = 293 \text{ K (20}^\circ\text{C)}$
Fixed critical area	$A_{cr} = 6.32 \text{ mm}^2$
Fixed outlet area	$A_{out} = 10.57 \text{ mm}^2$
Monoatomic gas	Helium
Diatomic gas	Nitrogen
Initial gas to metal flow rate ratio	1
Metal jet velocity	2 m/s

Results of calculation for He are given in table 1.

Results of calculation for N_2 are given in table 2.

Thus, with increasing initial gas temperature its jet velocity increases, the effectiveness of the process improves (in case of Helium) or at least remains practically the same, its dynamic pressure remains constant. In the case of fixed nozzle area gas the mass flow rate will decrease reducing gas consumption of the process and at the same time provide better average velocity of the spray.

On basis of the tables 1 and 2 and plots shown in Fig.3-6 the following conclusions are drawn.

Using data from tables 1 and 2 several plots are built.

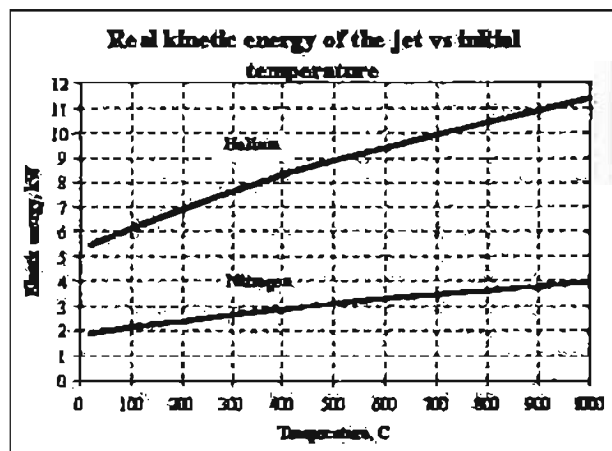


Fig. 3. Real kinetic energy of the gas jet vs Initial temperature of the gas

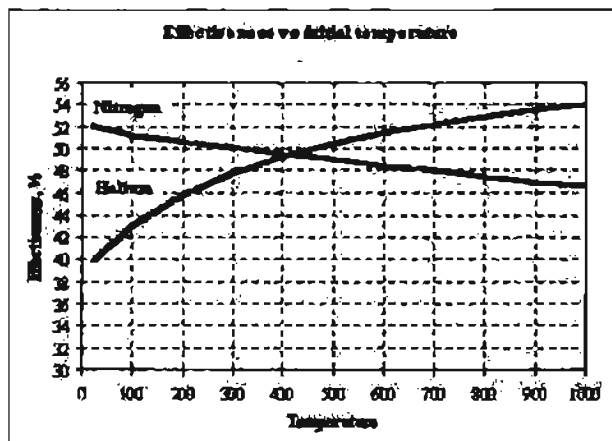


Fig. 4 Effectiveness of applied energy vs initial temperature of the gas

Table 1 Results of calculation for Helium

Data	Var1	Var2	Var3	Var4	Var5	Var6	Var7	Var8	Var9	Var10	Var11
Initial Pressure, P_m Bar	10	10	10	10	10	10	10	10	10	10	10
Initial Temperature, T_m C	20	100	200	300	400	500	600	700	800	900	1000
Fixed Critical Area, mm^2	6.32	6.32	6.32	6.32	6.32	6.32	6.32	6.32	6.32	6.32	6.32
Fixed Outlet Area, mm^2	10.57	10.57	10.57	10.57	10.57	10.57	10.57	10.57	10.57	10.57	10.57
Standard Dens, kg/m^3	0.179	0.179	0.179	0.179	0.179	0.179	0.179	0.179	0.179	0.179	0.179
Initial Density, kg/m^3	1.664	1.307	1.031	0.851	0.724	0.631	0.558	0.501	0.454	0.416	0.383
R of Gas, J/kgK	2079	2079	2079	2079	2079	2079	2079	2079	2079	2079	2079
Energy Compress, E_c kJ/kg	2301	2301	2301	2301	2301	2301	2301	2301	2301	2301	2301
Energy Preheat, E_p kJ/kg	0	415	935	1454	1973	2493	3012	3531	4051	4570	5089
Total applied Energy, kJ/kg	2301	2716	3235	3755	4274	4793	5313	5832	6351	6871	7390
Out Temperature, T_{out} C	-156	-124	-84	-44	-4	36	76	117	157	197	237
Out Density, kg/m^3	0.416	0.326	0.257	0.213	0.181	0.158	0.139	0.125	0.113	0.104	0.096
Out Velocity, w_{out} m/s	1355	1529	1722	1895	2054	2202	2340	2470	2594	2712	2825
Mass Flow Rate, G kg/min	0.357	0.317	0.281	0.255	0.236	0.220	0.207	0.196	0.187	0.179	0.171
Kinetic Energy 1 kg, kJ/kg	919	1170	1483	1797	2111	2424	2738	3052	3365	3679	3993
Dynamic Pressure, MPa	0.382	0.382	0.382	0.382	0.382	0.382	0.382	0.382	0.382	0.382	0.382
Kinetic Power at real mass flow rate, kW	5.467	6.169	6.947	7.646	8.286	8.880	9.437	9.963	10.463	10.939	11.396
Effectiveness, %	39.94	43.07	45.85	47.86	49.39	50.58	51.54	52.33	52.99	53.55	54.03
Average velocity of the spray, m/s	679	720	760	791	818	840	859	876	892	905	917

Table 2 Results of calculation for Nitrogen

Data	Var1	Var2	Var3	Var4	Var5	Var6	Var7	Var8	Var9	Var10	Var11
Initial Pressure, P_m Bar	10	10	10	10	10	10	10	10	10	10	10
Initial Temperature, T_m C	20	100	200	300	400	500	600	700	800	900	1000
Fixed Critical Area, mm^2	6.32	6.32	6.32	6.32	6.32	6.32	6.32	6.32	6.32	6.32	6.32
Fixed Outlet Area, mm^2	10.57	10.57	10.57	10.57	10.57	10.57	10.57	10.57	10.57	10.57	10.57
Standard Dens, kg/m^3	1.250	1.250	1.250	1.250	1.250	1.250	1.250	1.250	1.250	1.250	1.250
Initial Density, kg/m^3	11.647	9.149	7.214	5.955	5.070	4.415	3.909	3.507	3.180	2.909	2.681
R of Gas, J/kgK	297	297	297	297	297	297	297	297	297	297	297
Energy Compress, E_c kJ/kg	282	282	282	282	282	282	282	282	282	282	282
Energy Preheat, E_p kJ/kg	0	83	186	291	399	508	620	734	850	968	1088
Total applied Energy, kJ/kg	282	364	468	573	680	790	902	1016	1132	1250	1370
Out Temperature, T_{out} C	-121	-80	-28	24	76	127	179	231	283	335	386
Out Density, kg/m^3	2.249	1.766	1.393	1.150	0.979	0.852	0.755	0.677	0.614	0.562	0.518
Out Velocity, w_{out} m/s	542	611	688	758	821	880	935	987	1037	1084	1129
Mass Flow Rate, G kg/min	0.773	0.685	0.608	0.553	0.510	0.476	0.448	0.424	0.404	0.386	0.371
Kinetic Energy 1 kg, kJ/kg	147	187	237	287	337	387	437	487	538	588	638
Dynamic Pressure, MPa	0.330	0.394	0.394	0.394	0.394	0.394	0.394	0.394	0.394	0.394	0.394
Kinetic Power at real mass flow rate, kW	1.890	2.133	2.402	2.643	2.865	3.070	3.263	3.445	3.617	3.782	3.940
Effectiveness, %	52.07	51.27	50.61	50.06	49.55	49.03	48.50	47.99	47.49	47.01	46.56
Average velocity of the spray, m/s	272	288	304	317	328	337	344	351	357	363	368

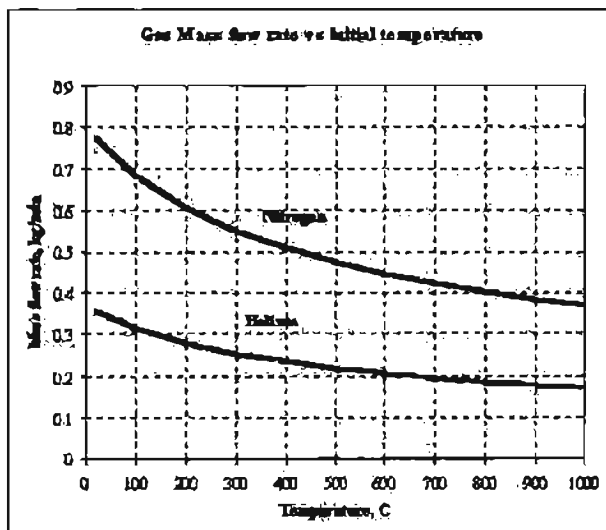


Fig. 5 Real mass flow rate of the gas through nozzle with fixed area vs initial temperature of the gas

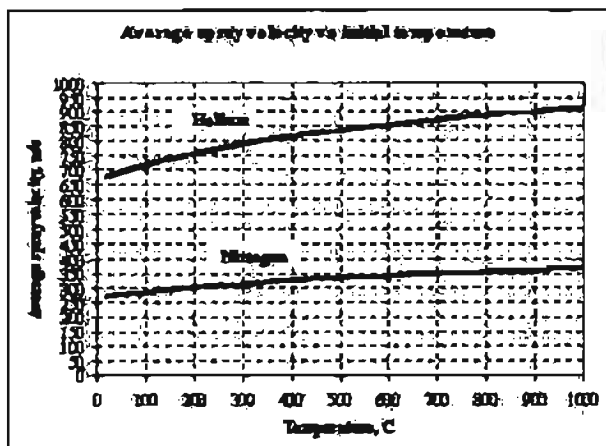


Fig. 6 Average velocity of the spray vs initial temperature of the gas

CONCLUSIONS

Preheating the gas greatly increases the jet velocity and its kinetic energy.

Despite the decrease of gas density and its mass flow rate through a fixed nozzle, the dynamic pressure of the jet remains constant.

The lighter gas (Helium) provides much higher value of kinetic energy despite the fact that its mass flow rate is half as much through the same fixed nozzle.

The effectiveness of applied energy in the case of the lighter monoatomic gas grows with increasing temperature and slightly reduces in the case of nitrogen.

Gas preheating, despite reducing the gas mass flow rate, increases the average spray velocity.

The lighter gas provides a much higher average spray velocity due to its higher initial jet velocity.

REFERENCES

- H Lubanska. Correlation of Spray Ring Data for Atomisation of Molten Metals. // *Journal of Metals*.- 1970, No22, .45-49
- Y. F. Ternovoy, S.S. Kudievsky, N. N. Pashetneva. *Engineering calculation of technological processes of molten metal atomization*. – Zaporizhia. State Engineering Academy Edition. – 2005. – p. 149.
- John J. Dunkley. Hot Gas Atomization – *Economical and Engineering Aspects*. – PM2004 World Congress Conference Proceedings. Volume 1 Powder Manufacturing and Processing. – Austria, Vienna. – 2004. – p. 13-19.
- J. T. Strauss. *Hotter gas increases atomization efficiency*. / *Metal Powder Report*. – Vol.54 No11 November 1999.
- J.T. Strauss. *Closed-coupled Gas Atomization Using Elevated Temperature Gas*. // *Advances in Particulate Materials*. – 1999. – Vol. 1. – p. 1-23 – 1-34.
- G. Wolf, K. Till, R. Scholz. Hot Gas Atomization.// *Advances in Particulate Materials*. – 2002. – Vol. 3 – p. 3-163 – 3-177.
- Dr. Fedorov. *Theoretical background of hot Gas atomization*. EuroPM2005 European Conference Proceedings. Volume 2. – Czech Republic, Prague – 2005. – p. 3-8.
- G.N. Abramovich. *Applied Gas Dynamics*. Moscow. – Nauka. – 1969. – 824 p.
- S.L. Ryvkin. *Thermodynamic properties of gases*. Moscow. – Energoatomizdat. – 1987. – 288 p.

MECHANICAL ALLOYING, REACTIVE- AND HIGH ENERGY MILLING

-encouraging industrial applications for High Kinetic Processing-

^{1,3} H. Zoz, ¹ H. Ren, ¹ H. U. Benz, ² G. Kaupp, ³ S. Diaz de la Torre and ³ David Jaramillo V.

¹ Zoz GmbH, D-57482 Wenden, Germany

² University of Oldenburg, D-26111 Oldenburg, Germany

³ CIITEC-IPN, Instituto Politecnico Nacional, Mexico City, C.P. 02250 México, D.F.

ABSTRACT

Zoz GmbH mainly based in Germany is manufacturing equipment for High Kinetic Processing like Mechanical Alloying, High Energy Milling and Reactive Milling and also using this equipment for the production of advanced materials e.g. in the range of MMC's, MCC's and CCC's and finally producing a limited number of parts with some of these materials by HIP and LPS/HIP. Significant efforts are spend in R&D in materials science and some in process engineering.

On the academic approach, since more than half a century scientists are using MA in order to synthesize new materials with new properties that cannot be created by conventional route e.g. due to a not present thermal equilibrium or immiscibility of their components. By structural design, important materials properties can be influenced (e.g. nanocrystalline, amorphous).

If the same technique is applied for particle size reduction and/or particle deformation of single-systems e.g. to receive a special particle geometry, this route is to be described as HEM and is suitable for rapid and large-scale production of ductile metal-flakes in dry process without solvents and less energy e.g. for paint-pigments, conductive pastes and anti-corrosives. On the contrary rapid particle size reduction of brittle solids like Enamels or Glass Fluxes has recently been introduced as a new application field.

By RM, ultra-fine (nanoscaled) dispersions of particles/grains in a matrix can be achieved which can additionally be cost/energy saving due to transformation by chemical reaction in direct/shorter route. Here an important goal are H₂-storage systems based on reversible soft-ionic bonding in the quasi-metal-lattice. Environmental concerns play an important role in the field of solid state synthesis and tribo-chemistry where e.g. organic solid-solid reactions can rapidly proceed without wastes in the absence of solvents at complete (100%) transformation.

After years of work in processing, materials science and potential application, HKP found and is finding it's way into daily use and daily products.

The present paper explains the processing, the materials science and applications in particular all mentioned above.

1. HIGH KINETIC PROCESSING

Mechanical alloying (MA) has been described as a process where powder particles are treated by repeated deformation, fracture and cold welding by highly energetic collisions of grinding media in a milling process [1-3]. By this technique it is possible to synthesize new materials with new properties that cannot be created by conventional route e.g. due to a not present thermal equilibrium or immiscibility of their components. By structural design, important materials properties can be influenced (e.g. nanocrystalline, amorphous). Basically we want to transfer energy into powder material where the proportion of total energy consumption and energy in system is of high interest for any commercial approach (energy balance) [4]

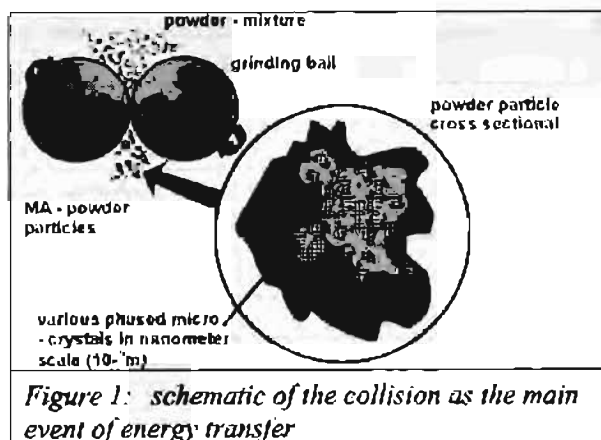


Figure 1: schematic of the collision as the main event of energy transfer

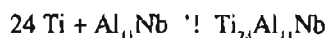
High energy milling (HEM) and reactive milling (RM) are performed by the same processing principle where the variation is in general based on the target of the processing, the transformation effect by the kinetic energy and the starting materials.

The different procedures can be described as High Kinetic Processing (HKP) where the collision of the grinding media is the main event of kinetic energy transfer from the milling tools into the powder [1-3]. Fig. 1 shows the schematic of the collision. The basic equation (1) describes the relation between the kinetic energy (E_{kin}) and the mass m and the velocity v of a single ball:

$$E_{kin} = \frac{1}{2} m v^2 \quad (1)$$

It is clearly seen that the maximum relative velocity of the grinding media is the most determining factor contributing to the kinetic energy.

A typical example of practical importance that demonstrates the effects that are inherent in Figure 1 has been described in detail [5] in the system:



In this work the influence of the milling parameters have been evaluated and basically the processing route of Cycle Operation for CMB-materials [6] had been invented. By this technique, the problematic agglomeration and sticking behavior of the in this case Ti-Al-based material in a dry milling process could be significantly reduced which did lead to an increase of the powder yield from < 4 % to 80 %. Later on similar effects were found in the Ti-Ni-system [7] and in the processing of a number of ductile metal flakes [8-9]. In 1999, Kim et al. investigated the difference of Cycle Operation and Constant Operation in the Fe-Co-system and

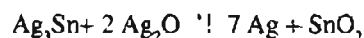
found tremendous effects on particle- and in particular crystallite-size reduction [10].

If the here described processing method is applied for particle and/or crystallite size reduction or particle deformation (e.g. flakes) in single systems, this route is described as HEM. The goal can be to receive a special particle geometry e.g. for rapid and large-scale production of ductile metal-flakes in dry process without solvents and less energy e.g. for paint-pigments, conductive pastes and anti-corrosives [11-12]. On the contrary rapid particle size reduction of brittle solids like Enamels or Glass Fluxes has recently been introduced as a new application field [13-14].

The definition of RM is suitable if during milling a chemical reaction is wanted and observed.

By this route, a dispersion of ultra-fine (nano-scaled) crystals and/or a homogeneous dispersion of transformed phases in a matrix can be achieved [15].

A typical example of practical importance here has been demonstrated in the Ag-Sn-system [16]:



Due to the CMB-behavior of this ductile system, again the processing has to be performed by applying Cycle Operation. With respect to the starting materials (e.g. Ag_2O instead of Ag), RM in this kind of principle can show economical advantage. Often these processes are environmentally benign as they avoid wastes e.g. in solid state synthesis where organic solid-solid reactions and others can rapidly proceed without any wastes and in the absence of solvents [17-18].





Table 1 Summarizes the most important application-fields of HKP:

Applications/products of High Kinetic Processing (HKP)		
High Energy Milling	Mechanical Alloying	Reactive Milling
➤ surface, shape, particle size	➤ alloys (pseudo)	➤ chemical reactions
• flakes (particle deformation)	• nanocrystalline materials	• contact materials
• particle coating (LPS, S)	• amorphous materials	• nanocrystalline materials
• nanocrystalline materials	• oxide dispersion strengthened alloys	• mechanochemistry
• highly dispersed materials	• iron and oxide based magnetic materials	• solid state syntheses
• soft magnetic materials	• bearing materials containing solid lubricants	• hydride - dehydride
• particle size reduction (e.g. enamel, ceramics)	• ceramic-metal composites (MMC, CMC, MMC, CCC)	• activation of catalysts
<i>Table 1: important applications/products of HKP</i>		

2. PROCESSING (MILLING) TECHNIQUES

Industrial mills of different types are in practical use for a number of commercial applications. Vibration-mills have to move the mass of the grinding chamber. This limits their size and in particular they are difficult res. impossible to be operated under controlled condition like atmosphere or closed circuit. The same is valid for simple (drum-)ball-mills with a rotating vessel [19]. Jet-mills use large streams of air or inert gas which limits their use in reactive milling. Next to this the non-presence of grinding media does not lead to significant kinetic effects. Bead-mills, horizontally or vertically, do not exhibit a significant kinetic impact as well, since here no high-level relative acceleration of the grinding media occurs which leads to shear- and friction effects but not to collision (Fig. 2a, b). Planetary ball-mills and shaker-mills are technically limited to laboratory size [20-21]. The most suitable choice are horizontal rotary ballmills (Simoloyer) that can be operated in dry processing at high relative velocity of the grinding media (up to 14 m s^{-1}) that cannot be reached by the other types (up to 5 m s^{-1}) under controlled condition like vacuum or inert gas (for charging, operation and discharging) [22] and in closed circuits [23].

Table 2 compares most corresponding devices that are in use for Mechanical Milling (MM) and partly for high kinetic processing (HKP) with respect to size and maximum velocity of the milling tools.

device	Simoloyer [®]	Planetary Ball Mill	Attritor [®]	Detonool/mill
max. diameter [m]	0.9	0.2	1	3
max. total volume [l]	400	8	1000	20000
max. rel. velocity [m/s]	14	3	4.5-5.5	4.5
grinding (cotton section)				

Simoloyer[®] is a brand of Zos GmbH, Germany; Attritor[®] is a brand of Union Process, U.S.A.

Table 2: Devices used for MM/HKP

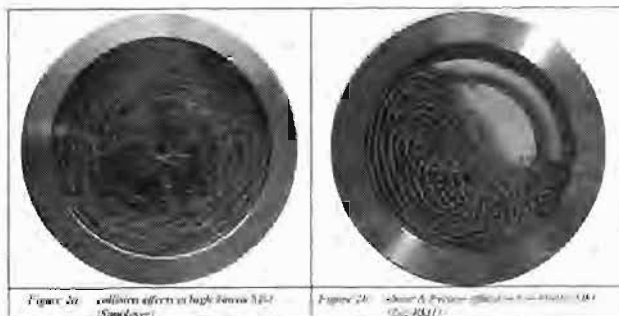


Figure 2a: collision effects in high kinetic ball-mill (Simoloyer)

Figure 2b: Shear & Friction effects in a horizontal ball-mill (Zos RQM11)

Once using these devices and obeying the before, we can expect to achieve an energy transfer, grinding, milling, mixing bonding etc. at a high energetic level (efficiency & balance), at short processing times (performance) and at a

low contamination level (compared to low kinetic ball-/ attritormilling). In particular the last mentioned advantage is important to be pointed out since in the literature MA and insofar on the contrary, sometimes has the bad nickname "dirty milling". This in fact is most usually caused by improper technique and/or not suitable parameters. E.g. after a processing time beyond 100 h or even much more (up to more than a thousand hours can be found !), it will not be surprising, that e.g. an Fe-pick-up of the product caused by wear of the milling tools might occur in a range of 3-10 wt-% which is most usually not acceptable. At Zos, any kind of HKP-process exceeding a processing time of 1 h is regarded as critical and any process exceeding 5 h time is expected to be not in accordance with economics. Also various work is available where impurity-levels are compared with different systems like Simoloyer versus Planetary Ball Mill [20], Simoloyer versus SPX-mixer/mill [21, 24].

3. THE HORIZONTAL ROTARY BALLMILL (SIMOLOYER)

Horizontal high energy ball-mills are known from academic as well as industrial applications in mechanical alloying (MA) [3-5, 7, 10], high energy milling (HEM) [8] and reactive milling (RM) [16]. They supply the highest relative velocity of grinding media, which leads to a high level of kinetic energy transfer, an intensive grinding effect and short processing times. The contamination of the processed powders by the milling tools is naturally lower since the process is based on the collision of grinding media rather than on shear and friction interaction of the same which usually leads to higher abrasion. Since the grinding media is accelerated by a horizontally arranged rotor inside the grinding vessel, these devices do not have to move unnecessarily any large masses like e.g. the entire chamber/mill in case of vibration-mills. The systems are presently available from 0.5 to 900 liter grinding chamber capacity [22] where larger volumes seem to be possible.

Various existing applications include MA of different metals and/or ceramics [25], room temperature inorganic syntheses, waste-free organic chemical solid-state syntheses with 100% yield and many others. In particular in HEM, we found very rapid processes in the range of minutes as well as in the range of seconds [13, 14]. Then, the application of the semi-continuous processing mode can be considered res. is applied. As of today's state of the art the processing time in batch operation shall be less than 20 min in order to expecting a chance to reduce this into second-range by using the continuous carrier-gas mode (see next chapter). In any other case, the approach for a large scale manufacturing process is followed by the auto-batch-mode (see next chapter also).

Figure 3 shows a horizontal rotary ballmill with a 2 liter chamber volume that can be placed on a table next to the process controlling computer which is operated with water cooling or heating at rotation frequencies up to 1800 rpm. Figure 4a shows a production unit with a 100 liter chamber. The cross sections through the grinding chamber in Figure 4b visualize the working principle where the rotor is the tool to transfer the kinetic energy into the grinding media and the grinding media transfers into the powder material. Finally Table 3 concludes 12 major features of this kind of equipment with respect to HKP.



Figure 3: horizontal high energy ballmill (Simoloyer[®] CM100) in high-temperature mode
 attached CM40 – sampling unit CM10 for
 4. charging
 5. operation and
 6. discharging (including sampling)
 under vacuum and/or inert gas
 12a) TRIZ-S.H.P. – process controlling PC in the
 hard

12 major features of a High Kinetic Processing (HKP) device	
1	a system made for MA/HEM in a dry process for industrial application
2	supplies 1 times higher relative velocity of grinding media than conventional devices
3	can not only be operated but also charged and discharged under vacuum/inert gas
4	allows easy sampling under sealed conditions
5	allows processing without dead-zones & negative gravity influence
6	can be operated by Cycle Operation
7	can be operated at high temperature due to separated cooling/heating systems
8	can be operated at low temperature (up to -30°C) by separated cooling systems
9	is fully software operated, allows parameter measurement, control and history
10	is technically scalable from 0.5 to 900 liters processing chamber capacity
11	can be operated in batch, semi-continuous and auto-batch mode (carrier gas)
12	is available with tools by stainless steel/titanium, WC-Co and SiC/Ni

Table 3: major features of a HKP device

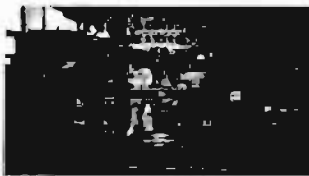


Figure 4a: horizontal rotary ballmill (Simoloyer[®] CM100-r2), production unit for nanocrystalline metal hydrides



Figure 4b: cross section of a grinding unit CM100-s2

4. BATCH PROCESSING, SEMI-CONTINUOUS AND AUTO-BATCH PROCESSING

4.1. Batch processing

The processing in batch operation is the most common and most simple procedure in HKP. The principle is to load a process chamber with starting material, to process the material and finally to unload the processed material. For charging, gravity is used which means the main-port of the

grinding unit is arranged in top-position. For discharging, the grinding unit is turned for 180° (main-port in bottom position) and gravity and centrifugal force of the rotating rotor are used.

The main criteria and issues in batch operation are:

- safe and complete charging (loading) of the starting material, e.g. under controlled condition like inert gas or vacuum
- safe processing of the starting material, e.g. under controlled condition like inert gas or vacuum including temperature control
- complete processing of the starting material, e.g. like no dead-zones or dead-layers during processing
- safe discharging of the processed material, e.g. under controlled condition like inert gas or vacuum
- complete discharging with a powder yield close to 100 %
- acceptable relation between processing and discharging time res. kinetic impact during the same

One of the major issues here is safety which means both, protection for human and hardware and also safety for a successful process. To make it shorter, only the most critical processing shall be considered which would be e.g. a Ti- or Al-base material. In order to avoid e.g. oxygen pick up and a high kinetic oxidation reaction after processing which usually would end in an explosion, the starting material would have to be handled in a glove-box where the charging container is loaded. This container is then connected with the air-lock at the Simoloyer, the entire system is evacuated and the material finally charged into the process-chamber. Then this is either flooded with inert gas or further evacuated. After processing, the material must be discharged in safe condition again which is in so far the most critical part. Air-lock and (charging) container can easily be disconnected and cleaned or exchanged, however, the processing chamber can not be opened to outside at any time. This means the entire process can only be executed with a drainingrating of Ask-type [26] which is shown in figure 2. And here it is already difficult to guarantee that during charging, first, the powder can pass the screen-grating in the first ball-valve and second, that no starting powder remains inside the drainingrating before this is locked since if not, then later during discharging, the processed powder would be polluted with non-processed powder. During processing it is important, not to have any dead-zones inside the chamber and not to create dead-layers during res. by the processing since then the process would not be successful and the powder product would not be



*Figure 5:
draingrating
Askv-08-20-50*

treated unique. For the here regarded CMB-material [7], Cycle Operation [5-6] must be applied in order to counter sticking and agglomeration tendency where in some cases even an addition of a PCA, e.g. a lubricant like stearic acid can not be avoided.

For discharging, it is additionally important, to completely unload the material which means a close to 100 % yield is important. This is first because the target of the process is to receive the material and second because remaining material in the chamber will cause severe problems in terms of opening the same.

For the entire process, a proper temperature control is necessary which is usually cooling but sometimes also heating or cooling to extremely deep temperature. The oxygen-content must be controlled either by vacuum- or oxygen measurement and the temperature by a number of sensors connected to the operating software of the device.



*Figure 6a:
Simoloyer CM01-2l*

*Figure 6b:
Simoloyer CM20-20l*

*Figure 6c:
Simoloyer CM100s2*

Figure 6a shows a laboratory-scale Simoloyer CM01-2l that can be placed on a table next to the process controlling computer and is operated with water cooling or heating at rotation frequencies up to 1800 rpm. The grinding unit is connected with an Ask-draingrating to the DN40-air-lock and DN16-sampling-unit and is in charging/operation position and the air-lock is connected to gas- and vacuum

supply. Figure 6b shows a semi-production Simoloyer CM20-20l with a DN50-air-lock in discharging position. Figure 6c shows a production Simoloyer CM100-100l with a special draingrating for metal-hydrides connected to a DN40-sampling-unit and just turned from operation- to discharging/sampling position.

4.2. Auto-batch processing

Auto-batch processing is in general a batch process with adapted and automatic charging and discharging procedure. The Simoloyer is then operated only in operation/charging position where for discharging not gravity but a carrier-gas flow [14, 23] is used. By this, also the before needed effect of centrifugal force by rotor rotation can be tremendously reduced which can be of important advantage (see chapters 2 and 4.1).

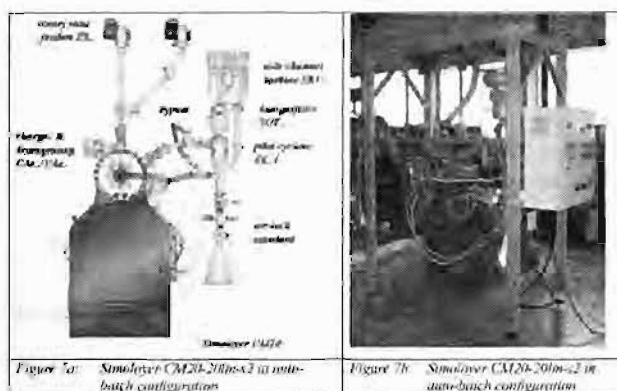


Figure 7a: Simoloyer CM20-20lms2 in auto-batch configuration

Figure 7b: Simoloyer CM20-20lms2 in auto-batch configuration

Figure 7 shows the configuration of a Simoloyer CM20 in auto-batch configuration. The grinding unit is equipped with a second main-port in order to adapt charging and discharging devices at the same time. The draingratings still must be Ask-type but equipped with automatic valves. The charging unit is equipped with air-locks (not shown) following in line the rotary vane feeders. The discharging unit is based on a closed carrier-gas circuit where the gas is entered at the side-port of the grinding unit, then inside the chamber a multiphase-flow (gas and powder) is formed which is separated outside the chamber in the cyclone (see chapter 4.4). The operating software of the Simoloyer is extended and controls also the 4 valves at the 2 draingratings as well as the side channel turbine (gas drive) and one or more rotary vane feeders at the charging unit.

By this configuration and in case of exchanging the charging- and discharging containers into much bigger ones, it is possible to use this device for a constantly repeated batch process automatically. But then a main requirement is that complete discharging can be guaranteed (see chapter 4.1).

4.3. semi-continuously processing

The semi-continuous operation procedure can be divided into two principles, the one using depression and the one using compression. The difference describes a different use of carrier-gas where in depression mode the gas system is open and suction is used to carry powder particles out of the grinding chamber into a cyclone. In compression mode, the carrier-gas is cycled in a closed gas-circuit which may also be divided into a primary and secondary circuit. In both cases, the Simoloyer is continuously fed with starting material and continuously processed material is discharged. Important issues here are the control of the amount of powder in the grinding chamber and the separation/res. classification of the product out of the gas-flow.

Figure 8a shows a graphic of the semi-continuous configuration of a CM100 Simoloyer in depression mode. The picture in Figure 8b shows an image of this unit where the cyclones are located in the second floor and can therefore not be seen on this picture.

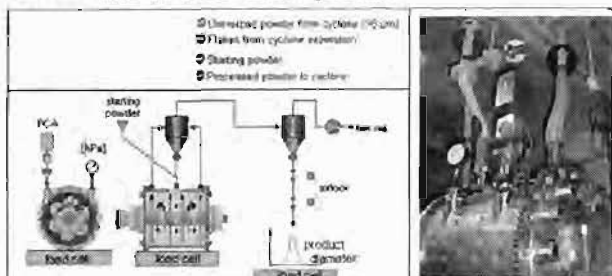


Figure 8a-b Simoloyer CM100-s1 in semi-continuous configuration (depression mode)

The entire unit is based on a load cell which is connected to a control unit that also controls the automatic feeder for the starting powder and in this case another one for a PCA. A fan is initiating depression through 2 cyclones that are connected with the grinding chamber where the first one separates to heavy particles and returns the separated fraction into the Simoloyer, the second one then separates product and gas.

Figure 9 shows a graphic of the semi-continuous configuration of a CM100 Simoloyer in compression mode.

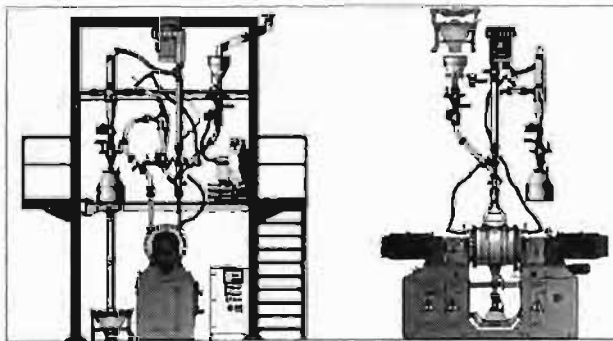


Figure 9 Simoloyer CM100-s1 in semi-continuous configuration (compression mode)

In general, in this unit the Simoloyer is equipped with a closed gas circuit where the side channel turbine on top blows the gas at high velocity through a heat-exchanger, then the carrier-gas picks up the starting material at the injection unit and goes into the grinding chamber at 2 tangential ports. On the other side of the unit, the multiphase flow leaves the chamber via 2 more tangential ports and goes into the first cyclone which has a return path into the chamber. In line after the first cyclone the classified multiphase-flow is separated in the second cyclone and the final material is collected in a container that is adapted with and automatic air-lock. Before the carrier-gas is returned into the turbine, it has to pass a filter-unit that automatically returns filtered dust into the second cyclone. In order to classify the multiphase-flow at the first cyclone, the gas system is equipped with various by-pass units which allow to adjust different velocities in each of the cyclones, the grinding chamber and the piping.

With respect to application, the main criteria is the remaining time. Up to now, this principle can only be realized for those processes that require in batch operation a processing time in the range of several minutes e.g. rapid particle size reduction of enamels [13-14]. Due to the effect, that the fine fraction of particles is continuously, which means here also immediately discharged out of the vessel, the dumping effect of this fraction (like liquid) is terminated and consequently the kinetic of the system is increased tremendously. Additionally it is important to understand, that in case of treating large brittle particles in up to several mm-scale by collisions of grinding media at high kinetic, these particles will collapse not just into two pieces but into a number of pieces of different size and finally with a size distribution. This means that also a very fine fraction is present right away. For the today's understanding, this all together leads then to the found extremely short processing times in continuously mode in the range of several seconds for these materials-systems which is also valid for OPC, enamels and glass fluxes and others [13-14].

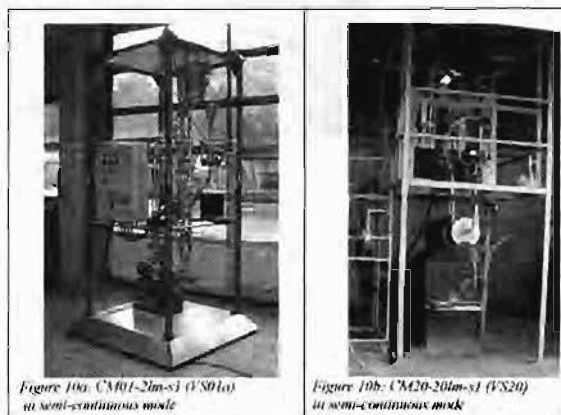


Figure 10a: CM100-20m-s1 (V501a) in semi-continuous mode

Figure 10b: CM100-20m-s1 (V520) in semi-continuous mode

Figure 10 a shows the initial experimental unit VS01a based on a Simoloyer CM01-2lm-s1 which is originally designed and used for the controlled and continuously production of ductile metal flakes [27] as well as rapid particle size reduction of brittle solids (e.g. enamels and glass-fluxes).

This unit (Figure 10a) is based on a closed carrier-gas system driven by a side-channel-turbine adapted to a Simoloyer CM01-2ls1 with 2 cyclones for separation/classification, some valves for circuit-control, rotary vane feeders with air-locks, filter, evacuation pump, computer- and electrical control, a special separation and other units. The system has two connected circuits, the primary and the secondary circuit. The secondary circuit is only needed for the processing of ductile metal flakes and therefore closed by means of a valve between the two cyclones. The bypass between the rotary vane feeder and the junction tube can be disconnected and used as the discharging route where the first cyclone is now only used for a solid-separation of the multiphase-flow coming out of the grinding chamber of the HEM-device. If no inert atmosphere is needed, the air-lock parts on the injection-side can be replaced by a simple plastic funnel for charging.

Figure 10 b shows a production unit VS20 based on a Simoloyer CM20-20lm-s1 where in difference to the unit VS01 (Fig. 10 a), only one gas-circuit is needed and realized. This unit has a manufacturing capability of several hundreds of kilos per day (HEM of brittle solids).

4.4. carrier-gas assisted discharging / processing of CMB-materials

In case of any Mechanical Milling (MM) process and so in HKP, the goal is to receive a processed material which means quality and quantity is expected. Quantity here means a good powder yield which is a yield close to 100 % and this means a complete discharging is necessary.

The Simoloyer is known to supply easily complete powder yield in case of non-CMB materials which would be materials that are easy to process and would here mean that show no significant sticking and agglomeration tendency during processing and discharging. Ameyama et al. compared the Simoloyer and the planetary ball mill with respect to MM efficiency in refinement of HS-steel [20] and confirmed the Simoloyer at a yield around 100 % and the PBM below 50 %.

But even in case of non-CMB material, just the complete powder yield is not always enough. Very important is also the relation of processing time and discharging time which is an expression for the kinetic impact during both processing steps. Discharging shall not supply kinetic impact at all but of course does because the centrifugal

force on the powder by rotor rotation is needed for discharging (in batch operation). Additionally, since during discharging, the relation between grinding media and powder inside the chamber is drastically increased (powder goes out, grinding media stays in), the kinetic is dramatically increased. In case of short discharging times after long processing, e.g. 2 hours processing and 10 minutes discharging, this is usually not problematic. But if this relation is completely different, like 3 minutes processing and 5 minutes discharging, then this cannot lead to a unique product since the material being discharged after 3+1 minutes must be expected to be different from the material being discharged e.g. after 3+5 minutes. Exactly this problematic with the given numbers was met in 1997 at a Cu-flake production with a CM100 Simoloyer [9] and this was the reason that this unit had to be operated in semi-continuous route [28] as given in figures 8.

This means sometimes it is a strict requirement to achieve a short discharging time at lowest kinetic impact and always this is of course a challenge for a more economical process.

In case of CMB-materials additionally we have the problematic, that the material tends to stick to the milling tools which in standard procedure would end in extremely long discharging times like more than 1 hour to receive a full powder yield, if this is possible at all. This must in particular be countered already during processing by Cycle Operation and if necessary and acceptable, also by the addition of a PCA in order to avoid the formation of dead-layers [29, 30] and strong agglomeration. Only "free" powder in the chamber is processed successfully and only "free" powder can be discharged. And of course it is very non-opportunistic to accept the formation of dead-layers and then later during discharging to try to loose them by grinding since this will end in non-unique powder as described before. Cycle Operation then shall also be applied for the discharging step.

If we conclude the topic here into groups, then the third group might be that in case of any commercial production, first a complete powder yield is favorable and second a quick processing time (including discharging) is wanted. Additionally, since production usually means ongoing processing, a kind of automatic procedure is wanted and this means there can be no increased residues after every processing acceptable because this would end in a kind of overloaded grinding chamber. Next to this, and also in case if only batch processing can be applied, any interruptions shall be kept as short as possible and labor intensity of the processing shall be reduced to the minimum.

And this last paragraph contains the motivation to use the carrier-gas flow as described in chapter 4.3. for mass-production.

The general idea of CAD is to use a carrier-gas to transfer processed powder-material out of the grinding chamber of a Simoloyer or any other MM-device. Here the main expected advantages are a decrease of discharging time, a decrease of kinetic impact during discharging (Simoloyer must only operate very slowly) and easier adaptation of any automatic process.

Figure 11 shows a picture of the carrier-gas discharging unit TGD20a (adapted to a CM20-Simoloyer). In general, TGD20a blows the carrier-gas (usually argon) at high velocity into the side-port of the grinding unit. The gas picks up the powder inside the grinding chamber where the rotor must only be operated very slowly in order just to mix the powder into the gas-flow. The multi-phase flow is exiting the grinding chamber at the main-port through the Ask-type drainingrgrating and then arrives into the TGD20a again. Additionally there is a by-pass short-cutting the grinding unit which allows to adjust a different gas-flow velocity inside the chamber and TGD20a.

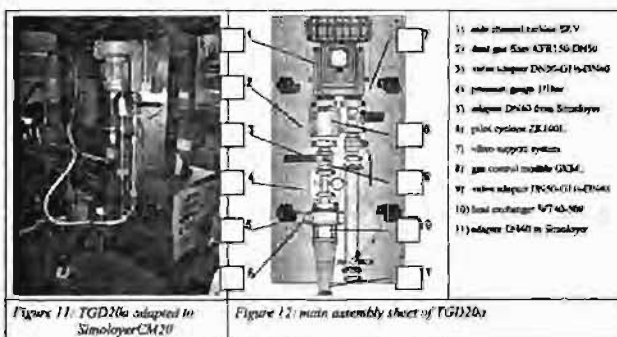


Figure 12 shows the graphic of the main assembly sheet of TGD20a. The side channel turbine is driving the gas-flow which first passes the gas-control-module where the oxygen-content is recorded and controlled. Then the gas enters the heat-exchanger in order to cool down the gas temperature that is mostly heated up inside the turbine by compression and expansion but also inside the grinding unit of course. Then the gas-flow is guided by some connecting pipes into the side-port of the grinding chamber res. into the by-pass short-cutting the same. After the gas-flow is loaded with powder particles inside the chamber and therefore is now called multiphase-flow, it returns to the TGD20a in the completely closed circuit and goes into the pilot-cyclone. In there, solids and gas is separated. The powder (solids) is than transferred into an adapted standard air-lock with a powder container (not seen on the graphic but on the picture). The gas is sent from the cyclone into a dust-gas filter which protects the turbine from extremely fine particles in submicron scale that my pass the cyclone without being separated. Then finally the gas enters into the turbine again and the circuit is closed.

Additionally TGD20a is equipped with a number of valves and flow-control units that are used for initial evacuation before TGD20a is flooded with inert gas (Argon) res. that are used for some process control e.g. in terms of by-pass effect etc. (see chapter 4.3.).

All before described units are fixed on the main assembly sheet (excluding some flow-control units) and this sheet is fixed in a kind of flexible connection to the base frame of TGD20a. Then the main assembly sheet carries 4 exocentric motors that initiate a vibration to the entire main assembly sheet with all the single units. Since all the flow-directions inside TGD20a are arranged vertically, this converter driven and in so far adjustable vibration supports the powder flow and avoids sedimentation inside the piping. In particular it is important for the function of the dust-gas filter since this unit (KFR I-DN50) is designed that the vibration will return filtered material trough the cyclone into the collection-container as soon as the turbine is stopped. Additionally this filter unit is equipped with 2 cleaning-gas ports that can be used for blowing argon-gas through the filter but in vice versa direction than the turbine does.

Since in the closed gas-circuit of TGD20a, a gas-flow loaded with powder particles is moved at high velocity, careful attention must be given to the problematic of electrostatic charge of the unit. Therefore it was very important, that no electrically isolated units are present in the entire gas-circuit. On the other hand the first used flex-metal-tubes for the connection of TGD20a to the Simoloyer turned out to be not suitable since they have no smooth inner surface at all. Therefore we finally had to replace them with self-made conductive flexible tubes where we use polymer-tubes with included Cu-wire and fit them with KF-adapters.

In 2004, Saito et al. reported the set-up of a TGD-unit for the manufacturing of PM-starting powder in a Simoloyer [31] where also interesting and challenging comparative results can be found.

5. POWDER PRODUCTS

HKP is still a kind of border technology and insofar not a common widely used and understood process. The business in manufacturing corresponding equipment is a typical niche market where the same does not go for the application necessarily. It all started in powder metallurgy which is itself a small niche in metallurgy. In the end we are moving in the niche of a niche where the synonym metallurgy today is not proper any longer since there are important applications going on in the range of ceramics and composites as well, maybe even most. In particular for existing products and even more in case of sensitive products (e.g. ductile metal flakes as pigment base for

automotive car-body) it is very difficult to convince industry even to trying a new and more sophisticated manufacturing route. Nobody there is basically interested in equations or diffraction patterns but in a given product and it's numbers and volume. That means believing to having available a superior technology is not enough since one must have the product in hand. The same of course goes for new materials as a result of a new process technology. In result it was necessary to not only develop the process, the market demanded and is demanding to also develop the product of this process as well. Then of course the step into a product manufacturing is not that far any longer and some of the results are reported in the following:

5.1. Ductile metal flakes

Metal flakes are an excellent pigment-base for metallic paints, in particular due to their metallic luster. Al-flakes can be found in sprays and lacquers for coating on metal surfaces with large applications in particular in automotive. Flakes based on Au, Cu, Ni and Au-Ag-Cu-alloys are mostly utilized for decoration purposes, e. g. on surface of ceramic or synthetic materials to make the golden color effect. The metal-flake is most frequently coated with a metal-oxide by CVD-process in order to increase the shiny effect. Metal-flakes can also be used to produce conductive thin-layers. This enables the production of special soldering material for micro-electronics, printable flake-pastes for computer-keyboards and high-quality screen-heating systems in automotive industry [8].

Additionally, flakes can be used in the liquid phase sintering (LPS) technique as a suitable starting geometry for coating the to be sintered component. A similar application is possible in soft magnetic materials, which consist of two different "overlay" and "core" materials. The encapsulation of a magnetic [32] by a nonmagnetic can be obtained by adding nonmagnetic and ductile flakes to spherical and less ductile magnetic powder in a correspondingly tuned milling process.

The conventional processing route is accomplished by a low kinetic milling process in a (drum) ball mill either in wet condition often using alcohol or in dry condition using stearic acid or other organic PCA's. This leads to milling times in the range of 5 hours up to several days.

In comparison, the HEM-route is 100 to 1000 times faster and therefore shows a large potential to become the future technique for an economic production of ductile metal powder flakes.

In particular processing in liquid condition under alcohol is very expensive with respect to environment costs due to later cleaning needs.

The parameters of the milling process do influence the geometry and the size of the final flakes. The important parameters are given in table 4.

manufacturing of ductile metal flakes

1. rotary speed of the rotor
2. powder/ball weight ratio
3. total filling ratio
4. process temperature
5. process atmosphere
6. PCA/lubricant if needed
7. operating model
8. milling time

Table 4: major parameters

Furthermore, the starting powder particle size is very important. As an example, in case of chemically precipitated and nanoscaled Au-starting powder (Figure 12a), the theoretical calculation [33] indicates that one single metal flake with a dimension of $d = 100 \mu\text{m}$, $t = 0.2 \mu\text{m}$ consists in minimum from 500.000 theoretical starting particles with a theoretical minimum number of 50 interfaces. Consequently, a stacked structure of the powder particles which possess a high density of displacement caused by deformation was produced. This leads to an increase of hardness and brittleness of the powder particles, which is not wanted in general.

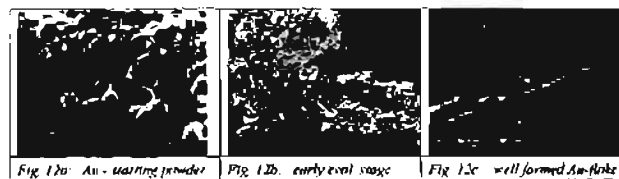


Figure 12b shows an SEM-micrograph of the Au-material in early evolution stage and gives an idea about co-agglomeration of a single flake by thousands of starting particles. This effect in detail has been studied once observing the solid solution formation in the Ag-Cu-system [21, 24]. Figure 12 c shows impressively the cross-section of a formed flake in later stage.

In particular for the processing of these kinds of very critical materials due to their milling behaviour, cycle operation is an essential factor to achieve the wanted goal. The corresponding parameters are displayed in figure 13a for the processing as well as figure 13b for the discharging procedure.

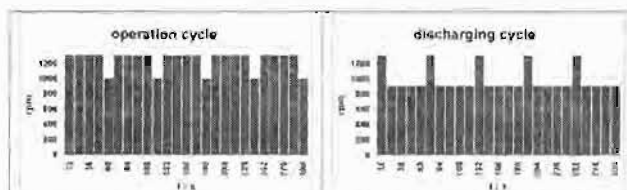


Fig. 13a Au-flakes Operation Cycle

Fig. 13b Au-flakes Discharging Cycle

For each of needed flake materials, a severe investigation of suitable starting material and parameters is necessary. The work in various kind of materials like [Au], [Ag], [Al], [Cu], [Ti], [Zn], [Fe] and others did lead to products as given in the following figures.

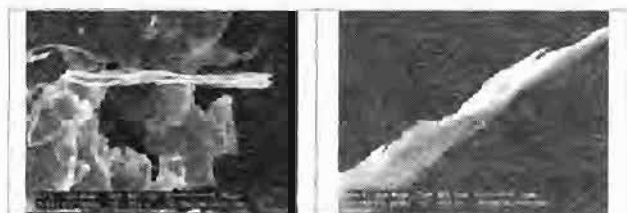


Fig. 15a Zn-Cu-flake ZC-UB17

Fig. 15b Zn-Cu-flake ZC-UB17

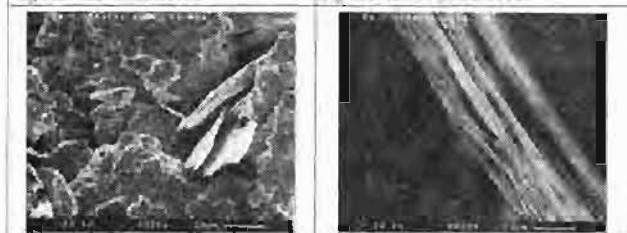


Fig. 16a Zn-Ag-flake ZAG1724

Fig. 16b Zn-Ag-flake ZAG1724

Copper and Silver-flakes are manufactured in small quantities only for relatively exclusive market-applications. After intensive work on Al-flakes as a potential introduction into automotive industry, it had to be realized that in particular the Al-pigment base used for the metallic paint on car-bodies is just too sensitive in order to be used as an introduction in a critical application. Even having a very interesting product at even more interesting cost in hand, it up to now could not move anything in this industry. An easier level of application but still also for automotive use, is represented by Zink-flakes used for corrosion protection of small parts in automotive such as nuts and bolts. A very close and large market is the entire fasteners industry and the even larger one is corrosion protection of road-rails, bridges, dams, naval vehicles etc. For this a group of Zink-flakes has been developed to be used in solvent and water-based paints to be applied air-dry or at heat-treatment. Also powder coatings are covered. These materials prove an outstanding corrosion protection, an excellent aspect ratio and are cost effective due to HKP as an advanced processing technique compared to conventional low kinetic ball-milling.



Fig. 15a Zn-Zn-flake ZN14

Fig. 15b Zn-Zn-flake ZN14 (optical microsc.)

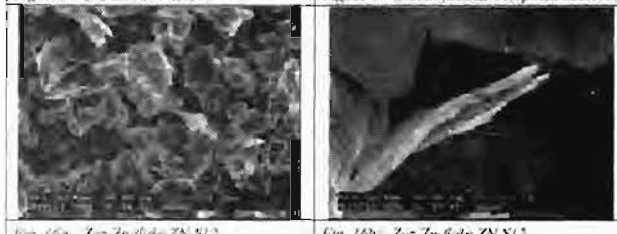


Fig. 16a Zn-Zn-flake ZN-S12

Fig. 16b Zn-Zn-flake ZN-S12

Figure 15a shows an SEM-micrograph of Zn-flake ZN14 where figure 15b shows an optical micrograph of the same. ZN14 is the most commonly used material for all kinds of corrosion protection coatings.

Figures 16a+b show SEM-micrographs of Zn-flake ZN-S12 which has been developed for an exclusive application at extremely low Fe content (<3ppm).

5.2. Nano-structured contact material Ag-SnO₂

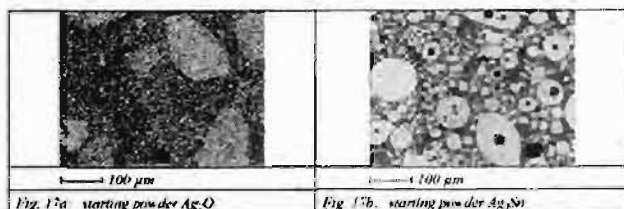
Silver cadmium oxide was res. is used as a conventional material for electrical contacts and other electrical components since a number of years as it is a good choice to achieving (electrical) properties such as [15]:

- low erosion both in make and break operations
- high extinction of the electrical arc
- low welding force
- preventing high temperature which leads to a superficial layer of oxide on the top of the contact

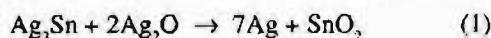
However, in particular concerning the problematic of toxicity of cadmium oxide, the application of this material is reduced to a minimum and has to be replaced by a suitable material with similar but minor harmful properties. A proper candidate for such an application is represented by the system silver tin oxide [16]. The tin oxide system does offer a very low welding force but unfortunately presents large contact resistance caused by a thick oxide layer formed on contact surface. The development of a new process had to be technologically superior and cost effective and did lead to silver cadmium free electrical contacts with a new method of manufacturing powder on a nanoscale for low tension application.

In result, very pure electrical contact material Ag-SnO₂ composite is produced by Reactive Milling (RM). The

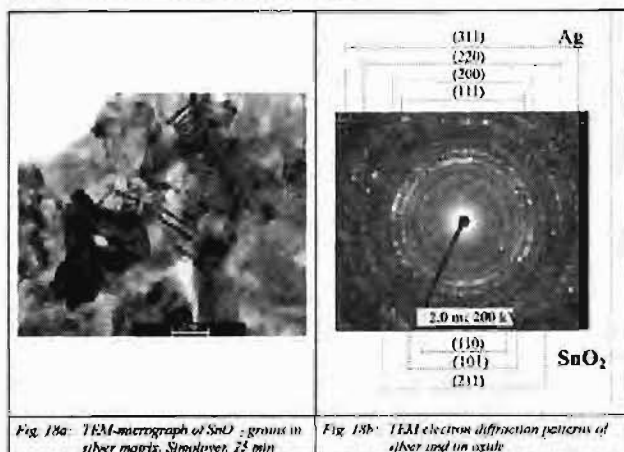
starting materials are a powder mixture of silver tin alloy Ag_3Sn (Figure 17a) and silver oxide Ag_2O (Figure 17b). Ag_2O is obtained by electrochemical deposition. Ag_3Sn is obtained after water atomization and sieving through different meshes.



After mixing in a specific concentration ratio, the material is processed in a Simoloyer (horizontal rotary ball mill). During the milling process a chemical reaction takes place:



and simultaneously, mechanical alloying is carried out which leads to a high dispersed phase distribution of nanoscaled SnO_2 -particles in a silver matrix. At optimized conditions, the process is performed at elevated temperature which means the HKP-device is preheated and continuously heated during the entire process.



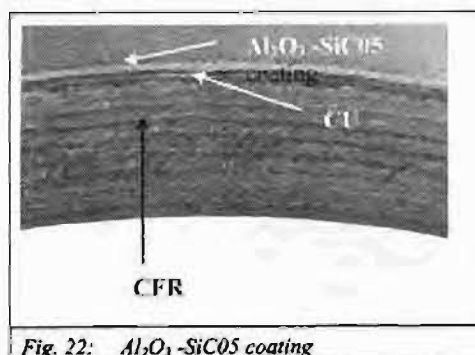
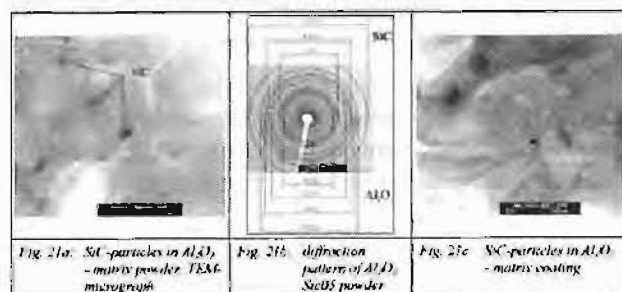
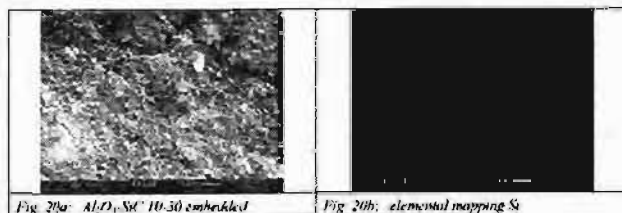
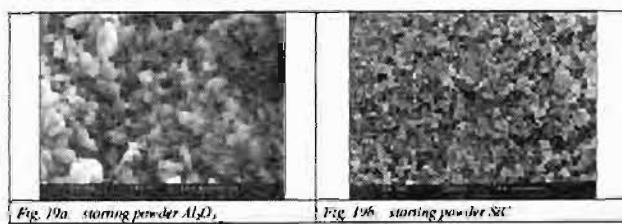
The contamination of Ag-SnO_2 composite by the elements such as Fe, Cr, Co and WC from the milling tools is very sensitive since it can be dramatically detrimental to the electrical properties. Therefore a short processing time (here 25 min) is essential as well as the proper type of grinding unit (milling tools) must be chosen.

This process results in an extremely fine dispersion of second phase particles in the matrix. Figure 18a shows the TEM-micrograph and figure 18b the corresponding diffraction pattern after the 25 minutes RM-process.

5.3. Nano-structured CCC-material Alumina-SiC05

Ceramic materials do have a high hardness and show a good corrosion resistance in general. However, due to their brittle nature that favours micro-cracks and further evolution of the same, conventional ceramics are limited in their application potential. Todd et al [34, 35] have shown in latest work, that the mechanical properties of alumina bulk-material can be significantly improved if the materials structure is refined into nanocrystalline and a second hard-phase is homogeneously dispersed in the alumina-matrix. By this structural design, hardness and toughness can be increased at the same time.

The alumina-SiC05 represents such a nano-structured CCC-material and is manufactured at economic conditions at no remarkable contamination and short processing time in a Simoloyer CM20-20lm.



Figures 19 a +b show the SEM-micrographs of the starting powders alumina and SiC respectively. Figures 20a and 20b the SEM-micrograph of embedded powder after 30 min HKP and the mapping over Silicon respectively proving a very homogeneous distribution in the alumina matrix. The TEM diffraction pattern given in Figure 21b exhibits the two existing phases in the processed powder where in the corresponding micrograph (Fig. 21a), SiC-grains in nanometric scale can be observed. Figure 21c shows a TEM micrograph of the plasma sprayed alumina-SiC proving that the nanometric structure can be maintained after consolidation. Figure 22 finally shows a cross section of a CFR-substrate-sample coated with the same and an interlayer of Cu.

5.4. Nano-structured MMC-material M-SiC

MMC911 is a metal matrix composite being strengthened by SiC in nanometric phase as a low-cost replacement for conventional hard-phased metals.

6. PM-BULK PRODUCTS

Following the explanations under the introduction chapter (for the) "powder products", this here is nothing but the logical consequence in maintaining to climbing-up along the value-adding chain of a product history. Developing a process, designing the needed equipment, producing advanced powder material by means of this equipment after finding product and application and finally manufacturing parts from or with this advanced powder material represents in minimum a 3-stage capitalisation of knowledge and experience and insofar can lead to very sophisticated solutions in applied materials science, in process- and in materials engineering and does of course not happen every day.

The PM-parts-production is consequently not forced forward in large steps but is a new sector that is occupied if preceding processing steps here demand or originate this.

6.1. Stellite-base Bearing-Bush D120-190 for liquid Zn-/Al-Systems by MA + HIP/LPS

So are results of a cooperative project [36, 37] being started in 1999 represented here by bearing bushes with a net-weight of 12 kg each and produced by Mechanical Alloying of Stellite®-based material, consolidated by HIP as well as LPS under HIP and finally machined and fitted on transfer-rolls. The consolidation here is not done in-house and shall not - at least in mid-term plan - be done so. The bearing bushes are used in the liquid metal bath of hot-dip galvanizing/aluminizing plants (HDG/HDA). Basically a Simoloyer CM20-20lm is used to incorporate a second phase of another metal into the Co-matrix carrying Cr- and W-carbides (MA) and in a second step at slightly lower

kinetic to coat the particles with a lower melting metal (HEM) for consolidation. Figure 22a shows the bearing-bush before fixing on one of the customers pott-rolls shown in Figure 22b.



Fig. 22a: 12-kg-Bearing-Bush D120 -190 for liquid Zn -Al-Systems by MA and HIP-LPS



Fig. 22b: 2000-kg-pot-roll of HDG-plant Fernöberg Thyssen -Krupp-Stahl in a Zor machine-shop

6.2. Stellite-base Bearing-Bush D120-190 for liquid Zn-/Al-Systems by MA + HIP/LPS

High-performance Nd-Fe-B Magnetic Filter for Separation of Metallic Impurities

In March 2000 we introduced a new magnetic filter with an NdFeB-magnetic-core MK-078105 which is in principle a combination of powder metallurgy and conventional design [32]. This part is based on modern advanced magnetic material in highly sophisticated magnetic-like design with approx. 1.5-2x higher magnetic-field-gradient and magnetic-field-strength than all other available to the cost of about 50 % at half needed space with impressive real-throughput, cleaning possibility and application-flexibility (funnels, pipe-line, pump-line etc.).



Fig. 23: magnetic filter system MF-DN100x110

In case of a magnetic filter application, high magnetic properties of the material are of major importance. Taking into account, that the insofar best commercially available materials (Nd-Fe-B) are limited to a maximum energy product of about 50 MGOe where the theoretical maximum

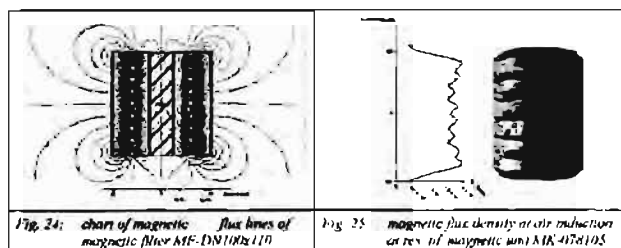
value is at about 64 MGOe [38-39], a promising improvement of magnetic filter systems must use these best materials but improve the application which can here mean the design of the magnetic field and the design of the technical / mechanical unit where the product is send trough.

One area where significant improvements were realized, is the design of the gaps where the product passes since here the magnetic field is loosing almost all of its performance due to the low permeability of air res. of the non-magnetizable base-product. This particular relation between distance and magnetic property is obviously not at all obeyed in case of most of the conventional systems, even the effect can easily be imagined if one try to take a piece of steel, bring it close to a permanent magnet and see what happens very close to it and see what happens just a few millimeters away from the magnet surface [40]. However, this approach is limited res. in direct interaction with the available throughput of any kind of gap or distance since a filter that would block the mass flow of product can not be suitable.

Also and this simply under economically view, it is not imaginable that all (solid) particles of the product can directly touch the surface of the magnet which might be described as a flat container or pipeline lined with a huge number of magnets. A device like this would be extremely huge on the one hand and even more expensive on the other hand.

If this is accepted, the main target must be to accelerate the magnetizable particles towards the magnet surface and collect res. fix them thereon [41, 42].

If it is further taken into account, that for the acceleration of a magnetizable particle in the magnetic field, the magnetic field gradient, which is described by the variation of the magnetic flux density over the distance to the magnetic source is a determining factor, then the product of field gradient and flux density must be of major importance for a magnetic filter system [43].



Since the magnetic flux density can be imagined like the density of magnetic flux lines, it was the main idea, to increase the density of these flux lines by arranging thin anti-polar ring-magnets around iron cores each and press

the single rings together and by this condense the magnetic filed in the same way. Since this would happen right at the surface of magnets and ring-cores initially, a significant increase of the field gradient could also be expected.

Figure 24 shows the chart of magnetic flux lines of the magnetic unit MK-078105 with a number of 10 anti-polar arranged areas that initiate in the intermediate Fe-areas magnetic fields with high magnetic flow-densities (figure 25, left) where the barriers inside and outside represent the inner and the outer circle limit built up by an inner tube called center unit as well as by the outer tube defined as standard pipe DN100 (see figure 23).

The chart in figure 25 exhibits the magnetic flux density determined on the gap-middle-axis of each circle-gap where here it can be seen what was meant with the statement of extremely reduced magnetic properties at air induction just some millimeters (here 4.25 mm) away from the magnet surface where it should be considered, that the here introduced design is strongly expected to achieve a significantly higher level than any other design. Additionally, by this technical solution, concentrating areas with highest field gradient inside 2 determined ring-gaps where the product can pass without any barrier at high throughput are performed. Since the entire magnetic filter system contains only a low number of single units (3), only assembled by one single screw, it can easily be disassembled, cleaned and adapted to pipe-lines carrying multi-phase flows and slurries.

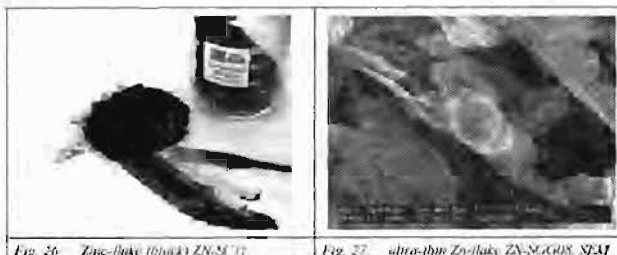
For a better removal of separated particles from the magnetic unit, the peaks of the same are non-magnetic which means the waste can be pushed up- or downwards to these peaks and easier removed from there.

In result and in fact more rapidly than expected, this advanced unit did occupy the market. As an example, Europeans largest and one of the worldwide largest dental-ceramic producers [32] is currently using more than 35 of these units.

7. PROJECT WORK

7.1. advanced Zn-flake

Since our today's major powder product based on HKP is Zn-flake, it is not surprising, that there are ongoing and strong activities in this field. The major goals can be divided in achieving a thinner flake < 0.5 μm and on the other hand designing colored Zn-flakes in particular black ones. On the contrary to conventional approaches, we are not just mixing a pigment but alloying the same where in a sub-approach this can also be defined as mechanical particle bonding resulting in a stable distribution of pigment and flake.



For determining metal-flake properties, a widely used parameter is the tap-density. However we could not find a proper measurement device on the market and therefore had to design and manufacture it ourselves exactly following DIN ISO 3953.

Figure 26 shows an optical image of black Zn-flake (ZN-SC11) and Figure 27 a SEM-micrograph of ultra-thin flake (ZN-SGG08).

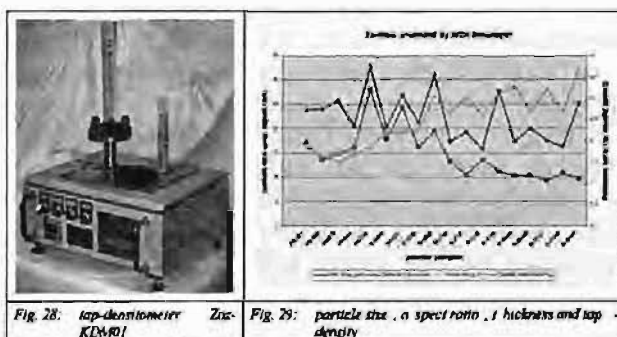
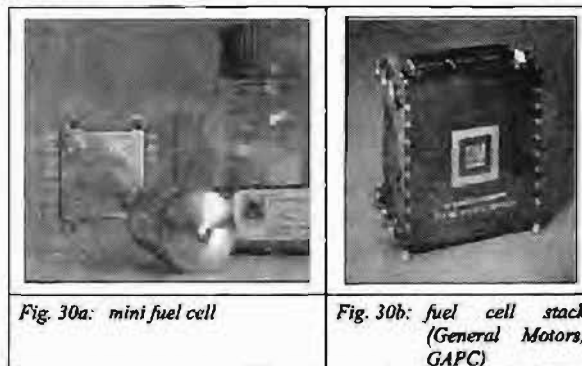


Figure 28 shows a picture of the lately developed tap-densitometer Zoz-KDM01 and Figure 29 shows the dependency of particle size, aspect ratio, thickness and tap-density of a series of Zn-flake samples.

7.2. H₂-Storage by Nanocrystalline Materials

The entire world is highly interested in using fuel-cells as an electrochemical energy transformer following the reverse of electrolysis (electrochemical oxidation), this in particular with the goal to operate automotive vehicles. The fuel-cell itself, first mentioned in the year 1839 is well known and understood and this is valid for all common types that differ along the operating temperature starting with solid oxide fuel cells (SOFC) at 1000 °C and slightly lower via MCFC, PAFC, AFC to Polymer Electrolyte Membrane Fuel Cells (PEMFC) at 100 °C and lower. The high temperature fuel-cells are advantageous due to much higher efficiency and e.g. SOFC due to the fact that they can convert e.g. natural gas (CH₄) and do not need to be fed with pure hydrogen (H₂). On the other hand, the largest market share in automotive is the private vehicle. And this private vehicle

on the contrary to e.g. public busses must operate within a second. The driver wants to come and go right away which is one of the key-factors in this high-mobility world. Since thermo-kinetic can not be accelerated at no limit in the ignition system of a vehicle, from today's point of view, there is no private vehicle with a high- but with a low temperature fuel-cell (Figures 30). These types (PEMFC) do need to be charged with pure hydrogen and this represents the today's not solved problematic. Also here, the fuel-cell itself is available under economic conditions.



Hydrogen is the smallest and lightest element in the periodic system. It is known since about 200 years and used in chemical industry since about 100 years. Hydrogen is built by one single proton (positive charge) and one single electron (negative charge) thus atomic number is 1 and atomic weight is 1. Hydrogen is the most present element in this universe but usually, as of it's high reactivity, exists only in compound form such as H₂O (water), CH₄ (methane), natural gas and oil etc. On this planet, free hydrogen (as H₂-molecule) does only exist in very small ratio in the atmosphere and in volcanic gases.

The hydrogen-molecule forms a gas with no colour that cannot be smelled and that is, at normal condition, 14 times lighter than air is the today's known fuel at highest energy level. E.g. compared to gasoline by weight, the energy-density is about 3 times higher.

At the Apollo-rockets, the second as well as the third rocket-engine level was driven by hydrogen where the same goes for the third rocket-engine level of the European Ariane-4 as well as for the main-engines of the Space Shuttle.

Hydrogen is neither toxic nor decomposable (e.g. as acetone-gas) and not oxidizing (e.g. as Oxygen or Chloride), is neither radioactive, nor corrosive nor foul-smelling, is not dangerous to water and not carcinogenic.

The danger of hydrogen is usually very much overestimated. E.g. at normal condition, hydrogen cannot form a combustible ratio with air and as most of the flammable gases is useless as explosives.

The PEMFC is also called low temperature fuel-cell with proton-conductive electrolyte (membrane). Basically it is an aggregate that performs the reverse of electrolysis (decomposition of hydrogen and oxygen by electric energy). This process is an electrochemical energy conversion, in detail it is electrochemical oxidation.

In order to explain the conversion model by the PEMFC, we need 2 hydrogen molecules [$2H_2$]. That means for the model we have 4 protons and 4 electrons. They are, at the anode of the fuel-cell, catalytically decomposed into 4 hydrogen protons [$4H^+$] and 4 electrons [$4e^-$]. The protons pass the proton-conductive membrane, the electrons cannot do so. They pass as an electric current e.g. through a light bulb (Figure 31a).

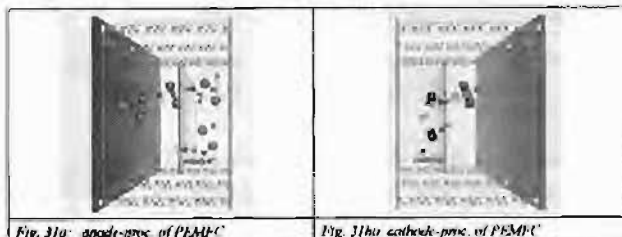
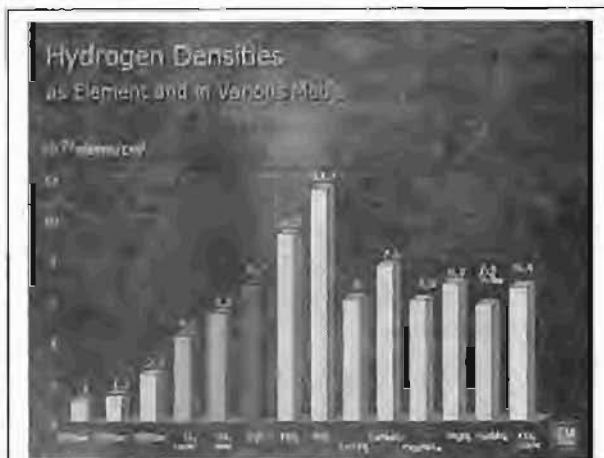


Fig. 31a: anode-proc. of PEMFC

On the cathode-side, proton- and electron-flow are meeting together. Additionally from outside (air), an oxygen-molecule [O_2] is catalytically decomposed into [$2O$]. Together with the 4 hydrogen-protons [$4H^+$] and the 4 electrons [$4e^-$], they react to [$2H_2O$] which is water (Figure 31b).

Common use of hydrogen-driven vehicles had been announced already 10 or 15 years ago for the year 2000 but still today this is not what we can see. And why is this? A common opinion is, that a decade has been lost for simple political/economical reasons where the large energy consortiums simply did block the development which might be true but certainly more on the side of stationary and then usually high temperature applications.

On the vehicle-side, it is the storage of hydrogen, which is probably the main barrier in terms of non-solved technological issues. But also here, the technological point of view only, is not enough. The potential drivers and customers for fuel-cell driven cars do not have a proper understanding for hydrogen yet. Nobody in the street would accept the fact that hydrogen is a way safer fuel than e.g. gasoline. This must be related to the imagination to sit in the same car with a hydrogen bomb or maybe to move a vehicle like the German Airship LZ 129 to Lakehurst.



source: Dr. Gerd Arnold, Global Alternative Propulsion Center (GAPC), D-65423 Rüsselsheim, Germany (Japan, 2001)

Fig. 32: H_2 -densities in various media

Figure 32 gives a comparison of H_2 -storage-capability of various media including no medium. Metal-hydride storage systems have a far larger H-atom-storage-capability/volume as e.g. compressed, liquid or solid hydrogen itself has. Thus, the achievable atom-density in case of hydrogen-gas at 700 bar is approximately 3 times smaller than the by diffusion achievable hydrogen-atom-storage-capability/volume in case of a nanoscaled magnesium-hydride (MgH_2). Simply spoken, a nanocrystalline structure of the material is needed in order to have a large surface of grain boundaries being used as diffusion highways for the hydrogen-atoms. Figure 33 shows the world-wide largest unit for the manufacturing of nanocrystalline MgH_2 , a Simoloyer CM100-s2 being established in Canada.

However, most of the metal-hydride systems do not exhibit a low decomposition and formation temperature and this is what is needed as well as for the operation of the fuel cell (around $400^\circ C$ for the MgH_2 -system). This is why we have been involved for years in a project on the development of the $NaAlH_4$ -system together with GM/Opel and MPI in Germany where we used a CM20-Simoloyer to scale up the materials manufacturing (Figure 34).



Fig. 33 Simoloyer CM100s2 at IREQ Hydrothermic production of MgH_2

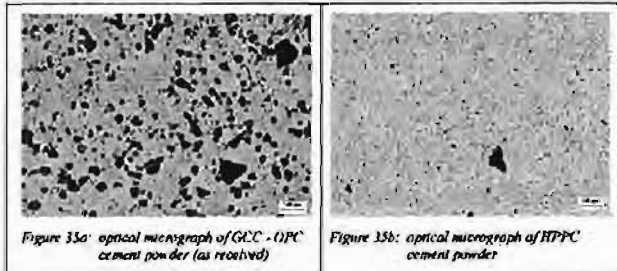


Fig. 34 Simoloyer CM20 at Zirc production of $NaAlH_4$

The NaAlH_4 -system, according to figure 32 does show an achievable atom-density 2.5 times higher than in case of hydrogen-gas at 700 bar and does have a formation and decomposition temperature around 100 °C. Most challenging work from the HKP point of view is to perform the synthesis (alanate and catalyst) right under hydrogen-atmosphere.

7.3. High Performance Cements & Advanced Ordinary Portland Cement by HEM- Refinement and Activation

Ordinary Portland Cement (OPC) is the material most widely used in construction industry all over the world and therefore consumed in super large volume. This causes general interest in improving this product with respect to materials properties. Compared to the raw material cost, the manufacturing cost is energy intensive and therefore cement industry has been and is interested in improvements in the efficiency of their milling operation and their rotary kilns [44].



We are using [45] High Energy Milling (HEM) for the grinding of cement which leads to substantial refinement ($< 2 \mu\text{m}$) after a short processing time (2-3 min) and mechanically activation of the powder particles that in conventional material exhibits a particle size in the order of $50 \mu\text{m}$.

Figures 35 a and b show optical micrographs of OPC and of processed OPC powder by HEM. Impressively the difference in microstructure and morphology is presented here. The non-refined cement appears as a very heterogeneous material with a huge number of large sized particles in the order of $30\text{-}60 \mu\text{m}$ and some very large particles in the order of $100\text{-}120 \mu\text{m}$.

On the contrary, the refined cement shows a much more homogeneous microstructure at very small particle size (D_{50} is given at about $2 \mu\text{m}$ by PSD) with a few ($< 10 \mu\text{m}$) mediums sized particles below $20 \mu\text{m}$ size and one large particle in the order of $100 \mu\text{m}$. The BET-surface area was found to be $15 \text{ m}^2/\text{g}$.



Figure 36: *sculptures made by conventional OPC (left) and by refined HPPC (right)*

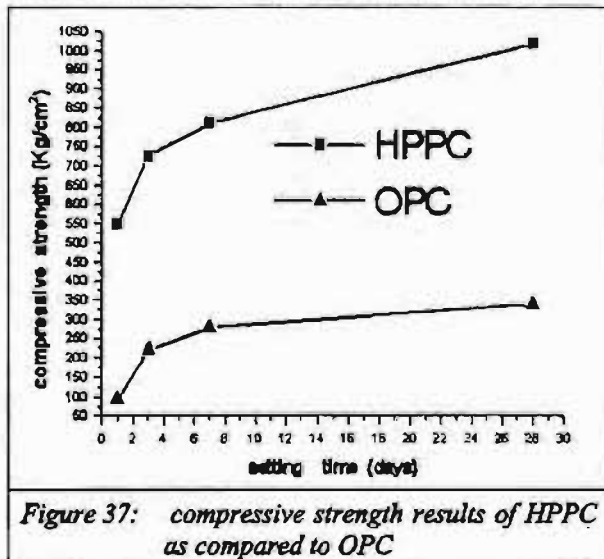
This superfine high performance cement (HPPC) exhibits a faster setting time, a faster curing time and in increased mechanical properties. Due to the far shorter grinding process at far higher energy efficiency, due to an expected reduced firing temperature in the processing and finally due to an expected significant saving in production space for the grinding step, an economically advanced manufacturing process of cement seems to be offered by HEM.

Due to a tremendous refinement into submicron range at high active surface, the material can result into a super fast setting cement (SFC $\approx 3 \text{ min}$) where this feature being available for repair-work of concrete constructions would also lead to an advanced product application which would be the first appliance imagined for short term range. Later this maybe spread out by reduced construction dimensions and faster building due to increased mechanical properties.

The two little sculptures shown on Figure 36 impressively demonstrate the filling capability of finer grade cement (left sculpture) for the expansion into fine and complex structures compared to the one of conventional material (right hand sculpture). The setting time of the fine graded high performance material was 2-3 minutes only. These sculptures are made exactly of the two different materials shown in figures 35a-b. Very fluid mortar-cement pastes were carefully prepared and molded applying no pressure. In particular the here shown properties can be of major importance for the future advanced repair of cracks and hollow spheres of concrete constructions like bridges or dams.

Figure 37 compares the strength of HPPC by HEM-refinement and activation with the ordinary material. The results are based on tests after 1, 3, 7 and 28 days using a universal testing machine 50-C-21H4 at a compressive rate of 900 N/s.

The compressive strength results of conventional OPC do agree well with typical expected values as reported by the C-109 ASTM standards. On the contrary, the HPPC achieves a very high early strength where already after 1 day the strength is about 70 % higher than the strength of the conventional material after 28 days. After 28 days, the strength of the HPPC is more than 3 times higher than the corresponding value of the conventional material.



Since cement is a super large volume product, a key question is about availability of the technology in proper large scale. Since cement is a basically very cheap product - compared to advanced materials -, cost is even more a main issue.

By means of the semi-continuous processing route as described before and also by means of using Si_3N_4 -milling tools, this process appears on a realistic level. Silicon nitride is here definitely not used in order to avoid Fe-contamination or other since cement anyway carries a lot of this. It is used to counter the challenge of a to be processed very abrasive material in super large volume where it would not be acceptable to stop a continuous plant every day in order to replace some milling tools.

Figure 38 shows vessel, flange and rotor of a disassembled grinding unit of a Simoloyer CM01-21-SiN (Si_3N_4 -lining) after a total time of 4000 hours of operation with a grinding media load of 2300 g and an OPC-powder load varying between 115-230 g at rotational speeds varying between 500 and 900 rpm. In detail figure 38a shows the inner Si_3N_4 -

lining of the vessel where in total (all components) 2 cracked plates have been found. One of these cracks is in the area of the given picture and is marked with an arrow. In both cases, no fracture of the plates did fall off which means the cracks are not considered as being problematic, in particular not after that long milling operation at relatively high kinetic.

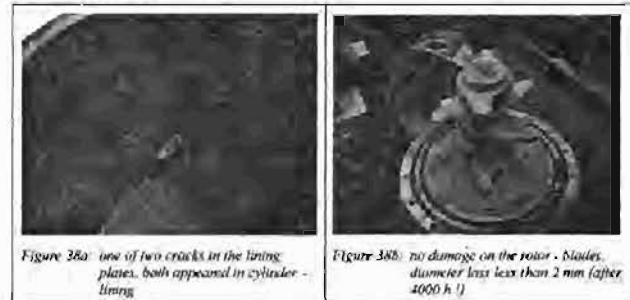


Figure 38b shows flange and rotor. No cracks or damage could be noticed in the flange-lining and most important, no damage or cracks could be found at the Si_3N_4 -bulk rotor-blades as well.

The diameter of the blades has been measured and a diameter-loss of less than 2 mm has been determined. This is an excellent result and it should be pointed out, that the given total processing time of 4000 hours would refer e.g. to a 24-h-operation for a period of more than 5 months. For this process, YTZ grinding media is used and suitable as well.

Since processing time is in the range of 1-3 minutes we can predict a production rate of several tons per day with a single CM100-system as given in figure 9. If we then take into account, that Simoloyer-systems are available up to 900 liters size with the potential of further enlargement, then this technique can offer the application for the here discussed super large volume product. In any case and from this point of view it is far capable to produce smaller volumes of High Performance Cement in the range of 10-100 t/day.

7.4. Reactive Dry-Milling for Environmental Protection, encouraging industrial applications for High Kinetic Processing

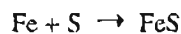
The Reactive (dry-) Milling technique [16] is still not widely used, even though mechanical alloying [1-2, 46] has a long tradition and inorganic or more recently organic chemical syntheses are known to proceed to completion without producing wastes [47]. These favorable findings contrast solution reactions that tend to be incomplete and produce side reactions with the necessity of waste producing purifying workup that is in most cases much more expensive

than the synthetic step. The alternative by very high temperature syntheses in inorganic solid or melt reactions requires much energy which can be saved if reactive milling succeeds at ordinary temperature. The nanoscopic nature of solid-state chemical reactions has recently been studied in numerous organic solid-state reactions using supermicroscopic techniques like atomic force microscopy (AFM), scanning near-field optical microscopy (SNOM) and nanoindentation/nanoscratching. A consistent mechanistic scheme emerged for the non-tribochemical reactions with far-reaching molecular migrations within the crystal along "easy" paths [47]. While the three-step mechanism of phase rebuilding, phase transformation and crystal disintegration is secured for molecular crystals, organic polymers or infinite inorganic covalent crystals undergo tribochemical reactions by mechanical breakage of covalent bonds. The extremely unsaturated fresh surfaces which occur upon cleavage of the crystals cause local plasmas which allow all kinds of chemical reactions at low temperature [18]. There may be borderline cases between these different mechanisms with salts and metals, but normal non-polymeric organic molecules cannot break covalent bonds upon mechanical interaction by milling unless very high forces are applied with Bridgman anvil type equipment [48]. The latter reactions are without preparative use. We describe here technical applications of reactive milling in the different fields.

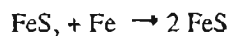
7.4.1. Inorganic Quantitativ Syntheses by Reactive Milling

Numerous inorganic syntheses of binary high melting insoluble salts are routinely performed at very high temperatures by glowing or melting of the components or by precipitation from aqueous solutions. Many of these may now be accomplished at room temperature or slightly above by high energy reactive milling (RM) of their components. Some examples of this new technique are presented here.

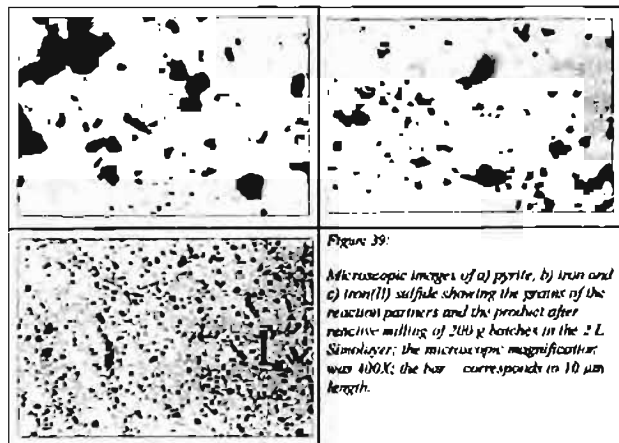
Iron(II) sulphide is a common source for the generation of hydrogen sulphide. It is easily formed if iron powder and sulphur are milled together in stoichiometric quantities:



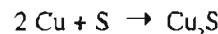
This waste-free solid-state reaction demonstrates the corrosive power of sulphur towards iron and steel, including steel balls. Therefore, ZrO_2 balls are used in these syntheses, while the stellite housing of the mill and the hard-metal rotor withstand virtually unaffected. The same is valid for the related synthesis of iron(II) sulphide from pyrite and iron powder or turnings by HEM/RM:



The solid material of FeS arises in sub-micrometer grains as shown in Figure 5. Both the pyrite and the iron started with grains of 1 - 3.5 and 1 - 2 μm diameter. The larger aggregates are composed from the small grains in all three cases.

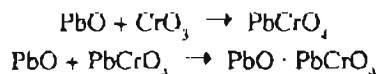


Similarly, copper powder and sulphur combined to copper(I) sulphide, which is a useful solid for the production of luminophors. This product arises free of water in μm -sized particles:



These waste-free low temperature syntheses may be useful and many applications of pyrite and sulphur for the synthesis of metal sulphides might be envisaged.

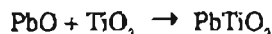
Furthermore, high melting metal oxides can be combined by HRM to mixed oxides (complex salts) such as chrome yellow (lead chromate, mp 844°C) from lead oxide (mp 888°C) and chromium trioxide (mp 197°C) which can be converted further to chrome red by milling with additional lead oxide:



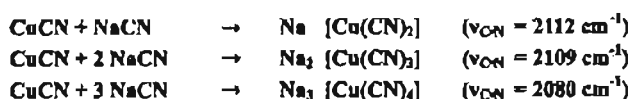
A slurry of the obtained PbCrO_4 in water reacts neutral and does not contain chromic acid. This test proves completion of the reaction more sensibly than the FT-IR spectroscopic analysis. Unlike the precipitation of lead chromate from aqueous solution, these dye pigments can be freely varied to non-stoichiometric composition in order to adjust the desired materials properties. The dry powders arise directly as μm -fine grains.

Further solid mixed oxides are important as ferroelectrics with high dielectricity constants for optoelectronic and piezoelectric applications (PLZT ceramics). For example HRM of stoichiometric mixtures of lead(II) oxide (mp 886°C) and titanium dioxide (mp 1830°-1850°C) in the

Simoloyer provides lead titanate (mp 450°C) as a fine powder. Clearly, this must be a tribochemical reaction that occurs after mechanical breaking of covalent metal-oxygen bonds.

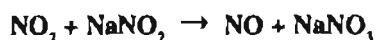


Still further applications of HRM were realized in the formation of complex salts. Examples are the quantitative syntheses of complex cyanides (useful in the galvanotechnique due to their solubility in water) from copper(I) cyanide ($\nu_{\text{C}\cdots\text{N}} = 2164 \text{ cm}^{-1}$) and sodium cyanide ($\nu_{\text{C}\cdots\text{N}} = 2091 \text{ cm}^{-1}$). For example, the stoichiometric ratio with sodium cyanide was varied from 1:1 to 1:3 and the position of the cyano vibration band in the FT-IR spectrum changed monotonously:



All of these reactions were performed with 200 g batches in the Simoloyer CM01-2l at 1300 rpm while excluding hazards from the poisonous cyanides. A wealth of related and further solid-state inorganic reactions by HRM is clearly envisaged.

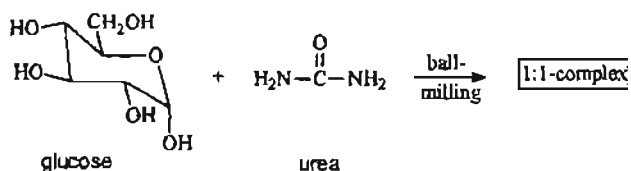
Equally interesting are inorganic reactions between gases and salts. If a passivating cover is formed on the crystals, milling is required in order to constantly create fresh surfaces. An example is the deoxygenation of nitrogen dioxide by sodium nitrite to give nitrogen oxide [49] that was performed with 200 g batches (2.9 mol) and provided the more precious reactive gas in pure form.



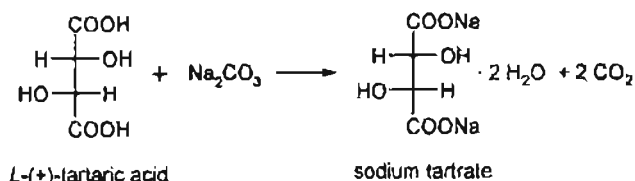
The Simoloyer was evacuated, filled with NO_2 (0.8 bar, 0.07 mol) and operated for 30 min, the colorless gas filled to a pressure container and the reaction continued with further NO_2 until the sodium nitrate was used up, etc.

7.4.2. Organic Solid-State Syntheses without Wastes

More than 1000 stoichiometric organic solid-state reactions proceed with 100% yield and do not require purifying workup, i.e. they are solvent-free and waste-free [47]. Some of these reactions have now been successfully scaled-up with the Simoloyer [18, 50]. Glucose and urea formed the stoichiometric crystalline 1:1-complex within minutes that can hardly be obtained from solution.

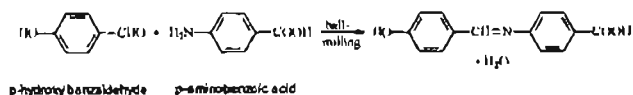


Also the solid-state neutralization of acids may be of technical importance, as many processing steps can be saved if solvents are avoided. For example, 200 g batches of stoichiometric mixtures of *L*-(+)-tartaric acid and sodium carbonate liberated carbon dioxide upon HRM at 1300 rpm in the water cooled Simoloyer and provided cleanly sodium tartrate dihydrate as a powder.

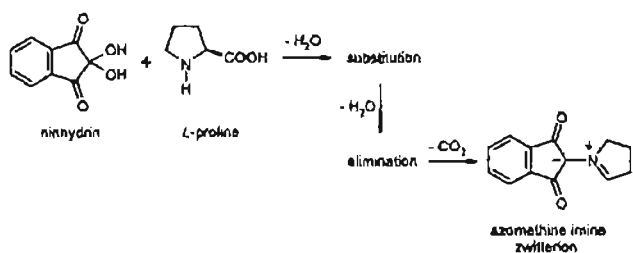


Sodium tartrate is a well known food additive (E 335). Similarly, sodium hydrogentartrate hydrate is prepared by milling stoichiometric mixtures of *L*-(+)-tartaric acid and sodium bicarbonate. These crystals are in use for the preparation of powders or tablets for refreshing drinks. Energy consuming evaporations are avoided that burden the common techniques in water. No excessive heating was observed in this solid-state reaction. The liberated CO_2 was released by a safety-valve.

The formation of covalent bonds is even more important in organic syntheses. Imines (Schiff bases) are versatile building blocks that have been quantitatively synthesized by reactive milling. The scaling-up of the *p*-hydroxybenzaldehyde condensation with *p*-aminobenzoic acid yielded 200 g batches of the substituted solid imine hydrate that could be dried in a vacuum at elevated temperature if desired [50].



The scale-up is also possible for much more complicated quantitative solid-state cascade reactions [29].



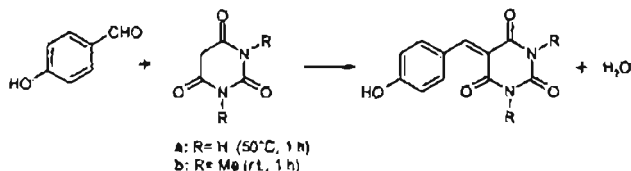
We checked the stoichiometric reaction of the widely used solid reagent ninhydrin with the solid amino acid *L*-proline that gives the versatile solid azomethine imine which is a zwitterion and has interesting properties and uses. Azomethine imines are hard to obtain in pure form.

Here we use a solid state reaction cascade of 1.) substitution, 2.) elimination and 3.) decarboxylation at room temperature upon dry-milling and obtain 100% yield: 200 g of a stoichiometric 1 : 1-mixture of ninhydrin and *L*-proline was milled in the Simoloyer® CM01-2I charged with 2 kg of steel balls (100Cr6) with 5 mm diameter at 1100 rpm for 40 min when the liberation of carbon dioxide was terminated. The temperature varied from 15°C at the water cooled walls to a maximum of 21°C in the center. The power was 800 W. Quantitative reaction was secured by weight (146 g, 100%) and purity by spectroscopic techniques [51].

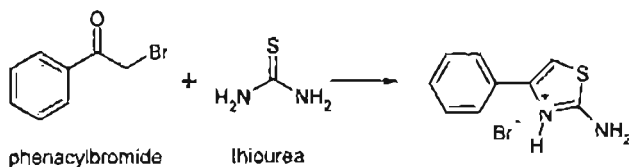
The zwitterion and the water of reaction formed a highly dispersed solid which did not form a loose powder but mostly a solid film on the balls and the walls of the mill. In this exceptional case, a different collection technique was applied: the product (its low solubility in water at 22°C is 0.20 g L⁻¹) was not separated in a cyclone (see Fig. 2) but easily milled out with 4 times 250 mL of water each, and the highly disperse (<1µm) pure azomethine imine product (m.p. 239°C) was obtained after centrifugation and drying in a vacuum.

This is an economic, environmentally friendly and essentially waste-free synthesis of a highly interesting reagent, the only 'by-product' being 1 L of water containing 0.2 g of the zwitterion, that can, of course, also be isolated by evaporation of the water. The previous syntheses of this zwitterion in solution provided only a 82% yield with much wastes also from the purifying workup [52]. The solid-state technique is by far superior and fully benign.

Further C-C forming reactions of highest synthetic potential are Knoevenagel condensations. These were obtained in solution by catalysis, but more recently also "solvent-free" on solid catalysts or supports with microwave heating, but never quantitatively. Our really solvent-free technique by milling stoichiometric quantities of the reactants in the absence of any auxiliaries provides the alkene products directly in the pure state and, unlike the previous techniques, no solvent consuming workup is necessary [53]. The scaling-up to 200 g batches was successfully achieved using the Simoloyer CM01-2I with *p*-hydroxybenzaldehyde and barbituric acid without external cooling (at temperatures up to 50°C) or dimethylbarbituric acid at ca. 20°C (with external water cooling):



An example for the heterocyclic ring formation from phenacylbromide and thiourea [54] was scaled up to 200 g batches in the Simoloyer CM01-2I at room temperature. The 2-aminothiazole hydrobromide salt is quantitatively obtained in a complicated cascade reaction sequence (substitution, cyclization, dehydration, isomerization) and represents a versatile building block for organic syntheses with the acid catalyst already attached to it.



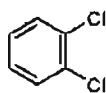
Many further waste-free organic solid-state reactions can be scaled-up in the large-scale horizontal ball mill. The gain in efficiency is enormous and the savings in resources and time are highly rewarding. If the heat production is not excessive as in most organic solid-state reactions there is no reason to stop at 2-liter-size horizontal ball-mills. Scaling-up of the benign technique to the industrially useful scale in 400 liter mills will be possible.

7.4.3. Tribochemistry with Oxides

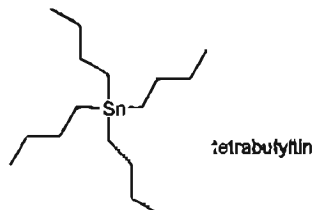
Ball-milling is very versatile. A further technique with the same equipment is tribochemical milling with mechanochemical breaking of covalent bonds of infinite covalent crystals which are present in many oxides. For example, sand consists of quartz (SiO₂) which forms an infinite covalent crystal lattice. If the crystal is split, all Si-O bonds are broken that existed between the two fragments and the freshly cleaved faces are completely unsaturated with free '%Si' and 'O-Si%' surface radicals and other highly reactive species. They represent a local plasma. This plasma tends to be saturated immediately, a fact that has been used for more than 5000 years to ignite fire by hitting flint in air. Such tribochemistry should be also useful for the mineralization of dangerous environmental poisons such as chlorinated aromatics (PCBs, etc.) or tin alkyls etc., if milling with sand is performed. Such endeavour is much easier and more benign than the reductive removal of halogen from polyhalogenated aromatics by milling sea sand with large excesses of metallic sodium or magnesium (after thermal drying followed by drying with calcium oxide) and ethanol [55] in planetary ball mills (typically 5 h) or eccentric swing-mills (typically 90 min) to form the corresponding (aromatic) hydrocarbons besides hazardous hydrogen that forms explosive mixtures with air.

In order to use benign tribochemistry 0.8 g of *o*-dichlorobenzene (a polychlorinated aromatic) and 1 g of tetrabutyltin (a hazardous tinorganic) were milled with 200

g of air-dry quartz sand (Sakret Trockenbaustoffe GmbH & Co KG; 0.1-0.5 mm; washed and dedusted) at 1300 rpm for 1 h in the Simoloyer® CM01-21.



o-dichlorobenzene

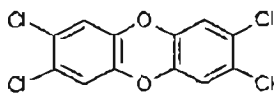


tetra-butyltin

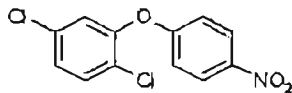
Mass spectrometric analysis of the solid powder or ^1H NMR analyses of extracts (dichloromethane, ethyl acetate, or ether) did not exhibit the starting materials any more. At 1 g of o-dichlorobenzene and 200 g of sand, there were some traces of the starting material and of chlorobenzene still detectable in the mass spectrum, but benzene was not present if the milling was performed either in the presence of air or under argon atmosphere. This points to mineralization of the hazardous compounds in the plasma of the freshly broken surfaces of the quartz sand. The final diameters of the quartz particles were 1 - 2 μm wide.

These results suggested industrial decontaminations of PCBs, HCHs, DDT, nitrofen, $\text{R}_{(3-20)}\text{SnX}_{(n+1)}$, polychlorinated dibenzodioxines (PCDD) and -dibenzofurans (PCDF), etc.

We therefore studied the system in more detail. XPS measurements showed that the carbon of the halogenated organic compounds was completely graphitized. The chlorine content of the graphite formed was at the detection limit of the XPS technique. The chlorine was transformed to HCl and neutralized by the basic impurities or components of the tribomaterial to form the corresponding metal chlorides. Surprisingly, it was even possible to graphitize methane by high energy tribochemical milling with sand. It is very important, that not only quartz sand but also glass, CaO, MgO, TiO_2 , Fe_2O_3 , Fe_3O_4 , ZrO_2 , B_2O_3 , FeS, FeS_2 , BN, Si_3N_4 , B_4C , SiC, WC, FeSi_2 , TiSi_2 , Si, B, granite, quartz porphyry, enamel, ceramics can equally be used for tribochemical decontaminations. For example, we are able to completely mineralize TCDD or nitrofen also in the presence of congeners.



TCDD



nitrofen

A mixture of TCDD (210 mg) with congeners (295 mg) and KCl (200 mg) or 0.8 g of pure nitrofen was completely detoxified (graphitized) by 30 min milling with 200 g glass (crushed window glass or Duran) at 1300 rpm. No organic materials could be detected any more by mass spectrometry. The μm fine glass powder was melted when the graphite burned to carbon dioxide. After crushing, the glass can be used again for tribochemical detoxification. This is a benign closed cycle low temperature decontamination process for safe and complete removal of the hazards with non-disposable wastes which contain dioxines, or the other poisons mentioned and are mostly stored in barrels at various sites on earth. The up-scaling from the two liter mill to now more than 400 liter horizontal ball-mills is possible and these mills can be operated at the site of such wastes. Thus, even problems with the transportation of such dangerous wastes to other sites are avoided.

In result of chapters 7., HEM/RM are environmentally benign versatile techniques that can be performed at the kg scale and can be scaled-up to technical importance. Applications are manifold in mechanical alloying, waste-free inorganic room temperature syntheses, waste-free organic solid-state syntheses and decontamination of dangerous residues by tribochemistry. The size of horizontal high energy mills with carrier-gas operation may be increased to more than 400 liter. Thus, the application to industrial production and decontamination in the various fields that were treated in this survey will be only a matter of time, as environmentally friendly new processes are inevitable for the well-being of our environment.

8. REFERENCES

- [1] J.S. Benjamin, Metall. Trans., Vol. 1, 2943 (1970)
- [2] J.S. Benjamin, T.E. Volin, Metall. Trans. Vol. 5, 1929 (1974)
- [3] D. Ernst, H. Weiss, H. Zoz, Structure and Properties of Nanophase Materials, TMS, eds. B.T. Fultz, C.C. Koch, P.J. Maziasz, R.D. Shull, 1995
- [4] H. Zoz, R. Reichardt, H. Ren, Energy Balance during Mechanical Alloying, Measurement and Calculation Method supported by the Maltoz®-software, PM2Tech'99 Conference MPIF/APMI, June 20 - 24, Vancouver, Proceedings 1999
- [5] H. Zoz, D. Ernst, H. Weiss, M. Magini, C. Powell, C. Suryanarayana, F. H. Froes, Metall. Vol. 50, 09/96, pp. 575-579 (1996)
- [6] H. Zoz, D. Ernst, Mechanical Alloying using Cycle Operation - A New Way to Synthesize CMB-Materials, 5th International Conference on

- Advanced Particulate Materials and Processes, West Palm Beach, Florida 1997, Proceedings
- [7] H. Zoz, D. Ernst, I. S. Ahn, W.H. Kwon, Mechanical Alloying of Ti-Ni-based Materials using the Simoloyer®, TMS Annual Meeting 1997, eds. C.M. Ward-Close, F.H. Froes, S.S. Cho, D.J. Chellman: Synthesis/Processing of lightweight Metallic Materials, (Proceedings 1997)
- [8] H. Zoz, R. Reichardt, H. Ren, H.U. Benz, Ductile Metal Flakes based on [Au], [Ag], [Cu], [Ti], [Al], [Ni] and [Fe] by High Energy Milling (HEM) – Part I, PM2Tech'99 Conference MPIF/APMI, June 20 – 24, Vancouver, Proceedings 1999
- [9] H. Zoz, D. Ernst, T. Mizutani, H. Okouchi, Metall 51, pp. 568-572 (1997)
- [10] J.Y. Chung, J. Kim, Y.D. Kim, Formation of Nanocrystalline Fe-Co Powders Produced by Mechanical Alloying, Dept. of Metallurgy and Materials Science, Hanyang University, Ansan, Korea, 1999
- [11] A. Bose, K. Ameyama, S. Diaz de la Torre, D. Jaramillo V., D. Madang and H. Zoz, 2002 World Congress on Powder Metallurgy & Particulate Materials, proceedings (2002)
- [12] R. Savin, H.U. Benz and H. Zoz, Zn and Zn-Ni-flakes for anti-corrosives, unpublished exploitation report 05.02.-08.02.2000, Palm Springs, CA
- [13] H. Zoz, H. U. Benz, G. Schäfer, M. Dannehl, J. Krüll, F. Kaup, H. Ren, R. Reichardt and D. Jaramillo V., INTERCERAM International Ceramic Review, Vol. 50 (2001) [5] pp 388-395
- [14] H. Zoz, H. U. Benz, G. Schäfer, M. Dannehl, J. Krüll, F. Kaup, H. Ren, R. Reichardt and D. Jaramillo V., INTERCERAM International Ceramic Review, Vol. 50 (2001) [6] pp 470-477
- [15] Report of Brite Euram Project BE-95-1231, 1996-1999
- [16] H. Zoz, H. Ren, N. Späth, Metall 53, 423-428 (1999)
- [17] G. Kaupp, J. Schmeyers, M. R. Naimi-Jamal, H. Ren, H. Zoz : Reactive milling with the Simoloyer: environmentally benign quantitative reactions without solvents and wastes, Elsevier, Chemical Engineering Science 57 (2002) 763-765
- [18] G. Kaupp, M.R. Naimi-Jamal, H. Ren, H. Zoz, Chemie Technik 31, 58-60 (2002)
- [19] H. Zoz, R. Reichardt, J.S. Kim, Keramische Zeitschrift, 53 [5], 384-392 (2001)
- [20] K. Ameyama, S. Umekawa, H. Ren, D. Jaramillo V. and H. Zoz : Alternative Mechanical Milling routes for grain-refinement of conventional High-Speed Steel powder for later consolidation by SPS, proceedings of PM2TEC'2003, MPIF (2003)
- [21] H. Zoz, S. Morales and D. Jaramillo V.: Comparative routes of solid-solution-formation by MM of Ag-70Cu (at%), proceedings of PM2TEC'2003, MPIF (2003)
- [22] US-patent 5,464,163
- [23] US-patent 6,019,300
- [24] H. Zoz, I. Vernet and D. Jaramillo V. :Solid-solution-formation by MM of the Ag-70at%Cu alloy, proceedings of PM2TEC'2003, MPIF (2003)
- [25] U. Koester, Material Science Forum, 235-238, 377-388 (1997)
- [26] US-patent 5,678,776
- [27] TPW-project/State of NRW/Germany # 25072000 [2000-2003]
- [28] H. Zoz, R. Reichardt and D. Ernst, Metall Vol. 51, 09/98, pp. 521-527, 1998
- [29] R.W. Rydin, D. Maurice, T.H. Courtney, Milling Dynamics: Part I. Attritor, Metall. Trans. Vol. 24a, pp175-185 (1993)
- [30] N. Burgio, A. Iasonna, M. Magini, S. Martelli, F. Padella, IL NUOVO CIMENTO, Vol. 13 D, No. 4 (April 1991)
- [31] H. Zoz, H. U. Benz, T. Suzuki, H. Ikehata and T. Saito, PM2TEC'2003, proceedings-MPIF (2003)
- [32] H.U. Benz, M. Bommert, J. S. Kim, D. Jaramillo V. and H. Zoz, INTERCERAM International Ceramic Review, Vol. 52 [3] (2003) pp 146-156
- [33] H.U. Benz, H. Zoz: Particle deformation ($V=const$) - Investigation and Production of the CMB-metal-flakes Au, Ag, Cu, Ti, Ni, Al, Internal Report Zoz GmbH, 1998
- [34] R. I. Todd: Alumina/SiC Nanocomposites: Big Things from Small Packages, British Ceramic Proceedings, 55, 1996, 225-238.
- [35] H. Ren, E. Kern, H. U. Benz, H. Weiss, D. Jaramillo V. and H. Zoz, PM2TEC'2002, 2002 World Congress on Powder Metallurgy & Particulate Materials, (2002), MPIF proceedings

- [36] H. Zoz, H.U.Benz, K. Hüttenbräucker, L. Furken, H. Ren: Stellite bearings for liquid Zn-/Al-Systems with advanced chemical and physical properties by Mechanical Alloying and Standard-PM-Route, Part I, Metall Vol. 54, 11/2000, pp. 650-659, 2000
- [37] H. Zoz, H. U. Benz, K. Hüttenbräucker, L. Furken, H. Ren, D. Jaramillo V.: Stellite bearings for liquid Zn-/Al-Systems with advanced chemical and physical properties by Mechanical Alloying and Standard-PM-Route - Part II : PM2TEC' 2002, 2002 World Congress on Powder Metallurgy & Particulate Materials, (2002) MPIF, proceedings
- [38] K. Schnitzke, C. Kuhrt, L. Schultz, Siemens Zentralabtlg. F&E, Erlangen (1993)
- [39] Group Arnold, Company Profile (2001)
- [40] Ozaki-Yukiko; Fujinaga-Masashi; Technical Research Lab, Kawasaki Steel, Magnetic properties of high permeability iron powder 'KIP MG270H' for line filter cores, Journal article: Kawasaki Steel Technical Report (2000) n 42, May, p 30-35, 13 Refs.
- [41] J.H.P. Watson; Permanently magnetized high gradient magnetic air filters for the nuclear industry. INTERMAG '95, 1995 IEEE International Magnetism Conference, 18-21 April 1995, San Antonio, TX, USA, IEEE Transactions on Magnetism, 31 (1995) 6, PT.2, pp 4181-4183
- [42] A.C. Lua; R.F. Boucher; Magnetic filtration of fine particles from gas streams. Proceedings of the Institution of Mechanical Engineers, Part E (Journal of Process Mechanical Engineering), 207 (1993) E2, pp. 109-122
- [43] Authors discussion with F. J. Börgemann, Hanau, Germany, November 2000, August 2001
- [44] H. de la Garza-Gutiérrez, J. P. Muñoz-Mendoza, O. A. Chimal-Valencia, R. Martínez-Sánchez, S. D. De la Torre, A. García-Luna and P. García-Casillas: Optimizing Milling Parameters for Refining Portland Cement, Journal of Metastable and Nanocrystalline Materials 15-16 (2003) pp 395-400
- [45] H. Zoz, D. Jaramillo V., Z. Tian, B. Trindade, H. Ren, O. Chimal-V. and S. D. De la Torre : High Performance Cements and Advanced Ordinary Portland Cement: Manufacturing by HEM-Refinement and Activation, ZKG International vol. 57 (2004) no.1, pp. 60-70
- [46] C. Suryanarayana, Guo-Hao Chen, F.H. Froes, Scripta Metallurgica et Materialia, 26, 1727 (1992)
- [47] G. Kaupp in Comprehensive Supramolecular Chemistry, Vol. 8, pp. 381-423, Ed. J. E. D. Davies, Elsevier, Oxford, 1996; G. Kaupp, J. Schmeyers, J. Boy, Chemosphere, 43, 55-61 (2001)
- [48] V.A. Zhorin, V.Y. Rochev, O.P. Kevdiv, L.B. Kukushkina, V.I. Gol'danskii, N.S. Enikolopyan, Russian J. Phys. Chem. 55, 82-86 (1981)
- [49] G. Kaupp, J. Schmeyers, J. Org. Chem. 60, 5494-5503 (1995)
- [50] G. Kaupp, J. Schmeyers, M. R. Naimi-Jamal, H. Zoz, H. Ren, Chem. Engin. Sci. 57, 763-765 (2002)
- [51] G. Kaupp, M. R. Naimi-Jamal, J. Schmeyers, Chem. Eur. J., 8, 594-600 (2002)
- [52] W. Johnson, D. J. McCaldin, J. Chem. Soc. 1958, 817-822
- [53] G. Kaupp, M. R. Naimi-Jamal, J. Schmeyers, Tetrahedron, submitted.
- [54] G. Kaupp, J. Schmeyers, J. Boy, J. Prakt. Chem. 342, 269-280 (2000)
- [55] V. Birke, Terra Tech, 5, 52-57 (1998)

AN INVESTIGATION INTO EXTENSION OF SOLID SOLUBILITY OF Fe AND Ni, IN W BY HIGH-ENERGY MILLING

R. Malewar^{1*}, N. Alam³, B. Sarma¹, B. S. Murty² and S. K. Pabi³

¹DMRL- Hyderabad, ²Metallurgical and Materials Engineering Department, IIT- Madras, ³Metallurgical and Materials Engineering Department, IIT-Kharagpur.

ABSTRACT

Tungsten has excellent mechanical and physical properties viz., melting point of 3420 C, density of 19.3 g/ml, hardness of 9.75 GPa, and elastic modulus of 407 GPa. However, solid state sintering of elemental tungsten requires very high temperature (≥ 2400 C) due to poor self-diffusivity. This has lead to the W-Ni-M (M = Fe, Cu) alloys sintered by liquid phase sintering of elemental blend of PM grade W, Ni, and Fe powder, wherein Ni and Fe do not show any solid solubility in W. Mechanical alloying is known to extend the solid solubility in immiscible systems. The present investigation attempts to study mechanical alloying of W-Ni and W-Fe, and extension of solid solubility of Ni and Fe in W, by high-energy milling. Although intermediate phase formation is not revealed during milling of W-Ni and W-Fe compositions, transformations are observed during DSC of the milled samples, suggesting thermally assisted phase formations in the milled samples.

1. INTRODUCTION

Tungsten has excellent mechanical and physical properties viz., melting point of 3420 C, density of 19.3 g/ml, hardness of 9.75 GPa, and elastic modulus of 407 GPa [1]. Bulk tungsten is produced by resistance sintering of elemental W powder at a temperature of ≥ 2400 C [2,3]. In order to overcome size and shape limitations, as well as the high temperature in resistance sintering of tungsten, liquid phase sintering of W with Ni and Cu was first proposed and thereupon Cu was replaced by Fe [4]. Under equilibrium conditions W does not have any solid solubility for Ni, however Ni has a solid solubility for W up to ~ 30 wt.% [5]. Similarly, under equilibrium conditions W and Fe do not show any mutual solid solubility [5].

Besides normal applications of W-Ni-Fe alloys, W-Ni and W-Fe alloys are also finding useful applications viz., W-Ni alloys are used in radiation absorption [6] (collimation) and for better high temperature oxidation resistance than that of W [7-9]. Similarly W-Fe alloys have attracted attention for high temperature magnetic properties [10-12]. Mechanical alloying is also known to extend solid solubility of the constituent elements in many systems [13]. Therefore, the present investigation is attempted to introduce solid solubility of Ni and Fe, respectively, in W by high energy

milling process. The formation of intermediate phases at room temperature by high-energy milling is also investigated. The thermal characteristics of different W-Ni and W-Fe compositions are studied to see the thermal assisted transformations.

2. EXPERIMENTAL

Nanostructured powders of compositions W_yNi_{1-y} ($y = 10, 15, 20, 33, 50, 56, 66, 95$ at.%) and W_xFe_{1-x} ($x = 3, 11, 23, 33, 39, 50, 73, 85, 90$ at.%) were produced by high energy milling in a Fritsch (P5) planetary ball-mill using WC grinding media at a mill speed of 300 r.p.m. using ball to powder weight ratio of 10:1 and toluene as the process control agent. The powders were characterized by high-resolution X-ray diffractometer (Make: Phillips, Model: X'pert pro). The crystal size and accurate lattice parameter estimation of the specimens were made from the XRD spectra. DSC (Make: Netzsch, Model: STA 409PC) was used to study thermally driven transformations in the milled W-Fe and W-Ni powders respectively. Samples were evacuated and purged with Argon gas twice before actual heating of the sample started to take out the adsorbed gases on the powder sample. Heating of the samples was carried out at 10C/min in alumina crucible. During heating and cooling continuous Argon flow is maintained viz., 60ml/

min purging on to sample and 20 ml/min flow rate for protecting heating elements, respectively.

3. RESULTS AND DISCUSSION

W-Ni: There was no intermediate phase formation till 15 h of milling in the compositions corresponding to the stoichiometric compositions of Ni_4W , NiW and Ni_2W (Fig.1). Contamination of grinding media was noticed after 15 h milling only in case of W_{95}Ni_5 (at.%) composition. This means that presence of adequate amount of soft phase viz., Ni, provided the cushioning effect and avoided the wear of grinding medium. Although there was no significant effect on lattice parameter of W, reduction in crystal size of W became difficult with more Ni content (Fig.2 (a)). Similarly there was no significant effect on the lattice parameter of Ni with varying contents of W as shown in Fig.2 (b). In the case of W-Ni terminal compositions viz., $\text{W}_{15}\text{Ni}_{85}$ and W_{95}Ni_5 (at.%), there was no significant change in the lattice parameter of W and Ni respectively with milling time (Fig.3 (a), (b)). These results showed that there is no mutual solid solubility or solid solution formation at room temperature within 15 h of milling.

The DSC analysis of $\text{W}_{30}\text{Ni}_{70}$, $\text{W}_{33}\text{Ni}_{67}$ and $\text{W}_{50}\text{Ni}_{50}$ (at.%) compositions, although did not reveal any transformation (Fig.4), a very close analysis of $\text{W}_{33}\text{Ni}_{67}$ pattern revealed two small exothermic peaks at 500°C and 750°C with enthalpy of 0.098 kJ/mole and 0.118 kJ/mol respectively (Fig.5). Hence, there is no solid-state phase transformation in $\text{W}_{33}\text{Ni}_{67}$, rather it suggests a second order transition [5], which could not be substantiated further in the present paper.

W-Fe: Intermediate phases did not form at the stoichiometric W-Fe compositions viz., Fe_2W and FeW or in between them (Fig.6), even after extended mechanical milling up to 30 h. Similar to W-Ni, there was a negative effect on W- crystal size reduction with Fe addition (Fig.7 (a)), due to possibly cushioning effect. This also reduced the contamination of grinding media. The lattice parameter of W and Fe did not show significant change (Fig.7 (a), (b)) in the 30 h milled W-Fe samples, suggesting there is no inter-diffusion of Fe and W atoms. The terminal compositions viz., W_3Fe_{97} and $\text{W}_{73}\text{Fe}_{27}$ (at.%), (Fig.8 (a), (b) respectively) did not show any significant variation in the lattice parameters of W and Fe with milling time up to 30 h. Hence no mutual solid solubility could be introduced, although mutual solid solubility in W-Fe was demonstrated by Jartych *et.al.* [14] with tool steel grinding media. The values of change in lattice parameter of W and Fe are presented in Table-2.

The DSC plots of all the W-Fe compositions showed nearly same transformation temperature (Fig.9 and Fig.10), except in case of W_3Fe_{97} it showed two very different

transformation temperatures in two consecutive runs. The low transformation temperature of 753°C corresponds to the magnetic transformation temperature of 770°C in equilibrium Fe (W) [14], with a transformation enthalpy of -0.0935 kJ/mole. However, since elemental Fe also shows similar ferro-magnetic transition [5,14], and inter-diffusion of W, Fe during heating in DSC could not be substantiated in the present paper, formation of Fe (W) solid solution could not be ascertained. Similar transformation temperatures in all W-Fe compositions except W_3Fe_{97} , suggests inter-diffusion of W and Fe during heating in DSC and subsequent transformations as per the thermally driven equilibrium W-Fe phase diagram [5]. In $\text{W}_{90}\text{Fe}_{10}$ an incipient melting was observed in the first heating and in $\text{W}_{30}\text{Fe}_{70}$ also incipient melting was seen in the second heating (Fig.10). However, in all the remaining W-Fe binary compositions no such melting was observed. This phenomenon is attributed to the minima in the reduced crystal size [15] of Fe in these compositions of W-Fe (Fig.7 (b)).

4. CONCLUSIONS

Intermediate phases did not form in W-Ni as well as in W-Fe binary stoichiometric compositions by high-energy milling. Mutual solid solubility also could not be introduced, after 15 h milling in W-Ni and even after 30 h milling in W-Fe system. Thermal assisted phase transformations, similar to those in the thermally driven equilibrium W-Fe phase diagram, were seen in W-Fe systems milled for 30 h. However, $\text{W}_{33}\text{Ni}_{67}$ and W_3Fe_{97} exhibited second order transitions.

5. ACKNOWLEDGEMENT:

R. Malewar and B. Sarma are extremely grateful to the Director, *Defence Metallurgical Research Laboratory – Hyderabad, D.R.D.O., Ministry of Defence, Govt. of India*, for technical and financial support to carry out the present work.

REFERENCES

- 1) W. F. Smith, 'Structure and Properties Of Engineering Alloys', 2nd Edition, McGraw Hill, N.Y., 1993.
- 2) A. Gruger, R. Vaben and F. Mertens, International Journal of Refractory Metals & Hard Materials, 16 (1998) 37.
- 3) Z. Kolczynski, W. Rutkowski, M. B. Swierczynska, and M. Trzaska, Powder Metallurgy International, 20 (1988) 22.
- 4) A. Upadhyaya, Materials Chemistry and Physics 67 (2001) 101

**AN INVESTIGATION INTO EXTENSION OF SOLID SOLUBILITY OF Fe AND Ni,
IN W BY HIGH-ENERGY MILLING**

- 5) E.A. Brandes and G. B. Brook – editors, Smithells Metals Reference Book, seventh edition, 1997.
- 6) Minlin Zhong, Wenjin Liu, Guoqing Ning, Lin Yang and Yanxia Chen, Journal of Materials Processing Technology 147 (2004) 167–173
- 7) C. Louro, A. Cavaleiro, Surface & Coatings Technology 116–119 (1999) 121
- 8) C. Louro, A. Cavaleiro, Surface & Coatings Technology 74–75 (1995) 998.
- 9) C. Louro, A. Cavaleiro, Journal of Electrochemical Society 144 (1997) 259.
- 10) L. Uray, Journal of Physics F: Metal Physics, 17 (1987) 1021
- 11) J. J. Houser, Physics Review B, 33 (1986) 5073
- 12) B. Persson, H. Blumberg, and D. Agresti, Physics Review 170 (1968) 1066
- 13) C. Suryanarayana, Progress in Materials Science 46 (2001) 1-184
- 14) Elzbieta Jartych, Jan K. Zurawicz, Dariusz Oleszak and Marck Pekala, Journal of Magnetism and Magnetic Materials 218 (2000) 247
- 15) G. L. Allen, R. A. Bayles, W. W. Gile and W. A. Jesser, Thin Solid Films 144 (1986) 297

Table-1. Change in lattice parameter of W and Ni in W-Ni compositions.

	Change in lattice parameter of W, (δa_w , %)	Change in lattice parameter of Ni, (δa_{Ni} , %)
Effect of Ni additions in W-Ni, milled for 15 h	-0.07%	-0.01%
Effect of milling time in $W_{15}Ni_{85}$, milled for 15 h	-0.05%	-0.1%
Effect of milling time in $W_{85}Ni_{15}$, milled for 15 h	0.009%	—

Table-2. Change in lattice parameter of W and Fe in W-Fe compositions.

	Change in lattice parameter of W, (δa_w , %)	Change in lattice parameter of Fe, (δa_{Fe} , %)
Effect of Fe additions in W-Fe, milled for 30 h	-0.11%	-0.17%
Effect of milling time in W_3Fe_{97} , milled for 30 h	-0.1%	-0.07%
Effect of milling time in $W_{73}Fe_{27}$, milled for 30 h	-0.12%	-0.29%

AN INVESTIGATION INTO EXTENSION OF SOLID SOLUBILITY OF Fe AND Ni, IN W BY HIGH-ENERGY MILLING

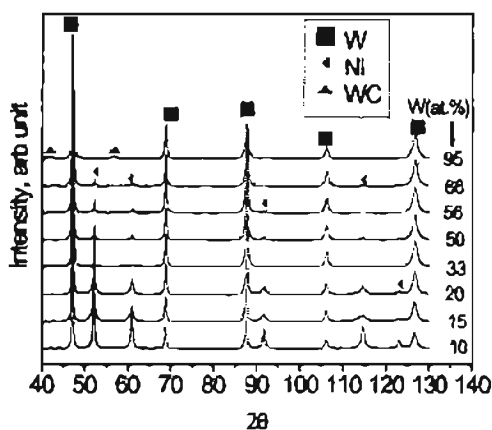


Fig.1: XRD pattern of W-Ni binary compositions milled for 15 h

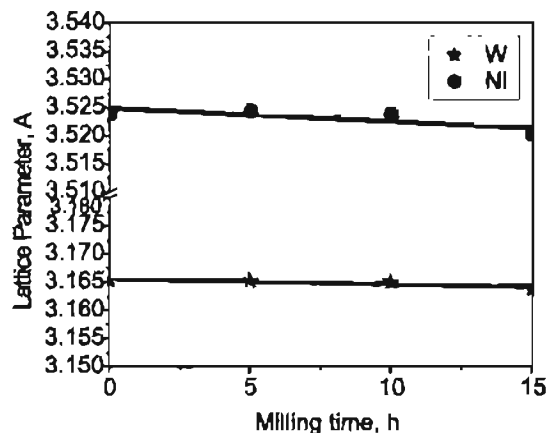


Fig.3 (a): Variation of lattice parameter of W and Ni in $W_{15}Ni_{85}$ with milling time

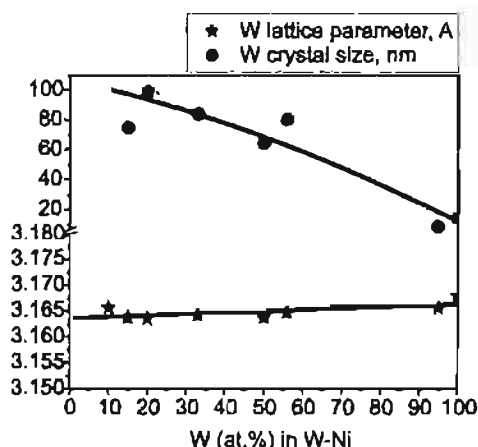


Fig.2 (a): Variation crystallite size and lattice parameter of W with different additions of Ni after 15 h of milling

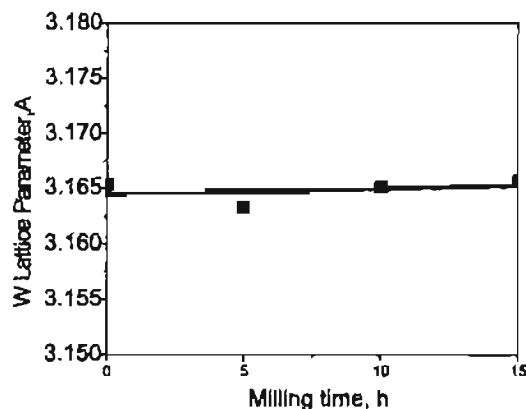


Fig.3 (b): Variation of lattice parameter of W in $W_{95}Ni_5$ with milling time.

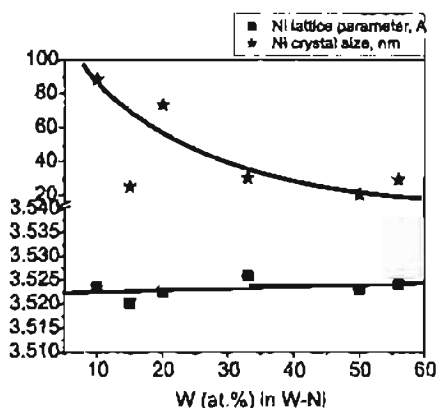


Fig.2 (b): Variation crystallite size and lattice parameter of Ni with different additions of W after 15 h of milling.

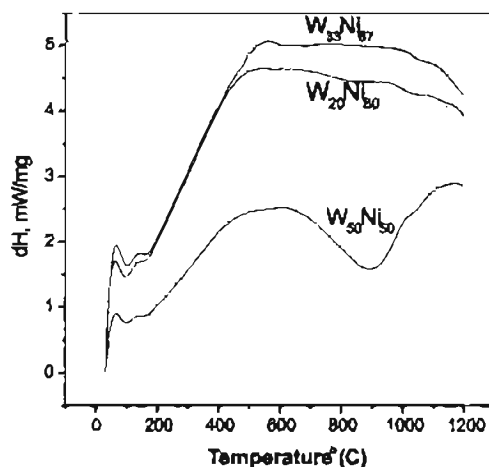


Fig.4: DSC pattern of stoichiometric $W_{20}Ni_{80}$, $W_{33}Ni_{67}$ and $W_{50}Ni_{50}$ (at. %) compositions milled for 15 h.

AN INVESTIGATION INTO EXTENSION OF SOLID SOLUBILITY OF Fe AND Ni, IN W BY HIGH-ENERGY MILLING

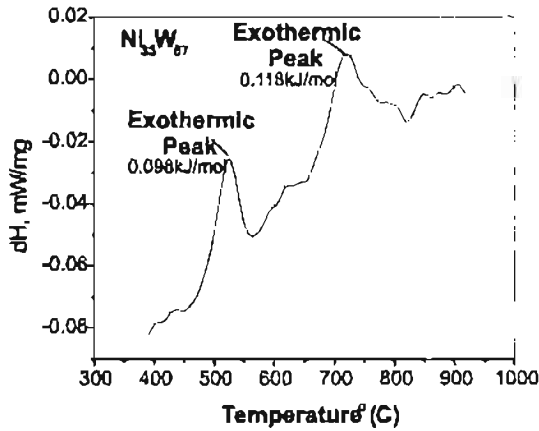


Fig.5: Exothermic peaks in the straightened DSC pattern of $W_{33}Ni_{67}$ (at. %) milled for 15 h

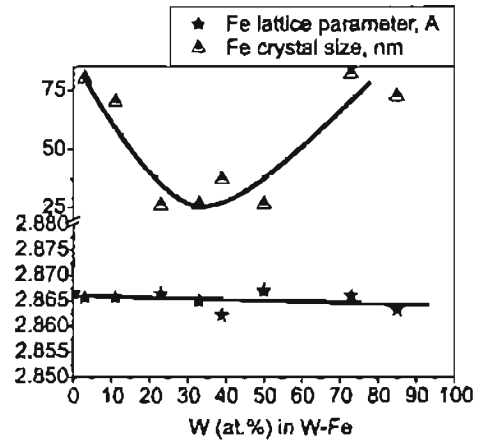


Fig.7 (b): Variation crystallite size and lattice parameter of Fe with different additions of W after 30 h of milling.

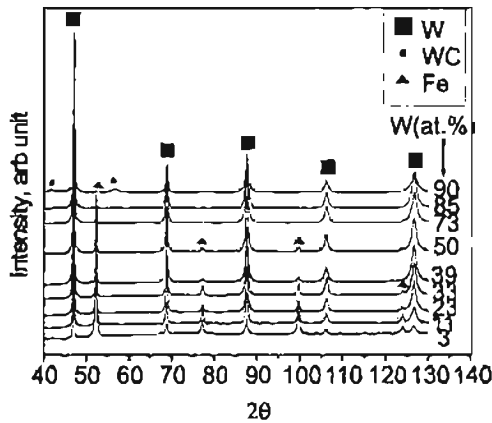


Fig.6: XRD pattern of W-Fe binary compositions milled for 30 h.

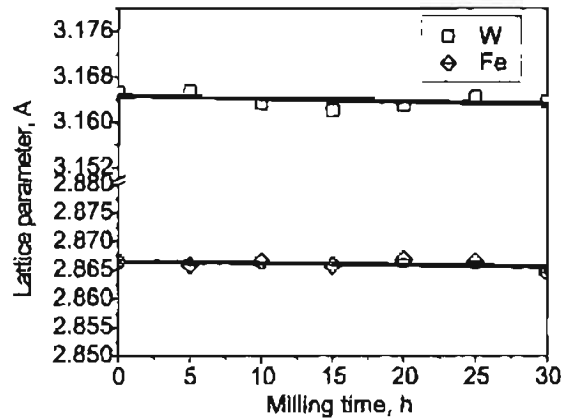


Fig.8 (a): Variation of lattice parameter of W and Fe in W_3Fe_{97} (at.%) with milling time.

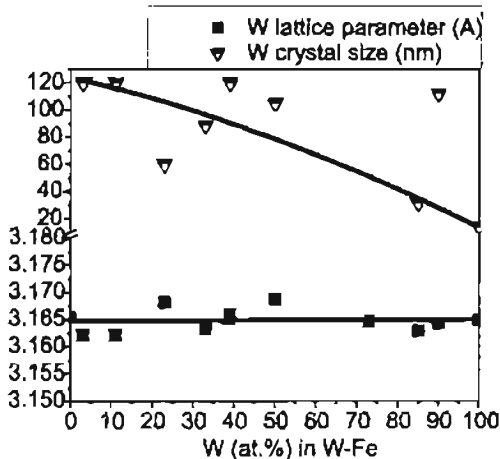


Fig.7 (a): Variation crystallite size and lattice parameter of W with different additions of Fe after 30 h of milling.

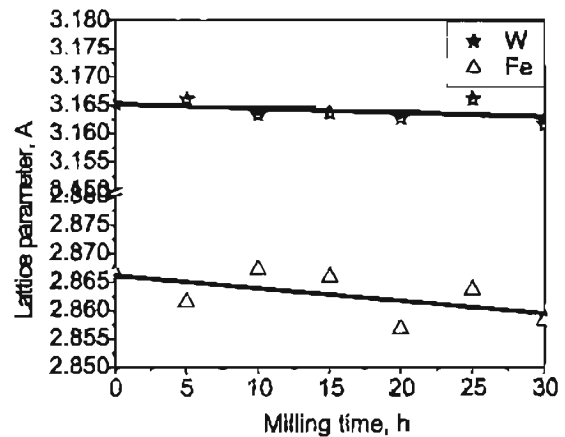


Fig.8 (b): Variation of lattice parameter of W and Fe in $W_{73}Fe_{27}$ (at.%) with milling time.

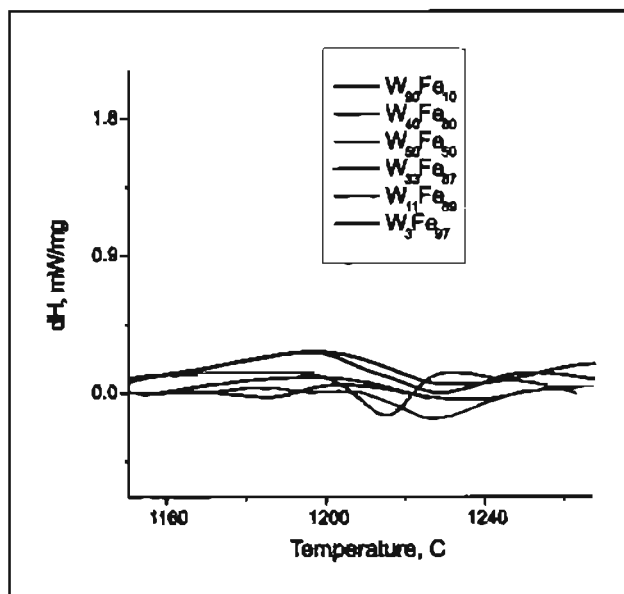


Fig.9: DSC pattern of stoichiometric W-Fe compositions (at. %) milled for 30 h.

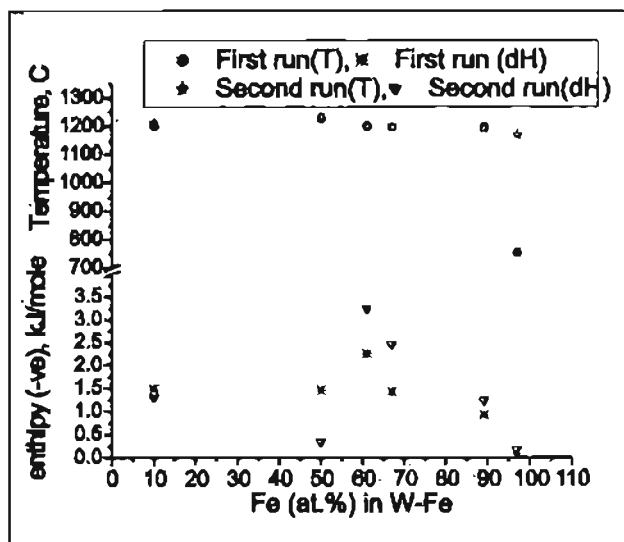


Fig.10. Variation of transformation temperature and enthalpy of transformation with Fe content in W-Fe milled for 30 h.

FORMATION OF SPHERICAL POWDERS OF GRAY IRON BY CARBOTHERMAL REDUCTION OF IRON OXIDE (Fe_2O_3)

R.V. Krishnarao, J.Subrahmanyam

DMRL, Kanchanbagh, Hyderabad-500058, India.

ABSTRACT

An attempt to reduce iron oxide (Fe_2O_3) in presence of K_2CO_3 and NiCl_2 has resulted in the formation of spherical powders of gray iron. K_2CO_3 which forms a low melting liquid and NiCl_2 which act as catalyst in gasification of carbon were used to supplement the reduction of iron oxide. Fe_2O_3 , NiCl_2 , K_2CO_3 , carbon black were reacted in a weight ratio (Fe_2O_3 : NiCl_2 : K_2CO_3 : C = 24: 2.5: 2.5: 6.5) and studied the reduction of iron oxide in the temperature range of 940°C to 1500°C in 1-atm. argon. Spherical particles of size around $2\text{ }\mu\text{m}$ were formed after reaction at 940°C . The size of spherical powders increased to $30\text{ }\mu\text{m}$ with increase in reaction temperature to 1100°C . Spherical powders of 1-2mm diameter and with metallic lustre were formed at 1300°C and 1500°C . The X-ray diffraction patterns and optical photomicrographs revealed that spherical powders are that of gray iron with graphite flakes and pearlite in ferrite matrix. Nickel was found to enhance the graphitization of carbon. However, the large size (1-2mm diameter) spherical powders were formed when both K_2CO_3 and NiCl_2 were present.

1. INTRODUCTION

Whiskers are used to reinforce metallic, ceramic, and polymeric materials. Though ceramic whiskers have been synthesized with a variety of chemistries, including SiC, AlN, TiC, TiN, Si_3N_4 , B_4C , and Al_2O_3 , the most developed and commercial whiskers are those based on SiC. [1]. Al_2O_3 reinforced with 25-30 wt% SiC whiskers is the material of choice for inserts used in high-speed cutting of high-nickel-content alloys. Cutting speeds of up to 450 m/min with reasonable life times could be achieved [2]. The superior behavior of the Al_2O_3 -SiC composite is not observed when machining steels. Recently attempts were made to develop other whisker materials that are more chemically stable than SiC and suitable for cutting stainless steel [3]. Whisker materials with different thermal expansion coefficients are required to reinforce different metallic materials. The development of new whisker materials has focussed mainly on carbides, nitrides and carbonitrides of transition metals such as Ti, Ta, and Nb [4-7]. There are few reports [8-13] on formation of TiC and TiN whiskers through carbothermal reduction of TiO_2 . Recently Carlsson *et al.* [14,15] reported a carbothermal reduction process for synthesis of TiB_2 and B_4C whiskers. They [15] used B_2O_3 and carbon as basic raw materials. Metallic powders of Co/Fe/Ni were used to form liquid catalyst to grow B_4C whiskers by VLS

mechanism. NaCl was used to supply Co and B as CoCl_2 (g) and BOCl (g) to catalyst liquid droplet. More recently, Krishnarao *et al.* [12,13,16,17] reported a process involving vapor-liquid-solid (VLS) growth mechanism for the formation of whiskers of TiC, TiN, TiB_2 , B_4C and BN.

All the above works [12,13,16,17], involve in carbothermal reduction of oxides of titanium and boron (TiO_2 and B_2O_3). K_2CO_3 which forms a low melting liquid, NiCl_2 which is well known as a catalyst in carbon gasification, were used to aid the formation of whiskers or platelets. In this work to examine the formation of crystals of iron carbide, iron oxide (Fe_2O_3) was carbothermally reduced in the presence of K_2CO_3 and NiCl_2 . This has lead to the formation of spherical powders of gray iron.

2. EXPERIMENTAL PROCEDURE

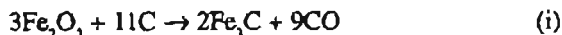
2.1 Materials

Laboratory reagent grade NiCl_2 was supplied by Qualigens Fine Chemicals, Bombay-400075, India. Specpure K_2CO_3 was procured from Johnson Matthey Chemicals Limited, Hertfordshire, England. Carbon black of grade N774 was obtained from Philips Carbon Black Ltd., Durgapur, India. Fe_2O_3 was obtained from J.J.Baker Chemical Co., Phillipsburg, New Jersey, USA. The level of impurities in above chemicals is given in Table. I

FORMATION OF SPHERICAL POWDERS OF GRAY IRON BY CARBOTHERMAL REDUCTION OF IRON OXIDE (Fe_2O_3)

2.2. Experimental

Fe_2O_3 , NiCl_2 , K_2CO_3 , and carbon black were taken in a weight ratio (Fe_2O_3 : NiCl_2 : K_2CO_3 : C = 24: 5: 5: 6.5). The molar ratio of Fe_2O_3 : C was chosen as per the following reaction.



Initially 5 g of K_2CO_3 was dissolved in 15 ml of D.I. water and the K_2CO_3 solution was poured in to 500ml beaker containing 24g of Fe_2O_3 . 5g of NiCl_2 was dissolved in 15 ml of D.I. water and added to the above paste and mixed thoroughly. The slurry obtained was dried in an oven at 90 C for 24h and the dried cake was crushed in mortar to fine powder. 5g of dried carbon black was added to it. The mixture was taken in an agate pot and mixing on a planetary ball mill was done for 5h. This powder mixture was designated as FNKC. After reviewing the results three more mixes were prepared to study the effect of potassium and nickel on the morphology of iron powders. Fe_2O_3 , NiCl_2 , K_2CO_3 , carbon black were taken in a weight ratio similar to that of FNKC. These three component mixes are designated as FNC, FKC. In another sample designated as FNKC II, very small quantity of NiCl_2 and K_2CO_3 was used. Fe_2O_3 , NiCl_2 , K_2CO_3 , carbon black were taken in a weight ratio (Fe_2O_3 : NiCl_2 : K_2CO_3 : C = 24: 0.3 : 0.3: 6.5).

Cylindrical graphite holder of 2.5-mm wall thickness and 40-mm inner diameter was filled with the powder mixture. The holder was closed with a graphite lid having a small hole allowing exchange of gasses between reactants and furnace chamber. The graphite reactor (sample holder) was placed in the hot zone of high-temperature graphite resistance furnace (ASTRO, U.S.A., Model 1000-3060-FP20). The furnace was evacuated to a moderate vacuum (5×10^{-2} torr) and back filled with 1 atm. argon. Experiments were conducted at 940°, 1100°, 1300° and 1500°C for 40 min. Temperature was maintained with a Model 939A3 Honeywell radiation pyrometer. Heating rate employed was 40°C min⁻¹. The samples of FNC, and FKC were reacted at 1300°C in argon.

Reacted samples were analysed by X-ray diffraction (XRD). A Philips X-ray diffractometer, Model PW3710, with Cu K_α radiation through Ni filter was used. The XRD peaks were identified by matching them to JCPDS-ICDD data cards of Fe (No. 6-0696) graphitic carbon (No. 25-284) and FeNi (No. 26-796). The morphology of the reacted powders was examined with an optical microscope and a Leo 440i, scanning electron microscope (SEM).

3. RESULTS AND DISCUSSION

After reaction at 940 C in argon, sample appeared like unreacted dried powder. After reaction at and above 1100°C,

samples contained glittering particles. At 1300°C and 1500°C the spherical powders formed were appeared like steel balls. In XRD patterns of the sample reacted at 940°C, peaks corresponding to Fe, graphitic carbon and FeNi were identified (Fig. 1). With increase in temperature to 1300°C the intensities of graphitic carbon and FeNi peaks decreased. The effect of potassium can be seen in Fig. 2 (c). In FKC three component system, Fe appeared as the major phase along with a very small peak for graphitic carbon. In the FNC sample, peaks of graphitic carbon are very prominent (Fig. 2 (b)).

The morphology of samples after reaction in Ar at different temperatures is shown in SEM photomicrographs (Fig. 3). Neither whiskers nor platelets were observed in the samples reacted at different temperatures. After reaction at 940°C, very fine (<10µm) spherical particles were formed. The size of the spherical particles increased with reaction temperature to 1100°C. The energy dispersive spectroscopic analysis (ESCA) revealed the presence of Fe and C in these particles. A small peak of Ni was also identified (Fig. 4). Formation of large size (1-2mm diameter) spherical particles was observed in FNKC sample reacted at 1300°C and 1500°C. Typical spherical particles formed at 1500°C are shown in Fig. 5.

In three component systems FNC and FKC very fine spherical particles of size around 1µm were seen after reaction at 1300°C (Fig. 6). Further a decrease in weight % of K_2CO_3 and NiCl_2 caused the formation of submicron sized spherical particles in FNKC II reacted at 1100°C (Fig. 7(a)). Iron and carbon were identified in ESCA of spherical particles formed in FNKC II (Fig. 7(b)). On comparing Fig. 7 (a) with Fig. 3 (b) it is evident that K_2CO_3 and NiCl_2 play a key role in forming large size spherical particles.

The typical microstructure of polished spherical particles formed at 1500°C is shown in Fig. 8(a). Graphite flakes are clearly visible (Fig. 8(b)). After etching the pearlitic islands in ferrite matrix were appeared (Fig. 9(a)). This microstructure (Fig. 9(b)) represents the gray iron with graphite flakes and pearlite in ferrite matrix.

The XRD patterns of FNKC, FNC, and FKC reacted at 1300°C in argon revealed the effect of nickel and potassium on carbon and iron (Fig. 2). In the presence of potassium alone the tendency of graphitization of carbon black which is basically amorphous, is less. In the FNC system, peaks of Fe as well as graphitic carbon were distinctly identified. From XRD patterns it is clear that nickel in combination with K is very effective in forming the graphitic carbon and Fe. Nickel is known to dissolve in the ferrite to harden it. Used alone, nickel is somewhat effective in reducing the amount of silicon which must be present to develop a

FORMATION OF SPHERICAL POWDERS OF GRAY IRON BY CARBOTHERMAL REDUCTION OF IRON OXIDE (Fe₂O₃)

gray iron, and thus cause refinement of the graphite and pearlitic structure.

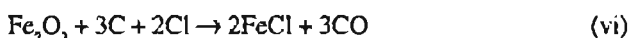
According to reactions presumed to take place inside the iron blast furnace, at 450°C iron oxide reduces to Fe and reoxidizes to FeO.



At a temperature of 900°C limestone flux dissociates into CaO and CO₂ (reactions (iv) and (v)).



Though CaCO₃ is not present in this work, potassium and nickel make the system more complicated. K₂CO₃ dissociates into K₂O and CO₂ at 891°C. K₂O can form a thin liquid layer around other particles and react with it. The important role of potassium is formation of a low melting liquid and bringing the reactants together. K₂CO₃ alone could not accelerate the formation of spherical particles. The catalytic affect of nickel on gasification of carbon is also important [24]. In the presence of NiCl₂ and Fe₂O₃ a complex K-Ni-Fe liquid droplet could form. Further chlorine available from NiCl₂ reacts with Fe₂O₃ to form FeCl.



Thus C and FeCl are continuously supplied to the complex liquid droplet of K-Ni-Fe. Reduced iron precipitates and carburises (Fe₃C) to form a low melting liquid. The separation of molten iron droplet from molten flux takes place. That is the reason for not finding potassium in ESCA of spherical particles (Fig. 4 and Fig. 7 (b)). The large size spherical particles of gray iron were formed in FNKC samples at 1350°C and 1500°C.

4. CONCLUSIONS

Reduction of iron oxide (Fe₂O₃) in presence of K₂CO₃ and NiCl₂ has resulted in the formation of spherical powders of gray iron. Spherical particles of size around 2 μm were formed after reaction at 940°C. The size of spherical powders increased to 30μm with increase in temperature to 1100°C. Spherical powders of 1-2mm diameter and with metallic luster were formed at 1300°C and 1500°C. From the microstructure the spherical powders have been identified as gray iron with graphite flakes and pearlite in ferrite matrix. Nickel was found to enhance the graphitisation of amorphous carbon. However, the large size (1-2mm) spherical powders were formed in samples containing both K₂CO₃ and NiCl₂.

ACKNOWLEDGEMENT

The authors thankfully acknowledge the financial support received from the Defence Research & Development Organisation, Govt. of India and technical support from XRD group and SEM group of DMRL in order to carry out the present research study.

REFERENCES

1. D. J. BRAY, *Bullet. Amer. Ceram. Soc.* **74** (1995) 152.
2. J. HOMENY, in "Ceramic Matrix Composites," edited by Richard Warren, (Chapman & Hall, New York, 1992) p.245.
3. M. CARLSSON, and M. JOHNSON, *Ceram. Engg. Sci. Proc.* **21** (2000) 375.
4. M. JOHNSON and M. NYGREN, *J. Mater. Res.* **12** (1997) 2419.
5. J-B. LI, G. Y. XU, E. Y. SUN, Y. HAUNG and P. F. BECHER, *J. Am. Ceram. Soc.* **81** (1998) 1689.
6. N. AHLEN, M. JOHNSON and M. NYGREN, *J. Mater. Sci. Lett.* **18** (1999) 1071.
7. M. CARLSSON, M. JOHNSON and M. NYGREN, *J. Am. Ceram. Soc.* **82** (1999) 1969.
8. M. NYGREN, M. JOHNSON, N. AHLEN and M. EKLUND, *Europ. Patent*, EP 0 754 782 A1, Jan. 22 (1997).
9. N. AHLEN, M. JOHNSON, and M. NYGREN, *J. Amer. Ceram. Soc.* **79** (1996) 2803.
10. C. E. BAMBERGER, P. ANGELINI and T. A. NOLAN, *J. Am. Ceram. Soc.* **72** (1989) 587.
11. C. E. BAMBERGER, D. W. COFFE and T. A. NOLAN, *J. Mater. Sci.* **25** (1987) 4992.
12. R. V. KRISHNARAO, J. SUBRAHMANYAM and V. RAMAKRISHNA, *J. Mater. Synth. & Process.* **9** (2001) 1.
13. R. V. KRISHNARAO, J. SUBRAHMANYAM and M. YADAGIRI, *J. Mater. Sci.* **37** (2002) 1693.
14. F. THEVENOT, *Key Eng. Mater.* **59** (1991) 56.
15. G. De WITH, *J. Less-Common Met.* **95** (1983) 133.
16. T. R. CHAPMAN, D. E. NIESZ, R. T. FOX, T. FAWCETT, *Wear* **236** (1999) 81.
17. A. GATTI, C. MANUSCO, F. FEINGOLD and R. MEHAN, In "Proceedings of International Conference on Crystal Growth, Boston, MA, June 1966," (Pergamon, Oxford, 1967) p.317.

**FORMATION OF SPHERICAL POWDERS OF GRAY IRON BY CARBOTHERMAL
REDUCTION OF IRON OXIDE (Fe₂O₃)**

18. L. AHMED, and G. G. CAPSIMALIS, In "Proceedings of the 6th International Symposium on Reactive Solids, 1968," (Wiley-Interscience, New York, NY, 1969) p.477.
19. I. D. R. MACKINNON and K. L. SMITH, In "Novel Refractory Semiconductors," (Mater. Res. Soc. Proc. 97 Pennsylvania, 1987) p.127.
20. D. ZHANG, D. N. MCILROY, Y. GENG and M. G. NORTON, *J. Mater. Sci. Lett.* **18** (1999) 349.
21. M. CARLSSON, P. ALBERIUS-HENNING and M. JOHNSON *J. Mater. Sci.* **37** (2002) 2917.
22. M. CARLSSON, F. J. GARCIA-GARCIA and M. JOHNSON, *J. Cryst. Growth* **236** (2002) 466.
23. R. V. KRISHNARAO, and J. SUBRAHMANYAM, *Trans. Indian. Ceram. Soc.* **61** (2002) 3.
24. P.L. WALKER (JR), M. SHELE, and R. A. ANDERSON, In "Chemistry and Physics of Carbon," 4, edited by P. L. Walker Jr., (Marcel Dekker Inc, New York, 1968) p.287.

TABLE I Purity of reactants used in carbothermal reduction of Fe₂O₃

Chemical	Manufacture	Impurity Level	
K ₂ CO ₃	Johnson Matthey U.K., England	Sr	3ppm
		Mg, Na	1ppm
		Ca, Fe, Li	<1ppm
NiCl ₂	Qualigens Fine Chemicals, Ltd. Mumbai, India	SO ₄	0.005%
		Co	0.002%
		Fe	0.002%
Fe ₂ O ₃	J.J.Baker Chemical Co., Phillipsburg, New Jersey, USA	SO ₄	<0.1%
		HCl	0.1%
		PO ₄	0.02%
		Cu	0.001%
		Mn	0.003%
		Zn	0.002%
C.Black	Philips Carbon Black Grade N220, ISAF-HM Durgapur, India.		

FORMATION OF SPHERICAL POWDERS OF GRAY IRON BY CARBOTHERMAL REDUCTION OF IRON OXIDE (Fe_2O_3)

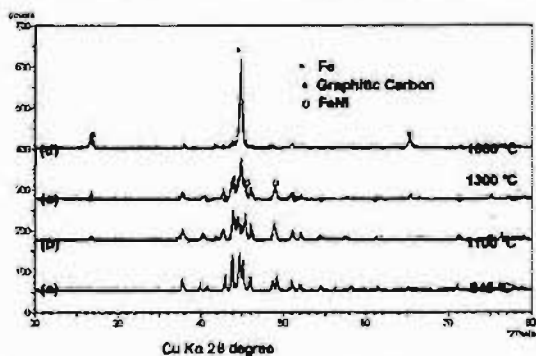


Figure 1 XRD patterns of FNKC after reaction in argon at different temperatures

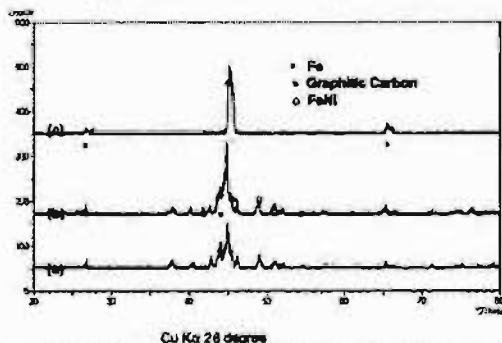


Figure 2 XRD patterns (a) FNKC, (b) FNC, and (c) FKC samples after reaction in argon at 1300°C

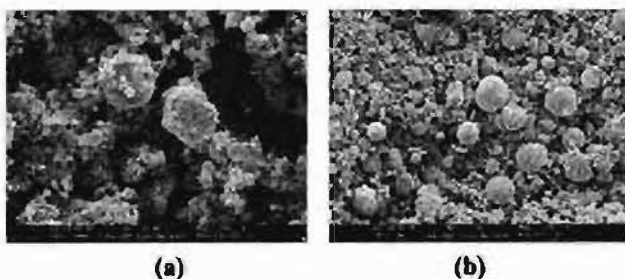


Figure 3 SEM photographs showing the morphology of FNKC reacted at (a) 940°C, and (b) 1100°C.

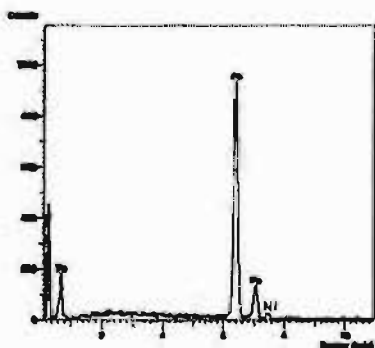


Figure 4 ESCA analysis of a spherical particle formed in FNKC reacted at 1100°C

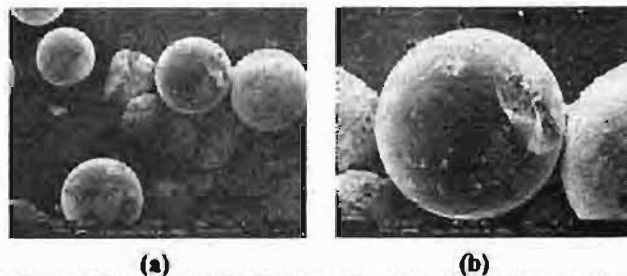


Figure 5 Typical spherical powders formed in FNKC after reaction at (a) 1500°C. (b) same as in (a) at higher magnification

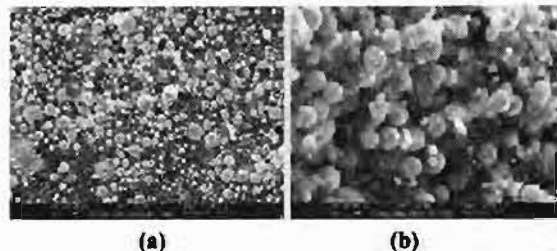


Figure 6 SEM photographs showing the morphology of (a) FNC, and (b) FKC after reaction in argon at 1300°C.

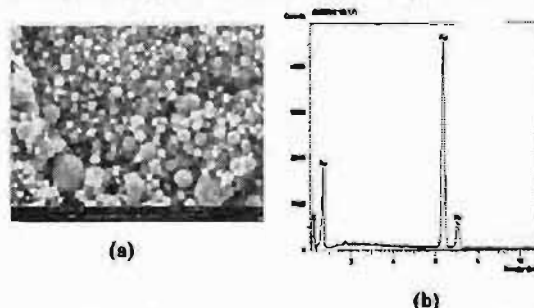


Figure 7 (a) SEM photographs showing the morphology of FNKCII after reaction in argon at 1100°C, (b) ESCA of a spherical particle formed in FNKCII at 1100°C.

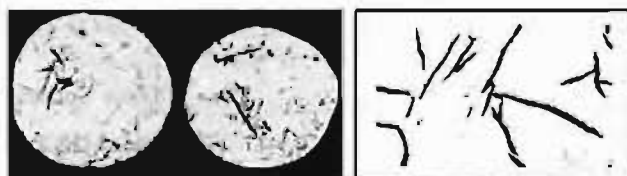


Figure 8 (a) Microstructure of spherical powders formed in FNKC at 1500°C. (b) same as in (a) at higher magnification

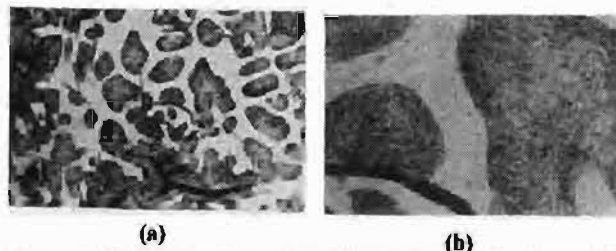


Figure 9 (a) Microstructure of etched spherical powders formed in FNKC at 1500°C. (b) same as in (a) at higher magnification.

COMBUSTION SYNTHESIS OF ULTRAFINE NiO POWDER FOR Ni-YSZ CERMET ANODE MATERIAL IN SOFC

A.R. Ballal ^{*#}, R. Lenka [§], T. Mahata [§], P.K. Sinha [§], P. Gopalan [#], S.N. Malhotra [#]

^{*} Department of Metallurgical Engineering and Materials Science,
Indian Institute of Technology, Mumbai- 400 076, India

[§] Energy Conversion Materials Section, Powder Metallurgy Division,
Bhabha Atomic Research Centre, Vashi Complex, Navi Mumbai, 400 705, India

ABSTRACT

Nickel yttria-stabilized zirconia (Ni-YSZ) cermet anodes have been extensively studied in solid oxide fuel cells (SOFC) because of their stability, conductivity, thermal expansion compatibility, and catalytic activity. In the present work, characteristics of NiO powder prepared by combustion synthesis using three different fuels have been studied. The fuels used were citric acid, glycine, and urea. Various molar ratios (m) of Ni-salt and fuel were used. The synthesized powders were calcined in air at temperatures ranging from 700 to 1000°C. The powders (as synthesized and calcined) were characterized for particle size and phase analysis. The powders obtained by urea (m = 3:5) and glycine (m = 1:0.75) route were observed to have ultrafine particle size having single NiO phase. The powder from citric acid and glycine (m = 1:1) route showed larger grain size and presence of NiO + Ni phases. Particle size was found increased after calcination because of agglomeration. It can be concluded that calcination step in processing can be avoided to form Ni-YSZ cermet.

1. INTRODUCTION

Solid oxide fuel cells (SOFC) are of significant interest as energy conversion devices owing to their high efficiency, design modularity, higher tolerance limits for impurity contents and environmentally friendly nature. Nickel yttria stabilized zirconia (Ni-YSZ) cermets have been extensively studied as anode materials for high temperature SOFC [1-3]. The cermet has to meet certain criteria in order to act as an effective anode material. It should have high electronic conductivity, appropriately porous microstructure (approximately 30% open porosity) and physical and chemical compatibility with other cell components [4]. Furthermore, both the Ni and YSZ phase should form continuous network structure in order to extend the effective Ni-YSZ-fuel triple-phase boundary. The performance of anodes is highly dependant on the particle size and the microstructure of the final electrode [5-7]. Literature on Ni-YSZ cermet synthesis [8-10] describes uniform and homogeneous distribution between the Ni and YSZ phases in the matrix. The cermet anode is usually prepared from a mixture of NiO and YSZ powders followed by reduction. The reduced anode becomes porous as a result of oxygen loss due to conversion of NiO to nickel. Among the various solution routes employed in the oxide materials preparation,

the combustion synthesis seems to be very promising [11-13]. Starting with the solution of all components, a maximum homogeneity of the mixed powder can be achieved. This method makes use of the strong exothermicity of redox reactions associated with the oxide synthesis. Such reactions proceed in the form of a self-sustaining front, which propagates through the reactants. Oxide powders are formed directly from the precursor gel. Ni-YSZ cermet preparation by using combustion synthesis has already been successfully applied by some authors. Ringuède et al. [14] established the reaction system employing nitrates and urea. Aruna et al. [10] prepared Ni-YSZ cermet powders using carbonylhydrazide as fuel component. The cermet powders were prepared by citrate/nitrate combustion synthesis by Marinsek et al [15]. Relatively high speed of propagated self-sustaining reaction front is achieved when combustion synthesis is based on nitrate-glycine [16] or Zr-NiO-Y₂O₃ [17] redox system.

The aim of present work was to apply the combustion synthesis technique based on system of metal nitrate and different fuel components for the formation of NiO powder. Different metal: fuel (m) initial molar ratios were used in order to manufacture ultrafine NiO powders that are characterized by very uniform distribution of Ni particles.

COMBUSTION SYNTHESIS OF ULTRAFINE NiO POWDER FOR Ni-YSZ CERMET ANODE MATERIAL IN SOFC

The particle size and phase analysis of thus prepared powders were studied.

2. EXPERIMENTAL

Sample	Fuel	Ni-nitrate: Fuel
S1	Citric acid	1:1
S2	Urea	3:5
S3	Glycine	1:1
S4	Glycine	1:0.75

Table 1 Fuels and molar ratios used

NiO powder was prepared by combustion synthesis using three different fuels. The fuels used were citric acid, glycine, and urea. Various molar ratios of Ni-nitrate and fuel were used. The molar ratios used are shown in Table 1. Gentle heating of the solutions resulted in evaporation of excess water, yielding viscous liquid. Further heating caused the precursor solution to ignite and the flame propagating throughout the mass in less than 2 minutes yielding voluminous fine powder or loose agglomerates. High temperature reactions were revealed by sudden release of fumes. The synthesized powders were calcined at various temperatures ranging from 700° to 1000°C for 2 h.

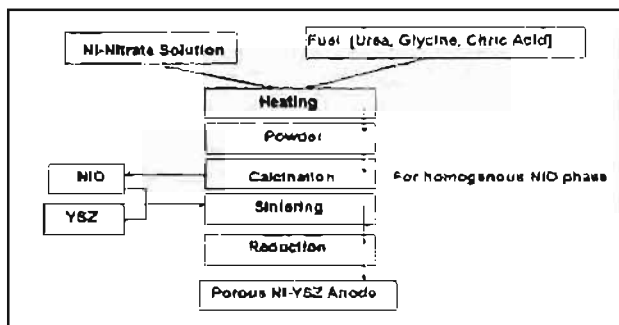


Fig.1 Preparation route of Ni-YSZ anode

Powders (as synthesized and calcined) were characterized for particle size and phase analysis. Particle size analysis was carried out by means of laser scattering technique using HORIBA LA-500 particle size analyzer and phase composition was investigated by X-ray diffraction using Philips PW-1830 instrument

3. RESULTS AND DISCUSSION

From the X-ray diffraction data, Fig.2 the peaks for NiO and metallic Ni were clearly identified for the S1 and S3 powder samples (as synthesized). S2 and S4 powder

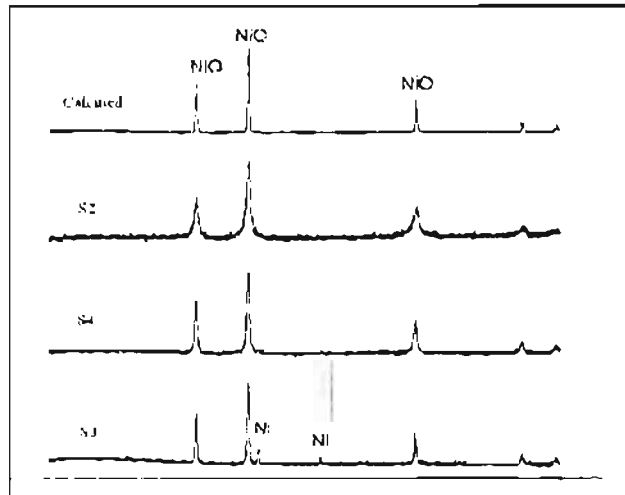


Fig.2 Diffraction patterns of calcined, S2, S4 and S3 samples

samples were found to be composed of single NiO phase. After calcination, all the metallic part (in S1 and S3) was transformed to the oxide and single NiO phase was obtained.

Particle size analysis (Fig.3) showed that, S2 and S4 samples had the desired narrow particle-size distribution with $d_{50} = 0.47$ and 0.53μ , respectively. Particle size of the powder prepared by citric acid was found to be highest with $d_{50} = 17 \mu$. Calcination resulted in agglomeration of particles causing increase in particle size ($d_{50} = 75-100 \mu$).

Conventional preparation route of Ni-YSZ cermet anode requires calcination to obtain single NiO phase to control the right composition [18]. This, in turn, increases the particle size which affects the subsequent microstructure on sintering. Narrower agglomerate size distribution has a great influence on the subsequent sintering and reduction. If the particle size distribution in the green body is narrow, the coarsening of the NiO grains, and subsequently, Ni grains are less pronounced [15].

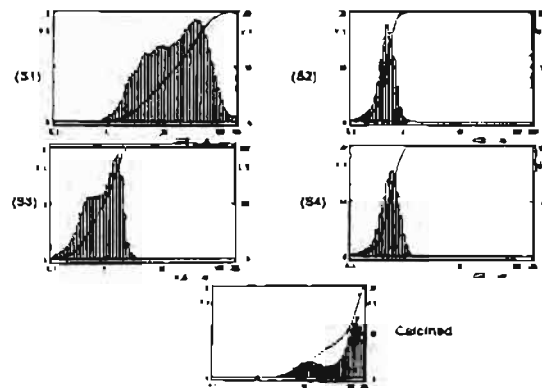


Fig. 3 Particle size data for S1, S2, S3, S4, and calcined samples

In the present study, single phase NiO with narrow size distribution was obtained directly using urea (metal: fuel = 3:5) and glycine (metal: fuel = 1:1). This can help avoid calcination step and, thereby its deleterious effects of agglomeration.

4. CONCLUSIONS

Ultrafine, single phase NiO powders was prepared by combustion synthesis by proper choice of fuel and metal: fuel ratio (m). Urea (m = 3:5) and glycine (m = 1:0.75) routes produced nanocrystalline, single phase NiO powder of narrow particle-size distribution. Such powder may be directly sintered avoiding the calcination stage. Particle size was found increased after calcination because of agglomeration.

REFERENCES

- [1] N.Q. Minh, Ceramic Fuel Cells, *J. Am. Ceram. Soc.* **76** (1993) pp. 563.
- [2] S.P.S. Badwal, K. Foger, Solid oxide electrolyte fuel cell review, *Ceram. Int.* **22** (1996) pp 257.
- [3] N.Q. Minh, T. Takahashi, Science and Technology of Ceramic Fuel Cells, Elsevier, New York, 1995.
- [4] D.W. Dees, T.D. Claar, T.E. Easler, D.C. Fee and F.C. Mrazek, Conductivity of porous Ni-ZrO₂-Y₂O₃ cermets, *J. Electrochem. Soc.* **134** (1987) pp. 2141.
- [5] S. Primdhal and M. Mogensen, Oxidation of hydrogen on Ni/yttria-stabilized zirconia cermet anodes Oxidation of hydrogen on Ni/yttria-stabilized zirconia cermet anodes, *J. Electrochem. Soc.* **144** (1997) pp. 3409.
- [6] M. Brown, S. Primdhal and M. Mogensen, Structure/performance relations for Ni/yttria-stabilized zirconia anodes for solid oxide fuel cell, *J. Electrochem. Soc.* **147** (2000) pp. 475.
- [7] B. de Boer, M. Gonzalez, H.J.M. Bouwmeester and H. Vermeij, Effect of the presence of fine YSZ particles on the performance of porous nickel electrodes, *Solid State Ionics* **127** (2000) pp. 269.
- [8] M. Marinsek, K. Zupan, J. Macek, Preparation of Ni-YSZ composite materials for solid oxide fuel cell anodes by the gel-precipitation method, *J. Power Sources* **86** (2000) pp 383.
- [9] Y. Li, Y. Xie, J. Gong, Y. Chen, Z. Zhang, Preparation of Ni/YSZ materials for SOFC anodes by buffer-solution method, *Mater. Sci. Eng. B* **8** (2001) pp. 119.
- [10] S.T. Aruna, M. Muthuraman, K.C. Patil, Synthesis and properties of Ni-YSZ cermet: anode material for solid oxide fuel cells, *Solid-state Ionics* **111** (1998) pp.45.
- [11] K.R. Venkatachari, D. Huang, S.P. Ostrander, W.A. Schulze, G.C. Stangle, Combustion synthesis process for synthesizing nanocrystalline zirconia powders, *J. Mater. Res.* **10** (3) (1995) pp. 748
- [12] K.R. Venkatachari, D. Huang, S.P. Ostrander, W.A. Schulze, G.C. Stangle, Preparation of nanocrystalline yttria-stabilized zirconia, *J. Mater. Res.* **10** (3) (1995) pp.756.
- [13] Z.A. Munir, U. Anselmi-Tamburini, Self-propagating exothermic reactions: the synthesis of high-temperature materials by combustion, *Mater. Sci. Reports* **3** (7-8) (1989) pp. 277.
- [14] A. Ringuede, J.R. Frade, J.A. Labrincha, Combustion synthesis of zirconia-based cermet powders, *Ionics* **6** (2000) pp. 273.
- [15] M. Marinsek, K. Zupan, J. Macek, Ni-YSZ cermet anodes prepared by citrate/nitrate combustion synthesis, *J. of Power Sources* **106** (2002) pp. 188.
- [16] S.J. Kim, W. Lee, W.J. Lee, S.D. Park, J.S. Song, E.G. Lee, Preparation of nanocrystalline nickel oxide-yttria-stabilized zirconia composite powder by solution combustion with ignition of glycine fuel, *J. Mater. Res.* **16** (12) (2001) pp. 3621
- [17] U. Anselmi-Tamburini, G. Chiodelli, M. Arimondi, F. Maglia, G. Spinolo, Z.A. Munir, Electrical properties of Ni/YSZ cermets obtained through combustion synthesis, *Solid State Ionics* **110** (1/2) (1998) pp.35.
- [18] A. Ringuede, J.A. Labrincha, J.R. Frade, A combustion synthesis method to obtain alternative cermet materials for SOFC anodes, *Solid State Ionics* **141-142** (2000) pp. 549.

DEVELOPMENT OF PREALLOYED METAL MATRIX POWDER FOR DIAMOND TOOL INDUSTRY

Shaik Imam, G.V.Murali Krishna

Innomet Powders, Hyderabad-502 032.

ABSTRACT

Present investigation includes study of the performance of metal bonded diamond tools using prealloyed metal matrix powders. Water atomized metal matrix powder using cobalt, iron, copper and tin was further processed and blended for use in all the hot pressing experiments. Diamond impregnated segments were hot pressed in resistance heated graphite moulds at various temperatures. The rates of heating and holding time were also varied. The effect of these variables on hardness and densification were studied and compared with premixed powders. Rockwell hardness tester was used to measure the hardness of the segments using Rockwell B Scale. Densification was measured using Archimedes principle. Micro structural investigation was carried out using optical microscope and also onfield sawing performance of the diamond impregnated circular saw was evaluated.

1. INTRODUCTION

Important factors in determining the performance of the diamond cutting tools is the bond characteristics of the metal matrix and diamonds. Primary function of the metal matrix is to hold the diamond firmly and bond surrounding the diamond must wear away continuously to keep re-exposing the diamonds for the tool to facilitate constant efficient cutting [1-3]. A too soft a matrix wears faster than the diamond, which results in the possibility of diamond loss before completing its effective working life, leading to excessive tool cost. On the other hand, as extremely wear resistant matrix could wear more slowly than the breakdown of the diamond, causing the segment surface to polish [4]. The bonding phase is usually made from cobalt, nickel and iron or a combination of these metals. Generally Cu-Sn is used as filling phase that usually melts at sintering conditions. [5]. Prealloyed powder used for diamond tools gives technical as well as economical advantages. It gives excellent metal distribution on much finer scale, much higher homogeneity than mechanical mixture of individual powders, minimal dimensional change, eliminates in-plant mixing, minimizes batch to batch variation, causes higher protrusion and affects stronger diamond retention with enhanced tool life and performance.

2. EXPERIMENTAL

2.1 Segment preparation:

In-house water atomized prealloyed powder consisting of Fe, Co, Cu, and Sn was used as metallic matrix for preparing the diamond tool segments. Powders were screened through 85 mesh (BSS) mixed along with 4 wt% 40/50 US mesh light yellow-green, blocky cubo-octahedral diamond particles in a turbula mixture. Initially rectangular (24X12X7 mm) segments were cold pressed in the uniaxial hydraulic press at 200 MPa. Hot pressing was done at three temperatures 800^o, 825^o and 850^oC with 40 MPa pressure in resistance heated graphite moulds. Segments with premixed powders were also prepared with same chemical composition under similar experimental conditions to compare between premixed and prealloyed powders.

2.2 Hardness measurements:

Hardness of the segments was measured by using Rockwell hardness tester with B scale (1/16" steel ball as indenter at 100 Kg load). Average of three readings was considered in reporting the hardness.

2.3 Density measurements:

Density of the segments was measured by Archimedes principle.

DEVELOPMENT OF PREALLOYED METAL MATRIX POWDER FOR DIAMOND TOOL INDUSTRY

2.4 Saw-blade specifications:

Sawing operations of the granite using the experimental diamond blade were carried out for the evaluation of the sawing performance. The diamond saw-blade used in the tests had a diameter of 1000mm and a steel core of thickness 7mm. 30 pieces of diamond-impregnated segments (24X12X7 mm) were brazed to the periphery of a circular steel core with a standard narrow radial slot. During the sawing trials, the saw operating parameters are depth of cut, peripheral speed and feed rate, specific removal rate, power and specific cutting energy. Water was used as the flushing and cooling medium, and the flow rate was maintained at constant 20 lit/min.

3. RESULTS AND DISCUSSION

Table I and Fig.1 show the hardness of the prealloyed metal matrix segments hot pressed at 800°, 825°, 850°C with 40 MPa as 93, 94 and 94 HR_B respectively and 82, 84 and 85 HR_B respectively in case of premixed metal matrix segments. Increase in the hardness (fig. 1) could be attributed to the solid solution strengthening of the matrix in case of prealloyed metal matrix powder segments. More over the phase distribution was very fine and uniform in prealloyed powders compared to its premixed counterpart.

Densification of the segments was calculated using Archimedes principle. Table I and Fig.2 show the densification of the prealloyed metal matrix segments hot pressed at 800°, 825°, 850°C with 40 MPa as 94, 95 and 96% theoretical respectively where as 93, 94 and 94% theoretical respectively in case of premixed metal matrix segments. This could also be seen from the microstructure shown in the Fig.3 and Fig.4. Microstructures revealed a much homogeneous distribution of phases and less porosity in case of prealloyed metal matrix powder segment. Low average cutting time, reduction in powder consumption and higher productivity were observed in initial experimental onfield testing.

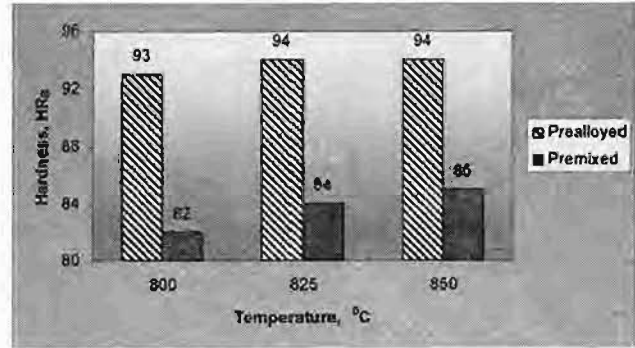


Fig.1. Variation of hardness with hot pressing temperature.

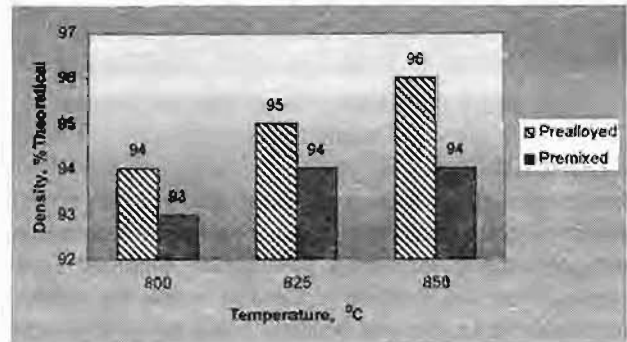


Fig.2. Variation of density with hot pressing temperature

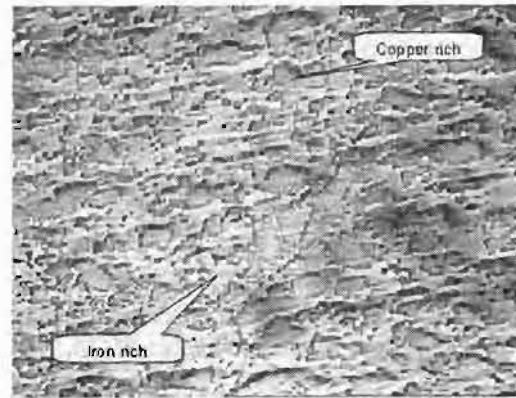


Fig.3. Phase distribution in premixed metal matrix segment. The phases were identified by the material contrast on the polished surface.

Table.I. Variation of hardness and densification with hot pressing temperature.

Temperature, °C	Pressure, MPa	Hardness, HR _B		Density, % Theoretical	
		Prealloyed	Premixed	Prealloyed	Premixed
800	40	93	82	94	93
825	40	94	84	95	94
850	40	94	85	96	94

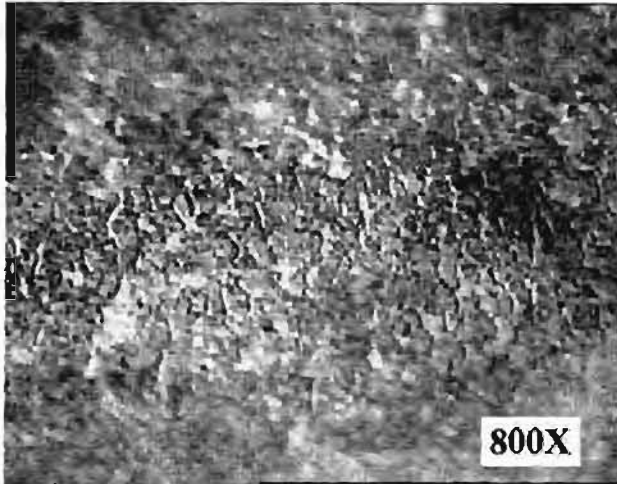


Fig.4. Phase distribution in prealloyed powder segment.

4. CONCLUSIONS

Prealloyed metal matrix powder has shown much better properties in terms of hardness as compared to its counterpart premixed metal matrix powder for Diamond Tool segments. Fine and uniform phase distribution caused the improvement in the tool quality. Filed trails although indicating a faster cutting speed for prealloyed metal matrix, are in progress and therefore inconclusive. Developments of improved metal matrix powders are under trails.

5. REFERENCES

1. J. Konstanty, Production and application of diamond tools, *Int. PM Direct.* (2002-03) 45.
2. J. Konstanty, A. Romanski, H. Frydrych, Effect of mechanical properties of the matrix on its diamond retention capacity and wear characteristics during sawing hard stone by means of diamond impregnated tools, in: *Proceedings of 2000 Powder Metallurgy World Congress, Kyoto, November 12-16, 2000*, pp. 1629-1632.
3. O.M. Ivasishin, D.D. Savvakina, F. Froes, V.C. Mokson, Synthesis of alloy Ti-6Al-4V with low residual porosity by a powder metallurgy method, *Powder Metall. Metal Ceram.* 41 (7-8) (2002) 382-389.
4. A. Biittner, Diamond tools and stone, *Ind. Diamond Rev.*, 34 (1974) 89-93.
5. Stockwell BH. Macro matrix powders. The metallurgy of diamond tools. Istanbul: De-Beers/Eskanazi Seminar; 1987.

DEVELOPMENT OF TEXTURED SINGLE LAYER AND MULTILAYER COATED SUPERCONDUCTOR SUBSTRATES BY THE POWDER METALLURGY ROUTE

P.P. Bhattacharjee, R.K. Ray and A. Upadhyaya*

Department of Materials and Metallurgical Engineering, IIT, Kanpur, 208 016, India.

ABSTRACT

Development and stability of cube texture has been studied in a sintered Pure Ni, Ni-5at. % W alloy and a multilayer tape of configuration Ni/Ni-5at. % W after cold rolling (~ 95%) and annealing. The deformation textures of pure Ni and Ni-5at. % W are similar. However, Ni-5at. % W alloy shows a much sharper cube texture after annealing as compared to pure Ni, which strengthens with increasing annealing temperatures upto 1250 C. The cube texture is also found to be much sharper on the Ni side of a Ni/Ni-5at. % W multilayer tape as compared to pure Ni in similar annealed condition. EDS analysis of the multilayer Ni/Ni-5at. % W tape in the sintered and annealed conditions shows significant amount of W diffusion into the Ni layer which clearly indicates the beneficial effect of W in the development of sharp cube texture in Ni. Analysis of inverse pole figures shows that W increases the volume fraction of the cube component in Ni by decreasing the volume fraction of RD-rotated cube grains. The results obtained indicate that powder metallurgy processing can be effectively used to prepare highly textured substrates for coated superconductor applications.

1. INTRODUCTION

The RABiTSTM process developed at ORNL, USA demonstrated the huge potential of using highly cube textured ($\{100\} \langle 001 \rangle$) nickel base alloy tapes for coated high temperature superconductor applications [1-3]. In the RABiTSTM method FCC polycrystalline metals or alloys are cold rolled to high deformation and annealed subsequently to develop a sharp cube texture. The notation for the cube texture has been shown in Figure 1. The implication of such high degree of grain alignment is that the grain boundaries will be of low angle type only. It is mandatory to eliminate the presence of high angle boundaries as they offer resistance to the supercurrent flow (weak links) when buffer and high temperature superconducting layers are epitaxially grown on such substrates [4, 5]. Pure Ni is not considered suitable for such applications due to its low mechanical strength in the annealed condition. Hence, the focus has gradually shifted to developing substrates using Ni base alloys with improved mechanical strength. However, alloying elements and presence of impurities are detrimental to the cube texture formation in pure metals [6]. For example, as little as 0.6 at. % Mg suppresses the cube texture formation in Ni [7]. Minor impurity concentration like S even in 100 ppm level can be effective in suppressing the cube texture in Ni after cold rolling and annealing [8]. Ni base alloys, particularly,

Ni-W alloys have generated much research interest due to the possibility of developing a strong cube texture coupled with improved mechanical strength after annealing. Recently, tapes with multilayer architecture have been suggested where backup layers are used to provide strength to outer layer consisting of pure metals [9]. Such a multilayer tape can develop sharp cube texture in the outer layer and it has better mechanical property compared to the pure metal owing to the stronger backup layer. Tapes with multilayer architecture have been prepared by making a preform of one materials inserted into another followed by hot rolling of the preform to form the mechanical bonding followed by intense cold rolling and final annealing treatment to make the final tape. Most of the alloys for investigations so far have been prepared by the traditional melting and casting route. However, the melting and casting route can inadvertently introduce some impurities which may degrade the intensity of the cube texture after cold rolling and annealing as already mentioned. Greater control over the material purity is possible in the powder metallurgy route starting with very pure initial powders. Despite its advantages development of recrystallization textures in powder metallurgically processed materials, in general, has not been studied to any significant extent. One of the reasons could be that the P/M processing is mostly a near net shape processing route and hence cold rolling of sintered compacts is not very common. In addition, a high amount of rolling

DEVELOPMENT OF TEXTURED SINGLE LAYER AND MULTILAYER COATED SUPERCONDUCTOR SUBSTRATES BY THE POWDER METALLURGY ROUTE

reduction in sintered compacts may be particularly difficult to achieve due to the presence of residual pores. Hence, the possibility of formation of a strong cube texture after heavy cold rolling and annealing in a powder metallurgically prepared alloys remains an issue at large. The current work explores the possibility of preparing single layer Ni-5at.%W and multilayer Ni/Ni-5at.% W substrate tapes using the P/M route and the role of addition of W on the development of deformation and recrystallization textures in pure Ni.

2. EXPERIMENTAL

The important characteristics of the Ni and W powders used in this study are summarized in Table 1. Figure 2 shows the SEM micrographs of the Ni and W powders used in this study. Pure Ni and Ni-5at.% W alloy was prepared by mixing constituent powders in appropriate proportion. The powders were compacted uniaxially at 250 MPa in a die of rectangular cross-section of dimension 8mm × 25mm. The green compacts were sintered at 1100°C for one hour in flowing H₂ atmosphere. A multilayer compact of configuration Ni/Ni-5at.% W was made by a process shown schematically in the flow diagram of Figure 3. The sintered compacts were cold rolled to 95% thickness reduction (~120-140µm final thickness). Small pieces of the cold rolled tapes were cut and annealed in vacuum (~10⁻⁵ torr) at various temperatures for one hour. For pure Ni the annealing temperatures were between 500° to 800°C and for the Ni-5at.% W alloy they were between 800° to 1250°C. The Ni/Ni-5at.% W multilayer tape was annealed at 500°C only. Samples for optical metallographic purpose were prepared using standard sample preparation techniques. The global textures of the cold rolled tapes were measured with a Siemens D5000 texture goniometer using Co K α radiation ($\lambda = 1.789 \text{ \AA}$). Due to high defect density in the cold worked state the Kikuchi patterns from cold worked materials are often very diffused and unambiguous indexing of the patterns may be difficult to achieve. Hence, bulk texture analysis through x-ray diffraction was preferred over microtexture analysis through EBSD for the cold worked materials. Samples of approximate dimension 10mm × 14 mm were used for this purpose. The {111}, {200}, {220} and {311} pole figures were measured and the orientation Distribution functions (ODFs) were calculated from them using the series expansion method of Bunge ($l_{\max} = 22$) [10]. Microtextures of the annealed samples after careful electropolishing were determined by a fully computer controlled automated Electron Back Scattered Diffraction (EBSD) system (beam scanning mode) attached to a FEI scanning electron microscope (QUANTA 200) operated at 20 KV using TSL OIM Analysis V 4.0 software. Step sizes (distance between two successive points from where

patterns are collected) were chosen depending on the average grain sizes of the annealed samples such that Kikuchi patterns from at least 2-3 points per grain are collected and indexed. Volume fractions of the different orientations in all cases were determined with a tolerance of 15 about the ideal positions of the respective orientations.

3. RESULTS AND DISCUSSION

Figures 4 (a) and (b) show pure Ni and Ni-5at.% W alloy in the as sintered and final cold rolled condition and (c) and (d) the corresponding optical micrographs of the cold rolled tapes. The microstructures show elongated grains typical of cold rolled materials. Figures 5 (a) and (b) show the constant $\phi_2 = 0^\circ, 45^\circ$ and 65° sections of the ODFs of pure Ni and Ni-5at.% W alloy in the cold rolled condition determined through X-ray diffraction. These particular sections of the ODFs have been chosen because of the fact that important texture components in the cold rolled FCC materials appear in these sections only. Figure 6 shows the volume percentages of the different texture components of pure Ni and Ni-5at.% W alloy in the cold rolled condition determined from their respective ODFs. It has long been established that the addition of most of the alloying elements to Ni reduces the stacking fault energy (SFE) which influences the rolling texture and subsequently the recrystallization texture upon annealing. High and Medium stacking fault energy FCC materials tend to develop a pure metal or copper type rolling texture. In contrast, low SFE materials develop a prominent brass type rolling texture. Ray [11] has studied this 'texture transition' behavior in the Ni-Co alloy system as a function of SFE. In fact, high alloying addition may completely suppress the cube component after recrystallization. However, here in case of Ni-5at.% W alloy the 'texture transition' phenomena has not taken place which is evident from both Fig. 6 and Fig. 7. Figure 7 shows the volume percentages of the cube component in pure Ni and Ni-5at.% W alloy in different heat treated conditions determined through EBSD. It can be seen from the figure that the volume fraction of the cube component has increased with increasing annealing temperatures in both pure Ni and Ni-5at.% W alloy. However, the cube volume fraction in the Ni-5at.% W alloy is much higher than in pure Ni. Figures 8(a) and (b) show the $\phi_2 = 0^\circ$ (the cube component appears in the $\phi_2 = 0^\circ$ and 90° sections of the ODFs) sections of the ODFs of pure Ni after annealing at 800°C and Ni-5at.% W alloy after annealing at 1100°C and (c) and (d) the corresponding orientation maps showing the cube oriented grains and their twins ($\{221\} \langle 122 \rangle$) in different colors and their spatial distributions through the microstructures. These particular temperatures were chosen for comparison as they correspond to the highest volume fractions of the cube

component in their respective classes. It may be seen from the ODFs that there is some amount of scatter of the cube component around the rolling direction (RD) in pure Ni. However, in case of Ni-5at.% W alloy the cube component is rather sharp and perfect. From the orientation maps it may be seen that the twin volume fraction is higher in Ni-5at.% W alloy indicating that Ni-5at.% W alloy is more prone to annealing twin formation. Figures 9(a) and (b) shows the orientation maps of pure Ni after annealing at 500°C and Ni/Ni-5at.% W multilayer tape after annealing at 500°C measured on the Ni side depicting the cube oriented grains and their twins. It can be seen that the volume fraction of the cube component is significantly higher on the Ni side in the Ni/Ni-5at.% W multilayer tape. Figure 10(a) shows the cross-sectional EDS analysis of the Ni/Ni-5at.% W multilayer tape after annealing at 500°C. It can be easily seen from the figure that W has diffused from the Ni-W side to the pure Ni side since it has high diffusivity in Ni. In fact, the diffusion of W has occurred during the sintering stage itself which can be easily seen from the cross-sectional x-ray area mapping of the multilayer compact (see Figure 10(b)) depicting the distribution of W. It can thus be inferred that W in solid solution in Ni increases the volume fraction of the cube component after cold rolling and annealing. In order to understand the reason behind the beneficial effect of W in increasing the cube volume fraction of Ni after cold rolling and annealing the EBSD datasets of Ni after annealing at 800°C and Ni-5at.% W alloy after annealing at 1100°C were partitioned. The partitioned datasets consisted only of the off-cube grains (>15° misorientation with the exact cube orientation in the Euler space). Figures 11(a) and (b) shows the inverse pole figures calculated from these datasets. Inverse pole figures give an idea about crystal directions which are aligned with a particular reference direction for e.g. the ND, TD or RD. Accordingly inverse pole figures of RD, TD or ND may be constructed. It can be seen from in the inverse pole figures of RD that in both this materials most of the off cube grains have their RDs parallel to a [100] direction. However, both TDs and NDs were away from a [100] direction. This implies that the grains must have been rotated about the RD, that is, most of the off cube grains are actually RD rotated cube grains. From the intensities of the contour lines it can be seen that in Ni-5at.% W alloy the fraction of RD rotated cube grains are smaller than in pure Ni. Figure 12 shows the orientation map of Ni-5at.% W alloy after annealing at 1250°C depicting the cube oriented grains and their twins. It can be seen that most of the grains are either cube oriented or their twins. The volume fraction of the cube component at this stage is almost 90% indicating that Ni-5at.% W can be textured to a very high degree and the cube texture is stable upto very high annealing temperatures which renders it

suitable for epitaxial deposition of the buffer and superconducting layers. Further in the figure an off cube grain has been marked with 'R'. The crystal direction parallel to the RD for this grain is only 1.2° away from a [100] direction which shows that it is actually a RD rotated cube grain.

4. CONCLUSIONS

Ni-5at.% W alloy develops a much sharper cube texture after cold rolling and annealing as compared to pure Ni although the cold rolling textures in these materials are similar. A much sharper cube texture on the Ni side of the Ni/Ni-5at.% W multilayer tape as compared to pure Ni in the similar heat treated condition with significant W diffusion into Ni layer detected from EDS studies amply demonstrates that the presence of W in solid solution in Ni is beneficial for the development of the cube texture. W increases the volume fraction of the cube component in pure Ni by decreasing the volume fraction of the RD rotated cube grains. Formation of a very strong cube texture which is stable upto very high annealing temperatures shows that powder metallurgy can be effectively used to prepare single layer and multilayered substrate tapes for coated superconductor applications.

REFERENCES

1. A. Goyal, D. P. Norton, J. D. Budai, M. Paranthaman, E. D. Specht, D. M. Kroeger, D. K. Christen, Q. He, B. Saffian, F. A. List, D. F. Lee, P. M. Martin, C. E. Klabunde, E. Hartfield, and V. K. Sikka, *Appl. Phys. Lett.* 69 (1996) 1795.
2. D.P. Norton, A. Goyal, J. D. Budai, D.K. Christen, D.M. Kroeger, E.D. Specht, Q. He, B. Saffian, M. Paranthaman, C.E. Klabunde, D.F. Lee, B.C. Sales, and F.A. List, *Science* 274 (1996) 755.
3. A. Goyal, S.X. Ren, E.D. Specht, D.M. Kroeger, R. Feenstra, D. Norton, M. Paranthaman, D.F. Lee and D.K. Christen, *Micron* 30 (1999) 463.
4. D. Dimos, P. Chaudhari, Mannhart J., and F.K. LeGoues, *Phys. Rev. Lett.* 61 (1998) 219.
5. S. E. Babcock, X.Y. Cai, D.L. Kaiser and D. C. Larbalestier, *Nature* 347 (1990) 167.
6. R.E. Smallman, *J. Inst. Metals* 84 (1955-56) 10.
7. K. Detert, G. Dressler, *Acta Metall.* 13 (1965) 845.
8. E.D. Specht, A. Goyal, D.F. Lee, F.A. List, D.M. Kroeger, M. Paranthaman, R.K. Williams and D.K. Christen, *Supercond. Sci. Technol.* 11 (1998) 945.
9. V.S. Sarma, J. Eickemeyer, A. Singh, L. Schultz, B. Holzapfel, *Acta Materi.* 51 (2003) 4919.
10. H. J. Bunge, in: *Mathematische Methoden der Texturanalyse*, Academic Press, Berlin, 1969.
11. R.K. Ray, *Acta Metall. Mater.* 43 (1995) 3861.

DEVELOPMENT OF TEXTURED SINGLE LAYER AND MULTILAYER COATED SUPERCONDUCTOR SUBSTRATES BY THE POWDER METALLURGY ROUTE

Table 1: Important Characteristics of the Ni and W powders

Powder	Ni	W
Vendor	Sigma-Aldrich	Teledyne Advanced Materials
Purity	99.99%	99.6%
Shape	spiky	irregular
Particle Size, μm		
D10	3.9	1.2
D50	9.7	5.6
D90	26	13.0

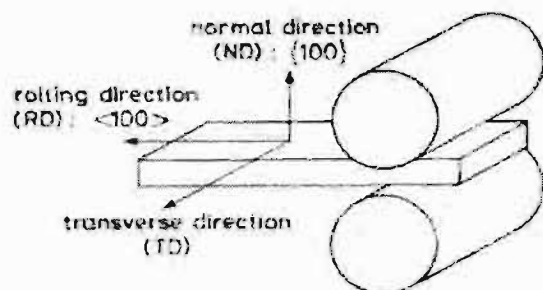


Figure 1: Notation for the cube orientation

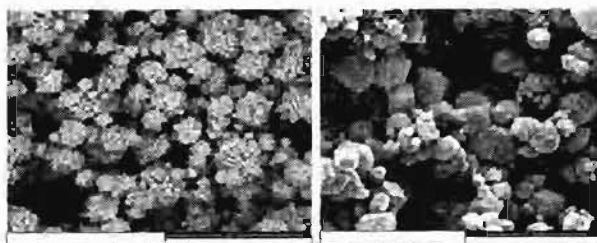


Figure 2: SEM micrographs of (a) Ni and (b) W powders.

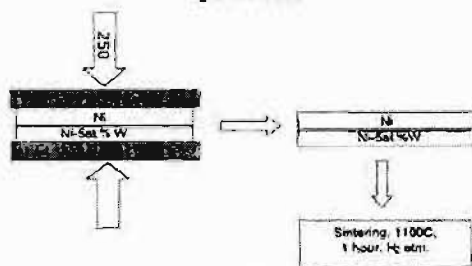


Figure 3: Flow diagram of the multilayer Ni/Ni-5at.% W compact preparation.

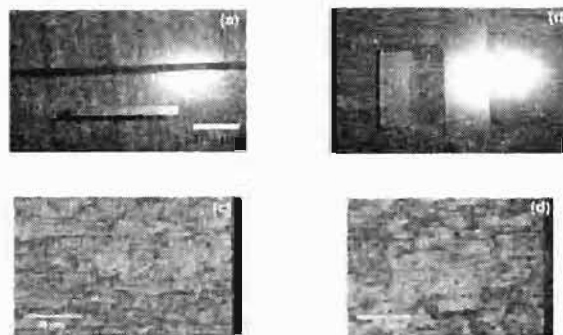


Figure 4: Macrographs of sintered compacts and cold rolled tapes of (a) pure Ni and (b) Ni-5at.% W alloy and optical micrographs of cold rolled (a) pure Ni and (b) Ni-5at.% W alloy.

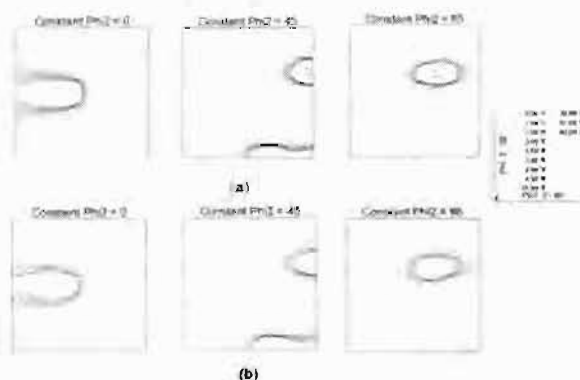


Figure 5: The constant $\Phi_2 = 0^\circ, 45^\circ$ and 65° sections of the ODFs of (a) pure Ni and (b) Ni-5at.% W alloy in the cold rolled condition (legends are the intensities of the contour lines).

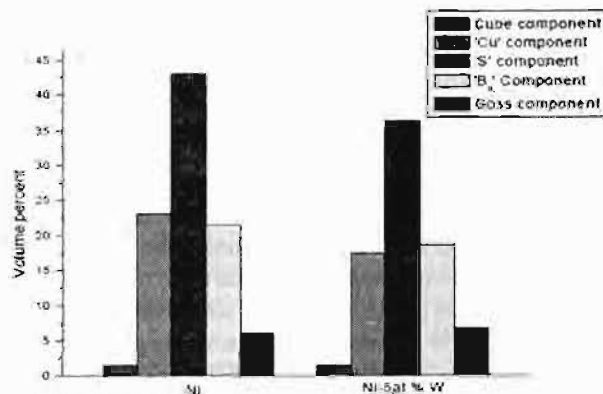


Figure 6: Volume percentages of different rolling texture component in pure Ni and Ni-5at.% W alloy.

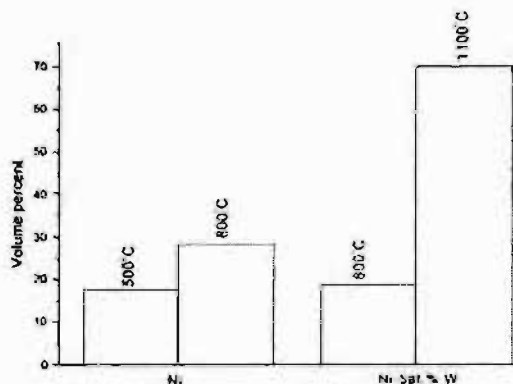


Figure 7: Volume percentages of the cube component in pure Ni and Ni-5at.% W alloy in different heat treated conditions.

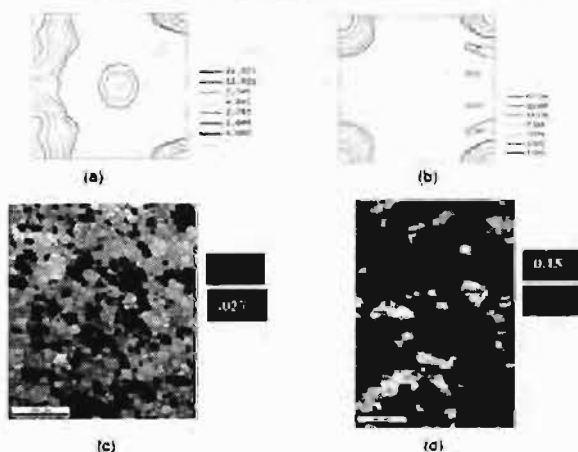


Figure 8: $\bar{O}2 = 0^\circ$ sections of the ODFs of (a) pure Ni after annealing at 800 C and (b) Ni-5at.% W alloy after annealing at 1100 C (legends are the contour lines) and (c) and (d) are the corresponding orientations maps depicting volume fractions of the cube oriented grains (blue) and their twins (red).

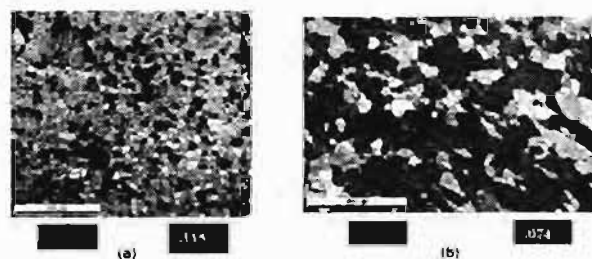


Figure 9: The orientation maps of (a) pure Ni after annealing at 500 C and (b) Ni side of the Ni/Ni-5at.% W multilayer tape after annealing at 500 C depicting volume fractions of the cube (blue) oriented grains and their twins (red).

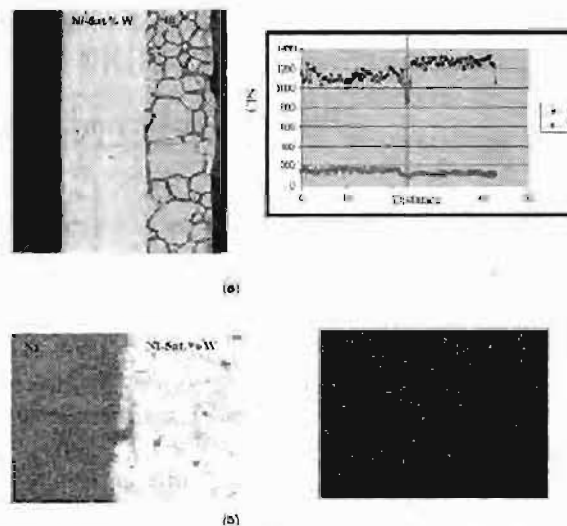


Figure 10: (a) cross sectional EDS analysis in the line mode (direction of beam travel is from the Ni-W side to the Ni side along the line in left figure) of Ni/Ni-5at.% W multilayer tape after annealing at 500 C showing the concentrations (given in terms of CPS) of Ni and W (right figure, position of the red line in the plot indicates the interface) and (b) x-ray mapping taken from an cross sectional area (left figure) of the sintered multilayer compact showing distribution of W (right figure).

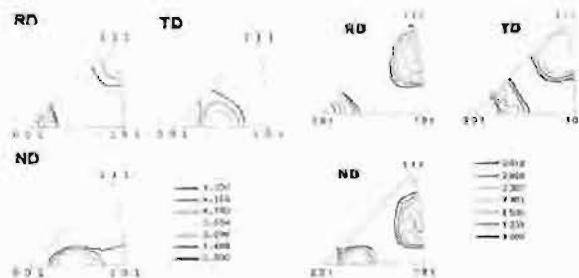


Figure 11: Inverse pole figures of the off cube grains of (a) pure Ni after annealing at 800 C and (b) Ni-5at.% W alloy after annealing at 1100 C (legends are the intensities of the contour lines).

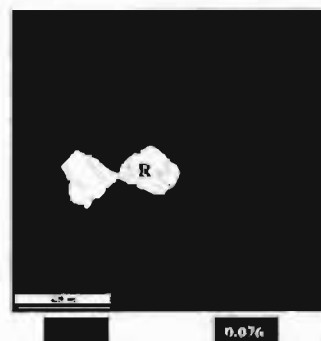


Figure 12: The orientation map of Ni-5at.% W alloy after annealing at 1250 C depicting the volume fractions of the cube oriented grains (blue) and their twins (red). A RD oriented cube grain has been marked with R.

POWDER SURFACE AREA REDUCTION AS A MEASURE OF EXTENT OF AGGLOMERATION

Palanki Balakrishna, M Anuradha and B Narasimha Murty

Nuclear Fuel Complex, Hyderabad 500 062.

ABSTRACT

Agglomerates are irregularly shaped clusters of particles present in ceramic powders. Their presence causes packing difficulties in the compaction die resulting in non-uniform and incomplete densification on sintering. Uranium dioxide powders suitable for compaction and sintering are usually made through the aqueous chemical route involving precipitation, drying, calcination and reduction. While conditions favourable for the formation of agglomerates can exist in the precipitation stage, conditions for their strengthening exist in subsequent thermal treatments. The change in BET specific surface area of calcined U_3O_8 upon reduction to UO_2 is a simple new measure, to quantify the degree of agglomeration in uranium dioxide powders.

1. AGGLOMERATES & GRANULES

The driving force for sintering being reduction in surface energy, it is essential to have as fine a starting powder as possible. Fine powders, however, tend to agglomerate into larger entities. 'Agglomerates' and 'granules' are both terms, which refer to particle clusters as against individual particles. 'Granules' are somewhat rounded particle clusters that are deliberately made in a specified size and density ranges as a process requirement, to improve the flow properties and packing efficiency [1,2]. On the other hand, 'agglomerates' are particle clusters of irregular shape and uncontrolled size, which hinder flow properties and cause packing problems during die filling for compaction. The poor packing of powders containing agglomerates results in several types of defects in the green and sintered compacts.

2. AGGLOMERATE TYPES

There are 'weak' or 'soft' agglomerates as well as 'strong' or 'hard' agglomerates. In soft agglomerates, the primary particles are held together by short-range surface forces. Van der Waals forces arise from electron motion within the atoms and protrude beyond the surface of the particle [3]. In hard strong agglomerates, the constituent particles are held by solid bridges, which are formed as a result of sintering, fusion, chemical reaction or setting of a binder

[4]. The most common type of agglomerate in a ceramic powder is one bonded by a diffusion bond formed during calcination. Such agglomerates are strong enough to retain their identity during green shaping.

The effects of agglomerates in ceramic processing have been reviewed [5]. The sintered density of cold pressed and sintered yttrium stabilized zirconia decreased as the agglomerate size was increased, whereas centrifugal cast material, which was free from agglomerates, sintered to near theoretical density [6]. Agglomerates in alumina powder were found to limit densification [7,8]

In the case of uranium dioxide too, defects in sintering have been attributed to the presence of agglomerates in the powder [9]. Early remedial measures included milling [10]. Ball milling, jet milling and attritor milling [11] have all been used. However, difficulties in containment of air radioactivity led to process innovations that give agglomerate free fine powders without the need for milling [12-14].

3. AGGLOMERATION PARAMETER

Several attempts have been made to quantify the extent of agglomeration in ceramic powders. Balek [15] defined an agglomeration factor as:

$$AF_{50} = \text{avg. aggl. Dia. (Coulter counter)} / \text{equiv. spherical dia. of crystallites (BET)}$$

POWDER SURFACE AREA REDUCTION AS A MEASURE OF EXTENT OF AGGLOMERATION

An agglomeration factor of the order of 1 corresponds to complete de-agglomeration while higher values indicate increased agglomeration. Roosen and Hausner [16] defined agglomeration parameter as the ratio of the median agglomerate size to the corresponding particle size. The particle size may be measured from a scanning electron micrograph.

The green density and the sintered density of zirconia decreased as the agglomeration parameter increased [17,18].

Since it is the coarse fraction of the powder that limits its ability to be sintered to theoretical density, another agglomeration factor AF_{10} was defined [19]

AF_{10} = dia. that 10% of aggl are larger than (Coulter counter) / equiv. spherical

dia. of crystallites (BET)

For one type of nuclear fuel pellets, where 100% densification is not desired and microstructural requirement not stringent, agglomerates smaller than 44 microns (-325#) are considered acceptable and the agglomeration factor is taken to be [20]:

$AF = (\text{percent quantity retained on 325\#}) / (d_{30}/44)$,

where d_{30} is the median particle cluster size above 44 microns.

German [21] defined an agglomeration number

$N_A = (D_{AM} \rho s)^3 / 2620$

where D_{AM} is the agglomerate median size (D_{50} on the cumulative particle size distribution) in μm as reported on a mass basis from laser light scattering, sedimentation, sieving, or time of flight measurements. The BET specific surface area s is in m^2/g and the pycnometer density ρ is in g/cm^3 . In this form the conversion factors cancel, giving

6. RESULTS

the number of particles in a typical agglomerate as directly calculated from the BET adsorption surface area, pycnometer density, and median particle size.

4. A NEW AGGLOMERATION PARAMETER

Highly sinterable fine ceramic oxide powders are usually made through the aqueous chemical route. The precursor precipitate is dried and calcined to get the oxide powder. The specific surface area decreases on calcination. We define a new agglomeration parameter for a ceramic powder as the reduction in surface area per unit increase of thermal treatment temperature.

Aggl. parameter = $\Delta s / \Delta T = (s_{T_1} - s_{T_2}) / (T_1 - T_2)$

Where s_{T_1} is the BET specific surface area of the powder when calcined at temperature T_1 and s_{T_1} and s_{T_2} is that when calcined at temperature T_2 . In the case of preparation of uranium dioxide powder, there are three thermal treatments in succession for the precursor ammonium diuranate, namely, drying, calcination in air and reduction in hydrogen. The product of calcination is U_3O_8 and the product of reduction is UO_2 . Here, the agglomeration parameter may be defined as

Aggl. parameter = $(s_{T_{\text{calcin}}} - s_{T_{\text{reduction}}}) / (T_{\text{calcin}} - T_{\text{reduction}})$

5. EXPERIMENTAL

In this paper, the agglomeration parameter as defined above, has been evaluated for powders supplied by two different vendors using the data furnished by the vendors and correlated with the sintered density. About 10 tons of powder from each vendor has been taken into account. The powder consists of lots of each about 500 kg, for which a set of process parameters such as calcination temperature, reduction temperature, U_3O_8 specific surface area, etc are recorded in a lot travel card. The travel cards of the material have been scrutinized for values of different parameters.

Table 1: Process Parameters of Vendor 'A' and calculated Agglomeration Parameter

Lot No	Calcination Temperature °C	Surface area U_3O_8 $\text{cm}^2/\text{g}^{-1}$	Reduction temperature °C	Surface area UO_2 $\text{cm}^2/\text{g}^{-1}$	sintered density g/cm^3	Aggl. parameter $\text{cm}^2/\text{g}^{-1} (\text{°C})^{-1}$
A-01	720	37600	590	32400	10.66	40
A-02	720	36500	590	32100	10.68	34
A-03	730	34100	580	26900	10.71	48
A-04	730	34200	580	26600	10.72	50.7
A-05	730	35000	580	27300	10.69	51.3
•	•	•	•	•	•	•
•	•	•	•	•	•	•
A-20	730	32000	560	26700	10.70	31.2

POWDER SURFACE AREA REDUCTION AS A MEASURE OF EXTENT OF AGGLOMERATION

Table 2: Process Parameters of Vendor 'B' and calculated Agglomeration Parameter

Lot No	Calcination Temperature °C	Surface area U_3O_8 cm^2g^{-1}	Reduction temperature °C	Surface area UO_2 cm^2g^{-1}	sintered density g.cm^{-3}	Aggl. parameter $\text{cm}^2\text{g}^{-1} (\text{°C})^{-1}$
B-01	660	37600	600	29000	10.62	143
B-02	680	38800	575	31600	10.62	68
B-03	675	41500	575	35000	10.51	65
B-04	675	44100	600	35900	10.64	109
B-05	665	41900	600	31400	10.64	161.5
•	•	•	•	•	•	•
•	•	•	•	•	•	•
B-20	670	41500	600	32100	10.59	134

Relation between Sintered Density and Agglomeration Parameter

Vendor	Avg. Sintered density g.cm^{-3}	Avg. Agglomeration Parameter $\text{cm}^2\text{g}^{-1} (\text{°C})^{-1}$
A	10.69	37
B	10.61	108

7. DISCUSSION

In the process of sintering of a powder compact, necks form at the contact points and grow, and the particle centers move towards each other, causing densification of the compact. On the other hand, in the case of loose powder, there is no compaction pressure to cause particle contacts necessary for neck formation. However, those particles which happen to be in contact with each other can develop necks, resulting in strongly bonded particle clusters. For a single sphere, there is no driving force for surface area reduction. For two spheres in contact, there is a driving force for neck formation and growth by surface diffusion. Thus neck formation, which is essential in compact sintering is unwanted in powder calcination. In the case where the particles exist independent of each other without clustering together, on heating, there is only a small change in surface area, by way of particle rounding. There can be no neck growth due to absence of contact between the particles. On the other hand, if the particles are in contact, reduction in surface area may be expected due to neck formation and growth.

The powder lots of vendor 'B' exhibited a higher agglomeration parameter than those from vendor 'A'. The mean sintered density of the powder lots from vendor 'B' is also found to be less than that of vendor 'A'.

There are a few differences in the process equipment of the two vendors. Vendor 'B' used a turbo-drier that operated at

300 °C for drying the precursor ammonium diuranate, while Vendor 'A' used a spray drier that operated at 120 °C. The spray drier seems to have given a less agglomerated ammonium diuranate (ADU) precursor that finally resulted in a less agglomerated UO_2 powder.

The draw back of the present work is that the data from several presses and sintering furnaces have been analysed, with the possibility of variation from press to press and furnace to furnace. A clear-cut correlation can not be expected due to the absence of controlled small-scale experiments. However, a clear difference is seen in the two powders, with respect to degree of agglomeration and sintered density.

8. SUMMARY

A new agglomeration parameter for ceramic powders, namely, change in specific surface area per unit temperature gradient in thermal processing, has been proposed. In the case of UO_2 , the change in BET specific surface area from U_3O_8 to UO_2 , divided by the difference between the calcination and reduction temperatures is taken to be the agglomeration parameter. The UO_2 powder supplied by one vendor was found to exhibit a higher agglomeration parameter and a lower sintered density relative to that of another vendor.

POWDER SURFACE AREA REDUCTION AS A MEASURE OF EXTENT OF AGGLOMERATION

ACKNOWLEDGEMENTS

The authors are grateful to Mr. Kalidas, Chief Executive, Nuclear Fuel Complex and Mr. N Jayaraj, Deputy Chief Executive, for encouraging this work and for permission to present in the form of a paper.

REFERENCES

- [1] Wolfgang Pietsch, "Successfully use agglomeration for size enlargement", *Chemical Engineering Progress*, [4] 1996 (29-45)
- [2] Wolfgang Pietsch, "Granulate dry particulate solids by compaction and retain key powder particle properties", *Chemical Engineering Progress*, [4] 1997 (24-46)
- [3] P. A. Hartley, G. D. Parfitt and L. B. Pol, "The role of the van der Waals force in the agglomeration of powders containing submicron particles", *Powder Technology*, 42[1](1985) 35-46
- [4] G Y Onada and L L Hench, "Physical characterization terminology" in: *Ceramic Processing before Firing*, G Y Onada and L L Hench (Eds), John Wiley, New York, 1970, p.36
- [5] P. Balakrishna, Ajit Singh, B.P.Varma, P.Ramakrishnan, "Particle aggregates in powder processing – a review", *Intercceram* 44 [1] (1995) 18-20
- [6] W H Rhodes, "Agglomerate and particle size effects on sintering yttria stabilized zirconia", *Journal of the American Ceramic Society* 64 [1] (1981) 19-22.
- [7] D.E. Niesz, R.B. Bennet, "Structure and properties of agglomerates" in: *Ceramic Processing before Firing*, G Y Onada and L L Hench (Eds), John Wiley, New York, 1970, p.61-73
- [8] J.W. Halloran, "Agglomerates and agglomeration in ceramic processing" in: *Ultra structure processing of ceramics, glasses and composites*, L.L. Hench, D.R. Ulrich (Eds), John Wiley, New York (1984) pp.404-417
- [9] W.J.S. Craigon, "Some properties of uranium dioxide powders and sintered pellets and their relationships to conditions of preparation", *Eldorado Mining and Refining Ltd. Report No. T62-23*
- [10] *Uranium dioxide: Properties and nuclear applications*, J. Belle (Ed), Naval Reactors, Division of reactor development, USAEC, Washington 1961.
- [11] 'Light attrition of uranium dioxide powder', Palanki Balakrishna, B Narasimha Murty, D V Ratnam, M Anuradha and C Ganguly, *CERAMICS INTERNATIONAL* (Elsevier) 29 [1] (2003) 99-105
- [12] P. Balakrishna, A. Singh, U.C.Gupta, K.K.Sinha, "Agglomerate-free fine ceramic UO₂ powders", in: *Top Fuel'97 British Nuclear Energy Society*, Thomas Telford, London, 1997, republished *Intercceram* 48 [2] (1999) 98-103
- [13] 'Special features in powder preparation, pressing and sintering of uranium dioxide', P Balakrishna, B Narasimha Murty, K P Chakraborty, R N Jayaraj, and C Ganguly, *MATERIALS AND MANUFACTURING PROCESSES* [Marcel Dekker] 15 [5] 2000 (679-693)
- [14] 'Influence of temperature of precipitation on agglomeration and other powder characteristics of ammonium diuranate', B Narasimha Murty, Palanki Balakrishna, R B Yadav and C Ganguly, *POWDER TECHNOLOGY* [Elsevier Publ.] 115 (2001) 167-183
- [15] V Balek, "Temperature dependence of characteristic properties of α -Fe₂O₃ powders", *J. Mat. Sci.* 5 (1970) 714
- [16] A. Roosen and H. Hausner, "Sintering kinetics of ZrO₂ powders", *Advances in Ceramics* 12 (1984) 714-726
- [17] Dean-Mo Liu and Jiang-Tsair Lin, "Influence of ceramic powders of different characteristics on particle packing structure and sintering behaviour", *Journal of Materials Science* 34 (1999) 1959-1972
- [18] Dean-Mo Liu, Jiang-Tsair Lin and W H Tuan, "Interdependence between green compact property and powder agglomeration and their relation to the sintering behaviour of zirconia powder", *Ceramics International* 25 (1999) 551-559
- [19] R.T.Tremper, R S Gordon, "Agglomeration effects on the sintering of alumina powders prepared by autoclaving aluminium metal" in: *Ceramic Processing before Firing*, G Y Onada and L L Hench (Eds), John Wiley, New York, 1970, p.170
- [20] 'Low density phenomena in sintered uranium', P Balakrishna, N P S Katiyar, G V S R K Somayajulu and N K Rao, *TRANSACTIONS OF THE POWDER METALLURGY ASSOCIATION OF INDIA* 11 (1984) 56 - 61.
- [21] Randall M. German, "A measure of the number of particles in agglomerates", *The International Journal of Powder Metallurgy* 32 [4] (1996) 365-373

DERIVATION OF YIELD FUNCTION CONSTANTS FOR MODELING THE PM-COMPACTION

Chidanand. G , Sachin B.M., Thilak B.T., Shashidhar, U.G. Shamasundar S.

ProSIM R&D Center, Bangalore 560096

ABSTRACT

Triaxial tests have been used to derive the yield function and constitutive equations of the powder mass undergoing compaction. The spring back due to elastic recovery of the green is an industrially important parameter which has received very little effort in modeling. The set of experiments conducted included the careful consideration of strain paths to study the elastic behavior during compaction. The bulk moduli, elastic moduli dilation angle and other parameters were derived by experiments. These parameters form a vital component in the FEM analysis of compaction process. Care to be taken in the design of the experiments, need for proper analysis of the experimental data, methodology for derivation of the constants is described in the paper.

1. INTRODUCTION

The compaction of powders to form both bulk materials and net-shaped parts has become a successful and well-established process for metals, alloys, polymers and ceramics. In the powder metallurgy (PM) industry a popular process route is cold compaction by rate-independent plasticity, followed by pressure-less sintering by diffusion flow. In hot pressing, compaction is by power law creep and/or diffusion flow. Although significant empirical progress has been made to optimize compaction procedures with respect to pressure, temperature and time, a concise and general micromechanical model, free from phenomenological assumptions, has been lacking. Early constitutive descriptions have been empirical in nature, with no underlying modeling (see for example, Kuhn and Downey, 1971; Shima and Oyane, 1976). Herein, a micromechanical model is developed for powder compaction by both plasticity and power-law creep, with the relative density in the practical range of 0.6-0.8. The essential physics are the relationship between the macroscopic strain and the local kinematics of particle contact, and the relationship between local contact loads and the resulting macroscopic stress. The model is appropriate for the so-called Stage I regime, with relative density of the compact approximately in the range 0.6-0.8.

The die compaction of powders has been used in manufacturing components for a broad range of applications. In engineering applications, the green compact of uniform density is a fundamental requirement for the production of a good quality and high strength part. Density inhomogeneity can be caused by friction force owing to interparticle movement and relative slip between the powder particles and the die wall. Also, the die geometry and the sequence of punch movement's results in a lack of density homogeneity for a compact of complex shape. Therefore, creating the right tooling design is very important for the success of powder compaction processes.

Generally, the design can be achieved by an empirical approach or a computer aided approach. A computer aided approach offers the designer a computational tool to reduce time and cost for process development, using an appropriate mathematical model to simulate and investigate the compaction process without actually constructing the system. For the computer aided approach, several mathematical models for porous material have been proposed.¹⁻⁵ Lee and Kim⁴ modified a yield criterion for porous material which was suggested by Doraivelu et al.³ and could incorporate one empirical parameter that can be estimated from the yield stress v. initial relative density data. Using the yield criterion, Han et al.⁵ formulated an

elasto-plastic finite element code and analyzed the deformation of sintered metals in simple upsetting, indenting, ring compression, and hot forging.⁷ Also, Han et al.⁸ calculated the forging limit curves of sintered porous metals with the Lee-Kuhn initial imperfection model.⁹

In the case of powder compaction at room temperature, the manner of densification differs from that of sintered porous material. In cold compaction, the densification of a powder compact can be classified into two stages.¹⁰⁻¹² In the first stage, where the arrangement of powder particles changes, powder particles rearrange by sliding and local plastic deformation or fracture at surface irregularities.¹² In the second stage where the relative motion among powder particles is small or negligible, the manner of densification becomes similar to that of sintered porous material.

The shape and initial porosity of powder particles are important material characteristics at the first stage, where sliding and local plastic deformation or fracture plays an important role. Generally, at the initial stage of compaction, the powder compact of high porosity or irregular shape shows low apparent relative density and can be densified more easily than the compact of low porosity or spherical shape. Thus, the effects of particle shape or porosity have to be taken into account in the yield criterion to simulate overall powder compaction. Park et al.¹³ modified the yield criterion suggested by Lee and Kim,⁴ so that the modified yield criterion could successfully incorporate empirical parameters which reflect the characteristics of copper powders of different particle shape during uniaxial compaction.

In the case of ceramic powders, it is not certain that the yield criterion proposed by Park et al.¹³ could be used in analysis of compaction or other densification processes, because ceramic powders have no plasticity. In the present paper, the densification behavior of ceramic powders is analyzed using the yield criterion suggested by Park et al.¹³ The relation between parameters in the yield criterion and morphological and mechanical characteristics of ceramic powders is investigated. Also, the elasto-plastic finite element calculation is carried out to simulate the uniaxial compaction process of ceramic powders.

2. YIELD CRITERIA

Recall that we say that the material yields when it exhibits an irreversible straining which is sustained once a certain level of the stress distribution is reached. A yield criterion indicates for which combination of stress components transition from elastic (recoverable) to plastic (permanent) deformations occurs.

We will start our discussion with initial yielding and then proceed to discuss how material yielding is sustained. In

one-dimension (Figure.1 (a)) yielding occurs when the uniaxial stress reaches the value of the yield stress Y in tension, i.e. at $\sigma = Y$. When does 'yielding' occurs in multi-axial stress states? (Figure.1 (b))? The answer is given with phenomenological theories called 'yield criteria'. Instead of presenting the requirements and constraints for a general form of a yield criterion, we will here only examine the two most important yield criteria for isotropic materials.

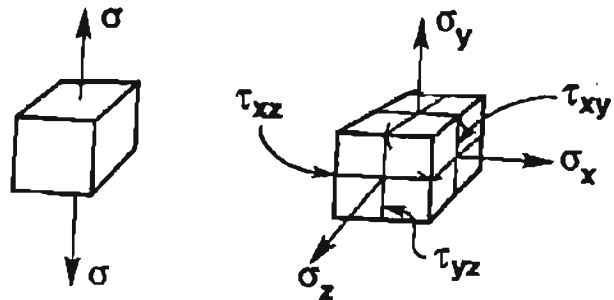


Figure 1: (a) To define yielding in one-dimensional stress states, we compare the uniaxial stress σ with the yield stress in tension Y . (b) When does yielding occurs in multi-dimensions?

3. CONSTITUTIVE MODELS

Constitutive models for the continuum, which include elasticity and several plasticity models like Mohr-Coulomb, Von Mises and Drucker-Prager, the last one coupled with a cap-closure, essential for nonlinear consolidation. A large variety of soils, and even concrete, can be adequately represented by these models. A tension cut-off for materials with limited tensile resistance is also included in most models.

In addition, new developments include a multilaminate model for layered media, Rankine plasticity and a Hoek-Brown type yield surface.

3.1 Plasticity

The basic plastic models, i.e. Mohr-Coulomb and Drucker-Prager require only the elastic constants E (Young's modulus), ν (Poisson's ratio), the cohesion C and friction angle ϕ .

3.1.1 Mohr-Coulomb criterion (M-C)

The Mohr-Coulomb surface is defined by two-constant C and ϕ . The equation of the criterion in two dimensional stress space is

$$\tau = C + \sigma \tan \phi \quad (3.1)$$

DERIVATION OF YIELD FUNCTION CONSTANTS FOR MODELING THE PM-COMPACTION

The corresponding surface in three-dimensional stress space is characterized by a cone with vertices in the deviatoric cross section. For convenience this surface is replaced by a smooth surface illustrated in Figure 2 [MEN, 1995]²¹ and defined by equations (3.2)

$$f = \frac{1}{2}(3 - \sin \phi)pr(\theta, e) + \sqrt{2} \sin \phi \xi - \sqrt{6}c \cos \phi \quad (3.2.a)$$

with

$$r(\theta, e) = \frac{4(1 - e^2)\cos^2 \theta + (2e - 1)^2}{2(1 - e^2)\cos \theta + (2e - 1)[4(1 - e^2)\cos^2 \theta + 5e^2 - 4e]^{1/2}} \quad (3.2.b)$$

$$e = \frac{3 - \sin \phi}{3 + \sin \phi} \quad (3.2.c) \quad \rho = \sqrt{2J_2} \quad (3.2.d) \quad \xi = \frac{1}{\sqrt{3}I_1} \quad (3.2.e)$$

and J_2 are the fundamental stress invariants.

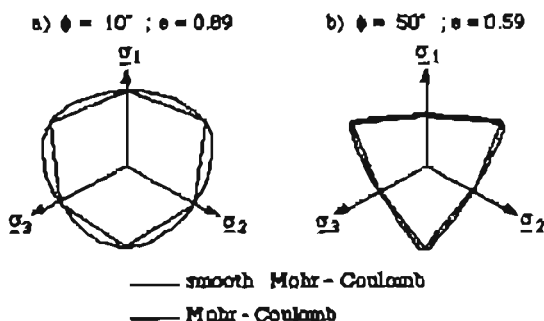


Figure 2 - Smooth Mohr-Coulomb surface [MEN, 1995]²¹

The plastic flow direction is an essential component of the plastic model. The most appropriate flow also may depend on the type of analysis (deformation or ultimate load). Default options are provided to help the user, which for ultimate load analysis will lead to a crisp and reliable capture of failure mechanisms.

3.1.2 Drucker-Prager criterion (D-P)

The Drucker-Prager criterion (Equation 3.3) is more convenient from the point of view of numerical efficiency, it is therefore often preferred to the Mohr-Coulomb criterion.

From the comparison of both D-P and M-C criteria it is obvious that different size adjustments are possible which correspond to different matching of the Mohr-Coulomb parameters C and ϕ with the Drucker-Prager parameters a and k , and this selection obviously affects the yield stress (Figure. 3)

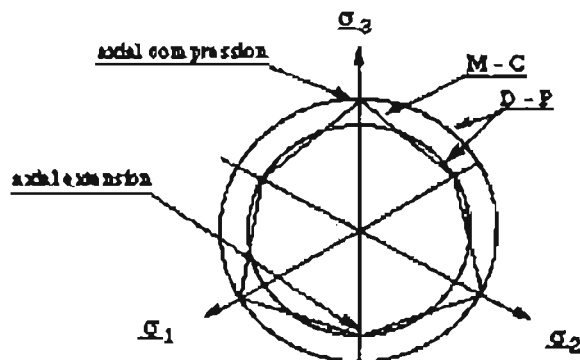


Figure 3 - Deviatoric section of Mohr-Coulomb criterion and Drucker-Prager with two different size adjustments

$$f(\sigma) = aI_1 + \sqrt{J_2} - k = 0 \quad (3.3)$$

I_1 and J_2 are stress invariants and constants a , k can be defined from common geotechnical data: cohesion C and angle of friction ϕ ;

$$a = \frac{\sin \phi}{3} \quad k = C \cos \phi \quad \text{for plane strain and deviatoric flow} \quad (3.3.a)$$

$$a = \left(\frac{\sqrt{3} \sin \phi / (9 - \sin^2 \phi)}{6\sqrt{3}C \cos \phi / (9 - \sin^2 \phi)} \right) \quad k = \left(\frac{6\sqrt{3}C \cos \phi / (9 - \sin^2 \phi)}{6\sqrt{3}C \cos \phi / (9 - \sin^2 \phi)} \right) \quad \text{for isotropy} \quad (3.3.b)$$

The plane strain adjustment corresponds to an adjustment of failure loads.

Cap model

A cap model coupled to the Drucker-Prager criterion is provided for the simulation of nonlinear consolidation. The model requires three additional data from an oedometer test: the initial void ratio e_0 , the vertical stress at yield and λ the compression index which characterizes plastic hardening (Figure 4).

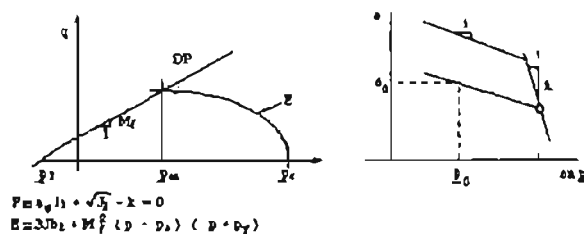


Figure 4.a - Drucker-Prager Model with cap closure
Figure 4.b - Oedometer test

3.1.3 Multilaminar model

One to three weakness planes orientations can be introduced which will remain fixed in space. Each is characterized by

DERIVATION OF YIELD FUNCTION CONSTANTS FOR MODELING THE PM-COMPACTION

a cohesion c^i , a friction angle and a dilatancy (non-associative angle ψ^i). A tensile cut-off can be specified with f_t^i the maximum tensile stress.

On each plane separately, the Mohr-Coulomb plasticity condition and the tension cut-off condition must be fulfilled.

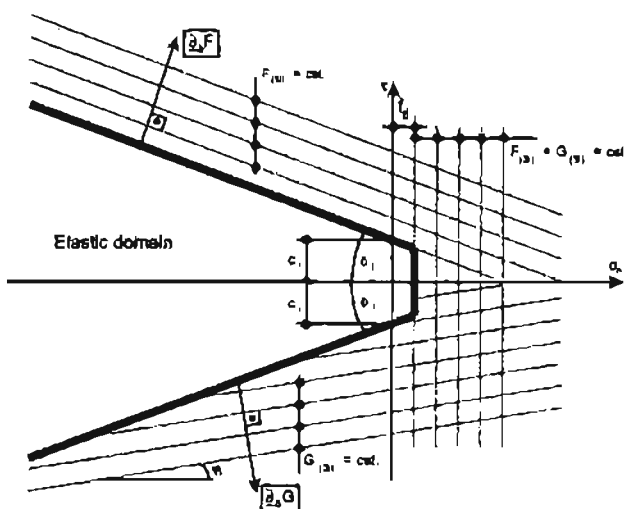


Figure 5 - Weakness plane plasticity conditions, yield function and flow potential isolines

Plasticity and flow rule conditions can be derived for each plane $i=1, \dots, 3$:

$$F^{(1i)} = \tau + \sigma_n \tan \phi^i - c^i$$

$$F^{(2i)} = -\tau + \sigma_n \tan \phi^i - c^i$$

$$F^{(3i)} = \sigma_n - f_t$$

4. EXPERIMENTAL PROCEDURE:

4.1 Index properties

4.1.1 Specific gravity: Specific gravity of the powder is determined as per IS: 2720- Part 3 (1980). The specific gravity of the powder is obtained as 7.18.

4.1.2 Grain size distribution: The grain size distribution of the powder is determined from sieve analysis conducted as per IS: 2720- Part 4 (1985). The powder has 65% of the particles passing through 75 μ sieve and 35% of the particles retained on 75 μ sieve (passing 300 μ sieve). The average size of the particle is close to the size of fine grained silty sand.

4.1.3 Maximum and Minimum dry densities: The minimum dry density of the powder is obtained by loosely pouring the powder into a cylinder of known volume. Maximum dry density under no compressive load is

obtained by vibrating the powder in a vibrating table for 8 mins. The values of minimum and maximum dry densities obtained are 3.7 and 4.4 g/cc respectively.

4.2 Shear Strength Properties

The triaxial compression test is used to determine stress-strain properties and shear strength parameters of the powder. The test is conducted according to IS:2720- Part 11 (1971). The schematic diagram of the test set-up used is shown in Figure 6.

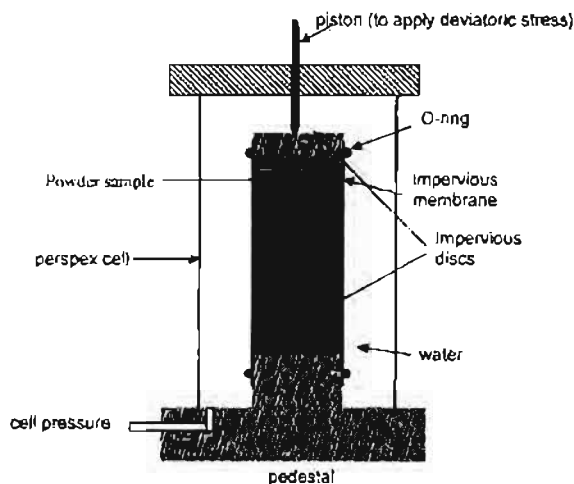


Figure 6. Triaxial compression test set-up

Cylindrical sample of the powder is prepared at a density of 3.7 g/cc for the triaxial test. The sample is 38 mm in diameter and 76 mm in length. Four tests were carried out at four different confining pressures (50, 100, 200 and 300 kPa) on four identical samples (prepared to same density).

Results from Triaxial Tests

The strain and corresponding stress of the sample is plotted with stress abscissa and stress-strain curve for the powder is drawn. The maximum compressive stress at failure and the corresponding strain and cell pressure are found out. The stress-strain curves of the samples obtained from triaxial compression tests at different confining pressures are given in Figure 7. The Mean p vs. q plot for the powder is shown in Figure 8. The failure envelope joining the peaks of p - q plot is also shown in the Figure 8.

$$\text{Mean } p = (\sigma_1 + 2 \sigma_3)/3; \quad q = (\sigma_1 - \sigma_3)/2$$

From the slope of p - q line the angle of internal friction (ϕ) of the powder is obtained as 45° . The powder is cohesionless as the p - q line has no y -intercept. The failure envelope is nonlinear at higher mean pressures.

DERIVATION OF YIELD FUNCTION CONSTANTS FOR MODELING THE PM-COMPACTION

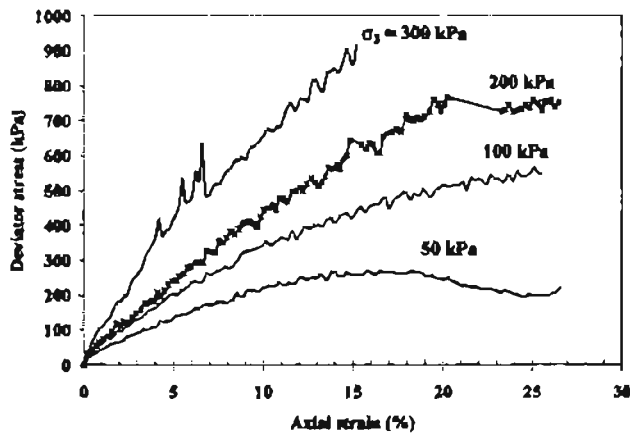


Figure 7. Stress-strain curves for the powder obtained from triaxial compression test

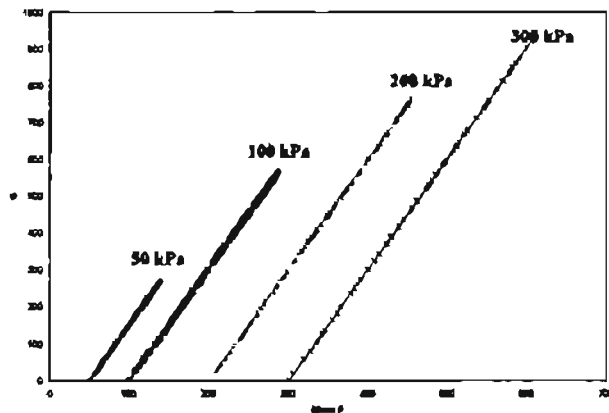


Figure 8. Mean p vs q diagram for the powder

4.3 Compression Properties

One dimensional compression test was carried out on powder in oedometer to determine the deformations in sample under uniaxial one-dimensional compression.

Procedure: Oedometer essentially consists of a steel ring of diameter 60mm and height 20mm in which the sample is prepared, loading device and dial gauge. Loading device consisting of frame, lever system, loading yoke dial gauge fixing device and weights. The powder is poured into the oedometer ring in loosest density. Initial load of 0.05 kg/cm² is applied to the powder sample placed between two end platens and allowed to stand until there is no change in dial gauge readings for two consecutive hours or for a maximum of 24 hours. Final dial reading under the initial load is noted. First load of intensity 0.1 kg/cm² is applied and dial gauge readings are recorded at various time intervals until there is no change in dial gauge reading for 30 minutes. Then the load intensity is doubled and the deformations are measured at time intervals. This procedure

is repeated for successive load increments. The loading intensities applied are: 0.1, 0.2, 0.5, 1, 2, 4 and 8 kg/cm². After the last loading is completed, the load is reduced to 1/4th of the value of the last load and allowed to stand for 1 hr. Then the load is reduced further in steps of 1/4th the previous intensity till an intensity of 0.1 kg/cm² is reached. Final reading of the dial gauge is noted.

Load-deformation Curve: The load deformation curve for the powder obtained from the one-dimensional compression test is shown in Figure 9.

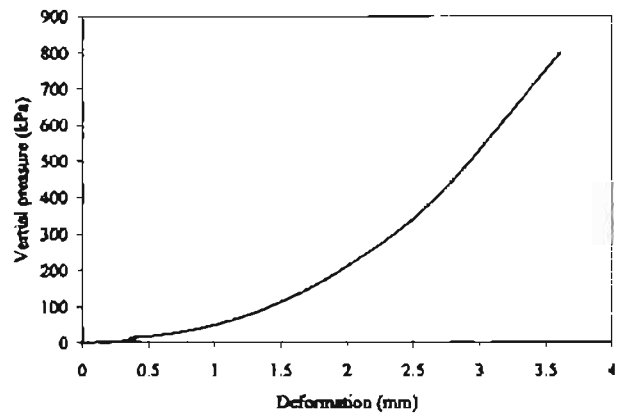


Figure 9. Load-deformation curve from One-dimensional compression test

5. CONCLUSION

The aim of this work was to Derivation of Yield Function for Modeling of PM-Compaction using the triaxial test data which has been developed by the oedometer under uniaxial one-dimensional compression. For developing a methodology for predicting the green density distribution using numerical simulations of powder compaction and of the ejection of the part from the die. This would enable sinter metal, hard metal, and ceramic part producers to optimize the tools and the press kinematics in the computer, before the tool is manufactured and tested, or to detect weaknesses in existing processes. The simpler part of this task is the prediction of the green density distribution.

REFERENCES

1. S. Shima and M. Oyane: Int. J. Mech. Sci., 1976, 18, 285-291.
2. L. Gurson: J. Eng. Mater. Technol. (Trans. ASME), 1977, 99, 2-15.
3. S. M. Doraivelu, H. L. Gegel, J. S. Gunasekera, J. C. Malas, J. T. Morgan, and J. F. Thomas, Jr: Int. J. Mech. Sci., 1984, 26, 527-535.

DERIVATION OF YIELD FUNCTION CONSTANTS FOR MODELING THE PM-COMPACTION

4. D. N. Lee and H. S. Kim: Powder Metall., 1992, 35, 275-279.
5. H. N. Han, H. S. Kim, K. H. OH, and D. N. Lee: Powder Metall., 1994, 37, 140-146.
6. H. N. Han, H. S. Kim, K. H. OH, and D. N. Lee: Powder Metall., 1994, 37, 259-264.
7. H. N. Han, Y. Lee, K. H. OH, and D. N. Lee: Mater. Sci. Eng. A, 1996, 206, 81-89.
8. H. N. Han, K. H. OH, and D. N. Lee: Scr. Metall. Mater., 1995, 32, 1937-1944.
9. P. W. Lee and H. A. Kuhn: Metall. Trans., 1973, 4, 969-974.
10. H. F. Fischmeister, E. Arzt, and L. R. Olsson: Powder Metall., 1978, 21, 179-187.
11. R. L. Hewitt, W. Wallace, and M. C. DE Malherbe: Powder Metall., 1974, 17, 1-12.
12. P. J. James: Powder Metall., 1977, 20, 199-204.
13. S.-J. Park, H. N. Han, K. H. OH, and D. N. Lee: Int. J. Mech. Sci., 1999, 41, 121-141.
14. B. Budiansky: J. Comp. Mater., 1970, 4, 286-295.
15. M. M. Gauthier: 'Engineered materials handbook'. 103; 1995, Materials Park, OH, ASM International.
16. [BOW, 1979] - Bowles J.E. Physical and geotechnical properties of soils, p. 323.
17. [CHE, 1975] - Limit analysis and soil plasticity. Elsevier.
18. [CHE, 1982] - Plasticity in reinforced concrete. Mc Graw Hill.
19. [CHE, 1990] - Chen W.F., Liu W.K. Limit analysis in soil mechanics. Elsevier.
20. [COX, 1961] - Cox A.D., Eason G., and Hopkins H.G. Axially symmetric plastic deformation in soils. Philosophical transactions of the royal society of London, 254, 1-45.
21. [MEN, 1995] - Men  trety Ph., William K. A triaxial failure criterion for concrete and its generalization. ACI Journal 92 (3), pp. 311-318.
22. [SCII, 1969] - Schiffmann R.L., Chen A.T., Jordan J.C. An analysis of consolidation theories. J. of the Soil Mechanics & Foundations Div., vol. 95, No 1, pp. 285-312.
23. [TRU, 1997b] - Truty A., Zimmermann Th., Commend S., Urbanski A., Li Y. Numerical simulation of stability and failure in elasto-plastic layered media. Trans. IACMAG, Wuhan, China, 1997.
24. ABAQUS Analysis User's Manual Volume-III:Materials, Ver. 6.5, HKS Inc., 2005, P. 317-339.
25. ABAQUS Theory Manual, Ver. 6.5, HKS Inc., 2005, P. 115.

GREEN STRENGTH OF METAL SPONGE COMPACTS AND CERAMIC POWDER COMPACTS

Palanki Balakrishna, Pradip Kumar Sahoo, T Gopalakrishna, Tapas Sanyal

Nuclear Fuel Complex, Hyderabad 500 062

ABSTRACT

Zirconium sponge compacts are required to be strong enough to prevent electrode failure by breakage in vacuum arc melting. Green strength is also required in uranium dioxide powder compacts, to withstand stresses during de-tensioning after compaction as well as during ejection from the die and for subsequent handling. The paper examines the factors governing green strength of both zirconium metal sponge and uranium dioxide powder compacts in the light of experimental evidence.

1. INTRODUCTION

Zirconium alloy and uranium dioxide are the two essential ingredients of nuclear fuel. Zirconium is obtained by the reduction of zirconium tetrachloride by magnesium (Kroll's process). The product is vacuum distilled at 900°C to remove residual magnesium and magnesium chloride. By this treatment, the zirconium particles are sintered together and the product is a metallic mass which is cut into pieces and crushed. The zirconium at this stage is a fairly well sintered material and denser than would be expected from the commonly used descriptive term of 'sponge' [1].

Purified uranyl nitrate solution (UNPS) with a concentration of 80 to 120 g/l is taken for batch precipitation with stirring. 8 to 12 N ammonium hydroxide solution is slowly added, first to neutralize free acidity and then to cause precipitation of ammonium diuranate (ADU). The ADU precipitate is filtered, washed, dried, calcined to U_3O_8 and reduced to UO_2 at closely controlled temperatures and heating rates in order to obtain ceramic grade powder [2].

Here, we describe two compaction processes, one concerning zirconium metal sponge and the other concerning a ceramic uranium dioxide powder. The green strength theory is applicable to both metal sponge compacts

and ceramic powder compacts. But there are a few differences. For example, the plastic deformation and cold welding that take place in metal compacts are much lower in the case of ceramic powder compacts. In this paper, the factors governing green strength in zirconium metal sponge compacts are examined along with those of ceramic UO_2 powder compacts in the light of experimental data.

2. THE WEIBULL DISTRIBUTION

When tensile testing is difficult to perform upon brittle materials, a measure of the tensile strength of the material may be obtained by performing a bend test in which tensile stresses develop on one side and compressive stresses on the opposite side. If the material is stronger in compression than tension, failure initiates on the tensile side and, hence, provides information for assessment of tensile strength.

Porous materials and ceramics tested under a three-point or four-point failure test exhibit a distribution of failures [3]. For samples of constant size and shape, the resultant distribution is:

$$\Phi = \exp [(-\sigma/\sigma_0)^m] \dots (1)$$

where Φ is the survival probability at a given stress, σ is the applied stress, σ_0 is the stress at which 1/e (37%) of the samples survive, and m is a parameter called the *Weibull*

GREEN STRENGTH OF METAL SPONGE COMPACTS AND CERAMIC POWDER COMPACTS

modulus. Weibull analysis assumes that (i) All defects are equally likely to be encountered (ii) All defects are independent (iii) There is a fixed, finite number of defects in the components at the start of testing (iv) The number of defects detected in a testing interval is independent of the number detected in other testing intervals for any finite collection of intervals.

Typical sintered ceramics have m values around 8, compared to metallic samples which have m values exceeding 100. On the other hand, green compacts are expected to have much lower m values due to the presence of extensive porosity. The greater the value of m , the steeper the transition from survival to failure. The higher the Weibull modulus is, the more consistent the material (which means that uniform "defects" are evenly distributed throughout the entire volume) and also the narrower the probability curve of the strength distribution. These values are determined for ceramic materials usually using the three or four-point bending method, since measuring the tensile strength of these materials is extremely difficult. We have applied the Weibull method to green compacts of UO_2 tested in compression [4] and to green compacts of metallic zirconium sponge, in three point bend test.

3. EXPERIMENTAL

Experimental zirconium sponge compacts (each weighing about 5 kg) were prepared in rectangular bars 51 x 40 x 500 mm. The load at which the compact fails when loaded as a simply supported beam in a three-point bend strength-testing machine was measured. The green strength was calculated using the expression:

$$\sigma = 3/2 F L / (wh^2) \quad (1)$$

where σ is the strength, h is the height of the compact, w is its width, L is the distance between the two rollers supporting the compact under test and F is the load at which the compact failed.

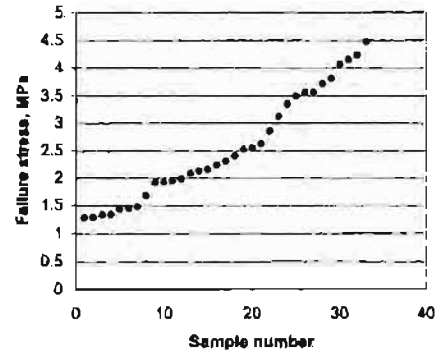
In the case of uranium dioxide, it was not possible to prepare samples as above. Instead, cylindrical compacts of length and diameter 18 mm were used and their crushing strength was determined. For this purpose a hydraulic compression test rig was fabricated in house and the green compacts made from unattrited and attrited uranium dioxide powder were subjected to the compressive stress.

Weibull moduli were determined for the zirconium compacts and uranium dioxide compacts.

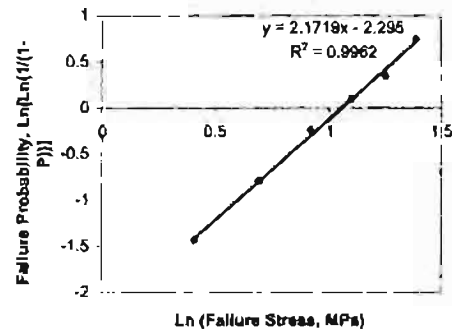
4. RESULTS

The failure stresses as measured for 33 zirconium sponge compacts are shown in Fig. 1 in ascending order and grouped in Table 1.

Fig.1 Failure stresses of Zr compacts in ascending order



Weibull plot for Zirconium sponge compact



Weibull plot for UO_2 green compacts

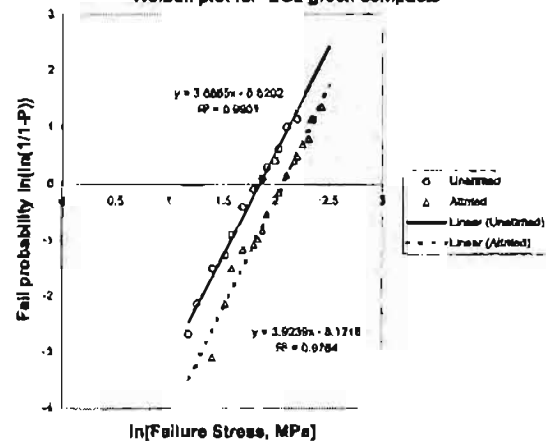


Table 1: Failure probability at different failure stresses

Failure Stress range, MPa	Number of compacts failed	Maximum Failure stress MPa	Number of compacts failed	Failure probability, P
0.5-1.0	0	1.0	0	0
1.0-1.5	7	1.5	7	0.21
1.5-2.0	5	2.0	12	0.36
2.0-2.5	6	2.5	18	0.55
2.5-3.0	4	3.0	22	0.67
3.0-3.5	3	3.5	25	0.76
3.5-4.0	4	4.0	29	0.88
4.0-4.5	4	4.5	33	1

Table 2: Comparison of Weibull slopes and failure stress for 67% failures

	Zirconium sponge	UO ₂ unattrited	UO ₂ attrited
m	2.17	3.69	3.92
σ for P= 0.63	2.88	6.36	7.92

It is seen from the Weibull moduli in Table 2 that zirconium compacts in tension are less reliable than UO₂ compacts in compression. There is an improvement in green strength of UO₂ on light attrition as indicated by the stress values 6.36 and 7.92 MPa for 63% failures.

5. DISCUSSION

5.1 Theories of Green strength

It was earlier believed that the strength of green compacts results mainly from mechanical interlocking of irregularities on the particle surfaces. Newton proved this argument to be false in 1738 when he demonstrated that two polished marbles by immediate contact stick together [5].

Another popular fallacy is that liquid bridges formed by moisture in the capillary gaps between particles are responsible for green strength. However, it has been demonstrated that perfect contacts between spheres are weakened by the presence of wetting fluids [6]. It is now believed that the atomic attraction between smooth, clean solid surfaces is the fundamental cause of green strength [7]. Bradley [8] demonstrated this in 1932, showing that the attractive surface force between two spheres was proportional to their diameter and to their surface energy.

5.2 Rumpf theory:

The strength of a powder compact is taken to be the sum of the attractive forces between individual particles, usually approximating the particles to spheres. The attractive force between two spheres is given by [9-11]

$$F_{at} = A r / 12 l^2 \quad (2)$$

where r is the particle radius, l is the distance between the spheres and A is a constant.

A summation of the attractive forces for a solid occupying a volume with different degrees of packing and space occupancy is taken as the strength of the green body.

$$\sigma = 1.1 \phi F_{at} / \{(1 - \phi) r^2\} \quad (3)$$

where ϕ is the solid volume fraction.

The measured compact strengths are usually lower than predicted, and show considerable variability. This points to the well-known ceramic strength problem, namely the existence of defects in and on the body.

Thus a natural development of theoretical green strength is to follow the theoretical development of mainline-fired ceramic strength and to consider a Griffith type energy balance theory [12]. This has been done by Kendall [13,14].

5.3 Kendall's theory

Two smooth elastic spheres are considered to pull each other into contact by van der Waal's forces, the resulting elastic deformation giving a nonzero contact area. The fracture surface energy is assumed to be the balance of the energy required to separate the two spheres and the elastic strain energy released on their separation.

The general expression for green body fracture energy is given by

$$\Gamma_f = 2.27 \phi^4 [\gamma_{gb}^5 / E^2 r^2]^{1/3} \quad (4)$$

where Γ_f is fracture energy.

Griffith [11] gives the green strength dependence on flaw size as:

$$\sigma = [E \Gamma_f / (\pi c)]^{1/2} \quad (5)$$

where E is the Young's Modulus and c is the flaw length.

Substituting for Γ_f

$$\sigma = 0.85 \phi^2 E^{1/6} \gamma_{gb}^{5/6} / (c^{1/2} r^{2/3}) \quad (6)$$

5.4 Thompson's theory:

Thompson [15] based his model on the premise that the tensile strength on any plane in a green compact is dependent on the real area of inter-particle contacts across the plane. Expressed mathematically, the green strength law is

$$\sigma_{max} = k A_R / A_p \quad (7)$$

σ_{max} is the tensile strength on a given plane, k is a fundamental binding constant, which depends on interparticle attraction (e.g. van der Waal forces), A_R is the real area of particle contact across the planes, and A_p is the apparent area of contact between the planes. Since pressed green powders are only ~ 50% dense, $A_R \ll A_p$. The adjoining planes can be thought of as fracture surfaces (i.e. the surfaces which would be formed if the compact was broken). It is the real area of contact that existed across the fracture surface, prior to fracture, which determines the green strength. From the above, Thompson derived the green strength law as below:

$$\sigma_{max} = (0.742 k P_d / E_p) (R/v)^{1/4} \quad (8)$$

where P_0 is the compaction pressure, E_p is the plastic modulus, related to the yield strength of R is the normalized radius of the interacting particles v is root mean square roughness of the contacting surfaces.

5.5 Inferences from green strength theory

It is seen from the above theories that green strength increases as

- (a) the particles become smaller
- (b) the particles are brought closer
- (c) the volume fraction of the compact is higher (porosity is low)
- (d) elastic modulus and grain boundary energy are high
- (e) flaw size is small
- (f) compaction pressure is sufficiently high for enhanced contact area, but not too high to cause spring back.

These requirements are fulfilled when the metallic sponge or ceramic powder is soft and readily crushable and when high green densities are achievable at moderate pressures.

6. SUMMARY

Green strength is important in zirconium metal sponge compacts used for vacuum arc melting electrodes, not only for handling before melting, but also for safety during melting. The factors influencing green strength of zirconium metal sponge and UO_2 ceramic powder compacts have been studied. For zirconium, the strength was determined by three-point bend test. Zirconium compacts in tension have shown a Weibull modulus of 2.17

Green strength is also important in UO_2 ceramic powder compacts for handling as well as for freedom from post compaction stress relief defects such as end capping and lamination. For UO_2 the strength was determined in compression. Light attrition milling increased the green strength of UO_2 significantly. The Weibull modulus of crushing strength is 3.69 and 3.92 for compacts from unattrited and lightly attrited categories.

REFERENCES

- [1] G L Miller, "Arc melting Kroll zirconium sponge", Vacuum 4 [2] (1954) 168-175
- [2] P. Balakrishna, A. Singh, U.C.Gupta, K.K.Sinha. "Agglomerate-free fine ceramic UO_2 powders", in: Top Fuel'97 British Nuclear Energy Society, Thomas Telford, London, 1997, republished Interceram 48 [2] (1999) 98-103
- [3] Standard Practice for Reporting Uniaxial Strength Data and Estimating Weibull parameters for Advanced Ceramics, ASTM C 1239-94a (American Society for Testing and Materials, Philadelphia, PA, 1994.
- [4] Palanki Balakrishna, B Narasimha Murty, D V Ratnam, M Anuradha and C Ganguly, 'Light attrition of uranium dioxide powder', Ceramics International (Elsevier) 29 (2003) 99-105
- [5] Isac Newton, Opticks (reprinted Dover 1952) 1730
- [6] K.Kendall, Contemporary Physics, 21(1980) 277
- [7] R. Bradley, Philosophical Magazine 7 (1932) 583
- [8] H Rumpf, "The strength of granules and agglomerates" in: Agglomeration, W A Knepper (Ed), Interscience, New York 1962, pp.379-418
- [9] H. Rumpf, *Zur theorie der zug festi gkeit von agglomeraten bei kraftubertragung*, Chem. Ingr. Tech 42 (1970) 538-540.
- [10] H. Schubert, W. Herrman and H. Rumpf, *Deformation behavior of agglomerates under tensile stress*, Powder Technology 11 (1975) 121.
- [11] Hans Rumpf, Particle adhesion in: Agglomeration 77. Vol.1, K V S Sastry (Ed), American Institute of Mining, Metallurgical and Petroleum Engineers, New York 1977, pp.97-129 (Proceedings of 2nd international symposium on Agglomeration, Atlanta, March 6-10, 1977)
- [12] A A Griffith, "The phenomena of rupture and flow in solids", Philosophical Transactions of the Royal Society, A 221 (1920) 163
- [13] K. Kendall, AIP Conference Proceedings No.107, ATP 1984, 78-79
- [14] L.J. Mc Coin and N.J. Clark, Forming, Shaping and Working of High Performance Ceramics, Chapman and Hall, New York, 1988.
- [15] R.A.Thompson, *Mechanics of powder pressing: III, Model for the green strength of pressed powders*, American Ceramic Society Bulletin, 60 (2) (1981) 248-251.

USE OF SODIUM STEARATE IN FABRICATION OF MIXED OXIDE ANNULAR PELLETS FOR FBTR

S.K.Shrotriya, B.K.Shelke, Y.G.Nehete, B. Surendra, K.Subbaraya, M.K.Yadav, Niraj Kumar, A.K.Mishra, P.S.Somayajulu, J.P.Panakkal, H.S.Kamath

Advanced Fuel Fabrication Facility, BARC, Tarapur-401502

ABSTRACT

Advanced Fuel Fabrication Facility is fabricating mixed oxide fuel for different thermal and fast reactors. A number of mixed oxide fuel bundles have been irradiated in BWR and PHWR. PFBR mixed oxide fuel subassembly contains 37 fuel elements for experimental irradiation in FBTR have been supplied. Binder and lubricant materials play a very important role in nuclear fuel fabrication. These materials are required to facilitate compaction. Earlier Zinc Behenate or Zinc Stearate was used as binder cum lubricant in nuclear fuel fabrication. The use of these materials require an intermediate dewaxing step before sintering. In order to avoid intermediate dewaxing step, a combination of Polyethylene Glycol (PEG) and Oleic Acid (OA) in liquid form was used for the fabrication of MOX fuel for hybrid core of FBTR. Sodium Stearate in solid form was also used as binder cum lubricant instead of Polyethylene Glycol and Oleic Acid for the fabrication of PuO_2 rich mixed oxide annular pellets for hybrid core of FBTR. This paper gives comparative study made at Advanced Fuel Fabrication Facility, Tarapur using Sodium Stearate and a combination of Polyethylene glycol and Oleic acid as binder & lubricant in fabrication of mixed oxide fuel for hybrid core of FBTR.

INTRODUCTION

MOX fuel for hybrid core of FBTR was fabricated at Advanced Fuel Fabrication Facility, BARC, Tarapur. The fuel of FBTR contains 44 wt% of PuO_2 and 56 wt% of Nat. UO_2 . The pellets were made in glove boxes using standard powder metallurgical route of cold compaction and sintering. During final compaction, binder is required to provide adequate strength to the pellet and lubrication is required to reduce friction. Previously various binders have been tried as the pellets require to meet stringent quality specifications. Proper choice of binders require to be made as it has considerable bearing in the fabrication of nuclear fuels and profound influence in its in-reactor performance

(1,2). A combination of Polyethylene Glycol and Oleic Acid was used as binder and lubricant respectively⁽³⁾. Sodium Stearate in solid form has many advantages over Polyethylene Glycol and Oleic Acid and was used as binder cum lubricant for the fabrication of MOX annular pellets for hybrid core of FBTR.⁽⁴⁾

EXPERIMENT

Natural UO_2 powder and PuO_2 powder were received from NFC Hyderabad and PREFRE Tarapur respectively. Specific characteristics of both the powders are given in Table No.1 and used for the fabrication of MOX annular pellets for FBTR.

Table No: 1 Characteristics of Raw Materials

Sr. No.	CHARACTERISTICS	Nat. UO_2	PuO_2
i)	Apparent Density (gm/cc)	1.75 ± 0.5	1.75 ± 0.5
ii)	Specific Surface Area (m^2/gm)	2.5 – 3.5	10.0 – 30.0
iii)	Heavy Metal Content	87 % By Wt.	86 % By Wt.
iv)	Moisture Content	0.4% By Wt.	6.5 % By Wt.
v)	Total Impurities	< 500 ppm	< 3000 ppm
vi)	E.B.C	< 1.0 ppm	< 5.0 ppm
vii)	O/M Ratio	< 2.15	< 1.95 – 2.0

USE OF SODIUM STEARATE IN FABRICATION OF MIXED OXIDE ANNULAR PELLETS FOR FBTR

Experimental batches of 200gms with different binder and lubricant addition were prepared as per flowsheet shown in Fig.-1 and processed. The details of the processing and Experimental Batches are given in Table No. 2.

Compaction & Sintering:

Milled powder of all the batches was pre-compacted at 5 TSI in double acting hydraulic press. These pre-compacts were granulated in oscillatory granulator and sieved through # 20mesh. Granules of all the batches were final compacted in rotary press. These pellets were sintered in batch type Molybdenum heating furnace at 1650°C for 4 Hrs. in $N_2 - H_2$ reducing atmosphere. Specifications of mixed oxide fuel pellets of FBTR are given in Tab. No.3.

RESULTS & DISCUSSION:

It was observed that pellets of all the Experimental Batches revealed better results except pellets of Experimental Batch No 2. During final compaction of granules of Experimental Batch No 2, considerable friction was generated at the time of ejection leading to defects in green pellets. It was attributed to presence of high percentage of PuO_2 whereby inherent heat generation and radioactivity combinedly were responsible in the disintegration of binder properties. Hence, Experimental Batch No 2 pellets were fabricated at lower pressure, thereby, leading to reduction in sintered linear mass. The results of the pellets of various batches are given in Tab. No.4.

Table No: 2 - Details of the processing & experimental batches

Sr. No	Details of Batches	Binder	Details of Milling	Storage Time	Binder Addition Over the Granules	Details of Sintering
1.	BATCH No. 1	1.0wt% Polyethylene Glycol (PEG) and 0.8wt% Oleic Acid (OA)	Planetary Ball Mill For 4 Hrs	Nil	Nil	1650°C for 4 Hrs
2.	BATCH No. 2	1.0wt% Polyethylene Glycol (PEG) and 0.8wt% Oleic Acid (OA)	Planetary Ball Mill For 4 Hrs	15 Days	Nil	1650°C for 4 Hrs
3.	BATCH No. 3	1.0wt% Polyethylene Glycol (PEG) and 0.8wt% Oleic Acid (OA)	Planetary Ball Mill For 4 Hrs	15 Days	0.5 wt% of Sodium Stearate	1650°C for 4 Hrs
4.	BATCH No. 4	1.0wt% Sodium Stearate	Planetary Ball Mill For 4 Hrs	15 Days	Nil	1650°C for 4 Hrs

Table No: 3 Specifications of MOX Fuel for FBTR

Sr. No.	CHARACTERISTICS	SPECIFICATIONS
i)	Outer Diameter of the pellet	5.52 ± 0.08 mm
ii)	Inside Diameter of the pellet	1.8 ± 0.20 mm
iii)	Length of the pellet	7.0 mm (Nominal)
iv)	Fuel Stack Length	430.0 ± 1.5 mm
v)	Insulation pellet height	6.0 mm
vi)	Linear Mass of the pellet	2.20 ± 0.1 gm/cm
vii)	Grain Size	5.0 – 50.0 μ m
viii)	Max. size of individual PuO_2 particles	< 100.0 μ m
ix)	O/M Ratio	1.98 - < 2.0
x)	Total Concentration of impurities	< 5000 ppm

USE OF SODIUM STEARATE IN FABRICATION OF MIXED OXIDE ANNULAR PELLETS FOR FBTR

It was observed that Sodium Stearate helped in salvaging the nuclear fuel material stored for long period prior to final compaction and offered flexibility of intermediate addition for meeting enhanced requirement of binder or lubricant during the processing of material compared to liquid binders.

The chemical analysis of sintered pellets of Experimental Batches revealed that the level of metallic and non – metallic impurities were within the specifications and the results are given in Tab. No. 5 and 6.

CONCLUSION

- 1) Sodium Stearate helps in salvaging the nuclear fuel material stored for long period prior to final compaction.
- 2) Addition of Sodium Stearate helps in improving the quality of the green pellets and reducing the friction during final compaction.
- 3) It does not affect the impurities specifications of the pellets and is also fabrication compatible.

Table No: 4

Sr. No.	MOX MATRIX	GREEN LINEAR MASS (gm/cm)	SINTERED LINEAR MASS (gm/cm)	Quality of Pellets
1	BATCH No. 1	1.9 - 2.0	2.1 - 2.37	Good
2	BATCH No. 2	1.8 - 1.9	1.90 - 2.0	Poor
3	BATCH No. 3	1.9 - 2.0	2.1 - 2.40	Good
4	BATCH No. 4	1.9 - 2.0	2.1 - 2.33	Good

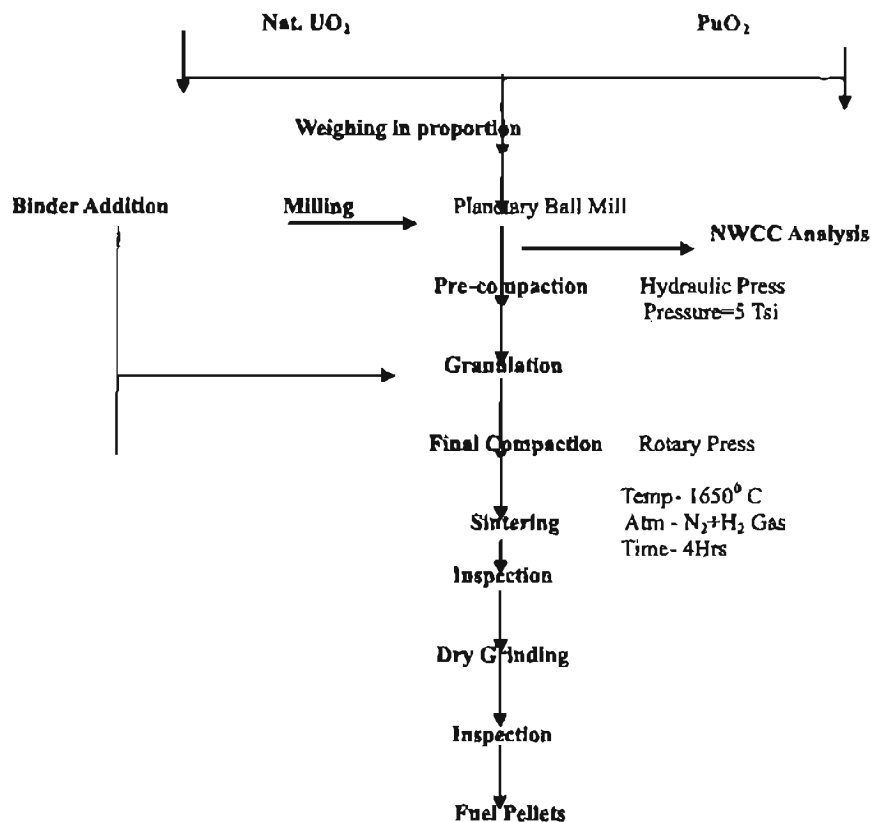
Table No: 5

Sr. No.	MOX MATRIX	NON METALLIC IMPURITIES (in ppm)				O/M Ratio
		C	H	Cl	F	
	Specified Value	500	03	15	10	1.98 - 2.0
1.	BATCH No. 1	124	1.5	8.5	< 1.0	1.99
2.	BATCH No. 2	200	1.9	6.2	< 1.0	1.99
3.	BATCH No. 3	310	2.0	9.0	< 1.0	1.99
4.	BATCH No. 4	432.2	2.4	5.84	1.24	1.99

Table No: 6

Sr. No.	MOX MATRIX	METALLIC IMPURITIES (in ppm)						
		B	Ca	Mg	Mn	Na	Fe	Al
	Specified Value	03	800	800	200	100	1000	500
1.	BATCH No. 1	1.2	180	510	<5.0	14	258	60
2.	BATCH No. 2	1.3	176	585	<5.0	15	312	58
3.	BATCH No. 3	1.5	155	515	5.0	21	725	40
4.	BATCH No. 4	1.6	160	740	<5.0	25	944	28

USE OF SODIUM STEARATE IN FABRICATION OF MIXED OXIDE ANNULAR PELLETS FOR FBTR



Fuel Pellet Fabrication Flow sheet (Fig. -1)

ACKNOWLEDGEMENT

The authors wish to express their sincere thanks to their colleagues at Advanced Fuel Fabrication Facility, for all their help and cooperation during this work.

REFERENCES

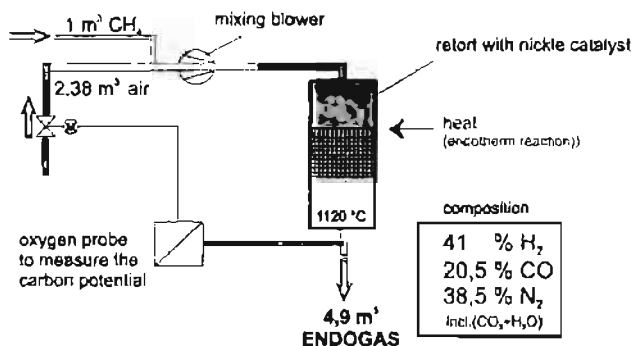
- 1) S. Majumdar, H.S.Kamath, M.N.B. Pillai, R.Ramchandaram and D.S.C.Purushotham "Choice of Proper Powder Lubricant for production of Ceramic Nuclear Fuel Pellets" Transaction of PMAI, Vol 10 (1983) 15-18.
- 2) Abigail S. Branes, James S. Reed, Edward and M. Anderson, "Using Cobindes to improve manufacturability". The American Ceramic Society, Bulletin, 76 [7], 1997, 77-82.
- 3) S.Mishra, S.N.Raul, I.D.Godbole, A.K.Mishra, Arun Kumar and H.S.Kamath "Use of Polyethylene Glycol and Oleic Acid in fabrication of Nuclear fuel pellets" Transaction of PMAI, Vol.-26, 1999.
- 4) P.S.Somayajulu, Y.G.Nehete, P.D.Sugathan, S.Mishra, A.K.Mishra, Arun Kumar and H.S.Kamath "New Techniques in Powder Processing and Pelletisation in Nuclear Fuel Fabrication" Transaction of PMAI, Vol. 27, 2000.

SINTER PROCESSES FOR STEEL P/M COMPONENTS IN VARIOUS FURNACE ATMOSPHERES MAHLER GmbH INDUSTRIAL FURNACES

Rolf Weiss

1. ENDOGAS

Endogas can either be generated in external generators, or what is very common today, directly in the furnace in a built in generator. Both systems possess the same chemical and physical principles; It originates from a partial combustion of hydro-carbons (methane, propane, etc) which are incompletely burnt with lack of air ($\lambda \approx 0,25$).



ADVANTAGES:

- + Obviously, from 1 m³ natural gas there originate about 5 m³ endogas. It also means, if a furnace needs about 50 m³/h protective atmosphere, only 10 m³/h of natural gas are needed, therefore costs are reduced.
- + Endogas is a high energy gas with a high CO and H₂ content. Large energy savings are possible if this energy can be used inside the furnace, e.g. to heat the dewaxing zone (principle of MAHLER rapid dewaxing zone)
- + The carbon potential can be measured inside the sintering zone and automatically controlled. This enables either a carbon-neutral sintering or a controlled carburising or decarburising process.

DISADVANTAGES

- A rather wet gas, therefore it cannot be used for some sinter processes, e.g. it is not suitable for stainless steels
- Requires some special knowledge of the operator (because there is a carbon correlation to the sinter parts)

- When mixed with air due to large content of H₂ and CO: requires special safety measures, for example pilot burners at the doors

2. N₂/H₂ - MIXTURES

Are today usually supplied from tanks and bottle bundles or are self-generated inside. Sometimes cracked ammonia gas is still used (rare in Europe).

ADVANTAGES:

- + Very dry gases (dew point -40 ...-60 °C), therefore suitable to sinter aluminium and stainless steels
- + Require little special knowledge of the operator (there is hardly anything that can be done wrong as long as there is the required volume of gas for the furnace)
- + With a H₂ content of < 5 % classified as non-combustible

DISADVANTAGES

- Rather expensive protective atmospheres
- The risk that the parts will be decarburised during the sintering process can be avoided only by manually added carburising gas (natural gas, propane)
- sooting danger, because of the very low dew point

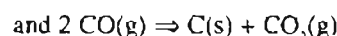
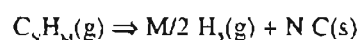
Influence on the sintering process/PM components:

3. INFLUENCE ON DEWAXING:

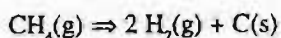
N₂/H₂ mixtures are very dry gases by nature. Their dew point ranges from -40 to -60 °C. Yet this low dew point negatively influences the dewaxing reaction of the parts as well as the furnace itself. The phenomenon that often occurs are the soot residues on the components, the belt and the furnace.

Soot residues in the dewaxing zone originate mostly from a poor dewaxing of the components through a thermal destruction of the hydro-carbon which are part of the waxes

The chemical equation of this reaction is:



and in case of e.g. methane



Soot residues on the components may have multiple causes, and are not explicitly due to an overly dry atmosphere. The guide of atmospheres and temperatures, the length of the dewaxing zone, the belt load, etc. play a part too, but we will not consider them today.

There are three different kinds of soot residues: adherent soot, granular soot and shiny soot, whereby the first two kinds are caused in the dewaxing zone. Shiny soot is the result of too much carburising gas in the sintering zone.

A counter measure often used to avoid soot in the dewaxing zone, or to minimise it, is the humidification of the atmosphere through air, water vapour or by installing an exogas retort which produces a "wet" protective gas (dew point at 900 °C approx. +35 °C).

Air can be easily injected by simply adding compressed air within the dewaxing zone. Water vapour is already a bit more extensive (wetting device). An exogas retort requires an exact setting of the gas - air mixture, since with an operating temperature between 900° and 950°C soot problems may occur. Disadvantages of these systems are found in the necessary control and the additional costs for the provision, operation and maintenance, e.g. compressed air, wetting device, exogas retort require approx. 1 m³/h natural gas. Much smarter is the use of an R.B.O. dewaxing zone which besides the heating also guarantees the automatic wetting, by generating a slightly oxidising protective atmosphere. In contrary to N_2/H_2 mixtures, endogas is more suitable as dewaxing atmosphere. Due to the relatively high dew point this gas is wet already and thus better capable to pick up the fission products of the waxes. During an operation under endogas the gas is normally not humidified anymore.

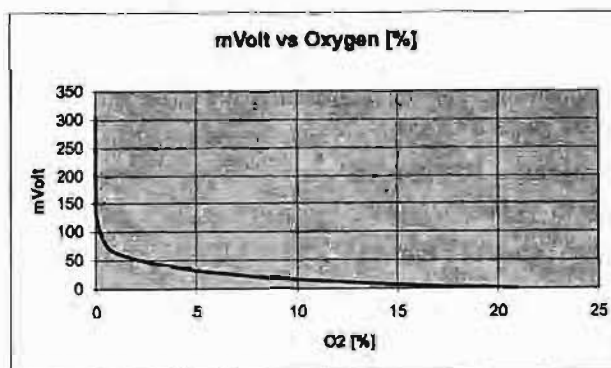
4. INFLUENCE ON SINTERING:

In the sintering zone the situation is reversed. Here the atmosphere should be as good and dry as possible. When dealing with N_2/H_2 it is possible and required to achieve a dew point as low as possible, with endogas the dew point must be set in relation to the carbon content of the components. This clearly shows the difference in the two kinds of gas: while in an N_2/H_2 mixture components with different carbon contents can be sintered at the same time, this is not possible with endogas. The carbon potential of the gas, C_p , has to be matched to the individual carbon content of the component. But this also shows that stainless steel cannot be sintered under endogas. On one hand it would add carbon to the steel, on the other hand sintering would not come about at all, due to the high dew point. For this only N_2/H_2 can be used.

5. MEASURING AND CONTROLLING OF THE QUALITY OF THE PROTECTIVE ATMOSPHERES

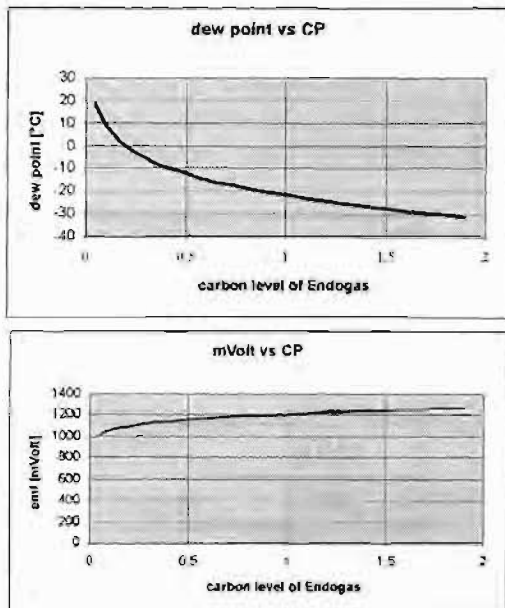
In state-of-the-art sintering furnaces the quality of the atmospheres is monitored continuously. Nowadays oxygen probes and/or dew point measuring devices are used for this. For H_2/H_2 atmospheres it is sufficient to measure with a dew point meter or normal lambda sensor. It measures the oxygen content in the furnace and indicates it as mVolt value.

Temperature 700°C	
mVolt	% O2
1	20,02
50	1,93
100	0,178
200	0,0015
300	1,28E-05
400	1,09E-07
500	9,19E-10
600	7,79E-12
700	6,61E-14
800	5,60E-16
900	4,75E-18
1000	4,02E-20
1100	3,41E-22
1200	2,89E-24
1300	2,45E-26



SINTER PROCESSES FOR STEEL P/M COMPONENTS IN VARIOUS FURNACE ATMOSPHERES MAHLER GmbH INDUSTRIAL FURNACES

In Endogas furnaces the atmosphere can also be controlled with dew point meters [°C] or ceramic oxygen sensors [mVolt]



Dew point and emf of an endogas made of natural gas at 1120 °C

6. ECONOMIC ASPECTS:

There is a big difference in running costs of a sintering furnace between Endogas and different N_2/H_2 -mixtures. It is also well known, from other heat treatment processes that Hydrogen is the dominating factor of costs for a protective atmosphere. Reducing hydrogen consumption will significantly lower the running costs of a furnace much more than reducing nitrogen consumption. Another alternative is to use endogas.

The following cost comparison will show the difference between the various protective atmospheres. It is based on a sintering furnace with a belt width of 600 mm and a sintering capacity of 350 kg/h. Dewaxing is carried out in a conventional dewaxing zone with muffle, i.e. the escaping protective gas will not be burnt in the dewaxing zone. Assumed consumption of protective gas: 50 m³/h. As costs for the gases we used:

Nitrogen: 0,08 Euro/m³

Hydrogen: 0,5 Euro/m³

Natural gas: 0,15 Euro/m³

Electric current: 0,06 Euro/kWh

Example for the calculation of the costs for the protective gas consumption for a N_2/H_2 mixture of 95/5:

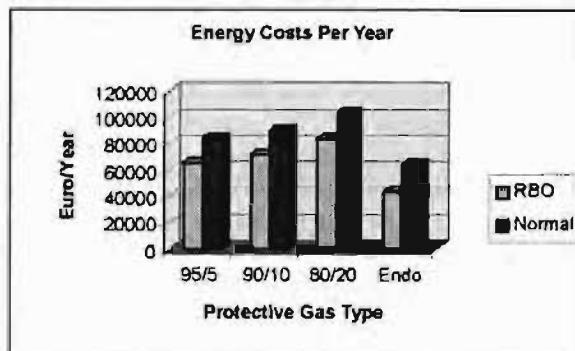
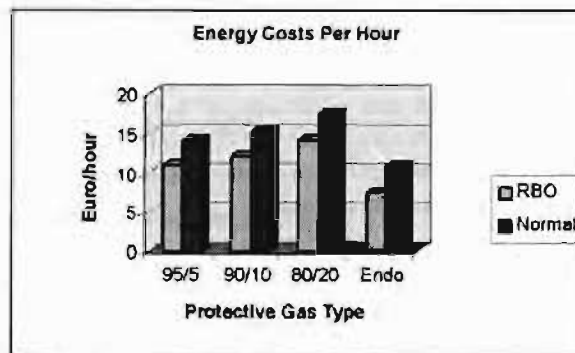
$$50\text{m}^3/\text{h} \times 0,95 \times 0,08 \text{ €/m}^3 + 50 \text{ m}^3/\text{h} \times 0,05 \times 0,5 \text{ €/m}^3 = 5,05 \text{ €/h}$$

	95/5	90/10	80/20	Endogas
Costs for the consumption of protective gas	5,05 €/h	6,1 €/h	8,2 €/h	1,31 €/h
Energy costs for heating of protective atmosphere	0,78 €/h	0,78 €/h	0,78 €/h	1,32 €/h
Costs for protective gas/hour	5,83 €/h	6,88 €/h	8,98 €/h	2,85 €/h

Results: the difference in the costs for the provision of protective gas is about 100 %, even when comparing 95/5 and endogas. When comparing endogas and 80/20 N_2/H_2 the difference is about 315 %.

Furthermore, the operating costs can be significantly reduced when the protective gas escaping from the sintering zone is thermally used, e.g. to heat the P/M components or to after-burn the waxes. For this the rapid burn-off zones, so-called R.B.O. zones, are well suited.

In the R.B.O. zone the protective gas coming from the sintering zone is mixed with air and afterwards burnt. This releases a certain quantity of heat which, under optimum conditions (endogas) is high enough to heat the "green product" to dewaxing temperature and then to dewax them. Another advantage is that the waxes in the "green products" are burnt, too and that their calorific value is also used. This also causes a certain cleaning effect and normally an after-burning can be omitted.



SINTER PROCESSES FOR STEEL P/M COMPONENTS IN VARIOUS FURNACE ATMOSPHERES

MAHLER GmbH INDUSTRIAL FURNACES

Energy consumption cost per operating hour and year for a sintering furnace with 350 kg/ sintering capacity in relation to various sintering atmospheres and dewaxing zone systems

We realise that the difference between the R.B.O. dewaxing system and the conventional dewaxing system, when looking at the same atmospheres, is about 3 Euro/h. This in itself is not an impressive value, but with about 6,000 annual working hours the savings would be 18,000 Euro.

The result is much more impressive when sintering under endogas is compared with 80/20 N_2/H_2 . Here the savings are about 10 Euro per hour, i.e. 60,000 Euro per year, no less.

The comparison of the usual atmosphere 95/5 with endogas shows an advantage in operating costs of 6.80 Euro per hour, or about 41,000 Euro per year, respectively, in favour of the endogas.

Taken into consideration that in a sintering factory normally several sintering furnaces are used, there is an enormous potential to lower running costs.

HIGH PERFORMANCE Si-BEARING MATERIALS PROCESSED IN A VERSATILE HIGH TEMPERATURE SINTERING FURNACE

N. Gopinath, Patrik King, S. Ashok***

Fluidtherm Technology P Ltd, Chennai, India, *Hoeganaes Corporation
Cinnaminson, NJ USA, **Sundram Fasteners Ltd, Hosur, India

ABSTRACT

As the demand for improved performance of P/M parts increases, requirements for proper alloy selection, processing methods and appropriate furnace technology are becoming more rigorous. Recently developed silicon bearing materials have shown excellent mechanical property combinations when processed at high sintering temperatures. This paper discusses the potential for combining high performance materials and processing conditions enabled by a versatile high temperature sintering furnace equipped with an improved quenching module. Critical design features of the furnace and gas-quenching module for tailoring process conditions are discussed. The effect of cooling rate on the microstructures of Si-bearing materials is presented.

INTRODUCTION

When designing any type of sintering furnace of a given capacity, an increase in the hearth loading causes a corresponding decrease in the thermal mass. Increasing the hearth loading can be achieved by stacking parts in tiered trays. Doing so in a mesh belt furnace with open ends, however, would cause several concerns. One such concern would be an increase in gas consumption.

The ability to move trays at different speeds to different sections of the furnace individually instead of at a constant (belt) speed makes it possible to use entry and exit doors that will reduce gas consumption. The accompanying ability to use intermediate doors makes it possible to isolate the atmosphere in different sections of the furnace. This becomes possible with either a closed pitch roller hearth furnace or with a furnace with different internal transport systems of which at least one is a walking beam mechanism. This has been the basis of the development of a "versatile" sintering furnace that has the following features;

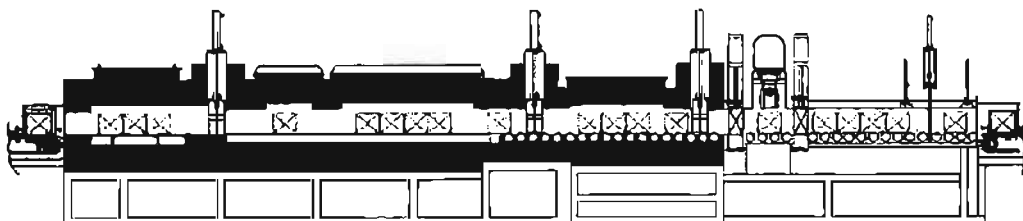
- Entry, exit & intermediate doors
- Atmosphere isolation between different furnace sections

The incorporation of a carburizing or carbonitriding section following the sintering section

The incorporation of a more effective sinter hardening section than is generally available with modern mesh belt furnaces.

Versatility lies in the ability to choose which of the sections are operated for a given part.

The furnace (Figure1) consists of a dewaxing section equipped with an entry vestibule, an exit atmosphere isolation door and a pusher mechanism. The end tray is picked up by a walking beam mechanism that transports it through a sintering section and an unheated section isolated from the following carburizing section which is equipped with a roller hearth mechanism and an atmosphere circulating fan. Following this section, across an isolating door is the sinter hardening module, also equipped with a roller hearth and a rear door through which the processed trays are discharged into open atmosphere, if required through another water jacketed section. Heating is achieved by metal or ceramic heaters that are disposed vertically along the sidewalls.



HIGH PERFORMANCE SI-BEARING MATERIALS PROCESSED IN A VERSATILE HIGH TEMPERATURE SINTERING FURNACE

Fig. 1 Schematic of a "versatile furnace" showing, from left; dewaxing section with pusher transport, sintering section with walking beam transport, carburising section, pressure gas quench section & water jacket cooling sections, all with roller hearth transport.

The large number of mechanisms and the consequent need for a comprehensive coordinating control system are at stark contrast to the elegant simplicity of a mesh belt furnace and can only be justified by;

- Lower energy consumed by a smaller thermal mass for a given sintering capacity which is made possible by higher (multi-tier) hearth loading.
- Lower gas consumption
- Higher sintering temperature (T Max. 1450°C)
- Elimination of subsequent heat treatment.

When the characterization of a prototype "versatile" furnace is completed, precise information will become available which would define the applications for which such a furnace would become the preferred option.

One concern that would occur at the first study of this concept would relate to consistency.

Parts being processed in a shallow layer in a mesh belt furnace equipped with a muffle which is heated from the top as well as bottom would heat up and cool down uniformly and would therefore have consistent properties. Parts stacked in trays one above the other and subjected to heating only from the sides would suffer by comparison. This is overcome by the design of the hearth and proper part stacking. Uniformity of $\pm 3^\circ\text{C}$ has been recorded.

Another significant aspect relates to hardening after sintering without need for reheating. This is achieved in mesh belt furnaces, generally by extracting, cooling, recirculating and impinging furnace atmosphere gas on the parts when they emerge from the furnace. The chamber of such a sinter hardening section has to be contiguous with the sintering & other furnace sections, all of which comprise one long through tunnel with open ends. The cooling rate of such systems necessitates alloying for higher hardenability.

The sinter hardening section in a multichamber "versatile" furnace uses isolating pressure tight doors that allow the cooling of parts (in a tray) with pressurized gas that has higher heat extraction properties than gas at or slightly above atmospheric pressure. The cooling rate can be controlled by varying the pressure and/or the fan speed. The use of a carburizing/carbonitriding section allows case hardening as well where required. Cooling curves of typical

gears under different cooling conditions are shown in Figure 2. The relation between the cooling rate ($^\circ\text{C}/\text{sec}$) and quench pressure is shown in Figure 3 for the range of 820° to 300°C.

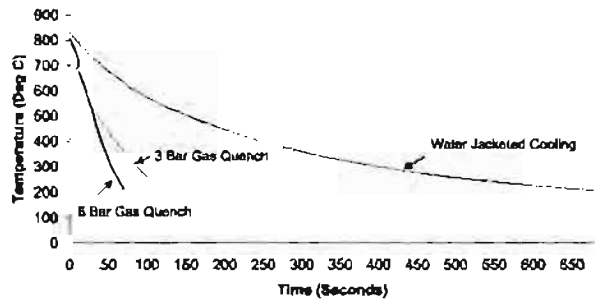


Fig 2. Cooling curves of sintered parts at different parts at different cooling conditions

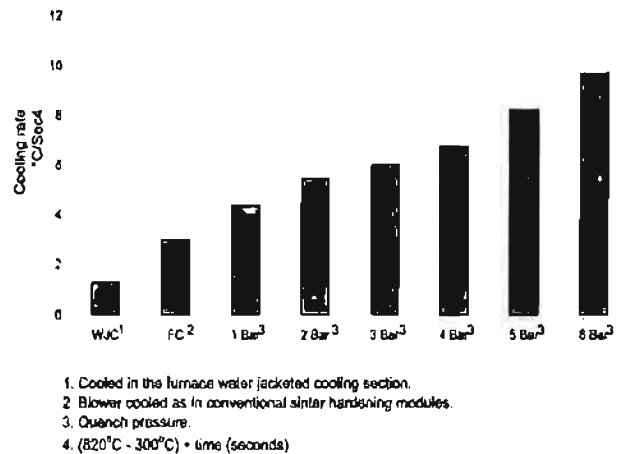


Fig 3. The relation between the cooling rate and the quench intensity

APPLICATION TO P/M MATERIALS

The increased heat extraction rate shown in Figure 2 extends the range of alloys that can be sinter hardened effectively compared to sinter hardening modules with lower heat extraction rates. Several methods currently exist to produce P/M sinter hardening grades [1].

The first method is a conventional admixture, in which elemental additions are made to pure iron powder. While maintaining good compressibility, this is the least effective method for improving hardenability.

The composition can also be diffusion alloyed, in which elemental additions are annealed to together with the iron powder. This bonds the alloy to the iron, and improves the hardenability while maintaining a fair amount of compressibility.

HIGH PERFORMANCE SI-BEARING MATERIALS PROCESSED IN A VERSATILE HIGH TEMPERATURE SINTERING FURNACE

Alternatively, hybrid compositions require a base powder that is prealloyed with hardenability agents such as Mo. These elements are added directly to the molten steel prior to atomization, therefore improving microstructural homogeneity and hardenability. Elemental additions are then made to the base powder to improve the hardenability further.

The final and most effective method to create sinter hardenable P/M steels is to fully prealloy the elemental additions such as Mn, Ni, and Mo. Elemental additions of copper and graphite are typically added to these powders. Fully prealloyed materials have the inherent advantage of homogeneity and the highest hardenability, but are traditionally lower in compressibility.

Actual components using the multichamber versatile furnace on a prealloyed grade (gear), an admixed grade (synchronizer key), and a diffusion-alloyed composition (push rod bearing) are processed. The results of these trials, all of which were sintered at 1120°C in a N₂ + 30% H₂ atmosphere are shown in Table I.

Table I. Core Hardness data of three alloys under different cooling conditions at 1120°C in a N₂ + 30% H₂ atmosphere.

	Prealloy	Diffusion-alloyed	Admixed ⁽¹⁾
Component	Gear	Push rod bearing	Synchronizer Key
Carbon (Wt.%)	0.5	0.8	0.4
Water jacket cooling	198 HV1	221 HV1	202 HV1
Fan cooling	504 HV1	265 HV1	230 HV1
3 Bar pressure	518 HV1	278 HV1	242 HV1
6 Bar pressure	544 HV1	411 HV1	394 HV1
Oil hardened	540 HV1	510 HV1	460 HV1

(1) This part normally Carbonitrided was gas quenched to gauge the response to alloying

The prealloy grade, as mentioned above, has better homogeneity than both the diffusion-alloyed and admixed compositions. As a result, increasing the cooling rate slightly (water jacket cooling to fan cooling) dramatically

increases the hardness in the gear. Further cooling rate increases incrementally improve the hardness. No benefit is achieved by the additional processing step of oil quenching compared to the 6 bar quench.

Both the diffusion-alloyed and admixed powder components see significant improvement as the gas quench rate is continuously improved. The hardness is increased further after oil quenching, indicating that a fully martensitic microstructure is not obtained in these two components with the 6 bar quench.

Metallography shown on the following pages lends support to these observations. Shown in Figure 4 is a photomicrograph of the gear (prealloyed grade) after cooling with the 6 bar quench. As expected, the microstructure is predominantly martensitic, with some amounts of bainite.

Figure 5 shows the microstructure of the synchronizer key (admixed grade) after cooling at the 6 bar quench. The microstructure is mostly bainite, with some divorced pearlite and ferrite dispersed throughout.



Fig 4. Core Microstructure of the gear sintered at 1120°C and then rapidly cooled at 6 bar pressure. Structure is martensite with little bainite.



Fig 5. Core Microstructure of the synchronizer key (admixed grade) sintered at 1120°C and then rapidly cooled at 6 bar pressure. Structure is bainite with fine pearlite and ferrite.

HIGH PERFORMANCE SI-BEARING MATERIALS PROCESSED IN A VERSATILE HIGH TEMPERATURE SINTERING FURNACE

While the preceding pages have shown the effectiveness of the new multichamber "Versatile" furnace on alloys at conventional processing temperatures, it is of interest to consider the impact on high performance materials processed at elevated sintering temperatures in this furnace.

Hoeganaes recently introduced a line of products containing Silicon which were designed to replace malleable and ductile cast irons [2,3]. The use of silicon helps to increase hardenability and enhance sintering at a modest cost [4]. When processed at high sintering temperatures, these alloy systems provide extraordinary property combinations. These properties, achieved using single press / single sinter (SP/SS) processing, were previously only possible in ferrous P/M by using costly double press / double sinter (DP/DS) processing.

One of these materials, Ancorloy® MDCL, has shown phenomenal properties at relatively low silicon contents. The nominal composition of this binder-treated high performance alloy is 4.4 wt.% Ni, 0.85% Mo, and 0.35% Si, with a typical graphite addition of 0.6 wt.%. Other advantages of this alloy include good compressibility (7.20 g/cm³ at 690 MPa / 50 tsi) and low oxygen contents. Maintaining a low oxygen level throughout sintering is important to both static and dynamic properties in alloys that contain elements that have a high affinity for oxygen [5,6].

Shown in Table II are typical data for MDCL [7] with 0.6 wt.% graphite processed using a relatively slow cooling rate of 0.7 °C/sec as measured over the range of 850° to 315°C. The samples were sintered at 1260°C in 90N2-10H2, and stress-relieved for 1 hour in air at 205°C after sintering. Even at this slow cooling rate, excellent properties combinations are achieved in this material.

The cooling rate used to produce these properties is slightly slower than that which is obtained in the water jacket cooling section of versatile furnace. The good ductility and high impact properties indicate that further enhancing the cooling rate could significantly improve the strength and hardness of this alloy system.

Shown in Figure 6 is the continuous sinter cooling transformation (CSCT) diagram of MDCL at a density of

7.15 g/cm³ [8]. This technique involves austenitizing a specimen in a dilatometer at 900°C, and subsequently cooling at various rates [8]. Dilatometric changes during the cooling cycle indicate the precipitation of various microconstituents. Quantitative metallography and apparent hardness measurements on the samples are used to characterize the different phase regions.

At the cooling rate in which the data in Table II were generated, the resulting microstructure that is produced is roughly 50% martensite, with 40% bainite and the remainder pearlite. A representative image of this microstructure is shown in Figure 7. Increasing the cooling rate to 137°C/min (roughly equivalent to the cooling rate achieved with fan cooling in the versatile furnace) produces essentially a fully martensitic microstructure. This is thus the critical cooling rate, the minimum rate required to avoid the "bainite nose" and produce a microstructure devoid of high temperature phase precipitations such as bainite and pearlite.

Further enhancement of the cooling rate for MDCL with 0.6 wt.% graphite would likely produce no change in the properties since the microstructure is already fully martensitic with fan cooling. The pressure gas quenching system would not be a good candidate for this graphite level for this reason.

However, lowering the graphite content to 0.3 or 0.4 wt.% would push the bainite nose sufficiently to the left side of the diagram. As a result, the cooling rate provided by fan cooling would not produce a fully martensitic microstructure. To do so, enhanced cooling rates such as those provided by the pressure gas quench system would be required. At these cooling rates, excellent strength would be achieved with a fully martensitic microstructure. The lower graphite levels would also allow for a significant increase in ductility and impact toughness. At the time of publication, work was ongoing to quantify the effect of sinter hardening MDCL with lower graphite contents in the new furnace. These data will be presented in a future publication.

**Table II. Mechanical properties for MDCL sintered at 1260°C in 90N2-10H2.
Stress-relieved for 1 hour in air at 205°C after sintering.**

Pressure (MPa / tsi)	SD (g/cm ³)	DC (%)	YS (MPa / 10 ³ psi)	UTS (MPa / 10 ³ psi)	Elg (%)	Imp (J / ft.lbf)	Hard (HRC)
415 / 30	6.95	-0.67	725 / 105	938 / 136	1.6	15/11	20
550 / 40	7.15	-0.54	807 / 117	1103 / 160	2.2	23 / 17	25
690 / 50	7.26	-0.44	827 / 120	1207 / 175	2.7	31 / 23	31

HIGH PERFORMANCE SI-BEARING MATERIALS PROCESSED IN A VERSATILE HIGH TEMPERATURE SINTERING FURNACE

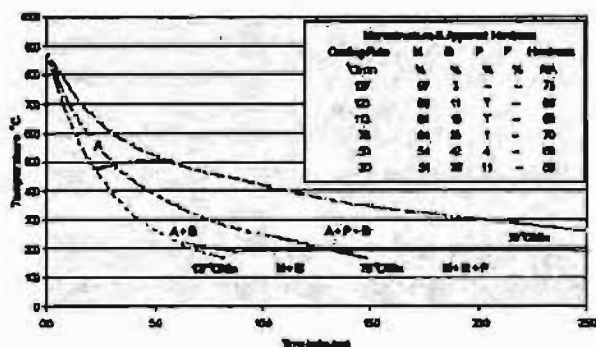


Fig 6. Continuous sintering cooling transformation (CSCT) diagram for Ancorloy MDCL with 0.6 wt.% graphite showing the expected microstructures at various cooling rates [8].

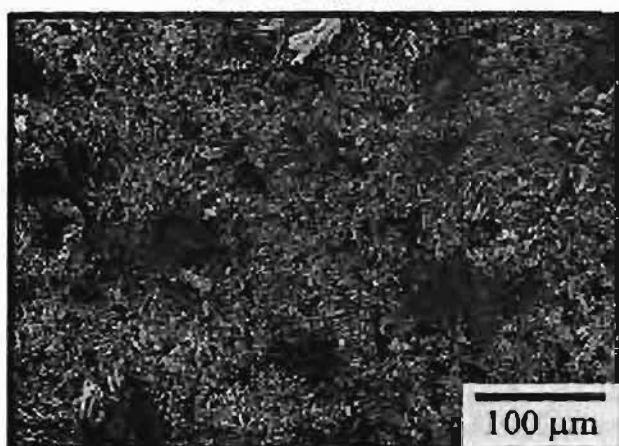


Fig 7. Microstructure of Ancorloy MDCL sintered at 1260°C in 90N2-10H2 with a cooling rate of 0.7°C/sec. Stress-relieved for 1 hour in air at 205°C after sintering.

CONCLUSIONS

The design features of a new multichamber versatile furnace were discussed. The furnace is equipped with an improved sinter hardening module that uses an isolating pressure tight door that allows the cooling of parts with pressurized gas that has higher heat extraction properties than gas at or slightly above atmospheric pressure. Trials on several components made from a variety of alloying methods were summarized. Also presented was the potential for processing high performance Si-bearing materials in the furnace and the implications of cooling rate on the final microstructure of these alloys.

REFERENCES

1. James, B. "What is sinter-hardening?" *Advances in Powder Metallurgy & Particulate Materials*, Metal Powder Industries Federation, Princeton, NJ, 1998.
2. James, W.B., Causton, R.J., Baran, M.C., and Narasimhan, K.S. "New High Performance P/M Alloy Substitutes for Malleable and Ductile Cast Irons" *Advances in Powder Metallurgy & Particulate Materials*, Metal Powder Industries Federation, Princeton, NJ, 2000.
3. Baran, M.C., Chawla, N., Murphy, T.F., and Narasimhan, K.S.. "New High Performance P/M Alloys for Replacing Ductile Cast Irons" *Advances in Powder Metallurgy & Particulate Materials*, Metal Powder Industries Federation, Princeton, NJ, 2000.
4. Salak, A., *Ferrous Powder Metallurgy*, Cambridge International Science Publishing, Cambridge, England, p. 235, 1995.
5. Motooka, N. et al. "Strength and ductility of Mn-Cr sintered steel" *MPR*, Nov. 1983, p. 629-631.
6. Sigl, L. S., Delarbre, P. "Impact of oxygen on the microstructure and fracture morphology of Fe(Cr,Mo)-PM steels" , *Advances in Powder Metallurgy & Particulate Materials*, Metal Powder Industries Federation, Princeton, NJ, 2003.
7. Fillari, G et al., Unpublished work, 2002.
8. Semel, F. "Ancorloy hardenability" , *Advances in Powder Metallurgy & Particulate Materials*, Metal Powder Industries Federation, Princeton, NJ, 2003.
9. Semel, F., "Cooling rate effects on the metallurgical response of a recently developed sinter hardening grade", *Advances in Powder Metallurgy & Particulate Materials*, Metal Powder Industries Federation, Princeton, NJ, 2002.

MODELING OF MICROWAVE HEATING OF PARTICULATE METALS

P. Mishra, G. Sethi**, and A. Upadhyaya*a*

* Department of Materials and Metallurgical Engineering
Indian Institute of Technology, Kanpur 208016, India

**Center of Innovative Sintered Products
The Pennsylvania State University, University Park, PA 16802, USA

ABSTRACT

Recent research has shown that metal powder compacts can be heated to high temperatures using microwaves. While microwave heating of ceramics is well understood and modeled, there is still uncertainty about exact mechanism and mode of microwave heating in particulate metals. The present study describes an approach for modeling the microwave heating of metal powder compacts using an electromagnetic-thermal model. The model predicts the variation in temperature with time during sintering. The effect of powder size, emissivity and susceptor heating on the temperature-time curve has also been assessed. These predictions have been validated by the experimental observations of the thermal profiles of Sn, Cu and Walloy compacts, using a 2.45 GHz multimode microwave furnace.

1. INTRODUCTION

Microwave heating has been a distinguished achievement in field of sintering of particulate materials [1]. As compared to conventional heating, microwave heating is more rapid, which results in sintering time compression. In addition to the cost efficiency, microwave heating minimizes grain coarsening and abnormal grain growth [2]. Thus, the densification kinetics is faster and the microstructure is more homogeneous. Recent studies on various systems have shown higher sintered density and mechanical property enhancement in microwave sintered compacts as compared to their conventionally sintered counterparts [3-7]. Despite the use of microwaves in sintering ceramics, it has only recently been shown that metals too can couple with microwave and get heated up provided they are in powder form [8]. This has resulted in wide-spread interest in sintering of these compacts in microwave furnace. Despite its potential scope for industrial applications, the phenomenology of microwave heating of metals is yet to be fully understood. Although the large surface area in powders makes coupling of metal powders with microwave more amenable, yet a clear understanding of microwave interaction and its absorption lacks in terms of modeling of the heating process. This paper describes a new approach to explain the microwave sintering of particulate metals

using a two-dimensional coupled electromagnetic-thermal model. As part of the present study, the temporal temperature distribution was simulated using two-dimensional Finite Difference Time Domain (FDTD) calculations to obtain the electromagnetic field parameters. The model also incorporates the effect of particle size, emissivity and susceptor on heating. The validation of predicted thermal profiles was done on tin, copper, and tungsten-alloys powders through careful measurements of the temperature variation with time in a multimode-cavity microwave furnace.

2. MODELING APPROACH

Modeling of microwave heating involves solving Maxwell's equations of electromagnetism simultaneously with the heat transfer equation [9]. To determine the electromagnetic fields in a cavity, FDTD technique was used by Yee [10] and Zhang *et al.* [11]. Zhang *et al.*'s [11] results showed that the numerical methodology can be used in proper designing of the microwave cavities for various applications. It was indicated that by appropriate selection of the field points, a set of finite difference equations can be formulated for a boundary condition involving perfectly conductive surfaces. These solutions were used for calculating power absorption, flow-fields and temperature

patterns in non-metallic systems [11-13]. Subsequently, a quasianalytical model was proposed by Lasri *et al.* [14] to examine energy conversion during the microwave sintering of a ceramic that is surrounded by a susceptor. Elsewhere, a simulation-package based on two-dimensional modeling of microwave heating of ceramics was developed Craven *et al.* [15] who used a coupled electromagnetic-thermal model. This approach was further extended by Alpert and Jerby [16] for microwave heating of temperature dependent dielectric media. In the present study, the calculated power absorbed is correlated with the temperature rise in the compact. The latter requires solving the heat transfer equation for the boundary conditions defined by the dimensions of the sample and its physical, thermal and dielectric properties. The dependency of these parameters on temperature necessitates the need for a dynamic simulation. Figure 1 shows the modeling approach adopted in this study through a schematic flow-chart.

2.1 Electromagnetic Power

Microwaves penetrate and propagate through a dielectric material like SiC. This generates an internal electric field (E) within a specific volume, which in turn, induces polarization and movement of charges. The resistance to these induced motions due to internal, elastic and frictional forces attenuates the electric field. These losses result in volumetric heating. The resulting electromagnetic power absorbed per unit volume (PEM) by a material is given by [17]:

$$P_{EM} = 2\delta \left(\epsilon_0 \epsilon_r''(\omega) |E_{rms}|^2 + \mu_0 \mu_r''(\omega) |H_{rms}|^2 \right) \quad (1)$$

where,

ω is frequency of the microwave (2.45 GHz),

ϵ_0 is absolute permittivity of free space (8.85×10^{-12} C²/Nm²),

ϵ_r is relative dielectric constant (imaginary), temperature dependent,

μ_0 is absolute permeability of free space ($4\pi \times 10^{-7}$ N/A²),

μ_r is relative permeability constant (imaginary), temperature dependent,

E_{rms} and H_{rms} are root mean square values of electric and magnetic field amplitudes, respectively.

Microwave heating in metals is different than that observed in dielectric materials (mostly ceramics). Being good conductors, no internal electrical field is induced in metals. The induced electrical charge remains at the surface of the sample. As a consequence, monolithic metals reflect microwaves; hence no bulk absorption (heating) occurs,

particularly, at temperatures below 500 C [18]. Microwaves interaction with metals is restricted to its surface only. This depth of penetration in metals, also known as skin-depth (δ), is defined as the distance into the material at which the incident power drops to $1/e$ (36.8%) of the surface value. The skin depth is mathematically expressed as follows:

$$\delta = \frac{1}{\sqrt{\pi f \sigma}} = 0.029 \sqrt{\rho \lambda} \quad (2)$$

where, f is microwave frequency (2.45 GHz), μ is magnetic permeability, σ is electrical conductivity, ρ is electrical resistivity, λ is incident wavelength (12.24 cm for 2.45 GHz waves). The skin-depth in metals typically varies between 0.1 to 10 μ m. Figure 2 shows the variation in skin depth with temperature for tin, copper, and tungsten calculated Equation 2. The respective electrical resistivity of the three metals is summarized in Table 1. From Figure 2, it is evident that metals with higher electrical conductivity have lower skin depths. For metals, as the resistivity increases with increase in temperature, the skin depth too increases. In general, the skin depth is relatively small in metals, however, most metallic powders typically have equivalent dimensions. In metal powders, the surface area and thereby the 'effective skin' (portion of metal powder that couples with microwaves) is high enough to contribute to its heating. Thus, it is likely that some of the submicron and nano-sized metal powders undergo volumetric heating when subjected to microwaves. However, for relatively coarse powders ($>100 \mu$ m), the heating may be conductive from outside (skin) to the interior of the powder. Thus, as compared to conventional furnace heating, microwave heating is expected to be more uniform as the particle size decreases [2]. The skin depth of the metal plays an important role in governing the power loss during the microwave-metal interaction which leads to its heating [17]. The tangential component of the magnetic field, H_t , of microwaves induces an electrical field, E , at the metal powder surface. The induced electrical field generates surface current which causes the resistive Joule heating in metal powders. The power lost during the interaction of microwave with metal can be related to its surface impedance. The power absorbed per unit area of the conductive surface, P , is expressed as [17]:

$$P = \frac{1}{2} \int \vec{E} \cdot \vec{J}_s \cdot dV = \frac{1}{2} \int \sigma |\vec{J}_s|^2 \cdot dV \quad (3)$$

The surface current, J_s , is expressed as:

$$\vec{J}_s = \vec{n} \times \vec{H} \quad (4)$$

The power can be further derived as:

$$P = \frac{\sigma}{2} \int |\vec{J}_s|^2 dV = \frac{\sigma}{2} \int |\vec{H}|^2 dV = \frac{2\sigma |\vec{H}_0|^2}{\eta_s} \quad (5)$$

where, R_s is surface resistivity ($R_s = 1/6\delta$, δ is electrical conductivity and δ is skin depth); E_0 is electric field amplitude at surface; and ζ_0 is impedance of free space (377 Ω).

Assuming spherical metal powder of radius, r_p , the electromagnetic power density (PEM) can be expressed as:

$$P_{EM} = \frac{3P}{r_p} = \frac{6R_s|E_0|^2}{\eta_e^2 \cdot r_p} \quad \dots\dots\dots(6)$$

2.2. Assumptions

To make the problem tractable for modeling, following assumptions were made:

- Since the particle size is much smaller than the wavelength of the microwave radiation, the field across the particle is spatially uniform and periodic in time.
- Powder size is small enough to cause volumetric heating.
- Powder coarsening is not assumed during heating.
- Mono-sized and spherical powders are assumed so that the calculated EM power density generated in a powder will be same when integrated over bulk aggregate.
- All metal powders within a compact are assumed to heat-up at the same rate so no heat conduction between powder particles occurs.
- A heat-factor is considered to account for the presence of susceptor.
- Effect of porosity, oxide layer formation, liquid formation, shrinkage is not considered in the present model.
- As the tungsten-alloy (W-Ni-Fe) consists of more than 93 wt. % W, therefore, only the interaction of tungsten powder with microwave is considered.
- The emissivity was assumed not to vary with temperature. Recent experiments with microwave heating of Sn, Cu, and bronze, tungsten compacts have indicated that their emissivity does not appreciably vary within the sintering temperature range typically used for their consolidation [19].

2.3 Electromagnetic and Thermal Model Formulation

2.3.1 Electromagnetic Model for Calculating Power Absorbed

Electro-magnetic model uses the codes based upon 2-D FDTD technique [10] to calculate the E-H field distribution inside cavity. These codes were developed by Sethi [20] and later modified by Mishra [21]. For any electromagnetic field and 6 perfectly conducting boundary conditions, Maxwell's equations in a two-dimensional 'transverse magnetic (TM)' mode can be written as:

$$E_x = E_y = 0, \quad H_x = 0$$

$$\epsilon \frac{\partial E_x}{\partial t} = \frac{\partial H_y}{\partial x} - \frac{\partial H_z}{\partial y}$$

$$\mu \frac{\partial H_x}{\partial t} = -\frac{\partial E_z}{\partial y}, \quad \mu \frac{\partial H_y}{\partial t} = \frac{\partial E_z}{\partial x}$$

Furthermore, these can be replaced by a set of finite difference equations and can be expressed as:

$$E_x^{n+1/2}(i, j) = E_x^{n-1/2}(i, j) + \frac{\Delta t}{\epsilon} \left(\frac{\partial H_y}{\partial x} - \frac{\partial H_z}{\partial y} \right)^n$$

$$H_x^{n+1/2}(i, j) = H_x^{n-1/2}(i, j) - \frac{\Delta t}{\mu} \frac{\partial E_z}{\partial y}^n$$

$$H_y^{n+1/2}(i, j) = H_y^{n-1/2}(i, j) + \frac{\Delta t}{\mu} \left(\frac{\partial E_z}{\partial x} \right)^n$$

Where,

$$\tau = ct = \sqrt{\frac{1}{\mu\epsilon}} t \quad Z = \sqrt{\frac{\mu}{\epsilon}} = 376.7$$

For the stability criteria, the necessary condition is [10]:

$$\sqrt{(\Delta x)^2 + (\Delta y)^2 + (\Delta z)^2} > c\Delta t = \sqrt{\frac{1}{\epsilon\mu}} \Delta t$$

Thus, for a specific material, the spatial Erms and Hrms distribution can be determined by feeding its dielectric properties. As shown schematically through Figure 1, these Erms and Hrms values in turn fed as input parameter into the thermal model.

2.3.2 Thermal Model for Predicting Temperature Rise

In the thermal model, basic heat equation is solved to determine the increment in temperature during a small step of time. As material properties are temperature dependent, therefore these are updated after each step of time and iterated in the program (Figure 1). The temperature rise in the metal powder compact is governed by heat equation which is expressed as:

$$\rho C_p \frac{dT}{dt} = P_{EM} - P_{conv} - P_{rad} \quad \dots\dots\dots(8)$$

where, PEM, Pconv and Prad are electromagnetic power density (Equation 6), power loss per unit volume due to convection, and radiation, respectively. To solve this first order differential equation, Euler-Cauchy numerical method was adopted. Accordingly, the temperature as a function of incremental time domain (Δt) and after (n+1)th intervals can be written as:

$$T_{n+1} = T_n + \Delta t \rho C_p (P_{EM} - P_{conv} - P_{rad}) \quad \dots\dots\dots(9)$$

Similarly, Pconv and Prad can be expressed as:

$$P_{conv}(n) = hA/V (T_{n+1} - T_a) \quad \dots\dots\dots(10)$$

$$P_{rad}(n) = \epsilon A A/V (T_{n+1}^4 - T_a^4) \quad \dots\dots\dots(11)$$

where,

h is convective heat transfer coefficient of incoming gas,

A/V is surface area to volume ratio for compact,

σ is Stefan Boltzman constant,

ϵ is effective emissivity of metal powder, and

T_a is surrounding temperature.

In Equation 9, Δt should not be too small as it increases the number of iterations,

hence, the round-off error is also increased. However, too large a Δt should also be avoided as it causes an increase in the truncation error per step. Therefore, a suitable value of Δt is chosen which satisfies stability criterion given below:

$$0.05 \leq \Delta t \leq 0.1 \dots \dots \dots (12)$$

where, K is upper bound of

$$[d(\epsilon C_p(P_{EM} - P_{conv} - P_{rad}))/dT].$$

Typically, in the initial stage of heating, the metal powder compacts require susceptor-assisted heating [18]. The susceptors usually couple very well with the microwaves and are used for initially raising the temperature of the compact. Beyond a critical temperature, the heating occurs primarily due to microwave-metal powder surface interaction. Recently, Anklesar *et al.* [4, 22] have confirmed this by sintering copper containing steels in microwave both with and without susceptor. Besides, assisting heating in the initial stage, the main role of susceptor is to prevent heat loss from the powder compact to the surrounding through radiation. In the present modeling scheme, the contribution of SiC as susceptor for compact heating was also included. To account for this effect, the heat transfer from SiC plates to compact is taken directly proportional to their temperature difference. Hence, an additional term $k_{SiC}(T_{SiC} - T_m)$ is included in Equation 9, wherein k_{SiC} is a proportionality constant that can be determined by simulation.

3. EXPERIMENTAL SETUP TO VALIDATE MODEL

To verify the thermal profiles predictions from the model, experiments were done with Sn, Cu and W-alloy powder compacts. Table I summarizes the physical and thermal properties of the metals powders used for the present investigation, which are input parameters in the model. Unlike ceramics, sintering of metal powder compacts necessitates the need of controlled atmosphere cavity. For conducting such an experiment, a 1.1 kW microwave furnace with a 2.45 GHz multi-mode cavity was

indigenously designed in collaboration with Bharat Heavy Electrical Ltd. (BHEL), Hyderabad, India. The detailed description of the furnace [model: Sinterwave TM] construction is given elsewhere [25,26]. Figures 3a and 3b show the schematic setup and photograph of the microwave furnace used for the present investigation. The size of the metallic cavity was 40 × 62 cm². A high density (99.9%), doubly recrystallized alumina tube of 7.1 cm diameter and 67 cm in length was positioned at the center of the furnace by drilling holes on the side faces, with ends projecting outward on both the sides (Figure 3). The alumina tube was cooled from the end by flanges with flowing water through them. Through leak-proof fittings, provision was made for gasinlet and outlet. All the sintering experiments were conducted in hydrogen. The full density alumina tube prevents any gas leakage. Furthermore, pore-free alumina is transparent to microwaves and does not heat up. Thus, the temperature rise during sintering is solely due to microwave-metal interaction. An insulation package made of FibrefraxTM boards was used to surround the tube at the center of the cavity to minimize heat loss. The design was so made that it could be used both with and without the use of susceptor or secondary coupler. The present sintering studies were conducted using the former configuration with SiC plates.

The Sn, Cu, and W-alloy powders were pressed in form of a cylindrical pellet (diameter: 1.27 cm, average height: 1 cm). The compaction pressure was optimized at 200 MPa to give sufficient structural rigidity to the compact for handling purpose. Unlike conventional sintering, thermocouple cannot be used to measure temperatures in microwave furnaces. The temperature measurement was done using an infrared pyrometer (model: M680, supplier: Mikron Inc., USA). The infrared pyrometer output was coupled with a PC-based data acquisition and display software.

4. RESULTS AND DISCUSSION

This section provides the modelling results based on the algorithm discussed in the previous sections. In the above sections, a theoretical approach has been formulated to predict the heating profile of metal powder compacts in microwave furnace. Figure 4 shows the electric field distribution in two dimensions, $E_z(x,y)$, produced inside the microwave cavity generated using the FDTD simulation. Figure 5 shows the corresponding variation in electric field amplitude at the centre of the empty microwave cavity. Note the overall periodicity and symmetry in field distribution in the cavity indicating standing waves. Figure 6 shows the variation in the E_z distribution at the centre of the cavity ($y = 21$ cm) and along the x -direction at three different time. From Figure 6 it is evident that the amplitude of the

electric field in z direction will vary with time as standing EM waves are produced inside the microwave cavity. The distribution of electric field across a particular section varies constantly with time. This underscores the relevance of the present approach of considering dynamic temporal distribution. Prior to simulating the heating curves of particulate metal compacts, the thermal model was tested for predicting the heating curve for SiC and Al₂O₃ (Figure 7). From the figure, it is evident that SiC is a good absorber of microwaves and heats upto 1300K in less than 5 min. Therefore, using SiC as susceptor is beneficial in assisted heating of metal powders. Unlike SiC, alumina is well-known insulator with reference to microwave radiation. Consequently, there is very little temperature rise in alumina when exposed to microwaves for varying time (Figure 7). Figures 8a to 8c shows the simulated temperature rise with time in Sn, Cu, and W-alloys, respectively. The experimental heating profiles for the powders have been superimposed for the three powders on their respective simulated curves. For all the three cases, the observed heating profile is close to that predicted using the electromagnetic-thermal model. As described above, the numerical simulation took into account the SiC- factor in the heat equation. The differences in experimental and numerical heating behaviour can partly be attributed to the fact that power input was kept constant in modeling, whereas, in the actual experiment, it was controlled through a PID processor. An interesting observation with the current simulation of thermal profile is that for a particular choice of experimental variables, the temperature rise is restricted to a certain level. This can be attributed to the fact that the heat generated in the compact (due to electromagnetic power absorbed) is balanced by the convective and radiative heat losses. To analyze the susceptor-aided heating a constant kSiC was introduced. From the thermal simulations it was found that its value is 103 times greater for Cu and Sn samples as compared to W-alloy compact. This implies that Cu and Sn need more susceptor-assisted heating in the initial stage, whereas, the W-alloy readily couple more easily with microwaves even at lower temperatures (Figure 2). Alternatively, this can also be inferred by the lower skin depth in high conductivity powders. A practical implication of this could be to activate the sintering of such powders either by dispersion or by coating with high dielectric loss materials (e.g. oxides). While the latter will be more effective in the heating, it will impart brittleness to the particle-particle interface. Thus, oxide/carbide dispersed metal-matrix composites will be more amenable to consolidation through microwave sintering. Figure 9 shows the variation in simulated temperature-time characteristic curve with respect to powder size in tungsten. Note that as the W-powder size

becomes smaller, the tungsten powder compact gets heated up at a faster rate. As can be seen from the results, metal powder size sharply influences the heating characteristics. From the above discussion, it is logical that a finer powder size will heat-up at a faster rate in microwave as the available area and hence the effective microwave-metal interactive surface becomes high. Vaidhyanathan and Rao [27] have experimentally showed faster heating in smaller powders as compared to coarser powder compacts. Another factor that influences the heating behavior is the emissivity of the metal powder compacts. Precise determination of emissivity has always been a problem as it changes with temperature and the property of the surface [19, 28]. Figure 10 shows the effect of varying emissivity on the heating curve for tungsten. Note that the maximum attainable temperature increases with decreasing emissivity. It is envisaged that a precise experimental determination of emissivity dependence on temperature will further fine-tune the heating predictions from the current thermal model).

5. CONCLUSIONS

For the first time a model has been developed for predicting heating of particulate metal compacts in microwaves. The present approach incorporates both the electromagnetic and thermal heating models. Using a 2D FDTD technique, both electrical and magnetic field components within the microwave cavity can be calculated, from which power absorbed by the compact is determined. The electromagnetic model is coupled with the thermal model, which incorporates the convective and radiative losses. The unique feature of this approach is that it incorporates the temperature-dependency on the physical, thermal and the dielectric properties of the materials, as well as the effect of susceptors (such as SiC) while predicting the heating profiles. The heating profile predictions from the model are validated experimentally by measuring the temperature rise of tin, copper, and tungsten particulate compacts sintered in a 2.45 GHz multimode microwave furnace.

6. ACKNOWLEDGMENTS

The authors thank Professors B. Deo and D. Gupta of Materials and Metallurgical Engineering Department, IIT Kanpur and Mr. G Swaminathan of Ceramic Technological Institute, BHEL, Bangalore for their valuable comments and insights. Helpful suggestions and technical feedback pertaining to modeling of microwave sintering from Prof. D. Agarwal and Dr. J.L. Johnson of The Pennsylvania State University is also gratefully acknowledged. This study was support by the grants from the Department of Science & Technology (DST) and Defense Research and Development Organization (DRDO), India.

7. REFERENCES

1. D.E. Clark and W.H. Sutton, "Microwave Processing of Materials," *Annual Reviews Material Science*, 1996, v. 26, pp. 299-331.
2. E. Kubel, "Advancements in Microwave Heating Technology," *Industrial Heating*, 2005, v. 62, n. 1, pp. 43-53.
3. T. Gerdes, M. Willert-Porada, and K. Rödiger, "Microwave Sintering of Tungsten-Cobalt Hardmetals," *Mater. Res. Soc. Symp. Proc.*, 1996, v. 430, 45-50.
4. R.M. Anklekar, D.K. Agrawal, and R. Roy, "Microwave Sintering and Mechanical Properties of PM Copper Steel," *Powder Metallurgy*, 2001, v. 44, n. 4, pp. 355-362.
5. R. Roy, R. Peelamendu, C. Grimes, J. Cheng and D. Agrawal, "Major Phase Transformations and Magnetic Property Changes Caused by Electromagnetic Fields at Microwave Frequencies," *Journal Material Research*, 2002, v. 17, n. 12, pp. 3008-3011.
6. A. Upadhyaya, G. Sethi, H. Kim, D.K. Agrawal, and R. Roy, "Densification of Premixed and Prealloyed Cu-12Sn Bronze during Microwave and Conventional Sintering," *Advances in Powder Metallurgy & Particulate Materials 2002*, MPIF, Princeton, NJ, USA, v. 13, 2002, pp. 364-375.
7. G. Sethi, A. Upadhyaya, and D. Agrawal, "Microwave and Conventional Sintering of Premixed and Prealloyed Cu-12Sn Bronze," *Science of Sintering*, 2003, v. 35, pp. 49-65.
8. R. Roy, D.K. Agrawal, J.P. Cheng, and S. Gedevarishvilli, "Full Sintering of Powdered Metals using Microwaves," *Nature*, 1999, v. 399, n. 17, pp. 668-670.
9. J.M. Hill and T.R. Merchant, "Modeling Microwave Heating," *Applied Mathematical Modeling*, 1996, v. 20, pp. 3-15.
10. K.S. Yee, "Numerical Solution of Initial Boundary Value Problems Involving Maxwell's Equations in Isotropic Media," *IEEE Transactions on Antennas and Propagation*, 1966, v. AP-14, n. 3, pp. 302-307.
11. Q. Zhang, T.H. Jackson and A. Ungan, "Numerical Modeling of Microwave Induced Natural Convection," *International Journal Heat Mass Transfer*, 2000, v. 43, pp. 2141-2154.
12. J. Tucker, M.F. Iskander, and Z. Huang, "Calculation of Heating Patterns in Microwave Sintering Using a 3D Finite-Difference Code," *International Journal Heat Mass Transfer*, 2000, v. 43, pp. 2155-2160.
13. J. Clemens and C. Saltiel, "Numerical Modeling of Materials Processing in Microwave Furnaces," *International Journal Heat Mass Transfer*, 1996, v. 39, n. 8, pp. 1665-1675.
14. J. Lasri, P.D. Ramesh and L. Schachter, "Energy Conversion During Microwave Sintering of a Multiphase Ceramic Surrounded by a Susceptor," *Journal American Ceramic Society*, 2000, v. 83, n. 6, pp. 1465-1468.
15. M.P. Craven, T.E. Cross and J.G.P. Binner, "Enhanced Computer Modeling for High Temperature Microwave Processing of Ceramic Materials," *Proc. 5th Symp. on Microwave Processing of Materials*, MRS, Warrendale, PA, USA, v. 430, 1996, pp. 351-356.
16. Y. Alpert and E. Jerby, "Coupled Thermal-Electromagnetic Model for Microwave Heating of Temperature-Dependent Dielectric Media," *IEEE Transactions Plasma Science*, 1999, v. 27, n. 2, pp. 555-562.
17. D.M. Pozar, *Microwave Engineering*, 2nd ed., J. Wiley & Sons, Toronto, Canada, 2001, pp. 1-49.
18. S. Gedevarishvilli, D. Agrawal, R. Roy, and B. Vaidyanathan, "Microwave Processing using Highly Microwave Absorbing Powdered Material Layers," U.S. Patent 6512216, January 2003, pp. 1-6.
19. D.R. Lide (ed.), *CRC Handbook of Chemistry and Physics*, 79th ed., CRC Press, Boca Raton, FL, USA, 1998.
20. G. Sethi, "Experimental and Theoretical Study of Microwave and Conventional Sintering of Bronze," B.Tech. Project Report, Indian Institute of Technology, Kanpur, India, 2003, pp. 10-40.
21. P. Mishra, "Microwave Sintering of Tungsten Heavy Alloys," B.Tech. Project Report, Indian Institute of Technology, Kanpur, India, 2004, pp. 12-30.
22. R.M. Anklekar, K. Bauer, D.K. Agrawal, R. Roy, "Improved Mechanical Properties and Microstructural Development of Microwave Sintered Copper and Nickel Steel P/M Parts," *Powder Metallurgy*, 2005, v. 48, n. 8, pp. 39-46.

23. E.A. Brandes and G.B. Brook (eds.), *Smithells Metals Reference Book*, 7th ed., Butterworth Heinemann, Oxford, UK, 2000.
24. A. Cezairliyan and J.L. McClure, *J. Res. of the National Bureau of Standards*, 1971, v. 75A, n. 4, pp. 283-290.
25. A. Upadhyaya and G. Swaminathan, "Tubular Microwave Sintering Furnace with Inert and Reducing Gas Flushing for Sintering Metallic Samples," Indian Patent, New Delhi, India, 2005 (submitted)
26. S.K. Tiwari, U. Ravikiran, and A. Upadhyaya, "Microwave Sintering of Non- Ferrous Metal Powder Compacts," Euro PM2004 Conference Proceedings, v. 2:Sintering, H. Danninger and R. Ratzl (eds.), EPMA, Shrewsbury, UK, 2004, pp. 149-154.
27. B. Vaidhyanathan and K.J. Rao, "Microwave Assisted Synthesis of Technologically Important Transition Metal Silicides, *Journal of Materials Research*, 1997, v. 12, n. 12, pp. 3225-3229.
28. A. Nayer, *The Metals Databook*, McGraw-Hill, New York, NY, USA, 1997.

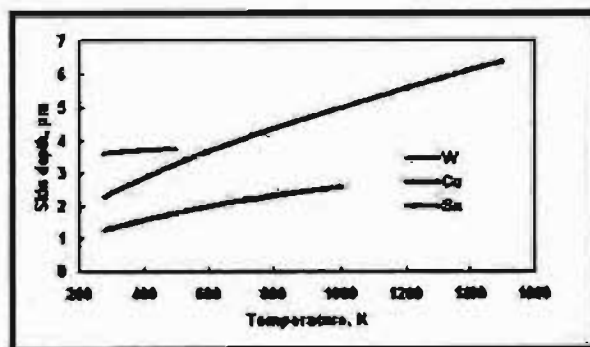


Figure 2. Effect of temperature on the calculated skin-depth of tin, copper and tungsten for a 2.45 GHz microwave.

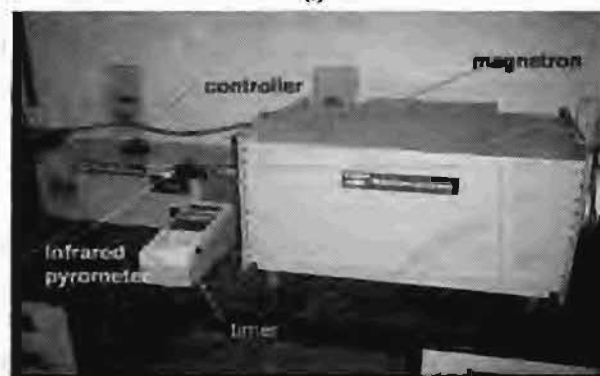
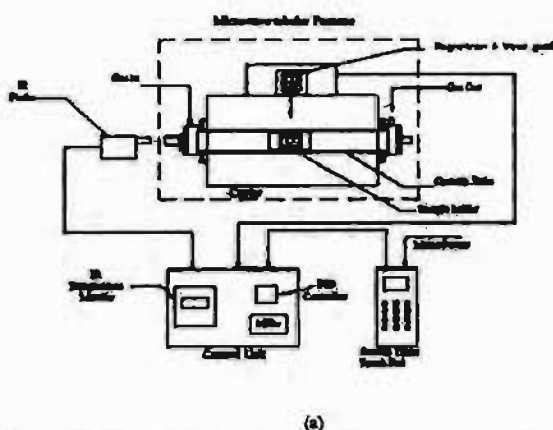


Figure 3. Schematic diagram (a) and photograph (b) of the microwave furnace used in the present study.

Table 1. Physical and thermal properties of metals in current study [23,24].

Properties	Sn	Cu	W
Average powder size, μm	75	75	6
Density, gcm^{-3}	7.3	8.9	19.3
Heat capacity (C_p), $\text{Jg}^{-1}\text{K}^{-1}$	$221.9 \times 10^{-4} T$ $+ 155.7$	$92 \times 10^{-4} T$ $+ 353.9$	$133.7 \times (12.7 \times 10^{-4} T)$ $- 42 T^2 + (6.4 \times 10^{-4} T^3)$
Electrical resistivity, $\mu\Omega\text{-cm}$	$4.2 \times 10^{-8} (T-293) + 12.8$	$6.8 \times 10^{-8} (T-293) + 1.3$	$8.07 \times (T/1400)^{1.2}$ [for $T > 400\text{K}$]
Emissivity	0.05	0.10	0.43

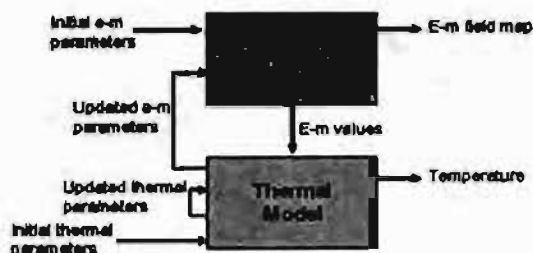


Figure 1. Schematic representation of the electromagnetic-thermal modeling approach adopted in the present study.

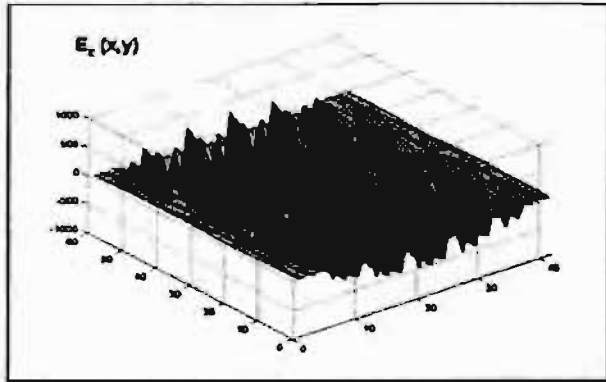


Figure 4. 2-D spatial distribution of $E_z(x,y)$, in V/m, inside cavity.

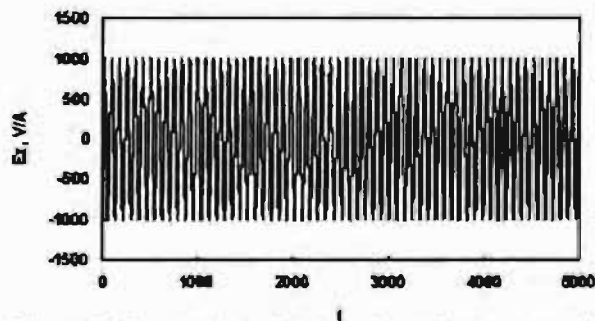


Figure 5. E_z varying with time domain at centre of the cavity.

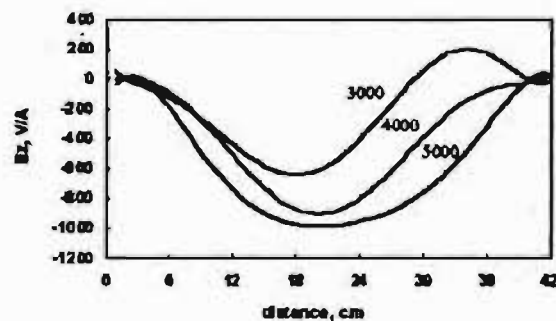


Figure 6. Cross-sectional view of Electric field (E_z) at centre of the cavity along x -direction at different time intervals.

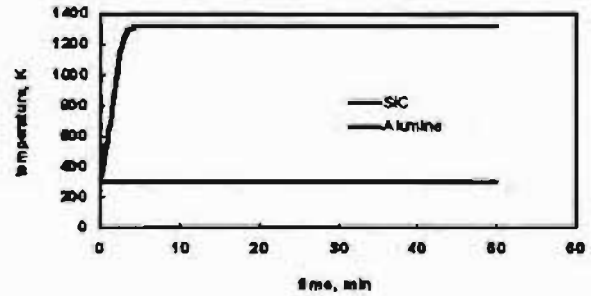


Figure 7. Temperature-time curve for SiC and Al_2O_3 .

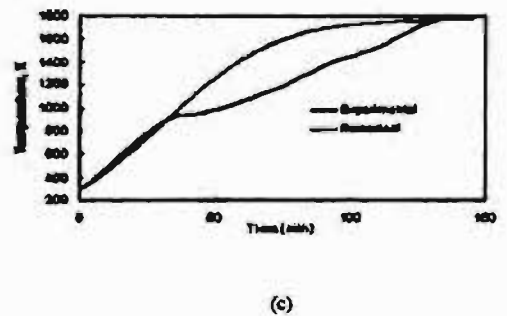
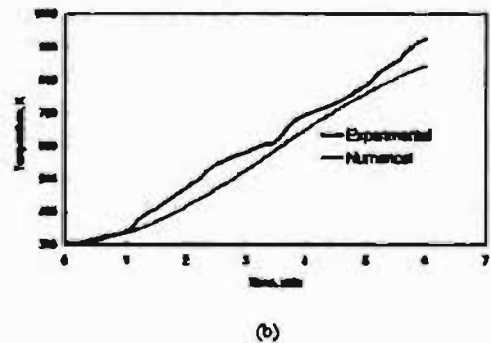
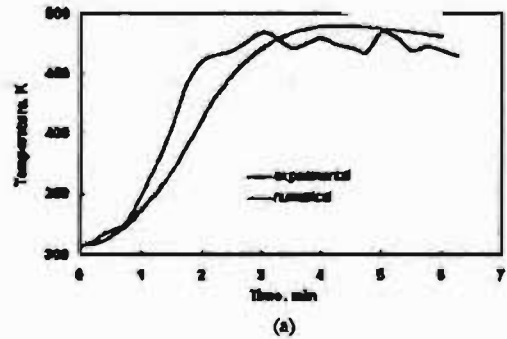


Figure 8. Comparison of the numerically simulated and experimentally determined heating profiles of (a) Sn, (b) Cu, and (c) W-alloy compact.

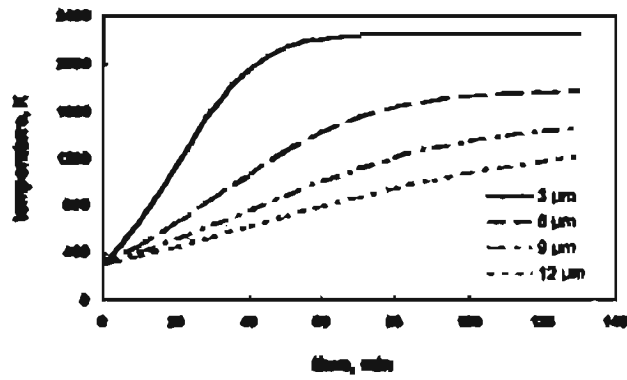


Figure 9. Effect of variation of initial powder size on the predicted heating profile of tungsten compact.

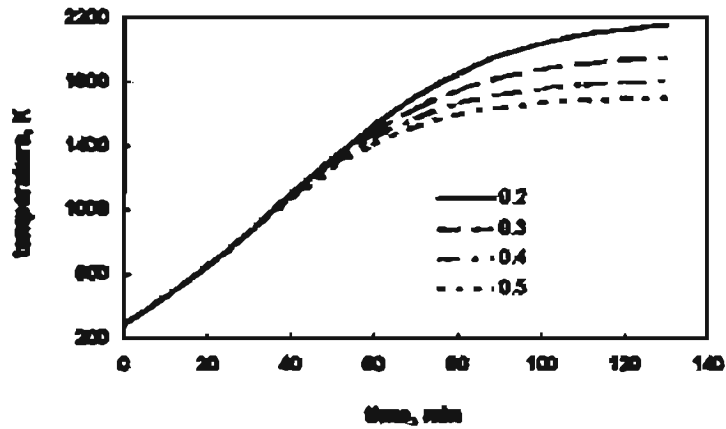


Figure 10. Effect of variation of emissivity on the predicted heating profile of tungsten compact.

MICROWAVE SINTERING OF TUNGSTEN HEAVY ALLOYS

S.K.Tiwari, P. Mishra and A. Upadhyaya

Department of Materials and Metallurgical Engineering, IIT,Kanpur 208016, India

ABSTRACT

In recent years, microwave processing of metal/alloy powders have gained a considerable potential in the field of material synthesis. The present paper compares the effect of microwave and conventional sintering on tungsten heavy alloys. Premixed 92.5W-6.4Ni-1.1Fe (wt %) were liquid phase sintered. Compacts were characterized for their sintered density. The present study also includes the stereological quantification, EPMA analysis, bulk hardness and micro hardness analysis of the compacts.

I. INTRODUCTION

Tungsten is a refractory metal with a melting point of 3420°C [1]. Typically, the composition of heavy alloys range from 60-98 (wt %) tungsten with addition of relatively low melting point transition elements, such as nickel, iron, copper, cobalt and manganese [2-4]. Primarily, liquid phase sintering (LPS) is used for consolidating these alloys, because full densification cannot be achieved through solid-state sintering. Sintered tungsten heavy alloys (WHAs) offer a unique combination of properties such as high density (16-18 g/cm³), high strength (1000-1700 MPa), high ductility (up to 30%), good corrosion resistance and easy machinability [5]. Nowadays, microwave processing is being applied for materials synthesis through sintering [6-9]. Microwaves belong to the portion of the electromagnetic spectrum with wavelengths ranging from 1 mm to 1 m with corresponding frequencies ranging from 300 MHz to 300 GHz [10]. However, the two most commonly used frequencies are 0.915 and 2.45 GHz [11]. During microwave heating, the entire part couples with the energy field, directly absorbing energy through out the volume. This means that the part is much hotter than the 2 surrounding atmosphere, so it will cool from the surface through radiation. It is called an "inverse profile" relative to the conditions in conventional heating where the surface is hotter than the core. This leads to certain intrinsic advantages of microwave heating over conventional heating such as rapid-heating rates, cost savings (time and energy, reduced floor space), volumetric and uniform heating, improved quality and properties and environmentally more clean [9]. Till recently, most of the microwave processing was restricted to ceramic materials [12] and cemented carbides [13-16]. Applicability of microwave sintering to metals was ignored due to the

fact that they reflect microwaves. Roy *et al* [17] reported that metals too can be processed by microwave heating provided they are in powder form. Subsequently, microwave sintering of P/M steel was conducted and it was reported that microwave sintered copper steel (FC-0208) when compared to conventional sintering, has higher sintered density, flexural strength and hardness [18,19]. Elsewhere, Upadhyaya *et al* [20] has shown the effects of microwave sintering on Cu-Sn alloy. It was found that there is no compact swelling during microwave sintering unlike conventional furnace sintering of premixed Cu-12Sn, which is beneficial for structural applications.

Density is the key requirement during sintering of tungsten based heavy alloys (W-Ni-Fe, W-Ni-Cu). One of the main applications of tungsten heavy alloys (WHAs) is in ordnance as kinetic energy penetrators, radiation shielding, where higher mechanical property is required. In conventional sintering, these alloys exhibit considerable microstructural coarsening. It is envisaged that restricting the growth of W-grains will further enhance the properties of these alloys. In order to validate the above hypotheses, microwave furnace offers a viable technique to heat up the compacts more rapidly and uniformly. The study therefore aims at investigating the densification response, microstructural evolution and mechanical properties of microwave sintered WHA (W-Ni-Fe) and compare those obtained via conventional sintering.

II. EXPERIMENTAL PROCEDURE

For present study, a 92.5W-6.4-Ni-1.1Fe (wt%) composition was selected, is the most commonly used in defense applications. The elemental powders were supplied by WIDIA Kennametal Ltd. The as-received powders were

characterized for their physical properties 3 using standard methods (Table 1). Subsequently, the powders were mixed in a required proportion in a Turbula mixer (Type 2C, Bachofen AG, Switzerland) for about 30 min. A die of 12.7 mm inner diameter was used for making green cylindrical compacts applying pressure of 200 MPa uniaxially using a semi-automatic hydraulic press (Model CTM 50) of 50 ton capacity. The as-pressed compact was conventionally sintered in a MoSi₂ (super kanthal) heated, microprocessor controlled automatic programmable tubular furnace (model: OKAY 70T-4, supplier: Bysakh & Co., Kolkata, India). The furnace had a heating zone of 110 mm, which can maintain the temperature profile with an accuracy of $\pm 3^\circ\text{C}$. The atmosphere maintained was reducing by supplying the commercially pure dry H₂ (dew point -35°C) with a flow rate of 1 lpm. The sintering was done at 1500°C for 1 hr. Subsequently the samples were furnace cooled. In another set of experiment, a 2 kW commercial microwave oven (Sinterwave, BHEL, Corporate R&D, Hyderabad, India) with a 2.45 GHz multi-mode cavity was used to sinter the 92.5W-6.4Ni-1.1Fe as pressed sample in H₂ atmosphere. The soaking time given at the sintering temperature was 20 min. The details of the microwave furnace construction have been summarized elsewhere [21]. Unlike conventional sintering thermocouple cannot be used to measure temperatures in microwave furnaces; instead we use infrared pyrometer (Mikron M680) to monitor the sample temperature. The infrared pyrometer was coupled with data acquisition and display software on a personal computer. The densities of cylindrical green compacts and sintered compacts were quantified by dimensional measurements. An analytical balance with upto four decimal points precision was used for all the measurements. Percentage theoretical density calculation was done with the help of theoretical density. Theoretical density (ρ_{th}) was calculated using inverse rule of mixture as per the formula

$$\frac{1}{\rho_{th}} = \frac{w_1}{\rho_1} + \frac{w_2}{\rho_2} + \frac{w_3}{\rho_3}$$

Densification parameter (ψ) was also calculated for both samples, to normalize the densification behavior, by the equation given below

$$\psi = \frac{\rho_s - \rho_g}{\rho_{th} - \rho_g}$$

where, ρ_g , ρ_s , and ρ_{th} are green density, sintered density and theoretical density, respectively. To study the elements

present and formation of any intermetallics in the samples, XRD patterns of both the samples were taken with the help of X-Ray Diffractometer (Model: RICH. SEIFERT & Co., GmbH & Co. KG, Germany). The experimental variables of the XRD are as follows: scan rate- $3.0^\circ/\text{min}$, target-Cu, and power- $30\text{ kV} \times 20\text{ mA}$. The microstructural characterization was done using Leica optical microscope with digital image acquisition capability. The elemental analysis was performed using EPMA (JEOL JXA-8600SX Superprobe, Japan) equipped with WDS. The operating conditions for EPMA such as magnification (1000x), spot size (2 μm), probe current ($5 \times 10^{-8}\text{ A}$) working distance, tilting angle and take off angle were all kept constant for all samples. Subsequently, microstructures were stereologically quantified using image analyzer (Leica mikroskopie & systeme, GmbH, Wetzlar, Germany). Solid volume fraction (V_s), grain size, interfacial area per unit volume (S_v), dihedral angle ($\bar{\theta}$), connectivity (C_c) and contiguity (C_g) were calculated both automatically as well as manually with the help of image analyzer. V_s was measured by drawing a binary grid of 5×5 matrix and calculating the point fraction ($P_s = V_s$). Grain size was measured by line intercept method, while as S_v was calculated by the following Equation $S_v = 2PL$ where, PL is the number of interface intercepts per unit length of the line drawn. The angle formed by grain boundary with liquid during sintering is called dihedral angle ($\bar{\theta}$). Dihedral angle calculation was done by measuring 200 angles on a micrograph manually. After measuring angles, a plot was drawn between percentage cumulative versus dihedral angle, and the angle corresponding to median value was determined.

Connectivity (C_c) is the two-dimensional grain co-ordination number and is measured by counting the number of nearest touching grains for 200 chosen central grains in a micrograph; and mean was taken as connectivity. The contiguity (C_g), which is microstructural measure of the relative interface area of solid-solid bonds versus the total interface area during liquid phase sintering, was calculated by the equation given below

$$C_g = \frac{2N_{WW}}{2N_{WW} + N_{WM}}$$

where, N_{WW} and N_{WM} are the number of tungsten-tungsten contacts and tungsten-matrix contacts respectively per unit length of any given intercept. Bulk hardness of sintered compacts were measured by an automated and preprogrammed Vickers hardness tester (LECO V-100C1, Supplier: Akashi Corporation, Japan) applying 2 kg load

on all the microstructural surfaces. Micro-hardness tester (model: Leitz 8299, Germany) was used to perform the micro-hardness tests on the tungsten grains and matrix phases. The loads applied for the tungsten grain and the matrix were 50 g and 5 g respectively for 15 s.

III. RESULTS

Heating Profile

Figure 1 compares the heating profiles and power consumption of 92.5W-6.4Ni-1.1Fe compacts during microwave and conventional sintering. In case of microwave heating, the sintering time reduces by 45% as compared to the conventional sintering. As depicted by figure, the microwave sintering is more efficient and cuts about 50% power consumption.

Sintered Density and Densification Parameter

The sintered density and densification parameter values for tungsten heavy alloy are compiled in Table 2. Both microwave and conventional sintered WHAs show similar densification parameter, though processing time for microwave sintering is quite low with compared to the conventional one. This could be attributed to both having similar sintered density and underscores the efficacy of microwave furnace in consolidating these alloys. As shown in Figure 2, the W grain size in microwave sintered condition is smaller (W-grain size-9.4 μ m) as compared to its conventional counterpart (W-grain size-17.3 μ m).

Stereological Characterization

All stereological parameters are summarized in Table 3. The corresponding values of solid volume percentage (Vs), connectivity (Cc), Contiguity (Cg) and interfacial surface area per unit volume (Sv) for both samples are plotted in Figure 3. Microwave sintered alloy has lower value of mean grain size (9.4 μ m) as compared to conventionally sintered alloy (17.3 μ m) as it can be seen from Figure 4. In case of microwave sintering, values of Cg, Cc and Vs are relatively higher. Grain boundary surface area per unit volume was calculated for both tungsten-tungsten (SWW) and tungsten-matrix (SWM). It was found that tungsten-matrix interface area is slightly more in case of conventional sintering, whilst there is large difference between tungsten-tungsten interfacial areas of both samples. Figure 5 shows the curve of percentage cumulative dihedral angle distribution. The conventionally sintered sample has lower value of mean dihedral angle ($\bar{\phi}$ 50).

Phase Analysis

Figure 6 compares the XRD patterns of the conventional and microwave sintered tungsten heavy alloy samples taken with the help of X-Ray Diffractometer. In XRD pattern of

the conventionally sintered sample, there were more number of peaks observed than the microwave sintered sample. Comparing with the standard patterns of W, Ni, Fe and the intermetallics formed by them, confirmed the formation of various intermetallics in case of conventionally sintered sample (FeNi, NiW, Fe7W6).

Electron Probe Micro Analysis (EPMA)

Figure 7a and 7b show the microstructures of microwave and conventionally sintered samples at 1000x taken during the EPMA analysis along with the X-Ray mapping results which depict that in the microwave sintered sample, tungsten content of matrix as well as of grains is nearly same in both cases.(see Table 4)

Hardness

Figure 8a shows the comparison of bulk hardness values (VHN) of both samples. It was observed that microwave sintered alloys has higher hardness value. Figure 8b shows the comparison of micro-hardness values of the alloys sintered by two different heating processes. It was found that microwave sintered alloy has higher value of micro-hardness in the grains but lesser in the matrix phase.

IV. DISCUSSION

As shown in Table 2, though processing time for microwave sintering is quite low, densification parameter of both samples is almost same i.e. 0.93 and 0.94 for microwave and conventionally sintered samples respectively. This is possibly due to the higher heating rate in microwave sintering which leads to faster densification. One of the implications of faster sintering is reduced microstructural coarsening [19]. At present, the issue of microwave effects is quite contentious. Many of the expected results from microwave processing such as rapid and uniform heating, inverse temperature profile, more uniform microstructure and selective heating are included in the category of microwave effects. However, this anomaly cannot be easily explained on the basis of our present understanding. Enhancement in the rates of activated process involving material transport is considered microwave effect because they require lower activation energy [22]. Freeman *et al.* [23] has suggested that the rectified potential, generated due to the microwave fields, causes the enhanced reaction and sintering rates. They used single-crystal NaCl and imposed a variable external bias voltage. Currents were measured during exposure to microwave fields. They found the increase in current applying the microwave fields. The additional driving force is attributed to the asymmetry in the defect density on surface of the crystal. The uneven distribution of surface charge introduces a space charge polarization that couples with the microwave field and

produces a rectified potential. They suggested that this phenomenon could be the reason for the enhanced reaction and sintering rates observed by several other investigators. It is evident from microstructures that volume fraction of solid (tungsten grains) is higher for microwave sintered alloy. In microwave sintering, short processing time also leads to less diffusion of W into the matrix and thus higher volume percentage of W grains as we know that the diffusion is proportional to the time. The liquid penetration studied by Fredriksson *et al* [24] shows that the penetration is proportional to the square root of time. The driving force for outward diffusion of tungsten is estimated from the capillary inflow creating a pressure gradient along penetrated grain boundaries and thus resulting in a concentration gradient. So, in case of microwave sintering the gradient is not so strong due to less time available, causing higher value of SW-W, solid volume fraction and contiguity. This means less diffusion of tungsten into the matrix leads to more number of tungsten-tungsten contacts remaining. Therefore, ductility and hence toughness of the specimen will be lesser in case of microwave sintering. The microstructural parameters determined by stereological quantification, have interrelationship with each other and the variations between them have been reported by Upadhyaya [25]. German compiled the variation of contiguity (C_g) with the volume fraction tungsten in WHAs for various dihedral angles (\hat{O}) and observed that the lower the dihedral angle, the smaller is the contiguity. He also correlated the effects of various processing parameters, such as interfacial energies, grain size ratios and solid content on the contiguity. His model suggests that the contiguity increases with an increasing solid content and dihedral angle. However, the grain size ratio is of little influential. German's empirical formula relating contiguity (C_g) with the solid content (V_s) and the dihedral angle (\hat{O}) is as follows:

$$C_g = V_s^2 (0.43 \sin \hat{O} + 0.35 \sin^2 \hat{O}) \dots \dots \dots (3)$$

When compared to the model provided by German, it is found that the quantified stereological parameters are in good consent with it and is illustrated in Figure 9. Gurland [26] empirically expressed the grain contiguity (C_g) as a function of the connectivity (C_c) and dihedral angle as follows:

$$C_g = C_c \left(\frac{1 - \cos \frac{\phi}{2}}{3 - \cos \frac{\phi}{2}} \right) \dots \dots \dots (4)$$

Figure 10 represents the variation in the contiguity as a function of dihedral angle for a given range of connectivities. As predicted, a higher connectivity and a large dihedral angle result in a highly contiguous microstructure. These microstructural properties have an important role in governing mechanical properties of tungsten heavy alloys. Both tensile strength and ductility decreases with increase in contiguity [27]. Hardness depends on the volume fraction of the harder phase and it decreases as the amount of matrix increases. Moreover the hardness decreases as the grain size increases, due to greater separation of grains. A high contiguity aids the hardness because of greater rigidity from the solid-solid contacts. It was observed that microwave sintered sample has higher hardness value, which confirms the hypothesis. The determined values of contiguity, dihedral angle, grain size and solid volume percentage also substantiate the hardness result. Micro-hardness of matrix phase depends on the amount of harder phase in the matrix. It is higher for higher value of tungsten solubility in matrix. In case of microwave sintered sample, solubility of tungsten in matrix is less than that of conventionally sintered. As in conventional sintering more time is provided which causes more diffusion of tungsten in the matrix phase. So in later case, we got the higher hardness of matrix phase. As compared to the microwave sintered WHA, the XRD pattern of conventionally sintered alloy shows formation of intermetallics (FeNi, NiW, Fe7W6). These intermetallics impart brittleness to the alloy and are attributed to slower thermal cycle which provides sufficient time for interdiffusion to attain equilibrium configuration as per the W-Ni-Fe phase diagram. It is well-known that any deviation from Ni: Fe ratio of 7:3 results in intermetallic phase formation [28]. The present composition had Ni: Fe ratio of 6:1 and hence the intermetallic formation was expected during conventional sintering. An implication of the result is that microwave sintering can be utilized effectively even for non-stoichiometric binder composition.

V. SUMMARY

This study compares the sintering behavior of W-Ni-Fe powder compacts in a microwave and conventional furnace. WHAs can be sintered in significantly lesser time in microwave furnace. The 92.5W-Ni-Fe alloy in the present study had non-stoichiometric binder composition and yet resulted in no intermetallic formation during microwave sintering. Moreover, the microwave sintered W-Ni-Fe showed significantly smaller W-grains as compared to conventional sintering, which led to enhancement in hardness. It is envisaged that microwave sintering offers a potentially viable means to consolidate tungsten heavy alloys for structural and high performance ordnance applications.

VI. REFERENCES

1. G.S. Upadhyaya, "Molybdenum and Tungsten- Their Relative Assessment," *International Journal of Refractory Hard Metals*, Sep. 1987, vol. 6, no.3, pp.
2. G.S. Upadhyaya, "Sintered Heavy Alloys- A Review," *International Journal of Refractory Hard Metals*, March 1986, vol. 5, no.2, pp.
3. R.M. German, *Powder Metallurgy Science*, 2nd edition, Metal Powder Industries Federation, Princeton, NJ, USA, 1994.
4. M.H. Hong, J.W. Noh, W.H. Baek, E.P. Kim, H.S. Song, and S. Lee, "A Study on the Improvement of the Sintering Density of W-Ni-Mn Heavy Alloys," *Metallurgical and Materials Transactions B*, 1997, v. 28, pp. 835-839.
5. A. Upadhyaya, "Processing Strategy for Consolidating Tungsten Heavy Alloys for Ordnance Applications," *Materials Chemistry Physics*, 2001, v. 67, pp. 101-110.
6. K.J. Rao and P.D. Ramesh, "Use of Microwaves for the Synthesis and Processing of Materials," *Bulletin Material Science*, 1995, v.18, pp. 447-465.
7. D.E. Clark and W.H. Sutton, "Microwave Processing of Materials," *Ann. Rev. mater. Sci.*, v.26, 1996, pp. 299-331.
8. W.H. Sutton, "Microwave Processing of Ceramic Materials," *Ceramic Bulletin*, 1989, v. 68, pp. 376-384.
9. D.M. Pozar, *Microwave Engineering*, 2nd ed., John Wiley & Sons, Toronto, Canada, 2001.
10. K.C. Gupta, *Microwaves*, New Age International, New Delhi, India, 1983.
11. R. Wroe, "Microwave Sintering Coming of Age," *Metal Powder Report*, 1999, v. 54, n. 7, pp. 24-28.
12. D.K. Agrawal, A.J. Papworth, J. Cheng, H. Jain and D.B. Williams, "Microstructural Examination by TEM of WC/Co Composites Prepared by Conventional and Microwave Processes," *Proceedings 15th International Plansee Seminar*, v. 2, G. Kneringer, P. Rodhammer and P. Wilhartitz (eds.), Plansee AG, Reutte, Austria, 2001, pp. 677-684.
13. D.K. Agrawal, J. Cheng, A. Lackner and W. Ferstl, "Microwave Sintering of Commercial WC/Co Based hard Metal Tools," *Proceedings of European Conference on Advances in Hard Materials Production EURO PM'99*, EPMA, Shrewsbury, UK, 1999, pp. 175-182.
14. T. Gerdes, M. Willert-Porada and K. Rodiger, "Microwave Sintering of Tungsten-Cobalt hard metals," *Material Research Society Symposium Proceedings*, 1996, v.430, pp. 45-50.
15. T. Gerdes, M. Willert-Porada, K. Rodiger and K. Dreyer, "Microwave Sintering of Tungsten Carbide-Cobalt hardmetals," *Mater. Res. Soc. Symp. Proc.*, v.430, 1996, pp. 175-180.
16. D. Agrawal, "Microwave Sintering of Ceramics, Composites, Metals, and Transparent Materials: Recent developments at MRL/PSU," *Proceedings 7th International Conference on Microwave and High Frequency Heating*, 1999, pp. 263-267.
17. M.J. Yang and R.M. German, *Advances in Powder Metallurgy Particulate Materials*, v. 1, n. 3, MPIF, Princeton, NJ, USA, 1999, pp. 207-219.
18. M. Willert-Porada and H.S. Park, "Heating and Sintering of Steel Powders with Microwaves at 2.45GHz Frequency- Relationship between Heating Behavior and Electrical Conductivity," *Microwaves: Theory and Application in Materials Processing V*, D.E. Clark, J.G.P. Binner and D.A. Lewis (eds.), American Ceramic Society, Westerville, OH, USA, 2001, pp. 459-470.
19. M. Anklekar, D.K. Agrawal and R. Roy, "Microwave Sintering and Mechanical Properties of P/M Copper Steel," *Powder Metallurgy*, 2001, v. 44, pp. 355-362.
20. A. Upadhyaya, G. Sethi, H. Kim, D.K. Agrawal and R. Roy, "Densification of Pre-mixed and Prealloyed Cu-12Sn Bronze during Microwave and Conventional Sintering,"
21. A. Upadhyaya and G. Swaminathan, "Tubular Microwave Sintering Furnace with Inert and Reducing Gas Flushing for Sintering Metallic Samples," *Indian Patent*, New Delhi, India 2005 (submitted).
22. D.E. Clark, "Microwave Processing of Materials," *Annual Reviews Material Science*, 1996, v. 26, pp. 21-31.
23. S.A. Freeman, J.H. Booske, R.F. Cooper, "Microwaves: Theory and Application in Material Processing III", *Ceram. Trans. Westville*, 1995, pp. 2042-45.
24. H. Fredriksson, A. Eliasson, I. Ekblom, "Penetration of Tungsten Grain Boundaries by Liquid W-Ni-Fe Matrix," *International Journal Refractory Metals Hard Materials*, 1995, n. 4, pp. 173-179.
25. A. Upadhyaya, "A Microstructure-Based Model for Shape Distortion during Liquid Phase Sintering,"

Ph.D. Thesis, The Pennsylvania State University, University Park, PA, USA, 1998.

26. J. Gurland, "The measurement of Grain Contiguity in Two-Phase Alloy," *Transaction AIME*, 1958, v. 212, pp. 452-455.
27. K.M. Ramkrishnan and G.S. Upadhyaya, "Effect of Composition and Sintering on Densification and Microstructure of Tungsten Heavy Alloys Containing Copper and Nickel," *Journal Material Science Letter*, 1990, v. 9, pp. 456-459.
28. S.G. Caldwell, "Variation of Ni to Fe Ratio in W-Ni-Fe Alloys: A Current Perspective," Tungsten and Tungsten Alloys -1992, Metal Powder Industries Federation, NJ, USA, 1992, pp. 89-96.

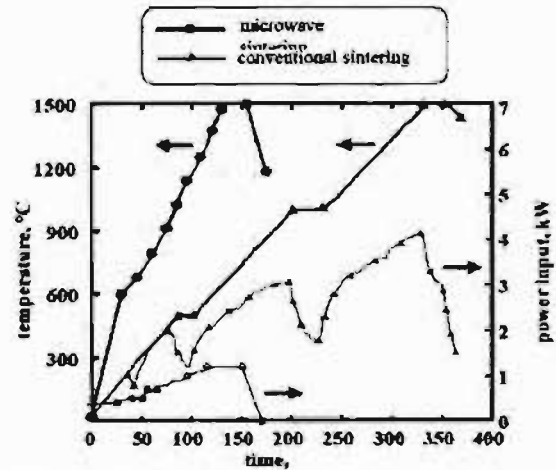


Figure 1: Comparison of heating profile and power consumption of microwave and conventionally sintered 92.5W-6.4Ni-1.1Fe alloy.

Table 1: Characteristics of the as-received elemental powders.

Supplier	W	Ni	Fe
	Widia Kona-metal, India		
Apparent Density, g/cm ³ (% theoretical)	5.2 (27)	2.7 (30.3)	3.6 (48.9)
Flow Rate (g/30s)	3.25	Non flowing	5.3
Particle size, μm	D ₁₀	2.0	3.8
	D ₅₀	4.2	11.0
	D ₉₀	6.2	31.8

Table 2: Sintered densities of microwave and conventionally sintered 92.5W-6.4Ni-1.1Fe alloy samples.

sintering mode	sintered density, g/cm ³ (% theoretical)	densification parameter
Microwave	17.2 (97.1)	0.93
Conventional	17.3 (97.8)	0.94

Table 3: Comparison of stereological parameters of microwave and conventionally sintered 92.5W-6.4Ni-1.1Fe alloy samples.

Characteristics	Microwave Sintered (wt%)	Conventionally sintered (wt%)
Tungsten content (vol. %)	86.7 ± 4.7	78.0 ± 1.8
Grain Size (μm)	9.40 ± 0.5	17.3 ± 0.8
S, (μm^{-1})	0.31 ± 0.02	0.19 ± 0.02
Connectivity (C _v)	1.92 ± 0.7	1.78 ± 0.8
Contiguity (C _p)	0.42 ± 0.1	0.32 ± 0.1
Dihedral Angle (θ_{90})	63 ± 8	53.5 ± 7

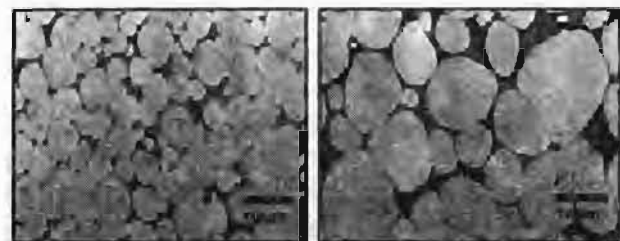


Figure 2: Scanning electron micrographs (a) microwave and (b) conventionally sintered 92.5W-6.4Ni-1.1Fe alloy.

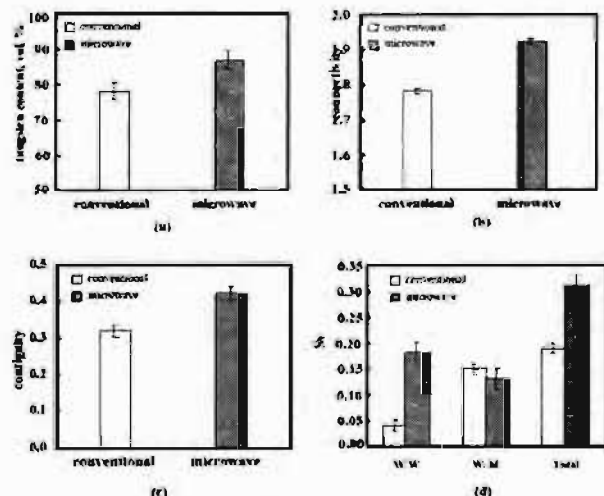


Figure 3: Effect of heating mode on the (a) tungsten content (vol. %), (b) connectivity, (c) contiguity, and (d) Sv of 92.5W-6.4Ni-1.1Fe alloy liquid phase sintered at 1500°C.

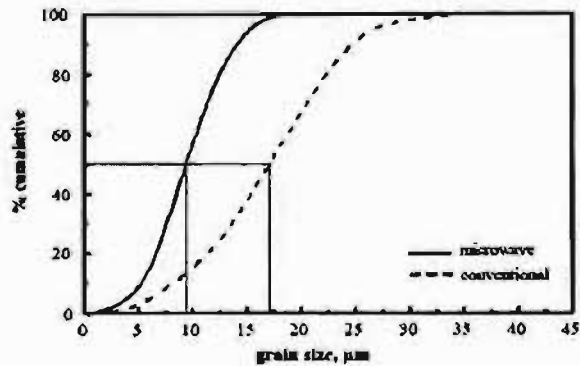


Figure 4: Tungsten grain size distribution in conventionally and microwave sintered 92.5W-6.4Ni-1.1Fe alloy.

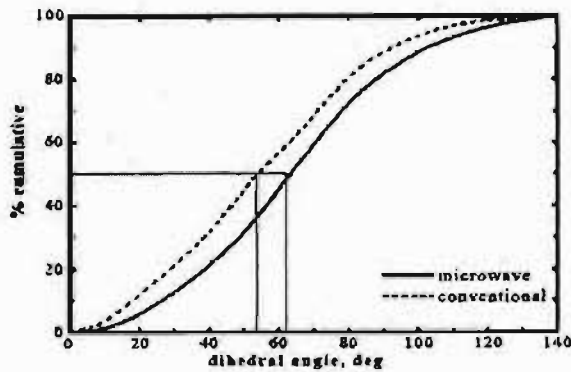


Figure 5: Dihedral angle distribution of 92.5W-6.4Ni-1.1Fe alloy liquid phase sintered at 1500°C in using microwave and conventional furnace.

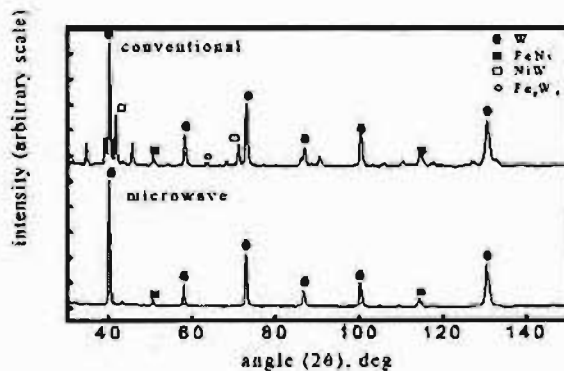


Figure 6: XRD pattern of microwave and conventionally sintered 92.5W-6.4Ni-1.1Fe alloy.

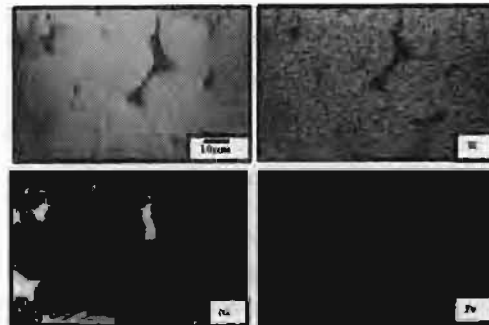
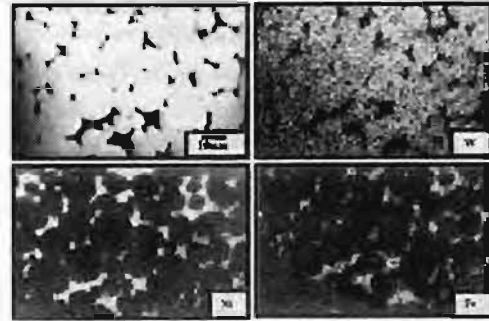


Figure 7: X-ray elemental mapping of 92.5W-6.4Ni-1.1Fe alloy liquid phase sintered at 1500°C in (a) microwave and (b) conventional furnace.

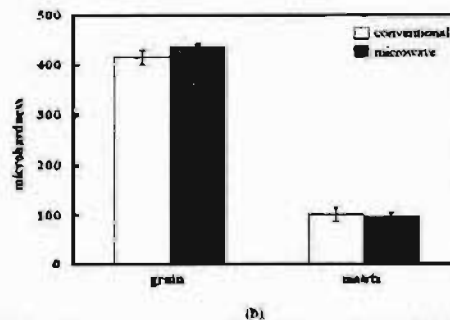
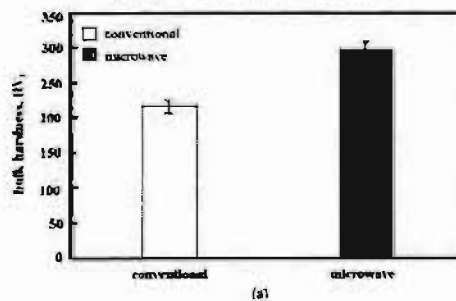


Figure 8: Effect of sintering mode on the (a) bulk and (b) micro-hardness of 92.5W-6.4Ni-1.1Fe alloy. The microhardness measurements were performed both on the tungsten grains as well as the matrix phase

EFFECT OF CONVENTIONAL VIS-À-VIS MICROWAVE SINTERING ON AUSTENITIC (316L) AND FERRITIC (434L) STAINLESS STEEL

S.S. Panda^{*}, V. Singh^{*}, A. Upadhyaya^{**}, D. Agrawal^{**}

^{*}Department of Materials and Metallurgical Engineering, IIT- Kanpur, India, ^{**}Materials Research Institute, The Pennsylvania State University, University Park, USA

ABSTRACT

This study takes a look into the field of Microwave Sintering and compares it with Conventional Sintering, as observed on the densification and properties of austenitic and ferritic stainless steel. After compaction, sintering was done at 1400 C in a radiatively heated (conventional) and 2.45 GHz microwave sintering furnace. Due to coupling with microwaves, the compacts heat up to the sintering temperature at a rapid rate. It was seen that though the compacts sintered in microwaves exhibit finer microstructure and take less time for sintering, yet there is no corresponding improvement in densification and mechanical properties. This occurs due to the presence of elongated, irregular pore structure in microwave sintered compacts.

INTRODUCTION

Powder metallurgical stainless steels represent a small fraction of the total amount of P/M products across the world. However, attractive combination of excellent corrosion resistance, a wide range of strength levels including strength retention at cryogenic and elevated temperatures, good formability and aesthetically pleasing appearance have made P/M stainless steels the material choice for a diverse range of application [1]. For stainless steel, P/M route offers many advantages over conventional casting techniques, which include lower processing temperature, near-net shaping, high final density, greater material utilization (> 95%) and a more refined microstructure that provides superior material properties. Typically, P/M stainless steels are consolidated through solid-state sintering, which, is conducted at a relatively lower temperatures. Consequently, the sintered compacts have residual porosity, which restricts their applications. In recent years, there has been a thrust to consolidate compacts at higher sintering temperatures through supersolidus liquid phase sintering [2, 3]. Supersolidus sintering involves heating between the solidus and liquidus temperatures to form the liquid phase. The presence of liquid phase generally enhances densification by increasing diffusion kinetics. Besides this, the capillary stress induced pore filling also contributes to densification. As stainless steels powders are typically fabricated through atomization, they have prealloyed, single phase structure, and therefore, are amenable to supersolidus sintering. However, one of

the limitations of using higher sintering temperature is microstructural coarsening. Typically, in conventional (electrically-heated) furnace compacts get radiatively heated during sintering. Consequently, to prevent thermal gradient within the compact, a slower heating rate coupled with isothermal hold at intermittent temperatures is provided, which increases the process time, thereby, contributing to coarsening. To eliminate this problem, a faster heating rate during sintering is envisaged. However, fast heating rates in conventional furnace result in thermal gradient within the compacts, which leads to compact distortion and inhomogeneous microstructure. One of the techniques to achieve relatively homogeneous as well as fast sintering in compacts is through microwave heating [4, 5]. Microwaves directly interact with the particulates within the pressed compacts and thereby provide rapid volumetric heating. This reduces processing time and results in energy saving. In addition, the uniform heating minimizes problems such as localized microstructural coarsening, thereby, yielding better properties. Recently, it was shown that metals too could couple with microwaves provided they are in powder form rather than monolithic [6]. Though there have been attempts to explain microwave heating of metal powders, still there is not yet any consensus on a comprehensive theory to explain the mechanism. Recently, it has been shown that steel powder compacts with Cu and Ni additives couple with microwaves and can be effectively sintered [7-9].

The present study investigates the microstructural, densification, and mechanical property response in straight 316L (austenitic) and 434L (ferritic) stainless steel consolidated using both microwave as well as conventional furnace sintering through supersolidus sintering route.

EXPERIMENTAL

The as-received gas-atomized 316L [Fe-16.5Cr-12.97Ni-2.48Mo-0.93Si-0.21Mn-0.025C-0.008S (in wt.%)] and 434L [Fe-17Cr-1Mo-0.2Mn-0.02C-0.02S-0.02P] stainless steel (supplier: Ametek Specialty Metal Products, USA) powders were uniaxially compacted at 600 MPa in to a green densities ranging between 80 to 82%. The sintering response on densification and microstructures were evaluated on cylindrical pellets (16 mm diameter and 6 mm average height). For measuring the tensile properties, flat tensile bars were pressed as per MIPF standard 10 [10]. The green (as-pressed) compacts were sintered using conventional and microwave furnace. The conventional sintering of green compacts were carried in a MoSi heated horizontal tubular sintering furnace (model: OKAY 70T-7, supplier: Bysakh, Kolkata, India) at a constant heating rate of 5°C/min. To ensure uniform temperature distribution during heating, intermittent isothermal hold for 15 to 30 min was provided at 500°C, 750°C, and 1000°C. The sintering temperatures selected for supersolidus sintering was 1400°C. Microwave sintering of the green compacts was carried out using a multi-mode cavity 2.45 GHz, 6 kW commercial microwave furnace (supplier: Cober). For both, sintering was carried out for 60 min in hydrogen atmosphere with dew point -35°C. Unlike a conventional furnace, the temperature of the samples inside a microwave furnace cannot be monitored using a thermocouple [11]. The temperature of the sample was monitored using an infrared pyrometer (Raytek, Marathon Series). The pyrometer is emissivity based; therefore temperature could not measure temperature below 700°C. Hence, for the temperature measurements for all the compacts was done by considering emissivity of steel (0.35) [12]. Typically, emissivity varies with temperature. However, as very little variation in the emissivity was reported in the temperature range used in the present study, hence, the effect of variation in emissivity was ignored in the present investigation.

The sintered density was obtained by dimensional measurements. The sinterability of the compact was also determined through densification parameter.

The microstructural analyses of the samples were carried out through optical microscope. The pore size was estimated by measuring the pore area, while pore shape was characterized using a shape-form factor, F , which is related to the pore surface area, A , and its circumference in the plane of analysis, P , as follows:

$$F = 24PA\lambda$$

Both pore area distribution and shape factor was directly measured using image analyzer. The shape factor of a feature is inversely proportional to its roundness. A shape factor of 1 represents circular pore in the plane of analysis and as it reduces the pores tend to become more irregular. Vickers bulk hardness measurements were performed on the samples at 2 kg load. The observed hardness values are the averages of five readings taken at random spots throughout the sample. The tensile test was conducted using a 10 kN capacity Universal Testing Machine at a constant cross-head speed 0.5 mm/min. From the tensile curves, the ultimate tensile strength and ductility were determined. To correlate the tensile properties with the microstructure, fractography analyses of the samples were carried out using SEM imaging (model: JSM-840A, supplier: JEOL, Japan).

RESULTS AND DISCUSSION

Figure 1 compares the thermal profiles of the 316L and 434L compacts sintered in conventional and microwave furnace. It is interesting to note that both 316L and 434L compacts couple with microwaves and get heated up rapidly. In case of microwave heating, temperature could only be measured from 700°C onwards. However, it takes about 5.5 min to heat up the compacts from room temperature to 700°C. The overall heating rate in microwave furnace was around 45 C/min. Taking into consideration the slow heating rate (5 C/min) and isothermal holds at intermittent temperatures in conventional furnace, there is about 90% reduction in the process time during sintering of stainless compacts in microwave furnace. In case of microwave sintering, a slight difference in the heating rates for the 316L and 434L compacts is observed which is attributed to dependence of microwave-metal coupling on the composition. Table 1 compares the densification response of both 316L and 434L stainless steel sintered in conventional and microwave furnace. In case of 316L stainless steel compacts, densification during microwave sintering is lower than that achieved through conventional sintering. In contrast, straight 434L compacts show almost comparable densification in both the sintering modes. This is also validated by comparing the densification parameters which follows similar trend as sintered density. It is interesting to note that irrespective of heating mode, the ferritic stainless compacts undergo higher densification as compared their austenitic counterparts. This can be attributed to relatively higher diffusivity in the more open bcc structure of 434L compacts.

Figures 2a and 2b compares the optical micrographs of conventional and microwave sintered straight 316L and 434L compacts. It is quite evident from Figure 2 that for

both stainless steels microwave sintering restricts microstructural coarsening. Furthermore, the optical micrographs of the sintered compacts reveal distinct differences in the pore morphology of microwave compacts *vis à vis* their conventional counterparts. For both straight 316L and 434L compacts, pores have relatively more rounded appearance in conventional sintering. In contrast, in microwave sintered compacts the pores appear distinctly elongated. This was verified by quantifying and comparing the distribution of pore area and shape factors of conventional and microwave sintered stainless steel compacts (Figures 3 and 4). Figures 3a and 3b compare the effect of heating mode on the pore area distribution in 316L and 434L compacts, respectively. For both stainless steels, microwave sintering results in smaller and narrower pore size distribution. This can be attributed to the lower propensity for pore coarsening due to lesser sintering time in case of compacts consolidated in microwave furnace. However, the trend in the pore shape factor distribution exhibits a reverse trend. In both austenitic as well as ferritic stainless steels, the microwave sintered compacts exhibit a broader range of shape factors and compared to their conventionally sintered counterparts and are skewed towards lower shape factor values, which is indicative of more irregular pores. The irregular porosity in microwave sintered austenitic stainless steel compacts is in contrast to trend shown in iron-copper steels. Anklekar *et al.* [9] have reported that Fe-2Cu-0.8C steels sintered in microwaves exhibit more rounded pore morphology. This could be attributed to the faster processing cycle, which does not yield sufficient time for pore rounding.

Table I shows the effect of heating mode on the bulk hardness, strength and ductility of sintered 316L and 434L stainless steels. It is evident that for both grades of stainless steel, microwave sintering invariably results in inferior mechanical properties. This trend is in contrast to recent observations by Anklekar *et al.* [8] on Fe-Cu-C steels wherein microwave sintered compacts exhibited higher strength as well as ductility. Figures 5a and 5b show representative fractographs of conventional and microwave sintered austenitic and ferritic stainless steel, respectively. Conventionally sintered 316L and 434L show distinct dimpled morphology which is characteristic of ductile failure. In contrast, the microwave sintered stainless steel compacts fail through intergranular decohesion. The inferior mechanical properties in case of microwave sintered stainless steel can be attributed to the elongated pore morphology (Figures 2 and 4), which act as stress-concentration sites and lead to premature, brittle failure at relatively lower load. While our results are conclusive for stainless steels, the effect of microwave sintering on the mechanical properties of other metallic powder systems

needs to be carefully assessed. The present study therefore underscores the need for fine tuning the sintering time compression strategies through microwave heating in ways that does not result in degradation of mechanical properties.

CONCLUSIONS

This study compares the effect of conventional and microwave heating on the densification, microstructural, and mechanical properties of 316L and 434L stainless steel sintered at 1400 C. For the first time, it has been shown that both 316L as well 434L compacts can be consolidated using a multimode microwave furnace. As compared to conventional furnace heating, the sintering time in a microwave furnace was reduced by about 90%. While in 434L steels, the sintered density of microwave stainless steel was higher than those sintered conventional, in 316L steels, microwave sintering resulted in lower density. The present study shows that despite restricted microstructural coarsening in both austenitic and ferritic stainless steel, microwave sintering results in lower hardness, strength and ductility. This has been correlated to the relatively irregular and elongated pore morphology in microwave sintered stainless steel compacts.

REFERENCES

1. R.M. German, *Powder Metallurgy of Iron and Steel*, John Wiley, New York, NY, USA, 1998.
2. R.M. German, "Supersolidus Liquid-Phase Sintering of Pre-alloyed Powders," *Metallurgical Materials Transactions A*, 1997, v. 28A, pp. 1553-1567.
3. L. Cambal and J.A. Lund, "Supersolidus Sintering of Loose Steel Powders," *International Journal of Powder Metallurgy*, 1972, v. 8, n. 3, pp. 131-140.
4. D.E. Clark, W.H. Sutton, "Microwave Processing of Materials," *Ann. Rev. Mater. Sci.*, v.26, 1996, pp. 299-331.
5. W.H. Sutton, "Microwave Processing of Ceramic Materials," *Ceram. Bull.*, v.68, n.2, 1989, pp. 376-384.
6. R. Roy, D.K. Agrawal, J.P. Cheng, and S. Gedevarishvili, "Full Sintering of Powdered Metals using Microwaves," *Nature*, v.399, n.17, 1999, pp. 668-670.
7. M. Willert-Porada and H.S. Park, "Heating and Sintering of Steel Powders with Microwaves at 2.45GHz Frequency- Relationship between Heating Behavior and Electrical Conductivity," *Microwaves: Theory and Application in Materials Processing V*, D.E. Clark, J.G.P. Binner, and D.A. Lewis (eds.).

EFFECT OF CONVENTIONAL VIS-À-VIS MICROWAVE SINTERING ON AUSTENITIC (316L) AND FERRITIC (434L) STAINLESS STEEL

- The American Ceramic Society, Westerville, OH, USA, 2001, pp. 459-470.
8. R.M. Anklekar, D.K. Agrawal and R. Roy, "Microwave Sintering and mechanical properties of P/M Copper Steel," *Powder Metallurgy*, 2001, v. 44, n. 4, pp. 355-362.
 9. R.M. Anklekar, K. Bauer, D.K. Agrawal, R. Roy, "Improved Mechanical Properties and Microstructural Development of Microwave Sintered Copper and Nickel Steel P/M Parts," *Powder Metallurgy*, 2005, v. 48, n. 8, pp. 39-46.
 10. "MPIF Standard 10: Tension Test Specimens for Pressed and Sintered Metal Powders," Standard Test Methods for Metal Powders and Powder Metallurgy Products, Metal Powder Industries Federation, Princeton, NJ, 1991.
 11. E. Pert, Y. Carmel, A. Birnboim, T. Olorunyele, D. Gershon, J. Calame, I.K. Lloyd, and O.C. Wilson Jr., "Temperature Measurement during Microwave Processing: The significance of Thermocouple Effects," *J. Am. Ceram. Soc.*, 2001, v. 84, n. 9, pp. 1981-1986.
 12. A. Nayer, *The Metals Data book*, McGraw-Hill, New York, NY, 1997.

316L		434L	
Conventional	Microwave	Conventional	Microwave
sintered density g/cm ³ , (% theoretical)	7.06 (87.5)	6.82 (84.6)	7.24 (92.1)
densification parameter	0.31	0.14	0.61
bulk hardness, HV _{0.05}	136	114	132
strength, MPa	398	156	378
elongation, %	63	3	29

Table 1: Effect of heating mode on the densification and mechanical properties of 316L and 434L stainless steel sintered at 1400°C.

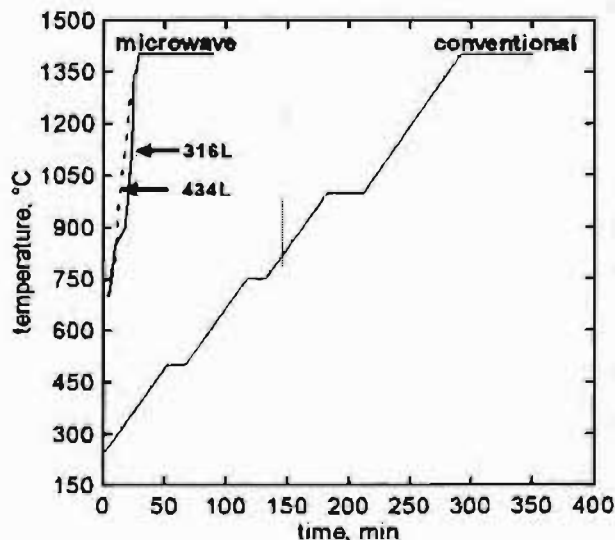


Fig. 1: Effect of heating mode on the thermal profiles of 316L and 434L stainless steel compacts.

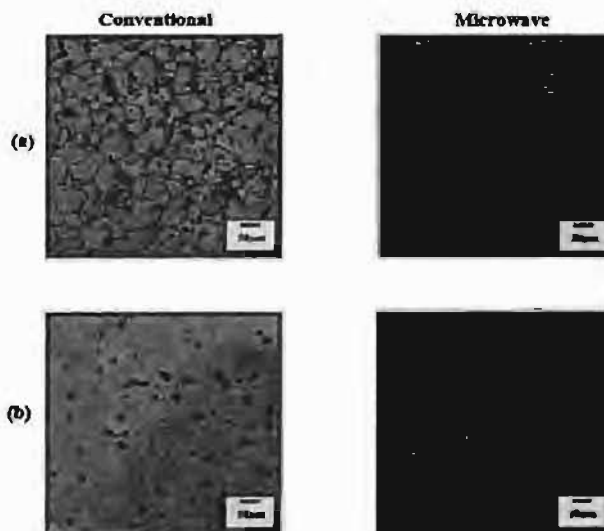


Fig. 2: Optical micrographs of (a) 316L and (b) 434L compacts sintered at 1400°C for 1h in conventional (left) and microwave (right) furnace.

EFFECT OF CONVENTIONAL VIS-À-VIS MICROWAVE SINTERING ON AUSTENITIC (316L) AND FERRITIC (434L) STAINLESS STEEL

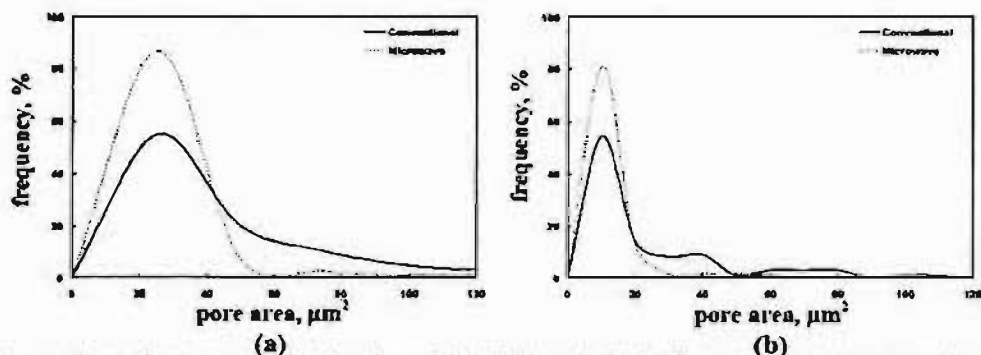
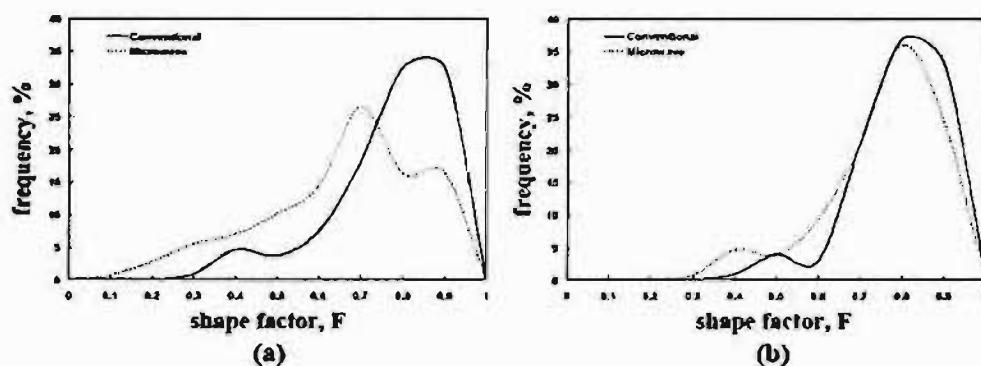


Fig. 3: Comparison of pore area distribution of (a) 316L and (b) 434L stainless steel compacts sintered in conventional and microwave furnace



4: Comparison of shape factor distribution of (a) 316L and (b) 434L stainless steel compacts sintered in conventional and microwave furnace at 1400°C

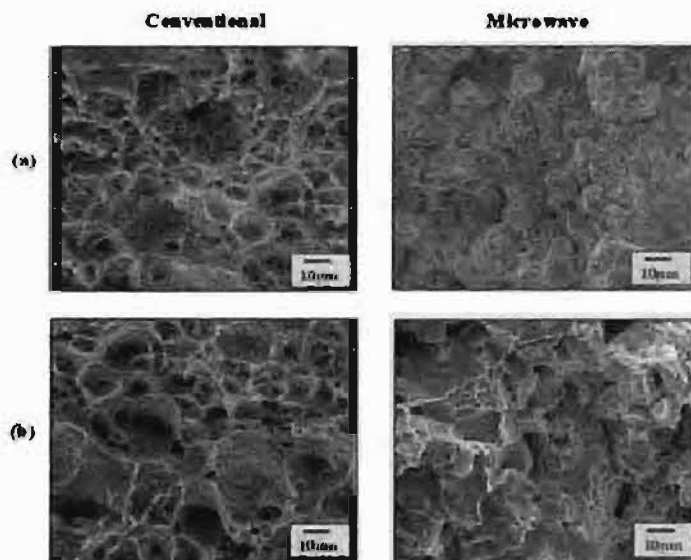


Fig. 5: SEM fractographs of (a) 316L and (b) 434L compacts sintered at 1400°C in conventional (left) and microwave (right) furnace

AN INVESTIGATION ON THE EFFECT OF HEATING RATE ON THE SINTERING OF URANIUM DIOXIDE

S. V. Ramana Rao, Debrupa Lahiri, M. Anuradha, B. Narasimha Murty, Palanki Balakrishna*

Nuclear Fuel Complex, Hyderabad 500062

ABSTRACT

Uranium dioxide green compacts made from one type of powder were heated at different heating rates in a dilatometer. Greater densification was achieved at the lower heating rates of 30 and 75 C/hr, compared to those at 120 and 300 C/hr. This is not in conformity with our previous results and other published literature. The phenomenon has been attributed to the presence of gross defects in sintered compacts, arising from packing problems in the compaction of inhomogeneous powder that contains flow hindering particle clusters. This is supported by observations of fractured surfaces of sintered compacts under low magnification scanning electron microscopy after re-sintering for prolonged periods.

1. INTRODUCTION

UO₂ is used as fuel in commercial light and heavy water thermal reactors. The main advantages in the use of UO₂ are its high melting point, good dimensional and radiation stability and its excellent chemical compatibility with the other reactor components. The main disadvantages are its low thermal conductivity and low fissile atom density. Large scale production of these pellets is carried out by powder metallurgical processes involving pre-compaction and granulation, final compaction and high temperature sintering in reducing atmosphere at 1700°C. Uranium dioxide crystallizes as stable fluorite structure, in which uranium mobility is very much less than that of oxygen. The rate-determining step for the diffusion controlled sintering is uranium diffusion. The diffusion coefficient of U in UO_{2,x} is proportional to $x^{1.5}$ [1]. The value of x is dependent on the temperature and the oxygen pressure in the (reducing) atmosphere of the sintering furnace. The higher the temperature and the higher the oxygen pressure, the higher is the value of x and the greater is the diffusivity of Uranium ions. The oxygen pressure needed is usually that naturally present by way of impurity in most commercial grade gases such as hydrogen or cracked ammonia. Then it is the temperature that controls the diffusion of uranium and thereby the progress of sintering. The thermal conductivity of UO₂ is poor, as in the case of many other ceramics. Further, the green compacts are porous, further lowering the conductivity. In addition, packing problems may be present by virtue of agglomerates in the powder. Hence the temperature across the compact will not be the same if the time to reach equilibrium is not

provided in the sintering cycle. Hence heating rate becomes a very important parameter for achieving the desired sinterability. It is more so with the larger diameter compacts. Lower heating rates provide greater chance for temperature equilibration whereas higher heating rates minimize coarsening. Optimum heating rates are therefore determined by dilatometry on the compacts.

2. EXPERIMENTAL

UO₂ green pellets of diameter and height 18 mm each were prepared and green densities measured. The pellets were heated in a vertical high temperature dilatometer (Anter Corporation and the model is 1161™) in a reducing atmosphere, namely N₂ + 5% H₂ by volume. Different heating rates, namely, 30°, 75°, 120° and 300°C/hr were employed. Shrinkage and shrinkage rate were obtained as a function of temperature. Sintered densities were measured. Polished and etched sections of the sintered pellets were observed in a scanning electron microscope.

3. RESULTS

Fig 1 gives the schematic of the dilatometer. Fig.2 shows SEM of UO₂ powder that was used in this work. Fig.3 gives shrinkage versus temperature for different heating rates. Fig.4 gives the shrinkage rates versus temperature for different heating rates. Table 1 lists the shrinkage parameters while Table 2 gives the increase in sintered density for different heating rates. Microstructures corresponding to different heating rates are shown in Fig. 5. Fig.6 shows the microstructure of an overheated (1000°C, 9 hrs) pellet. Figs. 7 & 8 are fractured surfaces of pellets with large packing defects.

AN INVESTIGATION ON THE EFFECT OF HEATING RATE ON THE SINTERING OF URANIUM DIOXIDE

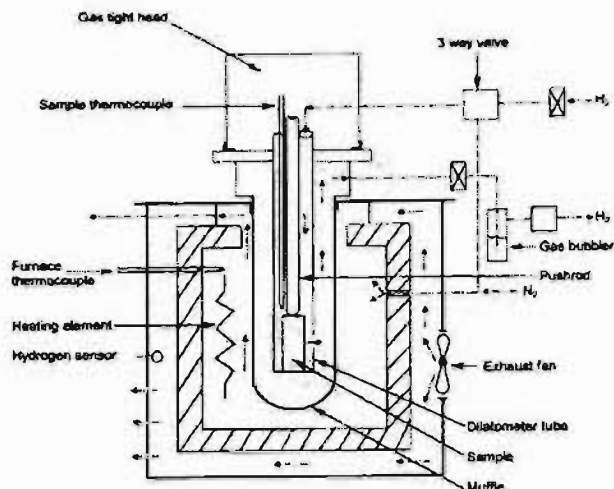


Fig 1. Schematic diagram of dilatometer.

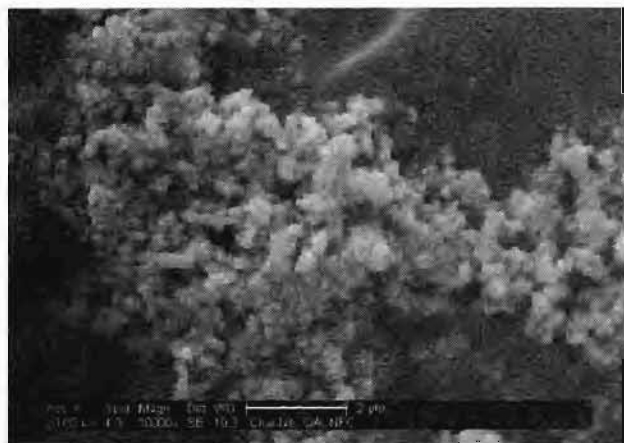


Fig 2. SEM of agglomerated UO_2 powder

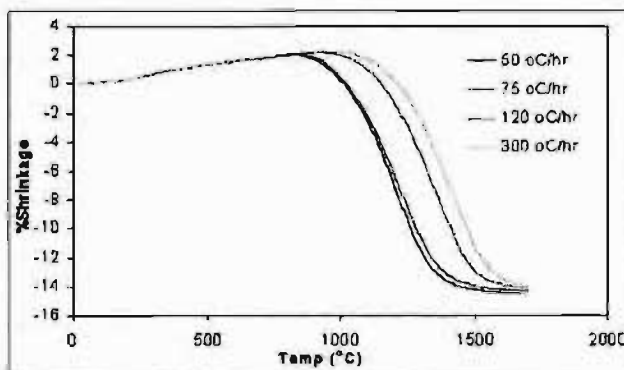


Fig 3. Shrinkage curves of pellets sintered at different heating rates.

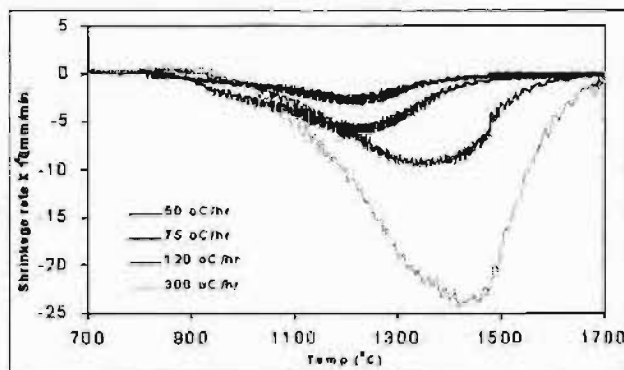
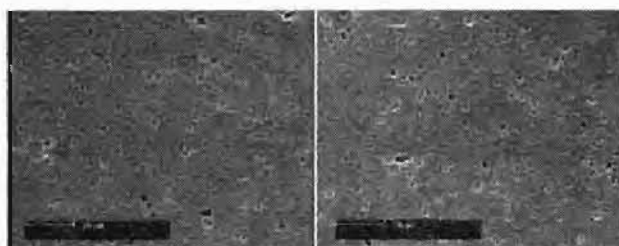
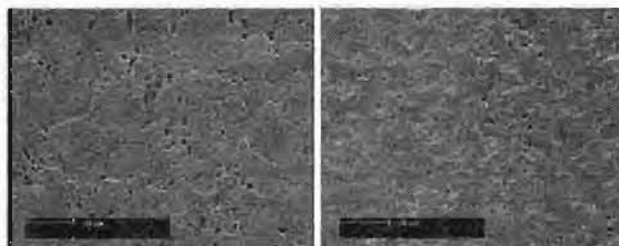


Fig 4. Shrinkage rate Vs Temperature curve for pellets sintered at different heating rates.



30 °C/hr, 1700 C, 1 hr

75 °C/hr, 1700 C, 1 hr



120 °C/hr, 1700 C, 1 hr

300 °C/hr, 1700 C, 1 hr

Fig 5. Microstructures of the UO_2 pellets, sintered at different heating rates

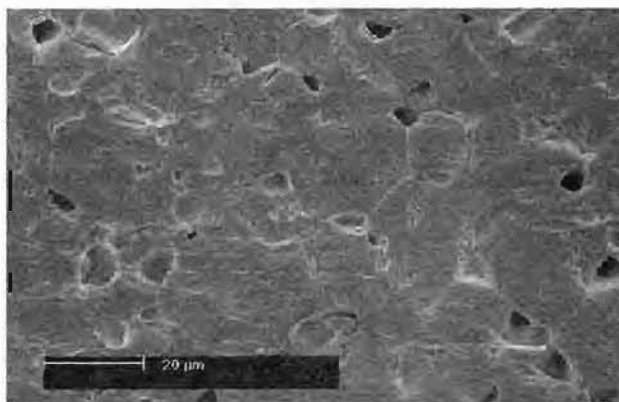


Fig 6. Microstructure after sintering at 1700 °C, 9hrs, indicating grain growth and pore growth

AN INVESTIGATION ON THE EFFECT OF HEATING RATE ON THE SINTERING OF URANIUM DIOXIDE



Fig 7 & 8 Gross packing defects in UO₂ compacts observed after re-sintering

The starting temperature of shrinkage is higher for fast heating rate samples compared to slow heating rate samples. The maximum shrinkage rate also is found to occur at a higher temperature for faster heating rate. Densification obtained at the higher heating rates of 120°C/hr and 300°C/hr was found to be lower than that at the lower heating rates of rate of 30°C/hr and 75°C/hr.

4. DISCUSSION

It is well known in ceramic sintering that fast heating rates lead to fine grain sizes. A fine grain means larger grain

boundary area and a greater chance of residual pores remaining linked to grain boundaries facilitating their ultimate closure by matter transport via grain boundaries. This is the basis for the development of fast firing processes in ceramic technology. In the present case, the microstructures do indicate a decreasing grain size with increasing heating rate. However, slower heating rates are found to have resulted in greater densification. This is not in line with our previous results, where faster heating (600°C/hr) resulted in greater densification on sintering at 1300°C in argon atmosphere when compared to slower heating (100°C/hr) [2]. The scanning electron micrograph of the powder used for pressing the compacts in the present work indicates agglomerated nature. Re-sintering of these compacts for prolonged period (9 hrs) has resulted in de-sintering. Based on this evidence, it appears that the agglomerated powder has caused packing difficulties in the compaction process leading to residual porosity. The de-sintering is more pronounced at faster heating rates and on prolonged sintering.

5. SUMMARY AND CONCLUSION

The heating rate plays an important role during sintering of UO₂ as with other ceramic materials. In this study, heating rates of 30°C/hr and 75°C/hr are found to result in higher sintered densities than of 120°C/hr and 300°C/hr. These results are not in conformity with our previous results according to which higher heating rates cause greater densification. The reason for the different behaviour in this study appears to be the agglomerated nature of the powder used in the preparation of the green compacts with possible packing problems and consequent non-uniform and large porosity. This is supported by the scanning electron micrograph of the powder, the lowering of density on re-sintering and the corresponding microstructure with large grains and large voids. An examination of gross defects in the sintered pellet and a study of the effect of heating rate on pellets made from other powder vendors is expected to throw more light.

Table1. Shrinkage Characteristics of pellets sintered in dilatometer using various heating rates.

Heating Rate (°C/hr)	T _{shrinkage start} (°C)	Total % Shrinkage	Max. Shrinkage Rate (mm/min)	T _{max. shrink. rate} (°C)
30	900	18.2	3.14X10 ⁻⁴	1230
75	910	18	6.18 X10 ⁻⁴	1250
120	1000	17.5	9.64 X10 ⁻⁴	1350
300	1050	18.1	23.4 x 10 ⁻⁴	1430

**AN INVESTIGATION ON THE EFFECT OF HEATING RATE ON THE SINTERING
OF URANIUM DIOXIDE**

Table 2. Increase in density for different heating rates.

Heating Rate (°C/hr)	Green Density g/cc	Sintered Density g/cc	%increase
30	5.57	10.60	90.3
75	5.53	10.56	91.0
120	5.56	10.42	87.4
300	5.59	10.48	87.5

REFERENCES

- [1] J F Marin and P Contamin, "Uranium and oxygen self diffusion in UO_2 ", Journal of Nuclear Materials 30 (1969) 16-25
- [2] Palanki Balakrishna, B Narasimha Murty, K P Chakraborty, R N Jayaraj, C Ganguly, "Coarsening – densification transition temperature in sintering of uranium dioxide", Journal of Nuclear Materials 297 (2001) 35-42

EFFECT OF HEATING MODE AND SINTERING TEMPERATURE ON DENSIFICATION AND MICROSTRUCTURE OF PREMIXED AND PREALLOYED BRONZE

A. Upadhyaya*, G. Sethi** and D. Agrawal***

* Department of Materials and Metallurgical Engineering, IIT, Kanpur 208016, India

**Center of Innovative Sintered Products

***Materials Research Institute

The Pennsylvania State University, University Park, PA 16802, USA

ABSTRACT

The present study compares the effect of microwave and conventional furnace sintering on bronze powder compacts. Bronze (Cu-12 wt.% Sn) powders - prepared by premix and prealloying route- were sintered in a range of temperatures corresponding to solid-state, transient and supersolidus liquid phase sintering conditions. The compacts were characterized for sintered density, densification parameter, macrostructure, microstructures, and elemental distribution using EPMA and X-ray image analysis. The results indicate that bronze compacts can be effectively sintered in a microwave furnace in significantly less time as compared to conventional sintering. The differences in the homogeneity of the microstructure in the conventional and microwave sintered bronze has been correlated with the Sn-diffusion distance determined during both isothermal and non-isothermal conditions.

1. INTRODUCTION

In recent years, microwave processing is being increasingly applied for materials synthesis and sintering [1-5]. The rapid heating by microwaves reduces processing time and results in energy saving. In addition, the uniform heating minimizes problems such as abnormal and localized microstructural coarsening, and thereby results in improved properties. Until recently, most of the microwave sintering was restricted to ceramic materials and cemented carbides [4-11]. Recently, it was shown that metals too can couple with microwaves provided they are in powder form [12]. Subsequently, microwave sintering of steel powder compact was conducted [13-16]. Though there have been attempts to explain microwave heating of metal powders, still there is not yet any consensus on a comprehensive theory to explain the mechanism [17-19]. In order to understand the interaction of microwaves with metal powders and compare the response of metal powder compacts in microwave *vis a vis* conventional sintering, experiments are required with a simpler system. Copper-tin based bronze is one such alloy system. Powder metallurgy is an established processing technique for consolidating Cu-Sn bronzes containing up to 15% Sn. In addition, the conventional sintering response of Cu-Sn system has been extensively studied over the last several decades [20,21]. Tailored composition of Cu-Sn

powders can be prepared by both premixing as well as prealloying route and are typically used for self-lubricating bearing and porous filters. Depending on the sintering temperatures and powder type, bronzes can be sintered in solid-state, transient and supersolidus conditions [22]. Hence, the Cu-Sn alloys not only have a simple chemistry, but it also offer a unique opportunity to investigate various sintering mechanisms all in one system at a relatively lower processing temperature (<1000°C). This study therefore aims at investigating the sintering response of Cu-Sn powder compacts as a function of powder condition and temperature during microwave heating and comparing the same with conventional sintering.

2. EXPERIMENTAL PROCEDURE

For the present study, a Cu-12Sn (wt.%) composition was selected. The irregular shaped wateratomized Cu powder had an average size of 25 μm whereas the Sn powder (gas atomized) was rounded in shape with an average size of 15 μm . The prealloyed Cu-12Sn powders had an average size of about 25 μm . The details of powder characteristics are given elsewhere [23,24]. Table 1 summarizes the experimental variables used in this study. To ensure homogeneity, the powders were mixed in a Turbula blender (model: 2C, supplier: Bachofen, Switzerland) for 30 min.

The loose powders were compacted at 150 MPa to cylindrical pellets (diameter: 12.7 mm and average height: 10 mm) using a 50-ton uniaxial hydraulic press. The as-pressed Cu-Sn compacts were sintered 'conventionally' at the various temperatures in a SiC heated tubular furnace. The microwave sintering was conducted in a 2 kW commercial microwave furnace (Amana Radarange, model RC/20SE) with a 2.45 GHz multimode cavity at Microwave Research Center at The Pennsylvania State University. The microwave furnace was modified to keep the external body temperature of the oven close to the ambient by circulating cold water through the copper tubes fixed at the top and the sides of the double jacketed oven by brazing. A mullite tube 31.8 mm in diameter and 914.5 mm in length was positioned at the center of the oven, by drilling holes on the side-faces, with ends projecting on both the sides. The mullite tube was surrounded at its center by an insulation package made from FiberfraxTM boards was used to surround the mullite tube at the center of the cavity for containing the heat from dissipation during sintering. The design is so made that it could be used both with and without the use of susceptor or secondary coupler. Often, susceptors such as SiC or graphite are used to obtain uniform heating and temperature distribution throughout the sample [13,25,26]. In the present study, in view of relatively small-sized compact, no susceptor was used. Unlike a conventional furnace, the temperature of the samples inside a microwave furnace cannot be monitored using a thermocouple. The presence of thermocouples can locally distort the electromagnetic field and can even lead to measurement errors [27]. The temperature of the sample was monitored using an infrared pyrometer (Raytek, Marathon Series) with the circular crosswire focused on the sample cross-section. The pyrometer is emissivity based; therefore temperature could not be measured below 350 °C. The infrared pyrometer was coupled to a data acquisition and display software on a personal computer. In order to further validate the reproducibility of microwave heating, the elemental Cu and Sn powders as well the bronze compacts were also sintered using a 1.2 kW, 2.45 GHz microwave furnace (model: Sinter-WaveTM) supplied by Bharat Heavy Electrical Limited (BHEL), Hyderabad, India. Further details of the experimental setup of microwave sintering are described elsewhere [28, 29]. The temperature during sintering was monitored using an infrared pyrometer (M680, Mikron Corp., USA). To measure the temperature in the tin compacts, thermocouple with platinum shielded tip was employed. The infrared pyrometers are based on emissivity measurements. As compared to Cu, tin has very low emissivity (0.04) [30]. Hence, for the temperature measurements for all the compacts was done by considering emissivity of Cu (0.15)

[31]. Typically, emissivity varies with temperature. However, as very little variation in the emissivity was reported in the temperature range used in the present study, hence, the effect of variation in emissivity was ignored in the present investigation. This was validated by correlating the infrared pyrometer and thermocouple-based temperature measurements during heating of the bronze compacts in conventional furnace. Both microwave and conventional sintering was done in flowing hydrogen (flow rate: 1 lpm) with a dew point of -40°C. The sintered samples were characterized for the density both through dimensional measurement as well as Archimedes displacement method. To take into account the influence of the initial as-pressed density, the compact sinterability was also expressed in terms of densification parameter δ . densification parameter implies sample shrinkage where as a negative densification parameter implies compact swelling. The sintered samples were characterized for macrostructure and microstructure. The quantitative analyses of Cu and Sn content in microwave sintered compacts at various temperatures were determined using an EPMA (JXA-8600SX Superprobe, JEOL, Japan) equipped with WDS and X-ray imaging.

3. RESULTS AND DISCUSSION

Prior to sintering bronze compacts, the effectiveness of microwaves in heating Cu and Sn powder compacts was evaluated. Figure 1 shows the thermal profiles of pure copper and tin powder compacts pressed at 150 MPa and heated in microwave furnace. Note that both Sn and Cu couple with microwaves and get heated up rapidly. To prevent compacts from melting, the power input was adjusted to restrict the peak temperature to 200 °C and 1000 °C, respectively. It is interesting to note from Fig. 1 that both Sn and Cu powder compacts undergo heating at similar rates (~100°C/min). This proves that non-ferrous metal powder compacts such as Cu and Sn can couple with microwaves. Figure 2 compares the thermal profiles of P/M bronze samples heated up to 830°C in microwave and conventional furnaces. The compacts sintered at 450°C and 775°C too exhibit similar trend. As expected, both the premixed as well as the prealloyed Cu-12Sn compacts are able to heat up in the microwave furnace. Subsequent evaluation revealed no cracking or other defects in the sintered compacts. From Fig. 2, it is quite evident that both the premixed and prealloyed bronze samples couple with the microwaves and get heated up. As described earlier, because of the limitation of pyrometers used in the present study, temperature below 350°C could not be measured in microwave furnace. Excluding the cooling time (Fig. 2), it takes about 3 h for the sintering in a conventional furnace, whereas in a microwave furnace the sintering time is reduced by more than 50%. It is interesting to note that

there is a slight difference in the heating rate of premixed and prealloyed bronze in microwaves. As compared to prealloyed Cu-12Sn, the premixed compacts heat up at relatively slower rate. This indicates the sensitivity of microwave coupling to powder homogeneity.

3.1. Effect of Sintering Temperature on Compact Densification

Figures 3a and 3b show the effect of powder condition (PM vs. PA), heating mode (conventional vs. microwave) and temperature on the sintered density and the densification parameter, respectively. For all the three sintering temperatures, in case of microwave sintered compacts, the density of premixed compacts is slightly higher than that of prealloyed ones. This can be attributed to the initially higher green density of premixed bronze as compared to the prealloyed sample at 150 MPa. Because of the solid solution formation, the prealloyed bronze powders usually have lower compressibility as compared to the premixed ones. Both the premixed and prealloyed microwave sintered samples show highest density at 775°C. Note that densification parameter (Fig. 3b) follows the same trend as sintered density. During supersolidus liquid phase sintering (at 830°C), there is a density drop in both samples. As compared to prealloyed (PA) compacts, the density drop for premixed (PM) compact is more. This can be attributed to the formation of transient Sn melt and its diffusion in the Cu matrix in PM compacts [32-34]. It is hypothesized that due to rapid heating in the microwave, there is very little time available for diffusion of Sn into Cu. Hence, most of the diffusion may be taking place during the sintering hold at 830°C. Usually, the diffusion of the 'primary' Sn-melt into the Cu will result in swelling of bronze compacts [34]. Figure 4 schematically shows compact swelling in premixed bronze compact during sintering as a result of Sn diffusion. During supersolidus liquid phase sintering at 830°C, there will be a formation of Cu-Sn melt at the grain boundary and within the grains. Figure 5 schematically illustrates the microstructure evolution during supersolidus sintering of bronze. Unlike the primary melt, this 'secondary' melt-formation is not transient and promotes compact densification. Thus, sintering of premixed bronze, the compact density

will depend on the nature of melt and its volume fraction. In case of prealloyed bronze, no primary (Sn) melt formation is expected at any stage, therefore, the compact is expected to show continued densification with increasing temperature. However, there is no such improvement is discerned during microwave sintering of prealloyed bronze at 830°C as compared to 775°C. Figure 3a also shows the variation in the density with temperature for conventionally

sintered premixed and prealloyed bronze compacts. Unlike microwave sintering, both the sintered density and densification parameter of conventionally sintered prealloyed bronze increases with increasing temperature and is highest for supersolidus sintered condition. For conventionally sintered premixed bronze, the sintered density at 775°C and 830°C is lower than that at 450°C. From Figure 3b, the densification parameter of premixed bronze at those two temperatures is negative which implies compact swelling. As discussed earlier, compact swelling is attributed to the diffusion of the primary or transient Sn-melt into Cu and therefore is a characteristic of premixed samples only. As indicated by the densification parameter, the compact swelling at 830°C is lower than that at 775°C. The decrease in compact swelling of premixed samples at 830°C is because of the supersolidus sintering conditions which aids in densification, and thereby minimizes the swelling tendency. On comparing the densification response of bronze compacts under conventional and microwave sintering, it is interesting to note that none of the microwave sintered samples swell, whereas the conventionally sintered premixed samples show dilation. Figures 6a and 6b show the premixed Cu-12Sn compacts microwave and conventionally sintered at 775°C and 830°C. Note that the microwave compacts are slightly smaller than the conventionally sintered ones. This is supported by negative densification parameter in the conventionally sintered premixed bronze, which indicates swelling. For the same conditions, the microwave sintered samples have positive densification parameter implying shrinkage. Figure 7 shows the photograph of prealloyed Cu-12Sn sintered conventionally and in microwave at 830°C for 30 min. Unlike the premixed samples, here both samples show densification, as indicated by their positive densification parameter. However, the microwave sintered sample has lower density as compared to the conventionally sintered samples.

3.2. Effect of Sintering Temperature on Microstructure

In equilibrium condition, tin is soluble in copper lattice to up to 15 wt.% in the temperature range of 500°C to 600°C. At those temperatures Cu-12 Sn would consist of single α phase [35]. But at lower temperature (below 350°C), solubility of tin decreases and second phase (δ and/or ϵ) should begin to appear. However, the decomposition of α phase requires extremely slow cooling rate, which was not the case in our experiments. Furthermore, through proper sintering practice, one can obtain a homogeneous α -phase in the microstructure where the Sn remains dissolved in solid-solution in Cu. The same is evident from the optical and SEM micrographs of conventionally sintered Cu-12Sn alloys, which do not show any intermetallic phases. The

absence of any intermetallic phases in both premixed as well as prealloyed bronze has been confirmed by Sukanta [23] through extensive X-ray diffraction studies. The predominant microstructural features of the sintered Cu-12Sn bronze include grains of Cu-Sn solid solution, melt formation (both intergranular and intragranular), porosity and annealing twins. Figures 8a and 8b compare microwave sintered microstructures of premixed and prealloyed Cu-12Sn. Both the compacts were sintered at 775°C. Note in case of microwave sintering of premixed bronze, sufficient time is not available for diffusion of Sn-rich melt into the Cu matrix. Hence, Figure 8a shows the Sn-rich regions near inter-particle boundaries. The insufficient time for Sn diffusion in the Cu grains could be the reason for premixed compacts not showing any swelling when sintered at 775°C (Figs. 3b and 6a). Unlike, the premixed composition, the prealloyed Cu-12Sn compact has a fairly uniform microstructure which is expected given the chemical homogeneity of prealloyed powder in as-received condition. Figures 9a and 9b compare the microstructure of premixed and prealloyed Cu-12Sn compacts supersolidus sintered at 830°C. Note that the premixed bronze shows both intergranular as well as intragranular porosity. The former is irregular and relatively larger than the latter, which appear rounded. The intragranular pores result due to the higher grain growth rates at the supersolidus sintering temperatures. Initially, the as-pressed or 'primary' pores in the compact are expected to be irregular. These primary pores however will tend to round-off during supersolidus sintering and will have more likelihood of becoming intragranular as sintering progresses. In addition to the rounded pores, the microstructure of sintered premixed bronze also shows contains irregular pores at the grain boundaries. These pores are not the as-pressed or 'primary' pores, rather they result from the melting of Sn during sintering and its subsequent diffusion into Cu grains. Such porosity can be termed as sintering or secondary pores. The irregular morphology of intergranular, secondary pores can be attributed to the irregular shape of the starting Cu powder. Our findings are in contrast with observations by Danninger [36] who has shown secondary pores to be more rounded than the primary porosity. Since the prealloyed Cu-12Sn alloy does not contain any 'free' Sn therefore no such signature of irregular pores were found in the sintered microstructure (Figure 9b). Furthermore, the melt in the premixed Cu-12Sn is bimodal in distribution, the intergranular liquid in general appears to be larger in size as compared to the intragranular melt. This may be attributed to the inhomogeneous distribution of Sn during mixing, which results in larger intergranular melt pools in regions with relatively higher concentration of Sn. In prealloyed Cu-12Sn microstructure (Figure 9b), the melt

in both grain boundary and within the grains are smaller and similar in size. Figures 10a and 10b show the microstructures of premixed and prealloyed Cu-12Sn microwave sintered at 830°C. As compared to their conventionally sintered counterparts, the microwave sintered bronze (both premixed and prealloyed) compacts have refined microstructure. This can be attributed to less processing time which restricts grain coarsening. Figures 11a to 11c compare the distribution of Sn – determined using X-ray mapping – in premixed bronze samples sintered in conventional furnace at 775°C (a) and microwave sintered at (b) 775°C and (c) 830°C, respectively. From Figs. 11a and 11b it is evident that in case of premixed bronze, irrespective of the heating mode, Sn is inhomogeneously distributed in 775°C sintered compacts. As discussed above, the Sn distribution in premixed compact is inhomogeneous and primarily concentrated at grain boundaries. This confirms the microstructural observation (Figure 8a) and the hypothesis that insufficient time is available for complete diffusion of Sn (rich) melt into the Cu grains during microwave heating at 775°C (Fig. 11b). Our experimental results do not support the recent hypothesis postulating substantial diffusional enhancement during microwave heating [14]. In contrast, in the same premixed compact, when microwave sintered at 830°C for 30 min (Fig. 11c), Sn is uniformly distributed through out the microstructure. This can be attributed to the higher sintering temperature which is sufficient for complete diffusion of tin in copper [37]. Figure 12 compares the effect of initial powder state (premixed versus prealloyed) on the distribution of Sn – determined using EPMA – in Cu-12Sn compacts microwave sintered at 775°C and 830°C. For each sample, the EPMA measurements were performed at five regions (labeled A to E in the figure) from intergranular to intragranular region. At each of the region about five measurements were performed so as to have a statistical estimate of the microstructural homogeneity. For both sintering temperatures, the prealloyed compacts show uniform Sn distribution in the microstructure. However, in case of premixed bronze sintered at 775°C, Sn is more concentrated at the grain boundaries. This further validates the previous observations and discussion. However, when supersolidus sintered at 830°C, the distribution of Sn attains uniformity.

3.3. Quantitative Determination of Sn Diffusion into Cu

To correlate the microstructural observations and EPMA results with the different thermal profiles during microwave and conventional sintering, the distance that Sn diffuses into Cu was determined both as a function of heating mode as well as the sintering temperature. Our investigation on

bronze does not yield any evidence of microwave sintering *per se* resulting in densification enhancement as postulated by Porada and Park [14]. Hence, the effect of microwave and conventional furnace sintering can be treated as compact consolidation under varying heating rates only. The faster heating rate will influence the extent of Sn diffusion into Cu, thereby, influencing both densification as well as microstructural evolution. The problem therefore simplifies into evaluating the diffusion of tin during heating as well as isothermal hold at the sintering temperature. To calculate the diffusion distance during non-isothermal condition, a modified approach proposed by Soucail and Bienvenu [38] was adopted. The details of the modeling approach are described elsewhere [39]. The model ignores diffusion of Cu in Sn and does not take into account microstructural coarsening. It is well established that the diffusivity of Sn in Cu is greater than that of latter into tin. However, there is a range of activation energy and the pre-exponential terms for Sn diffusion into Cu reported in the literature [40]. Modifying the Fick's law, the distance, x that the Sn diffuses into Cu is expressed as:

$$\operatorname{erf}\left(\frac{x}{2\sqrt{A\exp(-Q/RT)}}\right) = 1 - C_{Sn} \quad (1)$$

where C_{Sn} is the weight fraction of maximum Sn that is soluble in Cu at a temperature, T ; and ' t ' is the hold period at temperature T . In equation 1, A and Q are the pre-exponential term and activation energy, respectively. For the present investigation, the values of A and Q selected were $0.67 \text{ cm}^2/\text{s}$ and 184.4 kJ/mol as determined by Krauthelm *et al.* [41] for diffusion of Sn in α -Cu. It is assumed that these values remain unchanged for all temperatures. While it is easier to calculate the diffusion distance of Sn into Cu for the hold period at 775°C and 830°C , one also has to factor in the diffusion that the Sn will undergo in Cu during the heating stage. As the hold time at the sintering temperature is constant (30 min) for both microwave as well as conventionally heated samples, the distance Sn diffuses into Cu remains the same. Therefore, to rationalize the observed difference in microstructures, it is imperative to include the effect of heating rate on the Sn diffusion distance. However, equation 1 can not be applied directly for this. Thus, the heating profiles for (premixed) bronze samples shown in Figure 2 were approximated by a step temperature profiles. The model ignores diffusion of Cu in Sn and does not take into account microstructural coarsening. For the present work, a temperature increment of 5 degree was chosen. Consequently, for each of the temperature step a specific time-step was derived so as to approximate the simulated temperature-time plot with the observed thermal profile. Figures 13a and 13b compare the

effect of heating mode (microwave *versus* conventional) on the derived Sn diffusion distance into Cu at 775°C and 830°C , respectively. The corresponding modified thermal profiles have been superimposed on figures as well. As expected, in both microwave and conventional heating, the total distance that Sn diffuses into Cu increases with increasing temperature. For both conditions, it is interesting to note that considerable diffusion of Sn occurs during the heating stage itself. As microwave heating takes less time, the diffusion distance of Sn is significantly lower than that for conventionally sintered samples. Despite the assumptions, the Sn diffusion length predicted from our simulation closely relates to the observed results. In particular, the EPMA and X-ray mapping results showing the effect of sintering temperature on the Sn distribution in premixed bronze compacts (Figures 11 and 12) are now apparent from kinetics of Sn diffusion determined through physical modeling. As a consequence of the present analysis, it can now be stated that for achieving microstructural homogeneity during microwave sintering, the starting powder size must be low. This is supported by Vaidhyanathan and Rao [42] who had obtained higher absorptivity of finer particles leading to faster heating. This would give Sn more time to diffuse into Cu and lead to more homogenization. Alternatively, care has to be taken to ensure, grain coarsening during heating through use of additives/inhibitors.

4. CONCLUSIONS

For the first time, Cu-12Sn compacts prepared by using both premixed and prealloyed powders have been successfully sintered in a microwave furnace. As compared to conventional sintering, bronze was microwave sintered in significantly less time (<50%). The densification behavior and microstructural evolution in microwave sintered alloys have been compared with their conventionally sintered counterparts. In conventional sintering, the premixed bronze swells at 775°C and 830°C , whereas no swelling occurs during microwave sintering of both premixed as well as prealloyed bronze compacted at 150 MPa. The effect of heating mode on microstructural homogeneity was modeled using diffusing of Sn in Cu for premixed compacts. Both the experimental and the derived plots suggest that it is difficult to achieve uniform homogeneity of Sn distribution in Cu for premixed bronze compacts sintered up to 775°C . Usually, the application of conventionally sintered premixed bronzes is restricted to making filters and bearings. However, the lack of swelling in premixed bronze during microwave sintering, offers an opportunity of extending their use for structural applications as well over their prealloyed counterparts, which are

EFFECT OF HEATING MODE AND SINTERING TEMPERATURE ON DENSIFICATION AND MICROSTRUCTURE OF PREMIXED AND PREALLOYED BRONZE

costlier. Microwave sintering is found to provide better densification for prealloyed compacts.

5. ACKNOWLEDGMENTS

The authors thank Prof. R. Roy of Penn State, USA for his helpful suggestions and technical feedback by Dr. G. Swaminathan of Bharat Heavy Electrical Ltd. (BHEL), Hyderabad, India. The authors gratefully acknowledge the financial support from Department of Science & Technology (DST) and Defense Research and Development Organization (DRDO), India for the research. The microwave sintering studies were supported by the grant from the Defense Advanced Research Projects Agency (DARPA) and Office of Naval Research (ONR) [contract #: N0014-01-1-0353].

6. REFERENCES

1. K.J. Rao and P.D. Ramesh, "Use of Microwaves for the Synthesis and Processing of Materials," *Bulletin Material Science*, 1995, v. 18, n. 4, pp. 447-465.
2. S.L. McGill and J.W. Walkiewicz, "Applications of Microwave Energy in Extractive Metallurgy," *Journal Microwave Power Electromagnetic Energy*, 1987, v. 22, n. 3, pp. 175-177.
3. B. Vaidhyanathan, D.K. Agrawal, and R. Roy, "Novel Synthesis of Nitride Powders by Microwave-Assisted Combustion," *Journal Materials Research*, 2000, v. 15, pp. 974-979.
4. D.E. Clark and W.H. Sutton, "Microwave Processing of Materials," *Annual Reviews Material Science*, 1996, v. 26, 1996, pp. 299-331.
5. W.H. Sutton, "Microwave Processing of Ceramic Materials," *Ceramic Bulletin*, 1989, v. 68, n. 2, pp.376-384.
6. E. Wroe, "Microwave Sintering Coming of Age," *Metal Powder Report*, 1999, v. 54, n. 7, pp. 24-28.
7. D.K. Agrawal, A.J. Papworth, J. Cheng, H. Jain, and D.B. Williams, "Microstructural Examination by TEM of WC/Co Composites Prepared by Conventional and Microwave Processes," *Proceedings of 15th International Plansee Seminar*, v. 2, G. Kneringer, P. Rödhammer, and P. Wilhartitz (eds.), Plansee AG Reutte, Austria, 2001, pp. 677-684.
8. D.K. Agrawal, J. Cheng, A. Lackner, and W. Ferstl, "Microwave Sintering of Commercial WC/Co Based Hard Metal Tools," *Proceedings of European Conference on Advances in Hard Materials Production EURO PM'99*, EPMA, Shrewsbury, UK, 1999, pp. 175-182.
9. T. Gerdes, M. Willert-Porada, and K. Rödiger, "Microwave Sintering of Tungsten-Cobalt Hardmetals," *Material Research Society Symposium Proceedings*, 1996, v. 430, pp. 45-50.
10. T. Gerdes, M. Willert-Porada, K. Rödiger, and K. Dreyer, "Microwave Reaction Sintering of Tungsten Carbide - Cobalt Hardmetals," *Material Research Society Symposium Proceedings*, 1996, v. 430, pp. 175-180.
11. A.J. Berteaud and J.C. Badot, "High Temperature Microwave Heating in Refractory Materials," *Journal Microwave Power*, 1976, v. 11, n. 4, pp. 315-320.
12. R. Roy, D.K. Agrawal, J.P. Cheng, and S. Gedevarishvili, "Full Sintering of Powdered Metals using Microwaves," *Nature*, 1999, v. 399, n. 17, pp. 668-670.
13. M.J. Yang and R.M. German, *Advances in Powder Metallurgy and Particulate Materials*, v. 1, n. 3, MPIE, Princeton, NJ, USA, 1999, pp. 207-219.
14. M. Willert-Porada and H.S. Park, "Heating and Sintering of Steel Powders with Microwaves at 2.45GHz Frequency- Relationship between Heating Behavior and Electrical Conductivity," *Microwaves: Theory and Application in Materials Processing V*, D.E. Clark, J.G.P. Binner, and D.A. Lewis (eds.), The American Ceramic Society, Westerville, OH, USA, 2001, pp. 459-470.
15. R.M. Anklekar, D.K. Agrawal, and R. Roy, "Microwave Sintering and Mechanical Properties of PM Copper Steel," *Powder Metallurgy*, 2001, v. 44, n. 4, pp. 355-362.
16. R.M. Anklekar, K. Bauer, D.K. Agrawal, R. Roy, "Improved Mechanical Properties and Microstructural Development of Microwave Sintered Copper and Nickel Steel P/M Parts," *Powder Metallurgy*, 2005, v. 48, n. 8, pp. 39-46.
17. W.R. Tinga, "Fundamentals of Microwave-Material Interaction and Sintering," *Materials Research Society Symposium Proceedings*, 1988, v. 124, pp. 33-43.
18. M. Willert-Porada, "A Microstructural Approach to the Origin of 'Microwave Effects' in Sintering of Ceramics and Composites," *Microwaves: Theory and Application in Materials Processing IV*, D.E.

EFFECT OF HEATING MODE AND SINTERING TEMPERATURE ON DENSIFICATION AND MICROSTRUCTURE OF PREMIXED AND PREALLOYED BRONZE

- Clark, W.H. Sutton, and D.A. Lewis DA (eds.), The American Ceramic Society, Westerville, OH, USA, 1997, pp. 153-164.
19. A. Cherradi, G. Desgardin, L. Mazo, and B. Raveau, "What is the Contribution of Electrical Field to the Microwave Sintering of YBCO," *Superconducting Science Technology*, 1993, v. 6, pp. 799-802.
20. ASM Handbook, Powder Technologies and Applications, v. 7, ASM International, Materials Park, OH, USA, 1998.
21. H.E. Hall, "Sintering of Copper and Tin Powders," *Metals and Alloys*, 1939, pp. 297-299. 22. P.W. Taubenblatt (ed.), Copper Based Powder Metallurgy, MPIF, Princeton, NJ, USA, 1980, pp. 65- 75.
23. S. Ghosh, "Processing of Premixed and Prealloyed Bronze Through Transient and Supersolidus Liquid Phase Sintering," M.Tech Thesis, Indian Institute of Technology, Kanpur, India, 2001.
24. A. Upadhyaya, S. Ghosh, G. Wilde, and R.K. Ray, "Transient and Supersolidus Sintering of Premixed & Prealloyed Bronze," *Advances in Powder Metallurgy & Particulate Materials*, 2002, v. 13, MPIF, Princeton, NJ, USA, pp. 323-333.
25. J.W. Walkiewicz, G. Kazonich and S.L. McGill, "Microwave Heating Characteristics of Selected Minerals and Compounds," *Minerals Metallurgical Processing*, 1988, v. 5, n. 1, pp. 39-42.
26. A. Cherradi, S. Marinel, G. Desgardin, J. Provost, and B. Raveau, "Microwave Sintering of high Tc Superconductor Y-Ba-Cu-O," *Superconducting Science Technology*, 1997, v. 10, pp. 475-483.
27. E. Pert, Y. Carmel, A. Birnboim, T. Olorunyolemi, D. Gershon, J. Calame, I.K. Lloyd, and O.C. Wilson Jr., "Temperature Measurement during Microwave Processing: The significance of Thermocouple Effects," *Journal American Ceramic Society*, 2001, v. 84, n. 9, pp. 1981-1986.
28. A. Upadhyaya, G. Sethi, H. Kim, D.K. Agrawal, and R. Roy, "Densification of Premixed and Prealloyed Cu-12Sn Bronze during Microwave and Conventional Sintering," *Advances in Powder Metallurgy & Particulate Materials*, v. 13, MPIF, Princeton, NJ, USA, 2002, pp. 364-375.
29. G. Swaminathan and A. Upadhyaya, Tubular Microwave Sintering Furnace with Inert and Reducing Gas Flushing for Sintering Metallic Samples, Indian Patent, 2005 (submitted).
30. D.R. Lide (ed.), CRC Handbook of Chemistry and Physics, 79th ed., CRC Press, Boca Raton, FL, USA, 1998.
31. A. Nayer, The Metals Databook, McGraw-Hill, New York, NY, USA, 1997.
32. D.F. Berry, "Factors Affecting the Growth of 90/10 Copper/Tin Mixes Based on Atomized Powders," *Powder Metallurgy*, 1972, v. 15, pp. 247-266.
33. E. Deegan, A.D. Sarkar, "Effect of Sintering Variables on the Dimensional Changes of Copper-Tin Compacts upto 10% Tin," *Metallurgical Metal Forming*, 1973, v. 40, n. 8, pp. 148-151.
34. A.B. Backensto, "Changes in Dimensional Change for Bronze Premixes as Premix Components Changes," *Modern Developments in Powder Metallurgy*, v.19, P.U. Gummeson and D.A. Gustafson DA (eds.), MPIF, Princeton, NJ, USA, 1988, pp. 641-652.
35. G. Dowson, "The Sintering of Bronze," *Metal Powder Report*, 1984, v. 39, n. 2, pp. 71-73.
36. H. Danninger, "Homogenization and Pore Formation during Sintering with Transient Liquid Phase," *Powder Metallurgy International*, 1988, v. 20, n. 1, p. 21-25.
37. G. Sethi, A. Upadhyaya, and D. Agrawal, "Microwave and Conventional Sintering of Premixed and Prealloyed Cu-12Sn Bronze," *Science of Sintering*, 2003, v. 35, pp. 49-65.
38. M. Soucail and Y. Bienvenu, "Dissolution of γ Phase in a Nickel Base Superalloy at Equilibrium and under Rapid Heating," *Materials Science Engineering A*, 1996, v. A220, pp. 215-222.
39. A. Upadhyaya, "Effect of Heating Rate and Sintering Temperature on Densification and Microstructural Homogenization in Premixed Bronze," *Metallurgical Materials Transactions A*, 2005
40. E.A. Brandes and G.B. Brook (eds.), Smithells Metals Reference Book, 7th ed., Butterworth-Heinemann, Oxford, UK, 1998.
41. G. Krautheim, A. Neidhardt, U. Reinhold, and A. Zehe, *Phys. Lett. A*, 1979, v. 72, pp. 181-185.
42. B. Vaidhyanathan and K.J. Rao, "Microwave Assisted Synthesis of Technologically Important Transition Metal Silicides," *Journal of Materials Research*, 1997, v. 12, n. 12, pp. 3225-3229.

EFFECT OF HEATING MODE AND SINTERING TEMPERATURE ON DENSIFICATION AND MICROSTRUCTURE OF PREMIXED AND PREALLOYED BRONZE

Table I. Processing condition for bronze compacts in the present study.

condition	Premixed (PM) and Prealloyed (PA) Cu-12Sn (wt.%)	
compaction pressure	150 MPa	
Sintering Temperature	Condition for PM	Condition for PA
450°C	TLPS	SSS
775°C	SSS	SSS
830°C	SLPS	SLPS
isothermal hold time	30 min	

SSS: Solid State Sintering, TLPS: Transient Liquid Phase Sintering, SLPS: Supersolidus Liquid Phase Sintering

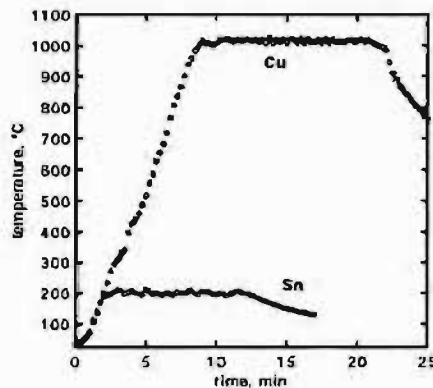


Figure 1. Thermal profiles of pure copper and tin powder compacts pressed at 150 MPa and heated in microwave furnace.

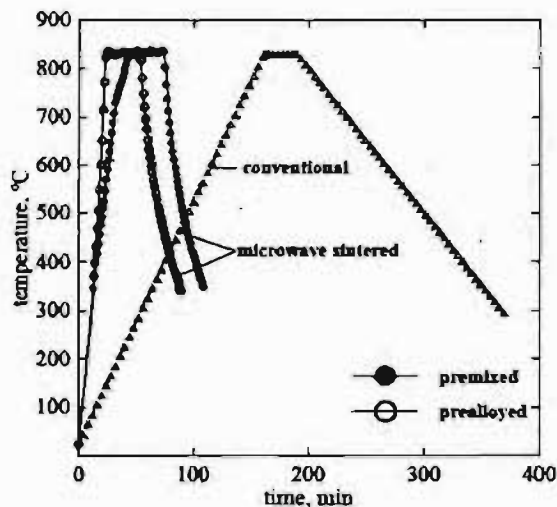


Figure 2. Thermal profiles of conventional and microwave sintered Cu-12Sn alloy

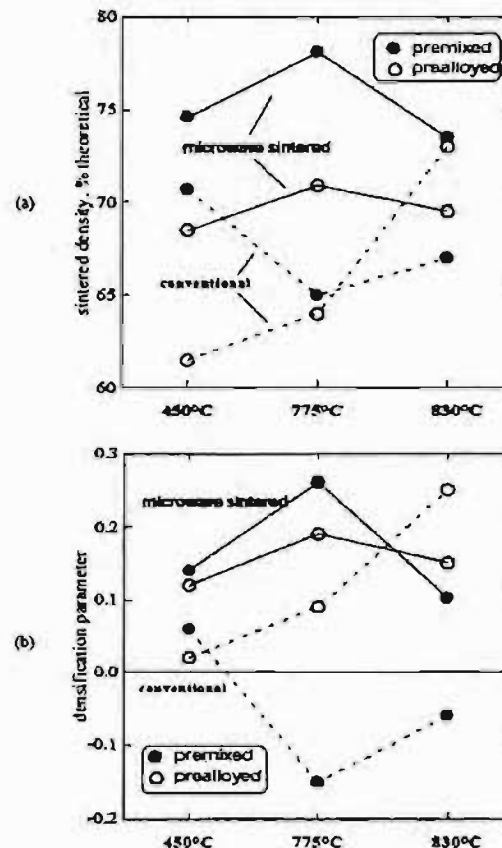


Figure 3. Effect of varying sintering temperature and composition preparation route on the (a) density and (b) densification parameter (DP) of conventionally and microwave sintered Cu-Sn alloy

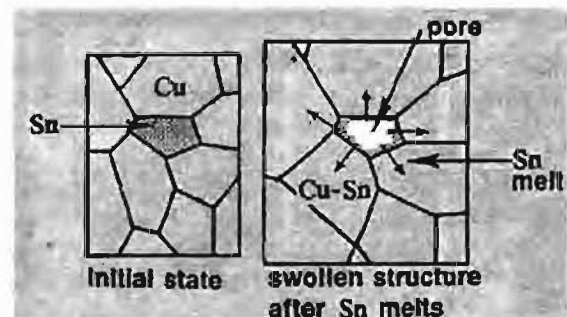


Figure 4. Schematic illustration of the swelling in the Cu-Sn system associated with melting of tin

EFFECT OF HEATING MODE AND SINTERING TEMPERATURE ON DENSIFICATION AND MICROSTRUCTURE OF PREMIXED AND PREALLOYED BRONZE

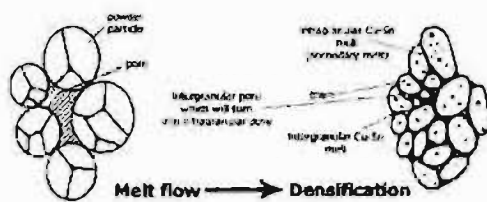


Figure 5. Schematic illustration of the densification in the Cu-Sn system associated with supersolidus liquid phase sintering

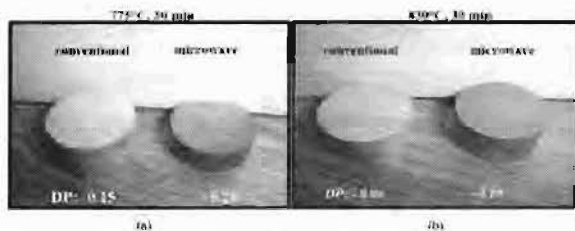


Figure 6. Photographs of the PM Cu-12Sn compacts conventionally and microwave sintered at (a) 775°C and (b) 830°C for 30 min.



Figure 7. Photograph of the PA Cu-12Sn compacts conventionally and microwave sintered at 830°C for 30 min

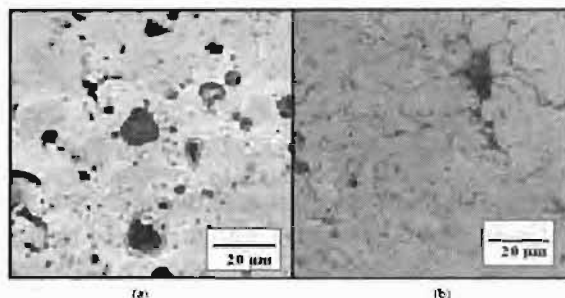


Figure 8. Microstructure of (a) premixed and (b) prealloyed Cu-12Sn microwave sintered at 775°C. The whitish region in Fig. 8a are Sn-rich

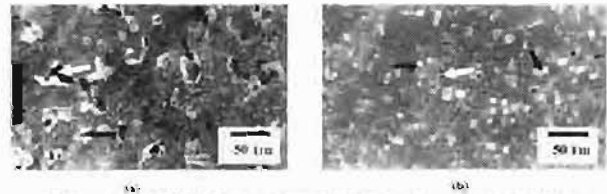


Figure 9. SEM micrographs of (a) premixed and (b) prealloyed Cu-12Sn alloys supersolidus liquid phase sintered (conventionally) at 830°C. The black arrows indicate the melt, whereas the white marker shows porosity

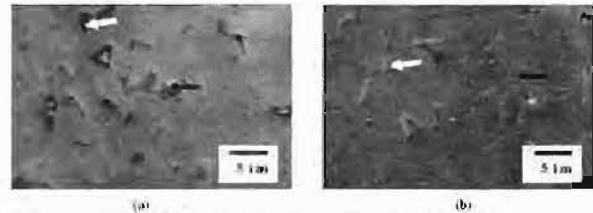


Figure 10. SEM photomicrographs of (a) premixed and (b) prealloyed Cu-12Sn alloy microwave sintered at 830°C

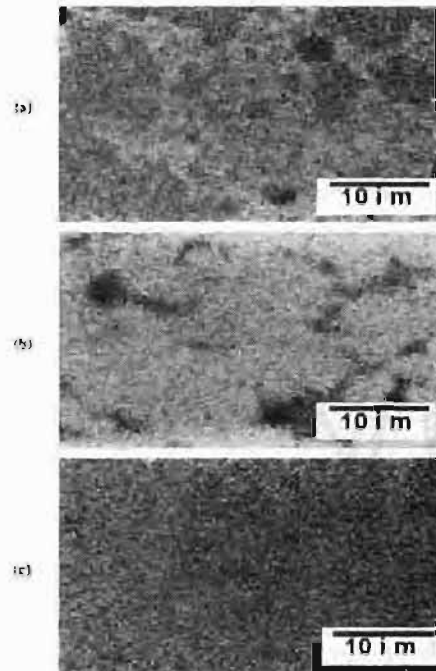


Figure 11. X-Ray map distribution of Cu and Sn in premixed bronze samples sintered in conventional furnace at 775°C (a) and microwave sintered at (b) 775°C and (c) 830°C. The white regions correspond to Cu and black regions correspond to Sn.

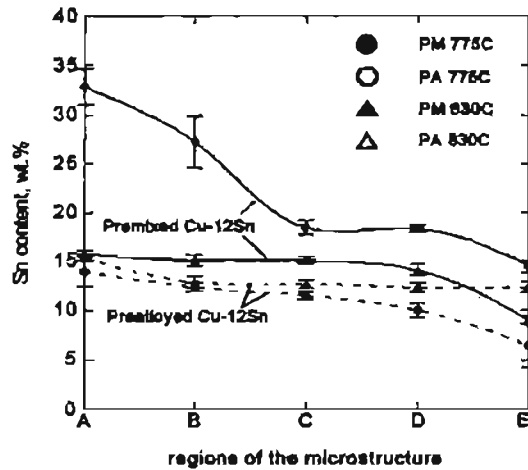


Figure 12. Sn content measured by EPMA from various regions (going from near grain boundaries (A) to within grains E) regions of the Cu-12Sn alloys microwave sintered at 775°C and 830°C

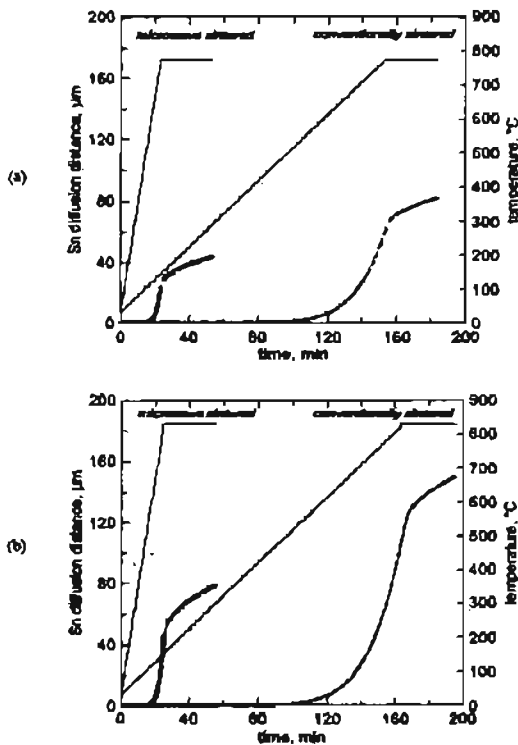


Figure 13. Effect of conventional and microwave heating on the Sn diffusion distance (in Cu) for premixed Cu-12Sn compacts sintered to (a) 775°C and (b) 830°C for 30 min. The thermal curves corresponding to both heating conditions – approximated using a stepped temperature-time profile – is superimposed on the diffusion distance-time plot.

EFFECT OF COPPER POWDER TYPE AND SINTERING TEMPERATURE ON SINTERING OF Cu-10 Sn ALLOYS THROUGH CONVENTIONAL AND MICROWAVE HEATING

Uddanti Ravikiran^a and Anish Upadhyaya^b

^aDMRL, Hyderabad, ^bDept. of Materials & Metallurgical Engg, IIT Kanpur

ABSTRACT

The current work examines the processing of premixed and prealloyed Cu-10Sn alloys through conventional and microwave sintering techniques. The compacts were consolidated at 700 and 840 C, which correspond to transient and Supersolidus liquid phase sintering, respectively. The objective of investigation is to determine the effect of powder type, sintering temperature and heating mode in Cu-10Sn bronze. The sintering response has been evaluated by quantifying, densification (sintered density and densification parameter); dimensional isotropy; and mechanical properties (strength and hardness) are critically examined in this paper

I. INTRODUCTION

The type of powder and sintering temperature are the important parameters in determining the sound final product. There are several techniques to produce the powders like atomization, chemical reduction, precipitation and electrolytic methods. Bronze powders are the most difficult of all powder metallurgical metals to sinter. This is because of their high growth characteristics and their sensitivity to density variations to minor temperature changes [1]. The sintering operation is believed to be affected by powder characteristics, sintering atmosphere, compact density, rate of heating etc. [2-3]. The difference in the sintering behaviour between the premixed and prealloyed compacts originates from the nature of distribution of tin. Tin is a low melting constituent and melts in the early stage of sintering of premixed compacts. The initial melt induces swelling, due to liquid tin penetrating grain boundaries [4].

The potential use of Microwave sintering is widely applied for materials synthesis [5-7]. The use of microwave energy as heat source for sintering has been studied in the ceramic and also in the hard metal sector over the last 15 years [8][9][10]. Roy et al. showed experimentally for the first time, coupling of pure metals with microwaves in the form of powder [11]. The advantages of microwave over conventional heating are rapid heating rate, cost savings (time and energy, reduced floor space), volumetric and uniform heating and improved microstructural homogeneity, which enhances the mechanical properties [12-14].

II. EXPERIMENTAL

Pometon Spa, Italy supplied the powders for copper and tin. Both prealloyed and premixed 10% bronze were used for the investigation. The type of powders, designation and their characteristics are given in table1. Cylindrical green compacts were pressed under a single acting hydraulic machine (APEX construction Ltd, UK) of 50 tons capacity was used for this purpose. The as pressed compacts were conventionally sintered in conventional and microwave sintering furnaces. The alloys were sintered at two different temperatures 700° and 840°C at 200 MPa pressure. N₂-20 H₂ was used as sintering temperature for all the samples. The green and sintered densities were determined by dimensional measurements and the Microstrutural studies were carried out on Leica optical microscope with digital image acquisition capability. The tensile testing was done using Instron 1195 tensile testing machine (Supplier: Instron, Germany).

III. RESULTS AND DISCUSSION

Thermal profile

Figure 1 shows the thermal profiles of conventional and microwave sintered samples. It takes about two and half hours to perform sintering in conventional furnace, where as in microwave sintering furnace it is around 30 minutes for full sintering cycle. The time reduced by 70% in microwave sintering furnace.

EFFECT OF COPPER POWDER TYPE AND SINTERING TEMPERATURE ON SINTERING OF Cu-10 Sn ALLOYS THROUGH CONVENTIONAL AND MICROWAVE HEATING

Table 1. Type of powders and characteristics

Condition	Premixed (PM) and Prealloyed (PA)		
Compaction Pressure (MPa)	200		
	Sintering Temperature (°C)	Condition for Premixed	Condition for Prealloyed
Sintering Temperature (°C)	700	TLPS	SSS
	840	SLPS	SLPS
Sintering Time (min)	15		
Sintering Atmosphere	$H_2 + 20 N_2$		

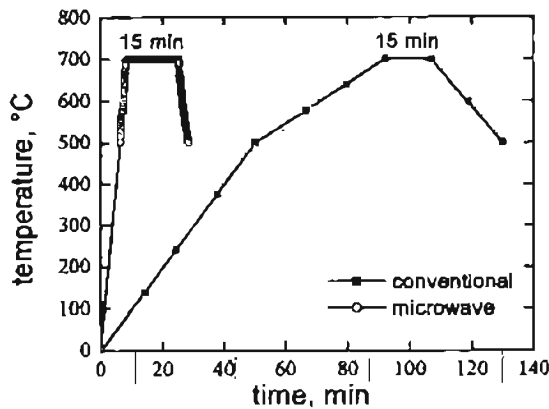


Figure 1. Thermal profiles of conventional and microwave sintered samples

Sintered Density

The sintered density values of conventional and microwave sintered samples are shown in Figure 2. Prealloyed bronze seems to show lower sintered density values compared to premixed bronze samples. This can be rationalized on the basis of the relatively poor compressibility of prealloyed powders wherein copper and tin already exist in solid solution. Microwave sintered prealloyed compacts show higher sintered densities compared to conventional sintered compacts at 840°C. It has been generally considered that the enhanced densification in the microwave sintering is due to a reduction in the activation energy for sintering, though the mechanisms responsible for this effect are not yet well understood [15-16].

Densification Parameter

Figure 3 gives the densification parameter comparison for both conventional and microwave sintered compacts. The densification behaviour is different for premixed and prealloyed compacts. Premixed compacts showing negative densification parameter, which implies compact swells during sintering. Microwave sintered premixed samples showing negligible swelling.

Axial and Radial Shrinkage

Figures 4 shows the effect of sintering temperature and powder state on the radial and axial shrinkage plots for conventional and microwave sintered samples, respectively. Premixed compacts expand both in axial as well as radial direction. As compared to premixed, the prealloyed bronze undergone shrinkage, however it is interesting to note that the shrinkage is not isotropic. Axial direction has more expansion compared to radial direction for both sintering techniques. In general terms, the sample grows or shrinks less in the radial direction compared to the axial direction. This could possibly be tied up with the direction of applied stress and locked-in elastic stresses [17]. Microwave sintered samples show negligible expansion when compared to conventionally sintered samples. This is due to less swelling tendency in microwave sintered compacts.

Microstructural Studies

Figure 5 shows the optical micrographs of premixed samples sintered in conventional and microwave sintering furnaces respectively. It is absorbed that conventional sintered samples showing non uniform porosity distribution and the pores are irregular in shape. The matrix contains free copper and tin phases. This means the poor sinterability of bronze in conventional sintering. Incase of microwave sintered compact no free copper phase is available in the matrix, which means bronze formation is completed.

EFFECT OF COPPER POWDER TYPE AND SINTERING TEMPERATURE ON SINTERING OF Cu-10 Sn ALLOYS THROUGH CONVENTIONAL AND MICROWAVE HEATING

Volumetric heating in microwave sintered sample leads to better sinterability.

Figure 6 shows the micrographs of premixed and prealloyed samples sintered in conventional and microwave sintering furnaces respectively. Premixed compacts show the formation of both primary and secondary pores, where as in prealloyed compacts no secondary pores are absorbed. The premixed compacts showing higher pore size compared to prealloyed compacts. Conventional sintered bronze shows higher pore size, when compared to microwave sintered ones.

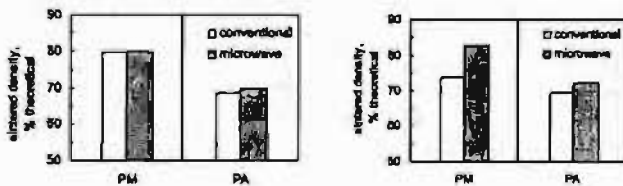


Figure 2. Density of premixed and prealloyed bronze sintered at (a) 700°C and (b) 840°C for 15 min in a conventional and microwave furnace.

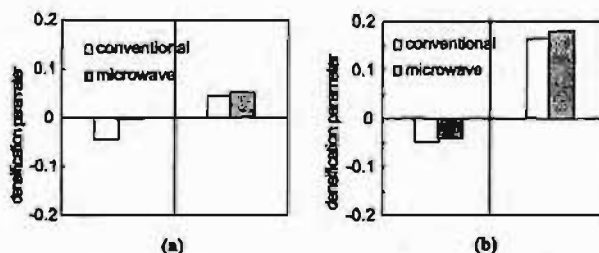


Figure 3. Densification parameter of the premixed and prealloyed bronze sintered conventionally and microwave furnace at (a) 700°C and (b) 840°C for 15 min.

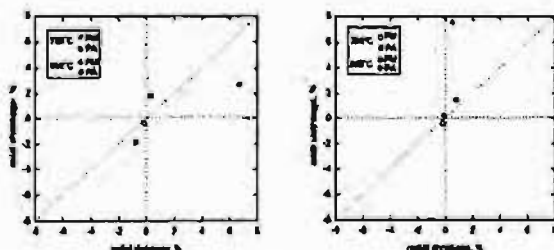


Figure 4. Effect of sintering temperature and powder state on the radial and axial shrinkage of Cu-10Sn bronze consolidated in a (a) conventional and (b) microwave sintering furnace.

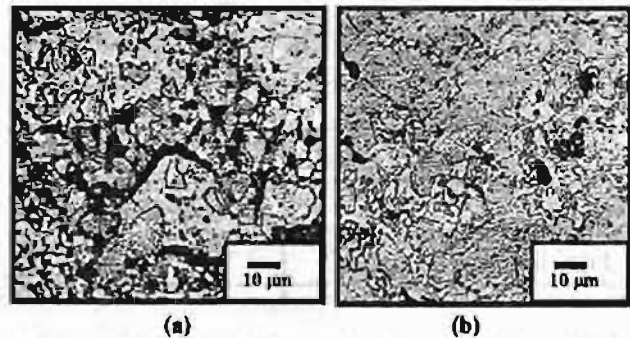


Figure 5. Optical micrographs of premixed sample in (a) conventionally and (b) microwave sintered at 700°C.

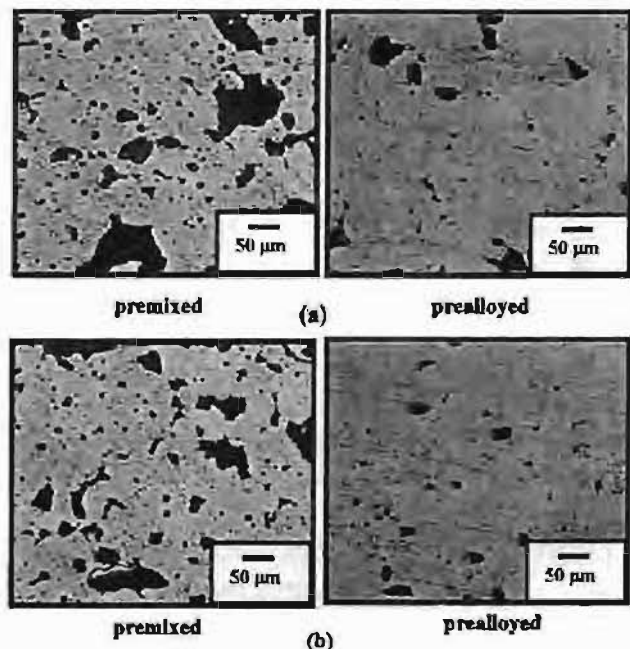


Figure 6. Optical micrographs of (a) conventionally (b) microwave sintered compacts at 840°C.

Tensile Properties

Ultimate tensile strength and ductility comparison of conventional and microwave sintered samples are given in figure 7. The conventionally sintered prealloyed powders showing low tensile strength values at both temperatures when compared to premixed powders, where as in microwave sintering the prealloyed powders exhibit higher strength when temperature is increased. The highest strength of 196 MPa is observed in case of microwave sintered prealloyed compact. As the temperature increases from 700°C to 840°C, the ductility is significantly enhanced in both conventional as well as microwave sintering. In microwave sintering high ductility is observed compared to conventional sintering.

EFFECT OF COPPER POWDER TYPE AND SINTERING TEMPERATURE ON SINTERING OF Cu-10 Sn ALLOYS THROUGH CONVENTIONAL AND MICROWAVE HEATING

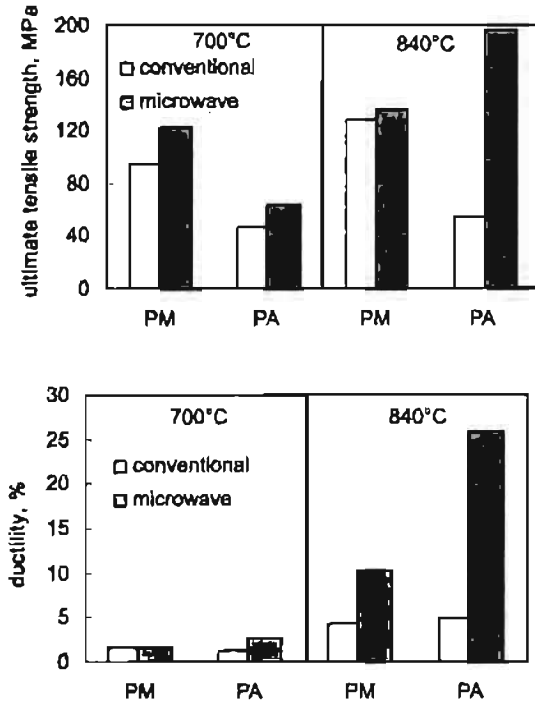


Figure 7 Effect of sintering temperature; powder state (premixed vs. prealloyed); and sintering condition on the (a) ultimate tensile strength (b) yield strength and (c) ductility of Cu-10Sn alloys.

IV. CONCLUSIONS

The present work was focused on the effect of powder type and temperature as well as conventional and microwave heating on the sintering behavior and microstructural evolution of Cu-10Sn alloys. Premixed and prealloyed powders behave differently even for the same composition (Cu-10wt. %Sn in this case). Prealloyed samples show shrinkage as the sintering temperature is increased, thereby showing the opposite trend compared to premixed samples. Supersolidus sintering for the prealloyed samples lead to the higher densification compared to the solid state sintering for both sintering techniques. The microwave sintered bronze compacts show 70% reduction in time, uniform porosity distribution, homogeneous structure, better strength and ductility values when compared to conventionally sintered compacts.

REFERENCES

[1] Copper base powder metallurgy ed.P.W.Tanbenblatt. 1980, MPIF.

[2] B.Krishnakant and M.Patel, "Superior Quality Bronze Bearings,"Modern Developments in Powder Metallurgy, v.19, P.U.Gummeson and D.A.Gustafson (eds.), MPIF, Princeton, NJ, USA, 1988, pp.621-640.

[3] G.Dowson, "Sintering of Bronze," *Metal Powder Report*, 1984,v, n.2, pp.71-73.

[4] R.M.German, Powder Metallurgy Science, MPIF, Princeton, NF, USA, 1994.

[5] K.J.Rao and P.D.Ramesh, "Use of Microwaves for the synthesis and Processing of Materials," *Bull. Mater. Sci.*, v.18, n.4, 1995, pp.447-465.

[6] D.E.Clark, W.H.Sutton, "Microwave Processing of Materials. *Ann.Rev.mater.Sci*" v.26, 1996, pp.299-331.

[7] W.H.Sutton,"Microwave Processing of Ceramic Materials, *Ceram.Bull*" v.68, n.2, 1989, pp.376-384.

[8] F.Petzoldt, B.Scholz, H.S.Park, M.Willert-Porada "Microwave Sintering of PM Steels," *Proc.8th Intern.Conf.On Microwave and High Frequency Heating*, BAYREUTH, Germany, September, 3-7, 2001.

[9] M. Willert-Porada. "Applications of Microwaves to Processing of Metallic, Ceramic and composite Materials" pp.271-276, *Proceedings of 2.International conference on Microwave Chemistry*, Inst.National Polytechnique de Toulouse.

[10] M.Willert- Porada, T.Gerdes, Ch. Gerk. " Neue Werkstoffe ausneuen Pulvern durch Sintern und Reaktionssintern und Prazis, Bd.14, (1998), pp.228-243.

[11] R.Roy, D.Agarwal, J.Cheng, S.Gedevanishvili, *Nature*, 399 (1999) 668.

[12] K.C. Gupta, Microwave, New Age International, New Delhi, India, 1983.

[13] R. Wroe, "Microwave Sintering Coming of Age," *Metal Powder Rep.*, v.54,n.7/8,1999,pp.24-28.

[14] D.M.Pozar, Microwave Engineering, 2nd ed., John Wiley & Sons, Toronto, Canada, 2001.

[15] B.T.K. Barry and C.J. Thwaites, Tin and its Alloys and Compounds, Ellis Horwood Ltd., West Sussex, UK, 1983.

[16] D.F. Berry, "Factors Affecting the Growth of 90/10 Copper/Tin Mixes based on Atomized Powders," *Powder Metallurgy*, 1972, v. 15, pp. 247-266.

[17] E. Deegan and A.D. Sarkar, "Effect of Sintering Variables on the Dimensional Changes of Copper-Tin Compacts upto 10% Tin," *Metallurgia and Metal Forming*, 1973, v. 40, n. 8, pp. 148-151.

MECHANICAL PROPERTIES OF BRASS POWDER COMPONENT PROCESSED THROUGH PARTICLE SURFACE HEATING (PSH)

Akhter H. Ansari

University Polytechnic, Aligarh Muslim University, Aligarh-202002, UP

ABSTRACT

During sintering brass powder component, the volatile material (i.e. zinc) evaporates at elevated temperature. The evaporation of Zinc causes non-uniformity in composition, loss in weight, change in dimensions etc. The strength of the component is also low as compared to powder components made up of alloys other than brass. Like other powder component, the compaction pressure is found to affect the various properties of brass powder component. In the work under investigation, an electric current is passed through a component. The area of contact between two particles is more than the cross-sectional area in the body of the particles the energy is got managed. This causes more heating at the inter-particle contact surface. In the present case, the effect of compaction pressure on the mechanical properties of the brass powder component is studied. It is found that compaction pressure has a direct effect on the mechanical properties of a component.

INTRODUCTION

The first attempt to produce brass powder metallurgy (P/M) parts was made in the United States and Britain in 1940s¹. The production of brass parts from a mixture of copper and zinc powders by conventional powder metallurgy technique (pressing and sintering) presented considerable difficulties because zinc evaporated during sintering, and it was not possible to decrease the porosity of parts to less than 7 - 10%. This high residual porosity had a deleterious effect on the physico-mechanical properties of materials. Apart from these, evaporation of zinc might have led to non-uniformity of chemical composition and hence physico-mechanical properties across the specimens. The heterogeneity of P/M brass decreased markedly with the use of copper powders pre-alloyed with zinc¹. The evaporation of zinc and the magnitude of volume shrinkage were closed and linearly related to each other². As the quantity $\Delta p/p$ (weight loss in sintering) grew, the level of strength of brass slightly fell, in particular by a factor of 1.5 at a fivefold increase in weight loss. Re-pressing and repress-re-sintering had also shown improvements in mechanical properties. Repressing the parts had increased the strength of brass. It was also found to increase the density of the material to 7.9-8.1 g/cc. The operation reduced the elongation of the material of a sintered part from 15-17 to 8%²⁻⁵. Subjecting parts to coining, which had also increased their density to 7.9-8.1 g/cc, increased the strength of P/M brass. However, coining decreased

ductility, from 5-7% to 2-3% for ordinary brass and from 13-15% to 8% for brass alloyed with phosphorus². Standard tensile test specimens⁶ were produced from 80/20 (lead) 70/30, 90/10 (non-lead) and several other copper-base alloys at a pressure of 775 MPa⁶. Under different conditions, specimens⁷ were sintered in partially covered graphite trays in dissociated ammonia for 30 minutes. It was observed that the mechanical properties increased with the zinc content.

Maximum strength characteristics (i.e. tensile strength σ_t = 250-270 MPa and elongation ϵ = 15%) were exhibited by brass alloyed with 0.3% P. An addition of 0.6% P decreased the tensile strength to 170 MPa, but increased the elongation to 17-18%². Metallographic examinations had shown that raising the phosphorus content had increased the grain and that had accounted for the fall in strength. The strength and ductility of sintered brass were increased when alloyed with small amount of red phosphorus (0.15-0.60 wt. %) ². Phosphorus was added in powder form (a ground copper-phosphorus or copper-zinc-phosphorus master alloy). The optimum amount was 0.3%. In that case the tensile strength was 250-270 MPa at an elongation of 15%. The addition of 0.6% of phosphorus decreased the tensile strength to 170 MPa while increasing the elongation to 17-18%. Humidity of an inactive atmosphere (nitrogen, hydrogen, dissociated ammonia, or endogas) also found to influence the evaporation of zinc. That should contain not more than 2% water vapor⁸. An increase of concentration

MECHANICAL PROPERTIES OF BRASS POWDER COMPONENT PROCESSED THROUGH PARTICLE SURFACE HEATING (PSH)

of water vapour to 5% decreased the values of physico-mechanical properties of brass by half¹. That was due to oxidation of zinc during its evaporation. In view of the marked volatility of zinc, high rates of heating, cooling, and minimum duration of sintering were recommended⁹. A P/M brass composition had been patented containing 1-7% cobalt. The addition of cobalt to a charge had appreciably decreased sintering shrinkage and had increased the hardness and strength of sintered parts¹⁰. The percent theoretical values of density, hardness and compressive strength of brass filing swarf components obtained through DERH technique were found to be comparable with those obtained through muffle furnace heating (MFH) technique and these properties were superior for compacts made from atomized brass powder¹¹. In an investigation it was observed that the current density affected the physical properties of atomized brass powder compacts¹².

The pertinent literature survey shows a need to develop an economically viable simple sintering process for manufacturing brass products through P/M route. Since a non-conventional route remains unexploited, in the present work an electric current is passed through a component and its mechanical properties are studied. In this work the effect of compaction pressure on the mechanical properties of atomized brass powder components is explored.

EXPERIMENTAL CONDITIONS

Details of various parameters with relevant features used in the present investigations are provided in Table 1.

TABLE 1. Details of parameters used in the present investigation.

Items	Parameters	Properties
Powder	Type	Pre-alloyed atomized brass powder
	Particle size	~100 μ m
	Chemical composition	Copper: 70.1%; Zinc: 29.9%
	Apparent density	3.51 g/cc
	Flow rate	19.4 seconds/50 g
Component	Shape	Cylindrical
	Diameter	8.0 \pm 0.3 mm
	Thickness	10 mm - 13 mm
	Mass	3 g - 5 g
Variables	Compaction Pressure	242 MPa to 725 MPa

Experimental Procedures

An electric current (d.c.) was passed axially through a powder component¹³. A predetermined current was maintained for a predetermined period. Likewise, 5 to 6 samples of components were treated for each set of predetermined experimental conditions. Standard deviation and mean were estimated for that experimental condition and used for analysis. Experiments were performed at three levels of compaction pressure.

RESULTS AND DISCUSSIONS

When an electric current is passed through a component, it passes through each particle at a constant level of current. As the particles are mechanically interlocked, the current flows through the particles by conduction. The particles are sphere in shape. The cross-sectional area in the body of particle is more than the area at the point of contact of the particle (Figure 1). Thus, the current density at the point of contact is higher as compared to that in the body of the particle. This higher current density enhances the temperature rise at the area of contacts as compare to the body of the particle. As a result the energy is get managed properly by virtue of the basic principles of electrical energy. Consequently, particle surface heating (PSH) at the inter-particle contact surface takes place. PSH provides a sufficient condition for inter-particle sintering reactions. This sintering technique is more efficient than conventional surface heating sintering technique and even volumetric sintering technique.

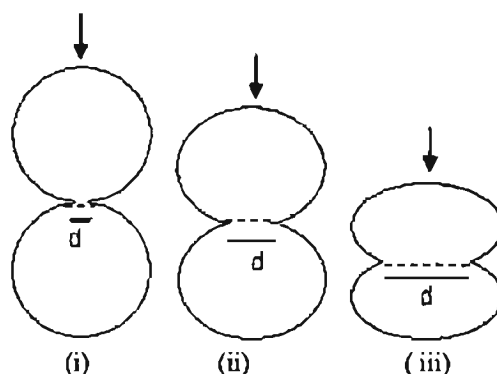


Figure 1. The figure shows the mechanism for particle surface heating (PSH) technique at the inter-particle surface. The diameter (d) is the contact area between the two adjacent particles at (i) low, (ii) medium and (iii) high level of contact pressure.

Hardness of component

Compaction pressure is found to show a major effect on product hardness. It is about 13 HB when specimens are compacted at 242 MPa (Fig. 2). Traces of zinc white are also observed on the surfaces of the components. This attributes evaporation of zinc and increase in porosity of the components. Evaporation of zinc in brass powder components was also observed in earlier investigations^{1, 8, 9}. Some of these vapours of zinc may have segregated in the pores between the particles. This might have caused low hardness of component.

The hardness of brass component is found to increase to about 30 HB with an increase in compaction pressure to 483 MPa. It may be due to higher packing that controls the

MECHANICAL PROPERTIES OF BRASS POWDER COMPONENT PROCESSED THROUGH PARTICLE SURFACE HEATING (PSH)

movement of zinc vapours. The increase in hardness attributes to fusion between the powder particles and strengthening inter-particle bonds. The increase in compaction pressure has reduced the pore size and the affinity for inter-particle fusion has increased. It also confirms the earlier findings^{13, 17} that the shrinkage of the components with an increase in compaction pressure is due to the fusion of powder particles at their boundaries. A further increase in compaction pressure to 725 MPa has caused a little decrease in product hardness. It is a deviation from the earlier findings. However, the ductility is better. It may have increased fusion between particles.

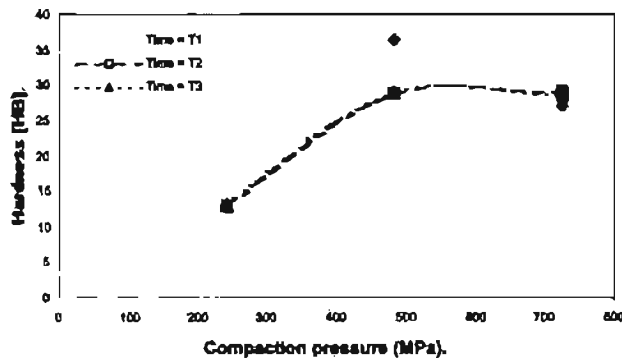


Figure 2. Effect of compaction pressure on the hardness of component.

Strength of components

Figure 3 shows the effect of compaction pressure on the compressive strength of brass powder components. The compressive strength of components is about 15 MPa when the powder is compacted at a level of 242 MPa¹³. Components undergoing second phase sintering may also depict low strength. Low compressive strength may be due to these phenomena

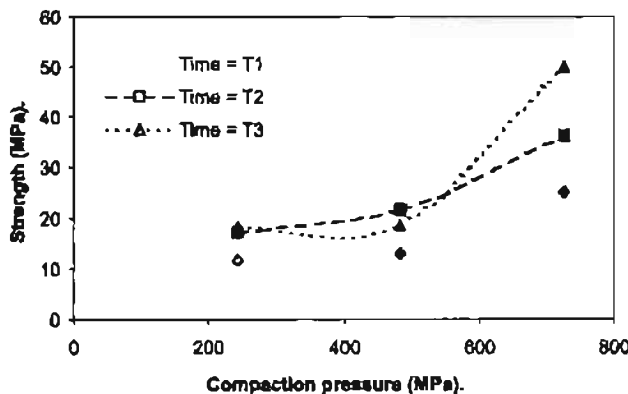


Figure 3. Effect of compaction pressure on compressive strength of component.

An increase in compaction pressure is observed to increase in compressive strength. The increase in strength is more when the compaction pressure exceeds 483 MPa. The behaviour of the curve deviates from that of hardness at this level of compaction pressure. The strength of the brass powder components is almost doubled when the compaction pressure is tripled.

CONCLUSIONS

It can be concluded that particle surface heating (PSH) affects sintering reactions. Moreover, compaction pressure affects the mechanical properties of brass powder components processed through PSH technique. An increase in the level of compaction pressure increases the affinity for inter-particle fusion. Inter-particle fusion is more significant at higher level of compaction pressure. The mechanical properties of component increase with an increase in the level of compaction pressure.

ACKNOWLEDGEMENT

It is also a proud privilege for me to note with deep sense of gratitude that Prof. M. Hamiuddin, Department of Mechanical Engineering, A.M.U., extended his help to conduct experiments regarding hardness tests.

REFERENCES

1. A.V. Dovydenkova and I.D. Radomysel'skii, "Production and Properties of Constructional Parts from Copper and Copper Alloy Powders, A Review". Poroshk. Metall., No. 3, (1982) 44-53.
2. V.E. Terletskii, V.S. Kalish, S.V. Bronin and V.A. Shatskii, "Production of Brass Powder and Constructional Brass Parts", in: Sintered Constructional Materials, [in Russian], Inst. Probl. Materialoved., Akad.Nauk Ukr. SSR, Kiev pp.17-25, 1972.
3. W. Cegielski, "Investigation of the Brass Powder Atomization Process", Prace Inst. Met. Niezaleznych, Vol. 7, No. 3, pp. 139-143, 1978.
4. V.E. Terletskii, I.Yu. Epshtein and S.V. Bronin, "Production of Sintered Brass from Unhomogenized Powder Mixtures by Liquid-Phase Sintering", in: Sintered Constructional Materials, [in Russian], Inst. Probl. Materialoved., Akad.Nauk Ukr. SSR, Kiev pp. 51-55, 1976.
5. P. Groat, "Manufacture of Parts from Iron Powder" [Russian Translation], Mashgiz, Moscow, 1960.
6. P. Mathews, "The mechanical properties of brass and developmental non-ferrous P/M materials", Int. J. of Powder Metallurgy, v. 5, n. 4, pp. 59-69, 1969.

**MECHANICAL PROPERTIES OF BRASS POWDER COMPONENT PROCESSED
THROUGH PARTICLE SURFACE HEATING (PSH)**

7. GT. Brown and R.R. Jones, "Experimental Aspects of the Powder Forging Process", Modern Development in Powder Metallurgy, Vol. 4, New York, pp. 369-371, 1971.
8. J. Willcock and R.J Woolfall, "Pressing and Sintering of Nickel Brasses", Metallurgiya, Vol. 63, No. 4, pp. 378-382, 1979.
9. E. Paller and D.A. Grimme, "Investigation of the Possibility of Producing Sintered Brass Parts", [in Russian], New Materials Produced by the Powder Metallurgy Method, Moscow, pp. 137-146, 1966.
10. U.S.A. Pat. No. 4139378, "Sintered Cobalt-Containing Brasses", 1979.
11. A. Afaq, and M. Hameedullah, "Potential of DERH technique in sintering the brass filing swarf compacts", Advances in Powder Metallurgy and particulate materials - 1995, v. 1, pt. 4, pp. 163-173, 1995.
12. A. H Ansari, M. Hameedullah and A. Afaq, Advances in powder metallurgy and particulate materials, MPIR, 1 part 4 (1995) 153 - 161.
13. A.H. Ansari, "Consolidation of brass powder components", Presented in International P/M Conference, PMAI, Mumbai, February 2-7, 2005.

DEEP SUB ZERO PROCESSING OF COMPONENTS MANUFACTURED BY POWDER METALLURGY TECHNIQUES

Kumar M. Iyer

Assab Sripad Steels Ltd., Mumbai.

ABSTRACT

PM components are fast replacing conventional materials in various applications. Whether it is WC or PM High Speed Steel for Cutting tools & Cold Work Tools, PM steels for various applications in warm forging or Plastic Moulding, the performance criteria established by PM tool materials are hard to replicate. Non Ferrous PM components are fast becoming the norm for exotic and non conventional applications and for hard to melt alloys. Hardening and heat treatment of such alloys may not be possible in all instances for tool life increase. Hence, the only solution is Deep Sub Zero Processing of these alloys. This paper dwells upon the Deep Sub Zero Technology & Processing of various PM alloys for improvement of wear resistance & product life and explores possible reasons for such improvements.

INTRODUCTION

Powder Metallurgy, which was considered for long as a subject of research and restricted to the realm of exotic or hard to melt alloys, is fast becoming a commonly accepted process in the industrial mainstream. Components which were earlier manufactured using conventional means are now being manufactured using powder techniques. The reasons for this may be many fold, either for achieving a level of porosity in the component as may be the case of self lubricating bushes or bearings, or for combining hard to mix alloys in the molten form, such as high Vanadium content in steels, or for achieving a high cleanliness level and desired microstructure in the material such as in the case of High Speed Steel where the Carbide Network is completely absent in the powder. Sintered Carbide tools have long been used for manufacturing but compulsions of processing demands have turned the attention of manufacturers towards other high alloy steels which are invariably manufactured by the PM route. Hence, the fact remains that PM technology is fast making inroads into the conventional manufacturing practice.

DEEP SUB ZERO PROCESSING

Deep Sub Zero Processing (DSZ Processing) is a vastly misunderstood subject which is attracting the attention of manufacturers and end users of tools and industrial machinery for a variety of reasons. As far as this technology is concerned there seems to be no middle ground. The proponents of this technology are willing to stake their all on the technology while the detractors are equally vehement

in dismissing the effects of this technology. The singular reason for this is the lack of scientific research on the process and the various process parameters associated with this operation. While time-temperature data are very well documented for the Heat Treatment operations on various materials, there exist little or no data on the exact time temperature profile to be adopted for processing various materials.

The concept itself is very simple. Cooling the material down to deep sub zero temperatures causes irreversible changes to take place in the crystal structure of the metals leading to enhancement of various properties in the materials.

DEEP SUB ZERO PROCESSING TECHNOLOGY

The word, "Cryogenics" comes from two Greek words – "kryos" which means cold or freezing, and "genes" meaning born or generated. Technologically, it means the study and use of materials at very low temperatures. The upper limit of cryogenic temperatures has not been agreed on, but the National Institutes of Standards and Technology has suggested that the term Cryogenics be applied to all temperatures below -150°C (-238°F or 123°K)

DSZ processing of metals and alloys is carried out in an automatic, computer controlled insulated environment chamber by means of "complex time temperature prescriptions" up to -200°C (73°K). The rate of temperature drop is controlled so as not to exceed a certain critical cooling rate. Cooling takes place by gas kinetics

and at no point in time does the payload come in contact with the cryogenic liquid.

This use of precisely controlled temperature profile avoids any possibility of thermal shock and thermal stress that is experienced when a tool or part is subjected to abrupt or extreme low temperature changes. By eliminating the need for circulation fans and onboard heating element, the process allows the chamber to remain 100% moisture free during the entire process.

METALLURGY OF DEEP SUB ZERO PROCESSING

Deep Sub Zero treatment of metals and alloys is a deep stress relieving technology. Whenever material is subjected to any manufacturing operation, be it machining, forming, stamping, grinding, wire cutting, EDM, etc. it is subjected to stresses. The stress manifests itself in the nature of defects in the crystal structure of materials. The most commonly observed defects are in the form of vacancies, dislocations, stacking faults etc. As the level of stress increases, the density of these defects increases, leading to increase in the inter atomic spacing. When the distance between the atoms exceeds a certain critical distance, cracks develop and failure takes place.

The third law of thermodynamics is usually stated as a definition 'the entropy of a perfect crystal of an element at the absolute zero of temperature is zero.' At the absolute zero of temperature, there is zero thermal energy or heat. Since heat is a measure of average molecular motion, zero thermal energy means that the average atom does not move at all. Since no atom can have less than zero motion, the motion of every individual atom must be zero when the average molecular motion is zero. When none of the atoms which make up a perfectly ordered crystal move at all, there can be no disorder or different states possible for the crystal.

Deep subzero treatment uses this principle to relieve stresses in the material. The materials are subjected to extremely low temperatures for a prolonged period of time leading to development of equilibrium conditions. This leads to ironing out of the defects in the material and also attainment of the minimum entropy state. Grain shape and size gets refined and is made uniform. Defect elimination takes place and inter atomic distance is reduced. When the material is brought back to room temperature, the defect level reflects an equilibrium concentration. Compaction of the crystal structure leads to much superior abrasive, adhesive and erosive wear resistance and homogeneity in hardness with enhancement in corrosion resistance as well as fatigue strength and resilience.

In Steels which have been heat treated, the deep sub zero treatment first converts any Retained Austenite into

Martensite, and the Martensite is tempered as the steel returns to the room temperature. The Martensitic structure resists plastic deformation much better than the Austenitic structure, because the small carbon atoms in the Martensitic lattice 'lock together' the iron atoms more effectively than in the more open face centered cubic Austenite lattice. Tempering the Martensite makes it tougher and better able to resist impact than untempered Martensite. Martensite is harder and more wear resistant structure.

EFFECT OF DSZ PROCESSING ON PM COMPONENTS

DSZ Processing has different effect on different PM materials. In hardened steels such as High Vanadium Tool Steels or High Speed Steels, the DSZ processing improves the dimensional stability and accuracy of the steels by reducing the Retained Austenite in the microstructure. More importantly, however, DSZ processing improves the surface finish of the steels drastically.

These steels are normally used either by themselves or with various types of PVD coatings. By reducing not only the Surface Roughness (Ra value) but also the amplitude of the fluctuations between the highest peak and the deepest valley on the polished surface (Ry value), it has a tremendous impact on the adhesion of the PVD coating on the surface of the steel. This leads to better coating performance and longer tool life. Tools have shown almost double life in operations such as deep drawing, bending and also for machining operations after they have been subject to a process route comprising Heat Treatment – DSZ Processing – Grinding – PVD Coating.

The second cause of failure of these high alloy tool steels is due to the various grinding marks/ polish marks on the surface, which can be potential sites for the nucleation of the cracks and subsequent failure of the cutting edge/work surface of the tool. By eliminating the incidence of such deep scratch marks on the surface, DSZ processing enhances the longevity of the tools and thereby improving tool performance and minimizing the tool failure by micro chipping.

In non ferrous materials, DSZ Processing has a very significant impact on the tensile and wear properties of the materials. Copper bushes made by PM route show an increase in wear life by over 75%. Copper-Chromium and Copper-Tungsten spot welding electrodes show an improvement in life of over 100%.

The reason for the improvement in life can be directly related to the compaction in the crystal structure which takes place in these FCC metal matrices due to better packing density of the atoms in the crystal and a reduction in the

DEEP SUB ZERO PROCESSING OF COMPONENTS MANUFACTURED BY POWDER METALLURGY TECHNIQUES

Bragg Distances. Measurements in annealed, electrolytic grade conventional copper metal bar show a decrease in Bragg Distances by 8 – 10% indicating a significant increase in the packing density of the crystals.

Besides, the DSZ Processing also reduces the stress levels in the materials drastically which leads to improvement in tensile properties such as YS of the materials. This has a direct correlation on properties such as Fatigue Strength and Resilience of the alloys.

CONCLUSIONS

Deep Sub Zero Processing of PM manufactured materials has a positive impact on the overall performance of the tools and machine parts made with these alloys. The effect

on various alloys depends on the end use of the component manufactured from the alloy whether it is in the form of a cutting tool in the case of High Vanadium or other High Speed Powder Metallurgy Steels, or various types of Bushes and Bearings made with various copper alloys. The exact mechanism of this improvement is not very clearly understood but prima facie evidence points to two factors viz. the reduction of stress levels in the alloy and the increase in the packing density of the alloy. Further investigation of the various phenomena coupled with scientific studies and advanced measurement techniques such as XRD, SEM, TEM and other microscopy techniques will enable other researchers to better understand the underlying reasons for this behaviour of PM components subject to DSZ temperatures.

POWDER METALLURGY & DIAMOND TOOLS – AN OVERVIEW OF THE INDIAN INDUSTRY

P. K. Korgaonakar

INTRODUCTION

Diamond Tools are designed and manufactured for the following sectors of industry:

- a. Oilfield drilling for oil exploration
- b. Mine Drilling for mineral exploration / Foundation investigation
- c. Engineering Industry
- d. Construction Industry
- e. Stone excavation & cutting Industry

SECTORS OF INDUSTRY

a. Oilfield drilling for oil exploration

In India, drilling for oil well exploration is done on land as well as sea. Oilfields are located in Gujarat, North-Eastern states, Rajasthan and possibly oil fields may be discovered in other states too. Oil wells are also drilled in the Western and Eastern offshores of India. Oil & Natural Gas Commission, commonly known as ONGC is drilling onshore and offshore oil wells alongwith many other Indian and foreign companies who have undertaken oil well drilling.

Oil well drilling still continues to increase as consumption and prices of oil are increasing rapidly.

b. Mine Drilling for mineral exploration/Foundation investigation

Mineral exploration is carried out to locate various mineral deposits below the surface of the earth. Geological Survey of India, Mineral Exploration Corporation and various departments of Mines and Geology of State Government are using diamonds tools to drill below the surface of the earth and take out samples of minerals at different depths. The recovered samples are analysed for its various mineral content. Deposits of minerals present in the area are calculated on the basis of the analysis report of the samples acquired.

Subsequently, mining is carried out to recover the minerals.

Foundation investigation is carried out to know the strata before the construction of dams, bridges, heavy

constructions, etc. Diamond core bits are widely used to extract samples of the rocks at the required levels. Foundation is decided on the analysis of the core samples.

c. Engineering Industry:

Engineering industries are using diamond tools for various applications such as cutting, grinding, machining, honing, etc.

d. Construction Industry:

Diamond tools are widely used in the construction of various infrastructures. Consumption of diamond tools for construction industry is the highest among all sectors of industries.

I understand that United States is the highest consumer of diamond tools in construction industry. These tools are used in the construction of roads, airports, bridges, buildings, etc. However in India, consumption of diamond tools in construction industry is relatively very low. We still use chisels, hammers, etc. in construction. Our focus should be on the development of machines, equipments as well as tools for the construction industry in India.

e. Stone excavation & cutting Industry:

Stone processing industry is the largest consumer of diamond tools in India. It gives employment to large population in rural areas.

Stone is quarried in Rajasthan, Gujarat, Madhya Pradesh, Karnataka, Andhra Pradesh, Tamilnadu, etc.

Until about 1975, marble was sawn with Steel plates using sand and water as the cutting medium. The steel plates were fitted on a frame of the a gangsaw machine and cutting speed was 8 – 10mm/hr. Machines would run continuously for 24 hrs with diesel engine. It took approx. 6 – 7 days for sawing one block of marble of about 1 mtr. ht. Today, similar sizes of blocks of marble are sawn with diamond tools in about 4 – 5 hrs. at much cheaper costs.

Change over from traditional method of diamond tools was not easy since the local people in rural areas still believe that theirs was a better method of cutting marble.

When young and enterprising entrepreneurs entered into this field, some modifications were made on old machines and trials were conducted with diamond tools. Cutting speed increased from 5-10mm/hr. to 30-40mm/hr.

At the same time, few imported diamond sawing machines were commissioned. Many entrepreneurs started production of diamond tools and in the next 10 years, diamond tools took over sand and water sawing of marble.

Another example that of Limestone, commonly known as Kota, Tandur, Cuddappah is extracted from quarries in slab form. Initially, thicker layers of limestone were blasted off and only required sizes of slabs were extracted from the lower depths. Although large manpower was employed, production was low.

Diamond tools were introduced in limestone industry in 1985. Instead of blasting off thick slabs, deep grooves were made by diamond tools in the limestone quarry and thicker slabs were extracted and process continued. Therefore, the entire quantity of slabs in the mine was fully utilized. Thick layer of upper strata were taken to factories and sawn/cut into required thickness by using diamond tools. The use of diamond tools reduced the cost of production by more than 50%.

Various types and colours of granite are used in stone industry. Diamond tools are widely used for cutting and polishing granites. The cost/ft. of cutting granite with diamond tools is decreasing due to falling price of diamonds and diamond tools. With improved technology, diamond tools have increased productivity and reduced cost of production.

Other decorative stones for building constructions are sandstone, slates, etc. These stones are cut extensively and economically with diamond tools.

With this introduction, I turn to product range i.e. type of diamond tools used in various sectors of industry.

MANUFACTURING PROCESS OF DIAMOND TOOLS

Manufacture of diamond tools was a closely guarded secret. It is a good sign to see that many technocrats are offering technology, machines, equipment, diamonds, metal powders and also giving demonstration of producing diamond tools, especially in the stone industry.

The following types of tools are used in the respective sectors of industry:

- a. Diamond drill bits and core bits for oil industry
- b. Diamond core bits for mines and foundation investigation

- c. Metal & Resin bonded diamond wheels, diamond honing sticks, diamond dressers, diamond indenters for Engineering industry
- d. Diamond core drills and diamond saw blades for construction industry.
- e. Diamond saw blades, Frame saws, Gangsaws, Diamond polishing tools and Diamond wire saws for stone industry.

a. Diamond drill bits and core bits for oil industry:

These bits are made in size from 5" to 12¼" dia. Cutting elements are natural diamonds or polycrystalline diamonds. Bit consists of alloy steel holder surrounded by Metal matrix, in which diamonds are embedded in the matrix as well as on the surface of the bits. The steel alloy called "Steel shanks" or "Steel blanks" is threaded at the top. Long and heavy steel tubes called "Drill Collars" are fitted at the top end. These Drill collars are connected to comparatively thinner tubes called "Drill pipes" and the assembly is suspended from a drilling rig. Drilling fluid called "mud" flows through the centre of the tubes which helps to drill bits and take away the rock cuttings. Drill collars control weight on the bit and drill pipe facilitates rotation of the bits. Presently hydraulic drill motors are used in drilling oil wells. Drill pipes are stationery and rotation of bit is done by Hydraulic drill motors.

Continuous logging of the mud over the well during drilling gives indication of the hydro carbon present in the area. Logging information is used for designing most suitable bits for the formation. Initial costs of these bits are very high because of the cost of cutting elements of the bits but, fast cutting speed and long tool life makes cost/ft. of drilling more economical than the conventional bits, especially when the rig costs are very high. The only drawback is that these bits do not give good performance in high compressive strength rocks.

Manufacturing process of Oilfield bits:

Mould is made from graphite rods. It is machined to the contour / profile of the bit. Location for diamond and fluid passages are made in a mould. Natural diamonds are set before sintering, but polycrystalline diamonds with cemented carbide substrate are brazed after the bit is sintered. Cast or Fused Tungsten Carbide in coarse and fine mesh is filled over diamonds and the alloy steel blank is placed over centre of the mould.

Binder material in rod form usually made of copper, nickel and zinc is placed over the matrix and graphite cover is placed over the mould. Mould assembly is heated in electric furnace at a predetermined temperature. The binder melts

and infiltrates in the metrix. Upon cooling it makes a strong bond between metrix, diamond and the steel shank. After cooling, the bit is separated from the graphite mould. The shank is machined to required dimension and threads are cut at the top end of the Shank. However, polycrystalline diamond bits are brazed to the bit crown, after the bit is sintered.

b. Diamond core bits:

These bits are manufactured in International standard sizes and ranges from 30mm-100mm outer dia. The cutting elements are natural diamonds or polycrystalline diamonds. These diamonds are embedded on the surface of the bits crown having steel shank.

Two types of bits are commonly used viz. surface set and impregnated type.

Bit is coupled to a steel tube and fitted in a mine drilling machine. Diamonds penetrate into the rock, depending on the weight and type of rock being drilled. As the drilling progresses, rock samples enter the drill bits and in steel tubes above the bits. After drilling required length, core is removed for analysis for its mineral contents. These bits are manufactured by infiltration, induction or hot press sintering technique. The process of manufacture is very similar to oilfield bits manufacture.

c. Metal bonded Diamond grinding wheels:

Diamond wheels are manufactured in a wide range of sizes and shapes for grinding non-ferrous components and tools. It consists of diamonds, metal metrix and disc. Proportionate mixtures of diamond and metal metrix are mixed and processed in special quality, thermally stable moulds. The moulds are heated to required temperature and then pressed to predetermined pressure.

Similar moulds are also sintered by induction heating.

d. Diamond Segmented Saw Blades:

Diamond segmented saw blades are manufactured in size 100mm to 2000mm dia although higher diameter blades are also manufactured. It consists of 2 components – Circular Steel Saw Blank and cutting element called “Diamond segment”. Raw material of diamond segments are:

- Synthetic Industrial Diamond Powder
- Metal Metrix Powder
- Additives

Following parameters are taken into account in the design and manufacture of diamond segments:

- Type of stone, its hardness, abrasive resistance, compressive strength, grain size, distribution of abrasion resistance material in the stone.
- Depth of cut and cutting speed desired.
- Machine HP and surface speed
- Cost/ft. of cutting desired by the end user
- Electricity and labour cost
- Machine Maintenance down time
- Profit desired in the manufacture and production of segments.

The desired properties of the segments are obtained by:

1. Quality, size, distribution and quantity or volume fraction of diamonds.
2. Choice of metal metrix powders, its properties and cost
3. Choice of additives, its properties and cost.
4. Condition of mixture / metrix
5. Granulation
6. Cold compression
7. Reduction
8. Sintering

Diamond segments are sintered in the temperature range of 680°C to 1050°C. Higher temperature may be used for special application subject to graphitization of diamonds.

Manufacturing process of Diamond Segments:

Diamonds and metrix weights are calculated on volume percentage basis. Metal metrix powder and diamonds are mixed and granulated. The powders are cold compacted at about 2 tons/cm². The cold compacted segments are assembled in a graphite mould machined to the dimension. Moulds are heated in hot press sintering machine at about 300 – 350 kg/cm² pressure. Total cycle time ranges from 10 – 20 mins. depending upon sintering parameters.

Wire saw diamond beads are also manufactured in hot press sintering technique.

Frame saw / Gang saw blades are used for slicing stone blocks into slabs. The steel blanks are 4000mm long x 180mm ht. and 2.5, 3 or 3.5mm thk.

Diamond segments are brazed at predetermined spacing on the steel blank to form frame saw blades. These blades are fitted on frame of Gangsaw machines. 50 – 100 blades form one assembly for sawing of marble blocks into slabs.

Wire saw consists of multi strand steel wire ropes in which cutting elements called "Beads" are inserted at regular intervals. These beads are of 11-12mm dia and 6-8mm long and are used for quarrying marble and granite blocks. Each wire saw is 25 – 50mtrs. long.

The cutting element of diamond tools are manufactured by one of the following sintering process.

1. Free sintering
2. Hot press sintering
3. Infiltration sintering
4. Hot Isostatic pressing
5. High Frequency induction sintering

Each of these processes has certain advantages and limitations.

SYNTHETIC INDUSTRIAL DIAMOND POWDER:

Diamonds are manufactured by Hot press sintering technique. At pressure over 150 tons/cm² temperature over 1400°C, graphite gets converted into diamonds in the presence of molten catalyst. The quality, quantity and size of diamonds produced depends upon pressure, temperature and time.

We manufacture diamonds in a cubic press with six cylinders each generating 1500 ton. The cold pressed compacts are fitted in an insulation cubic block, and this assembly is heated as in Hot press sintering process. The diamonds are recovered by acid treatment and separated into various qualities.

Very few tool manufacturers in India produce diamonds for their consumption.

PERFORMANCE CRITERIA

End users require diamond tools with lowest cost per foot of cutting together with fastest speed of cutting. Manufacturers compete to achieve these criteria. Electrical power consumption and manpower together with tool/equipment wear and tear are taken into account in calculating cost per tool of cutting.

MARKET SCENARIO

The diamond tool (for both stone and industrial use) industry was established in late sixties-early seventies.

The market grew and so the industry. The growth was rapid during eighties and early nineties. All through this period GE and Dee Beers (two USA/European) dominated the Synthetic Industrial Diamond Powder market with a small share left for Japanese and Korean suppliers.

The Chinese entered the market of industrial diamonds in mid-nineties. The quality was not up to the expectations. However, by late nineties the quality had improved substantially. The old players had to take steps to fight for the market share. The prices started dropping first slowly and then at a faster rate. Eventually, one USA supplier sold its diamond division to a finance company.

The diamond tools from China for stone processing started entering Indian market by late nineties. The quality was not up to the requirements. However, the prices were 60-65% of the Indian products. The quality eventually became acceptable and the prices dropped further in tandem with diamonds.

The Chinese also experimented with non-cobalt bonds aggressively and achieved a technical breakthrough. This further depressed the prices of tools.

Added to this, diamond tools entered India through grey markets. This has made our products still costlier. Today Chinese suppliers dominate tool market in some markets and also supply large quantities of Synthetic Industrial Diamond Powder to Indian tool manufacturers.

CONCLUSION

Challenges for Powder Metal fraternity:

- Cost effective sintering technology
- Cheaper bonding system
- Alternate manufacturing ways
- Quality upgradation
- Optional utilization of diamonds.
- Design of tailor-made products and corresponding process parameter for specific application Science & Technology at the services of the end user: Key to survival & success.

TRENDS IN DIAMOND TOOLS FOR STONE PROCESSING

R. R. Thorat

R&D Manager, Reliance Diamond Tools Pvt. Ltd., Sri Lanka

ABSTRACT

The paper presents a platform to discuss the trends in diamond tools used for stone processing. It gives selection criteria for the composition of matrix and diamond for the stones in Andhra Pradesh. The trend of developing iron and copper based matrix powders is discussed. Recent developments in stone cutting wires and segments, technical and commercial effect of Chinese diamond tools in India are discussed.

INTRODUCTION:

The dominance of cobalt powder in diamond tools is about to over due to the cost and availability, but it cannot be replaced totally because of its acceptable chemical compatibility with diamond at the processing temperature and good wear resistance for a number of cutting operations. The trend is set to develop the iron or copper based matrix powders with lower percentage of cobalt. The diamond tool companies are trying to use these matrices because of cost and performance issue. In addition, they are putting lot of money to develop their own bond material suitable for the specific stones. Table 1 shows recent pre-alloyed powders, which are in the market developed by mainly European companies and being used as a matrix material for stone cutting diamond tools.

i. NEXT Powders

Cu, Co and Fe in predetermined ratios have been produced and launched by a powder producer under the name NEXT. The pre-alloyed powders have certain advantages over cobalt powder as a matrix material for diamond tools.

ii. Cobalite HDR

Cobalite HDR is widely used pre-alloyed powder for hot pressed diamond tool segment. The use of HDR for free sintering is restricted by the lower percentage of Copper.

iii. Powder developed in P/M lab, IIT Bombay

The powder developed in the laboratory is premixed-pre-alloyed powder. Nitrates of copper, cobalt and iron were mixed in the water and heated to dryness. The dried mixture of salts was reduced in hydrogen atmosphere to get Cu-Co-

Fe pre-alloyed powder. The reduction temperature, heating rate and holding time were varied to obtain the pre-alloyed powder of higher purity and smaller grain size. {1-4}

Table 1: Pre-alloyed powders

1. NEXT Powders

Element	NEXT100	NEXT200	Cobalite HDR
	Wt %	Wt %	Wt %
C	0.039	0.039	2.42
O	1.07	1.04	0.76
Fe	25.2	14.7	63.96
Co	24.1	22.6	27.89
Cu	49.5	61.7	4.98
Total	100	100	100

Element	Wt %
C	4.31
O	0.83
Fe	26.45
Co	24.31
Cu	44.1
Total	100

Diamond segments:

The segment area of diamond tool is susceptible to fluctuation in the market cost and requirements of the user due to intrusion of Chinese circular saw segments. The logical way to cope with the Chinese invasion is by

developing low cost-stable quality bonds. It is wrong to conclude that the Chinese do not have quality. There are few companies, which are having top quality products with lower prices. However, there are few points to consider while competing with Chinese companies as follows:

1. Primary studies suggest that Chinese segments have basically iron-based premixed/pre-alloyed powder bonds.
2. The geometry of the segments (grooved, multilayered) is the important point to be considered.
3. Also, the stone material has to take into consideration.
4. Increasing the height is one option to tackle the balance between free cutting and high wear resistance bond.

Table 2 shows the cutting performance of the stone material usually found in south India against gang saw cutting.

Stone cutting	Response to sawing
Sapphire Brown	Hard
Sapphire blue	Hard
Black galaxy	Soft
Black	Hard
Tan brown	Hard
Red multicolor	Hard
Madurai (6-7 colors)	Soft
Paradise	Medium

Diamond Wires:

Despite loss in the profit margins in segment area, the diamond wires are still popular in diamond tool manufacturing companies. During this period, development in wire technology is seen as crucial as a long-term goal and vital development to diamond tool industry. R&D groups of various diamond tool companies are trying to replace the inevitability of pre-alloyed powder and cobalt content from the bond material. Currently, wires are being manufactured on the basis of their use in stone cutting and type of stone and thinner, more flexible, multistone cutting wires are the latest in wire technology for stone cutting. It has found out that Chinese companies are still not much into this part of diamond tool division.

Globalization in Diamond Tool Manufacturing:

In the words of Friedman, the world has become flat. Like USA, India is outsourcing the manufacturing jobs to cheap labor sites in another countries. Due to free trade policies of other countries, it is easy to transport powders from other countries to country of manufacturing plant instead of getting the powders to India. It's the international exposure that also matters in this case. Like for instance, the product is sold in India as an imported one, which has its effect on consumers. However, the communication gap between head office and manufacturing plant is a big problem. Although, electronic media helps to connect, online observations are of little help to effectively change or improve the production. There is also problem with quality control and performance evaluation, which affects production time.

Effect of Stone Material on The Wires of Same Composition:

One of the important points is the selection of right bond for right stone material. Most of the time it is falling outside the area of R&D manager to check the stone cutting response against the designed bond material. The selection of the composition partly depends on the stone material's composition, hardness and microstructure. The usual method is to prepare wires and segment sets and send it to the different distributors and so different users. The observation data, which includes the life of cutting and wear of the segments, is sent to the R&D manager for performance evaluation.

Table3 shows the stone materials at Ongole-Gurujapalli area of Andhra Pradesh. At the area of Coral Rocks, the stone material is stone 2 (softer material), which shows 30% more wire life when compared to stone 1. Another material found in the area, stone 3 has slightly different composition than that of stone1 and 2 leading to different performance of wires. Stone 3 proves to be harder material with respect to Stone 1 in terms of cutting. For, this kind of stones, the prices for the 50m wires are usually between 1Lakhs to 2.5 Lakhs depending on user's preference on the performance-cost balance and the type of cutting. However, it should be known as the general experience of the other quarry supervisors. Also, it is observed that most of the quarries do not have any subsequent accounting of the parametric details of cutting, which leads no written proof of wire performance.

Table 3 Stone Materials at Ongole-Gurujapalli Area of Andhra Pradesh

	Stone 1	Stone 2	Stone 3
SiO ₂ (%)	59.72	6.4	51.22
Al ₂ O ₃ (%)	14.17	12.24	12.14
Fe ₂ O ₃ (%)	3.34	6.97	14.37
Hardness (Mohr's scale)	6.5	6.5	7
Fe (%)	2.4	4.9	10

CONCLUSIONS:

1. The trend is set to develop the iron or copper based matrix powders with lower percentage of cobalt.
2. The selection of composition of matrix and diamond is based on stone composition and microstructure.
3. Chinese segments have taken large share of Indian market due to low prices-stable quality performance.
4. Diamond wire saw is still the area where the Indian companies get more margins in profit as compared to segments.

REFERENCES

- [1] M. del Villar, P. Muro, J. M. Sanchez, I. Iturriza, and F. Castro, "Consolidation of diamond tools using Cu-Co-Fe based alloys as metallic binders", *Powder Metallurgy*, 44, (2001), pp.82-90.
- [2] H. K. Tonshoff, H. Hillmann-Apmann and J. Asche, "Diamond tools in stone and civil engineering industry: cutting principles, wear and applications", *Diamond and Related Materials*, 11, (2002), pp.736-741.
- [3] I. E. Clark and B. J. Kamphuis, "Recent developments in pre-alloyed powders for diamond tooling", *Proceedings of European Conference on Hard Materials and Diamond Tooling: Euro PM2002*, Lausanne, Switzerland, Oct.7-9, (EPMA, UK, 2002), pp.35-42.
- [4] W. Tillmann, "Trends and market perspectives for diamond tools in the construction industry", *International Journal of Refractory Metals and Hard Materials*, 18, (2000), pp.301-306.